Biosphere-Atmosphere Gas Exchange Measurements using Fourier Transform Infrared Spectrometry

Zur Erlangung des akademischen Titels einer
Doktorin der Naturwissenschaften (Dr. rer. nat.)

von

Hella van Asperen

1. Gutachter Prof. Dr. Justus Notholt
2. Gutachter PD Dr. Annette Ladstätter-Weißenmayer

eingereicht am: 21. September 2015
Promotionskolloquium: 16. November 2015

Abstract

Field measurements of biosphere-atmosphere gas exchange are of great importance because they provide the possibility to study greenhouse gas dynamics and its feedback mechanisms in detail. This thesis contributes to the further development of concentration and flux measurement techniques to study biosphere-atmosphere exchange processes, by exploring the possibilities of using an in-situ Fourier Transform Infrared (FTIR)-analyzer for ecosystem research. This instrument is capable of measuring CO_2, CH_4, N_2O, CO, and $\delta^{13}CO_2$ simultaneously. It was combined with different flux measurement techniques, such as the flux gradient technique, the ratio-nocturnal boundary layer technique, and the flux chamber technique. The system was used in four different field campaigns and several laboratory studies, and details about the system were published in van Asperen et al. (2015a). This thesis focuses on the use of the system to a) apply and assess different (new) flux measurement techniques, and b) study different flux and ecosystem processes.

Several aspects of different flux measurement techniques were assessed. The parameterization of the diffusion coefficient, required for the flux gradient technique, was studied. In this thesis, it is shown that common parameterizations from the literature underestimate the ecosystem CO_2 fluxes. A new type of parameterization, which combines eddy covariance diffusion measurements and meteorological parameterizations, is described and evaluated. This approach enables reliable flux gradient measurements for multiple gases. Furthermore, a new flux measurement method, the ratio-nocturnal boundary layer (R-NBL) technique was tested. The R-NBL technique infers the fluxes from the simultaneous increase of at least two gases in the boundary layer, and the accompanying (eddy covariance) flux measurements of one of the gases. This technique was compared to eddy covariance flux measurements for the first time, and a good agreement was demonstrated. The measurements show that the R-NBL technique is able to detect very small N_2O fluxes, and a detection limit of 0.004 nmol m^{-2} s^{-1} for N_2O fluxes was estimated. Such a low detection limit is not reached by other micrometeorological techniques, which makes the R-NBL technique very suitable for measuring trace gas fluxes in homogeneous ecosystems. In addition to the direct flux measurements, the FTIR-analyzer was also employed in a forest ecosystem to investigate the spatial variation of gas concentrations in a forest, which is important in order to better understand the storage of gases below the forest canopy. The storage component is important for the flux calculations from forest ecosystems. Horizontal concentration measurements inside the canopy showed large spatial and temporal variation of gas concentrations within 10 meters distance. The vertical concentration profile was found to be very different for different gases. For correct determination of the storage component, it was concluded that multiple vertical concentration profile measurements are needed within the canopy.

Different process level studies were performed by use of the measurement set-up. N_2O production mechanisms could be studied in a ^{15}N-labeling experiment, in which different agricultural fertilizers were used. The results showed that the FTIR-analyzer is capable of measuring different isotopologues and isotopomers of N_2O at low concentrations. The experiment revealed the fast and relatively large loss of fertilizer-nitrogen (1%) via N_2O emission right after fertilizer application. Furthermore, the role of photo- and thermal degradation in arid ecosystem carbon dynamics could be studied in the field and the laboratory. No photodegradation induced CO_2 and CO fluxes were found in the field. Thermal degradation fluxes were observed in the field (for CO) and in the laboratory (for CO and CO_2). The thermal CO production in the field was

partly buffered by biological soil CO uptake. These findings are in contrast to several previous studies suggesting large photodegradation fluxes, wherefore it is suggested that these studies might have neglected the role of thermal degradation. Results of this study are published in van Asperen et al. (2015b). The system was also used to study CO_2 concentrations and its isotopic components by tower and flux chamber measurements. Keeling plots were used to derive the $\delta^{13}CO_2$ flux value of soil and ecosystem respiration. It was observed that total ecosystem respiration was less depleted than soil respiration alone. A diurnally varying soil respiratory $\delta^{13}CO_2$ flux value was observed. Different (new) theories concerning the biological and physical controls on the respiratory $\delta^{13}CO_2$ flux value are discussed and evaluated. It is suggested that the variation is caused by non-steady-state conditions in the soil profile during nocturnal boundary layer buildup. A manuscript with the results of this study has been submitted to the journal of Agricultural and Forest Meteorology.

Table of Contents

List of Figures

List of Tables

Acknowledgements

First of all, I am very grateful for the PhD student scholarship provided by the Helmholtz Earth System Science Research School (ESSReS). Also, I would like to thank ESSReS for the funding of my visits to several conferences such as the European and American Geosciences Annual Meeting. Also, I am thankful for the support of InGOS (Integrated non-CO_2 Greenhouse gas Observing System, European Community Seventh Framework Programme (FP7/2007-2013)) for funding different aspects of the PhD, such as material of the field and laboratory experiments, transport and logistics of the field experiments, and visits to conferences and project meetings. Also, I would like to thank TTorch who supported me in an exchange stay at University of Tuscia (TTORCH ESF Exchange Grant, part of the ESF 'Tall Tower and Surface Research Network for Verification of Climate Relevant Emissions of Human Origin'-project) and who supported my participation in the TTorch Summerschool 'Challenges in measurement and modeling of greenhouse gas concentrations and fluxes'.

I would like to express my gratitude to my supervisor Dr. Thorsten Warneke who advised me during all stages of the research presented here. His comments, enthusiasm, creative ideas and scientific insight, but also his practical help during the field experiments, helped me in many phases of the research. I am also thankful for the support of Prof. Dr. Justus Notholt who accommodated me in his group, for the comments and feedback he gave on my work, and for the time he spend on the review of this thesis. Also, I would like to thank both by supervisors for hosting my guinea pig during my external research stay.

I would like to thank my (ex-)colleagues from my working group for the many small and large help they have offered during the four years I have been at IUP. I would like to say thanks to Holger Winkler and Nadine Wieters for making me feel welcome in the beginning. I would like to say a special thanks to Denise Müller who, as in-situ FTIR-user in crime, helped me with several small and large (FTIR-related) issues. A very very large thanks goes to Matthias Buschmann, for the help in so many Python, Windows, Linux, Latex and German language crises, and for the many nice office chats we had during the last four years. Another special thanks goes to Thorsten Warneke for the fast proof reading of large parts of my thesis. Also, I would like to thank Dr. Annette Ladstätter-Weißenmayer for dedicating her time to be the second reviewer of this thesis.

Another thanks goes to ESSReS which has provided me with several courses concerning Earth System Science-related subjects, and which offered me various soft skill trainings. Also, I would especially like to thank Klaus Grosfeld, Stefanie Klebe, Ludwig Löwemark and Helge Meggers for the many social activities which they have organized during the last four years wherein an open and nice atmosphere among fellow PhD students was created, from which many friendships and activities have originated.

During the fieldwork preparation and experiments, I have received help from many different people. My thanks go to Lukas Ruhe, who has helped me during the preparation of two large field campaigns. I would also like to thank Marie Laborde from Ecotech for the remote support, and David Griffith from the University of Wollongong for the ideas and help via the email. Also I would like to thank Annika Wieferich for her additional laboratory measurements.

I would like to thank Prof. Dr. Lars Kutzbach from the University of Hamburg for providing the opportunity to perform a field experiment in their fieldsite Himmelmoor. I would like to especially thank David Holl and Norman Rüggen for the many joined trips to Himmelmoor, the maintenance in Himmelmoor during my absence and the given advices. Also, I would like to

thank Chris Caldow and Christian Wille for the help during the set-up of the Himmelmoor field experiment. Also, my gratitude goes to Hans Czerwonka and Klaus-Dieter Cherwonka from the Torfwerk Quickborn (Torfwerk Enfeld Carl Hornung Werk Quickborn) for allowing the research on their property, and for the many practical help I have received during the field campaign.

I would also like to express my gratitude to Prof. Dr. Per Ambus for the organization of the RISØ N_2O flux chamber intercomparison campaign and for the help I have received during and after the field campaign. I would also like to thank Andreas Ibrom for providing the EC data and for the many talks and advices. Also, I would like to thank Rainer Gaische and Georg Willibald from KIT for providing a housing for the FTIR-analyzer and for the other practical help offered during the field campaign. Also, I would like to say thanks to Arjan Hensen and Pim van den Bulk from ECN for the transport of the FTIR-analyzer back to Bremen.

I would like to thank Dario Papale from the University of Tuscia for providing the opportunity to let me work in his group and perform field experiments in the region of Viterbo. I would like to give many thanks to Alessio Boschi, Michele Tomassucci, Giacomo Nicolini, Simone Sabbatini and Sipko Bulthuis for all the work they have done during the set-up and maintenance of the two field experiments in Italy. A special thanks goes to Simone Sabbatini for all the moments he helped me out at the fieldsite and in the Italian culture. Also many thanks go to Dario Papale, Giacomo Nicolini, Tommaso Chiti and Simone Sabbatini for the feedback and help during the data processing and the writing of the journal manuscripts.

Also, I would like to thank all members of the IUP for creating a nice working atmosphere, and I especially would like to thank my fellow coffee-break-and-late-night-work people, Ola Wolanin, Jia Jia, Leonardo Alvarado and Matthias Buschmann, for the many fun breaks. Also, finally, I would like to thank my family, my friends and Sipko for the support and understanding which I received during the different phases and activities of the PhD. Thank you all.

Publications

Journal articles

- **van Asperen, H.**, Warneke, T., Sabbatini, S., Nicolini, G., Papale, D., and Notholt, J.: *The role of photo- and thermal degradation for CO_2 and CO fluxes in an arid ecosystem*, Biogeosciences, 12, 4161-4174, doi:10.5194/bg-12-4161-2015, 2015b.

- **van Asperen, H.**, Warneke, T., and Notholt, J., *The use of FTIR-spectrometry in combination with different biosphere-atmosphere flux measurement techniques*, Towards an interdisciplinary approach in earth system science, 77-84, Springer International Publishing, 2015a.

Journal articles under review

- **van Asperen, H.**, Warneke, T., Sabbatini, S., Höpker, M., Nicolini, G., Chiti, T., Papale, D., Böhm, M., and Notholt, J.: *Diurnal variation in respiratory CO_2 flux in an arid ecosystem*, submitted to 'Agricultural and Forest Meteorology'; August 2015.

Presentations at conferences and meetings

- AGU 2014, San Francisco, USA, oral presentation: *Field measurements of respiratory $\delta^{13}CO_2$ and photodegradation*, **Hella van Asperen**, Simone Sabbatini, Thorsten Warneke, Giacomo Nicolini, Dario Papale, Justus Notholt; December 2014.

- Helmholtz Research School on Earth System Science, Annual Retreat 2014, Bremerhaven,'Seefischkochstudio', Germany, poster: *Respiratory $\delta^{13}CO_2$ measurements in Central-Italy*, **Hella van Asperen**, Thorsten Warneke, Simone Sabbatini, Giacomo Nicolini, Dario Papale, Justus Notholt; November 2014.

- Annual InGOS project meeting, Florence, Italy, oral presentation: *FTIR field measurements of respiratory $\delta^{13}CO_2$ and photodegradation*, **Hella van Asperen**, Thorsten Warneke, Simone Sabbatini, Giacomo Nicolini, Dario Papale, Justus Notholt; October 2014.

- Annual InGOS project meeting, Florence, Italy, oral presentation: *Comparison of five chamber systems for N_2O flux measurements based on a field campaign*, Per Ambus, Mette S. Carter, Kim Pilegaard, Andreas Ibrom, Christian Brümmer, Arjan Hensen, **Hella van Asperen**, Rainer Gasche, Daniela Famulari, Werner Kutsch; October 2014.

- Annual InGOS project meeting, Florence, Italy, oral presentation: *Eddy covariance N_2O flux measurements at low flux rates: results from the InGOS campaign in a Danish willow field*, Andreas Ibrom, Christian Brümmer, Arjan Hensen, **Hella van Asperen**, Mette S. Carter, Rainer Gasche, Daniela Famulari, Werner Kutsch, Kim Pilegaard, Per Ambus; October 2014.

- ICOS science conference, Brussels, Belgium, poster: *Respiratory CO_2 & $\delta^{13}CO_2$-measurements in central-Italy*, **Hella van Asperen**, Simone Sabbatini, Thorsten Warneke, Giacomo Nicolini, Dario Papale, Justus Notholt; September 2014.

- EGU 2014, Vienna, Austria, poster, *Respiratory CO_2 & $\delta^{13}CO_2$-measurements in central-Italy*, poster, **Hella van Asperen**, Simone Sabbatini, Thorsten Warneke, Giacomo Nicolini, Dario Papale, Justus Notholt; April 2014.

- EGU 2014, Vienna, Austria, oral presentation: *Eddy covariance N_2O flux measurements at low flux rates: results from the InGOS campaign in a Danish willow field*, Andreas Ibrom, Christian Brümmer, Arjan Hensen, **Hella van Asperen**, Mette S. Carter, Rainer Gasche, Daniela Famulari, Werner Kutsch, Kim Pilegaard, Per Ambus; April 2014.

- Ttorch summerschool, Hyytiälä Forestry Field Station, Finland, poster: *Greenhouse gas emissions from a peatland in Northern Germany*, **Hella van Asperen**, David Holl, Thorsten Warneke, Christian Wille, Lars Kutzbach, Justus Notholt; October 2013.

- EGU 2013, Vienna, Austria: PICO-presentation: *Greenhouse gas emissions from a peatland in Northern Germany*, **Hella van Asperen**, David Holl, Thorsten Warneke, Christian Wille, Lars Kutzbach, Justus Notholt; April 2013.

- Annual InGOS project meeting, Bremen, Germany: oral presentation: *The use of FTIR-spectrometry for flux measurements*, **Hella van Asperen**, Thorsten Warneke, Justus Notholt; March 2013.

- Helmholtz Research School on Earth System Science, Annual Retreat 2012, Bremerhaven, 'Deutsches Auswandererhaus', oral presentation: *Measurement of greenhouse gas emissions in a Northern German Peatland*, **Hella van Asperen**, David Holl, Thorsten Warneke, Christian Wille, Lars Kutzbach, Justus Notholt; November 2012.

- Annual InGOS project meeting 2011, Haarlem, The Netherlands, poster: *The use of FTIR-spectrometry for quantifying greenhouse gas fluxes between the biosphere and the atmosphere*, **Hella van Asperen**, Thorsten Warneke, Justus Notholt; November 2011.

1 Motivation and objectives

The knowledge on climate and climate change has developed and grown over the last decades. The realization that climate is not a stable given has been known for centuries. The possibility that human beings might have an effect on climate was first suggested by Arrhenius in 1896; he suggested that a human-induced increase in atmosphere CO_2 could cause a temperature increase [189]. Scientific interest in the subject and the possibility of human-induced climate change slowly started in the 1930's and has grown ever since. The consensus among scientists that climate is changing is growing since the 1970's.

In 1988, the Intergovernmental Panel on Climate Change (IPCC) was established to evaluate the risks of climate change. Its objective is to assess and combine available scientific knowledge on climate change and to provide clear, objective and consensus-based information on current scientific climate knowledge and developments. The IPCC regularly publishes reports on different topics, such as on the 'Physical Science Basis of Climate Change', on 'Climate Change: Impacts, Adaptation and Vulnerability' and on 'Mitigation of Climate Change' and adapts its publications for different target groups. Concerning human impact on climate change, the IPCC stated the most clear message so far in their latest report:

'Human influence has been detected in warming of the atmosphere and the ocean, in changes in the global water cycle, in reductions in snow and ice, in global mean sea level rise, and in changes in some climate extremes. It is extremely likely that human influence has been the dominant cause of the observed warming since the mid-20th century.'[169]

Improving our understanding of ongoing climate change processes is necessary for the prediction of future climate and vital for mitigation and adaption of societies.

Earth system sciences embodies the study of the interaction of different earth spheres, and aims at a better understanding of the earth as a system. These individual spheres, such as atmosphere, hydrosphere, lithosphere, biosphere and heliosphere, interact on different spatial and temporal scales and their interaction consist of (a combination of) physical, chemical and biological processes. Therefore, dealing with earth system science related topics, such as climate change, requires an interdisciplinary approach.

One of the most clear drivers of climate change, is the change in (greenhouse) gas concentrations in the atmosphere which is caused by anthropogenic emissions. The biosphere interacts with the atmosphere and its gases by different biosphere-atmosphere exchange mechanisms. Current biosphere-atmosphere exchange rates, and the possible influence of climate change on them, are intensively being studied, modeled and evaluated. However, to further improve climate models, more qualitative data and knowledge are still needed.

Greenhouse gas flux estimates between the biosphere and atmosphere can be obtained via a top-down approach, by inverting the exchange fluxes using measurements of the spatial and temporal concentration variation in the atmosphere, and by a bottom-up approach, the upscaling of flux estimates, e.g. from field measurements of biosphere-atmosphere gas exchange. Field measure-

ments are of great importance; they provide the opportunity to study greenhouse gas dynamics and its (feedback) mechanisms in detail. However, field measurements are labor intensive and often spatially poorly distributed. Continuous in-situ measurement of different (greenhouse) gas concentrations and fluxes are still sparse, especially for remote areas, but are of high importance.

Objectives and outline of the thesis

The objectives of this PhD are as follows:

1. To set up, improve and evaluate different flux measurement techniques based on FTIR-spectrometry;
2. To assess the benefits of the addition of an FTIR-analyzer to ecosystem flux sites;
3. To study the role of photo and thermal degradation in different ecosystems;
4. To investigate atmospheric and respiratory $\delta^{13}CO_2$ values and patterns.

The thesis consists of the following chapters:

Chapter 2 introduces the basic concepts related to climate change research and describes the main biosphere-atmosphere exchange mechanisms for the gases CO_2, CH_4, N_2O and CO.

Chapter 3 gives a general introduction to the concept of FTIR-spectrometry and introduces the in-situ FTIR-analyzer, which was used for the measurements performed during the PhD. Different flux measurement methodologies are discussed and the measurement set-up used during the PhD is described and evaluated. Part of this chapter are modified from:

The use of FTIR-spectrometry in combination with different biosphere-atmosphere flux measurement techniques, Towards an interdisciplinary approach in earth system science, van Asperen, Hella, Thorsten Warneke, Justus Notholt, Springer International Publishing, 2015a.

Chapter 4 gives an overview of the four main field campaigns performed during the PhD and elaborates on the practical details and considerations of the measurement set-up. Also, improvements which have been implemented throughout the different experiments are described and explained.

Chapter 5 evaluates the benefits of adding an in-situ FTIR-analyzer to ecosystem flux measurement sites. Case studies are presented to show the different possibilities of the designed flux measurement system and its applications for different fields in ecosystem research.

Chapter 6 evaluates CO_2 and CO fluxes which were measured in an arid ecosystem and in a laboratory study, and which were used to study the role of photo and thermal degradation. This chapter is modified from:

The role of photo- and thermal degradation for CO_2 and CO fluxes in an arid ecosystem; van Asperen, Hella; Warneke, Thorsten; Sabbatini, Simone; Nicolini, Giacomo; Papale, Dario; Notholt, Justus: Biogeosciences, 12, 4161-4174, 2015b.

Chapter 7 describes field measurements, in which the FTIR-analyzer was used to measure atmospheric and respiratory $\delta^{13}CO_2$. The observed respiratory $\delta^{13}CO_2$ values and patterns are shown and possible biological and physical controls on the respiratory $\delta^{13}CO_2$ values are discussed. Parts of this chapter are modified from:

Diurnal variation in respiratory CO_2 flux in an arid ecosystem, van Asperen, Hella; Warneke, Thorsten; Sabbatini, Simone; Höpker, Martin; Nicolini, Giacomo; Papale, Dario; Böhm, Michael; Notholt, Justus, submitted to Journal of Agricultural and Forest Meteorology, August 2015.

Chapter 8 summarizes the results of this thesis and will give the main conclusions of the research.

Chapter 9 gives an outlook of possible future work based on the results presented in this thesis.

Chapter 10 is the Appendix wherein results from (case studies in) additional collaborative field experiments are shown, results from additional field and laboratory measurements are presented, and an overview is given of the concentrations and fluxes measured at the different fieldsites.

2 Gas exchange between biosphere and atmosphere

2.1 Introduction

The main components of the current atmosphere are nitrogen (78.08%) oxygen (20.95%) and argon (0.93%). Water vapor is another important component of the earth's atmosphere with highly variable concentrations: from 4 ppmv in colder regions to up to almost 6% in tropical regions. Other atmospheric components are present in smaller, so called trace amounts and are more variable over place and time (Table 2.1). Trace gases, and especially greenhouse gases, play a crucial role in the earth's climate system. Greenhouse gases affect the earth's energy balance: they absorb long-wave thermal radiation, which is emitted from the Earth's surface, and emit a part of it back, resulting in an additional heating; the so called greenhouse effect.

The most abundant greenhouse gases in the earth's atmosphere are, in order of importance: H_2O, CO_2, CH_4 and N_2O (Table 2.1). CO is considered an indirect greenhouse gas due to its effect on CH_4 concentrations. Due to increased anthropogenic (industrial) activities over the last centuries, atmospheric concentrations of CO_2, CH_4 and N_2O are increasing and are on the highest levels in 650.000 year [167]. Furthermore, the increase rate of greenhouse gas concentrations have not been precedented in the last 22.000 years (Figure 2.1, [169]). Also, average global temperatures have been recorded to rise. By the latest report of the Intergovernmental Panel on Climate Change (IPCC), the relationship between anthropogenic activities and observed climatic changes was stated to be clear, and anthropogenic factors are extremely likely the cause for the rise in global temperatures [169].

Scenarios for future climate change are diverse. Predicted future temperature increase for 2081-2100 indicate a global warming of 1.0-3.7 °C above current day temperatures, even if atmospheric concentrations stabilize at current levels [169]. Temperature increase is thought to be not spatially equally distributed. For example, some scenarios indicate that the polar temperatures even increase with 11 °C [169]. Other predicted changes include a decrease in sea ice coverage, a change in ocean pH, sea level rise (0.4-0.63 m for 2100), and a change in climate and precipitation patterns [167]. Climate change will also have consequences for societies, economics and political relationships. To be prepared for the challenges which climate change will bring, qualitative predictions are necessary, which can be done by use of climate models.

Different biosphere-atmosphere exchange mechanisms influence the atmospheric concentrations. One of the key uncertainties in current climate models is the response of the biosphere on the atmospheric concentration changes. Current biosphere-atmosphere exchange rates and the possible influence of climate change on them, are intensively being studied, modeled and evaluated. However, to improve climate models, more qualitative data and knowledge are still needed.

Table 2.1: Overview of the main and trace gases in the atmosphere.

Atmospheric component	**Concentration in dry air**
Nitrogen (N_2)	78.08%
Oxygen (O_2)	20.95%
Argon (Ar)	0.94%
Carbon dioxide (CO_2)	0.038%
Water vapor (H_2O)	0-4%
Methane (CH_4)	0.0002%
Nitrous oxide (N_2O)	0.00003%
Carbon Monoxide (CO)	0.00001%

Greenhouse gases in the biosphere and atmosphere
The importance of a greenhouse gas in the current climatic changes can be expressed in terms of radiative forcing (RF) and global warming potential (GWP). Radiative forcing can be described as:

Radiative forcing is the change in the net, downward minus upward, radiative flux (expressed in W m^{-2}) at the tropopause or top of atmosphere due to a change in an external driver of climate change, such as a change in the concentration of carbon dioxide. Radiative forcing values are for changes relative to preindustrial conditions defined at 1750, and are expressed in watts per square meter (W m^{-2}) [167].

Radiative forcing values are based on past and present atmospheric concentrations, and are not suitable for an indication for the effect on future climate. The global warming potential (GWP) is a relative measure of how much heat a certain mass of a greenhouse gas traps in the atmosphere and is defined as:

The time-integrated global mean radiative forcing of a pulse emission of 1 kg of some compound, relative to that of 1 kg of the reference gas CO_2 [79].

The focus of this thesis will lay on the gases which are measured by the in-situ FTIR-analyzer, which are CO_2, CH_4, N_2O, CO and $\delta^{13}CO_2$.

2.2 Carbon dioxide (CO_2)

Continuous and accurate measurement of carbon dioxide (CO_2) concentrations have started in 1957 and were initiated by Charles David Keeling [77, 90]. Because of this early measurement start, the CO_2 concentration increase has been well monitored. Global average atmospheric CO_2 concentration was determined to be 390.44 $\pm$ 0.16 ppm in 2011, and was estimated to have increased with 11.66 ppm since 2005 [78]. For perspective, CO_2 concentrations in 1750 are estimated to have been around 278 $\pm$ 2 ppm. CO_2 is considered to be the most important anthropogenic greenhouse gas in relation to climate change: it has the highest radiative forcing factor (1.66 W m^{-2}) [78]. CO_2 is practically inert in the atmosphere: the only small atmospheric internal source of CO_2 is the oxidation of CH_4 and CO to CO_2. However, inside the biosphere and at the biosphere-atmosphere interface, CO_2 concentrations are highly variable, and CO_2 plays a major role in the carbon transport inside ecosystems. A schematic overview of the global carbon cycle can be seen in Figure 2.2.

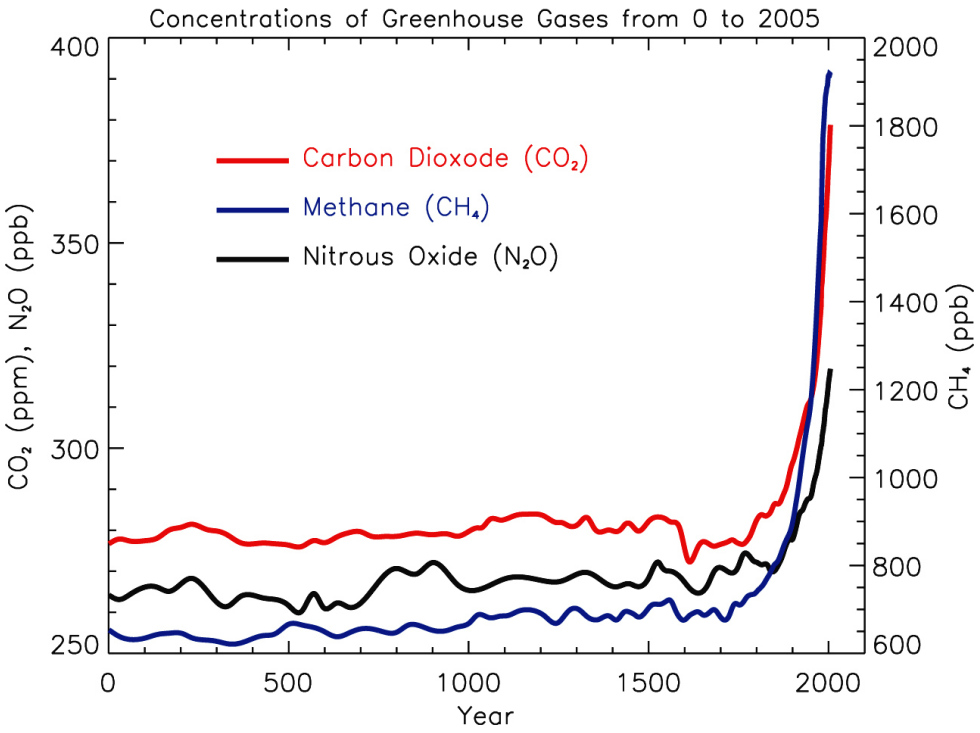

Figure 2.1: Atmospheric concentrations of CO_2, CH_4 and N_2O over the last 200 years. The figure is from IPCC [167].

2.2.1 Biosphere-atmosphere exchange

Above terrestrial ecosystems, atmospheric CO_2 concentrations are mainly regulated by the processes of photosynthesis, respiration and decomposition. Photosynthesis is responsible for a yearly uptake of 123 Pg C, and respiration and decomposition are together responsible for the emission of 118.7 Pg C per year, which points at a yearly net uptake of carbon. However, as can be seen in Figure 2.2, many different pathways exist for carbon to leave the biosphere, wherefore globally total biosphere carbon stocks are decreasing.

The effect of a changing climate on biosphere-atmosphere CO_2 fluxes is complex. Photosynthesis, decomposition and respiration are mainly dependent on temperature and moisture availability and, to a lesser extent, on radiation and atmospheric CO_2 concentrations. However, identifying the net effect of an environmental change is challenging. Drought reduces photosynthesis but also lowers respiration and decomposition rates. An increase in temperature has a positive effect on decomposition but, to a certain extent, also on photosynthesis and respiration. Studies on the effect of higher CO_2 concentrations on photosynthesis have been performed (FACE-studies, [108, 120]) and showed enhanced photosynthetic rates but also increased nitrogen-deficiencies [108]. An increase in radiation causes higher photosynthetic rates. On the other hand, UV-B radiation is known to inhibit microbial decomposition and, at the same time, cause abiotic carbon fluxes [93].

The simultaneous, different effects of climate change on carbon fluxes make the determination of the net effects challenging. Also, as can be seen in Figure 2.2, the net carbon flux into the biosphere is fairly small in comparison to its main components (photosynthesis, respiration and

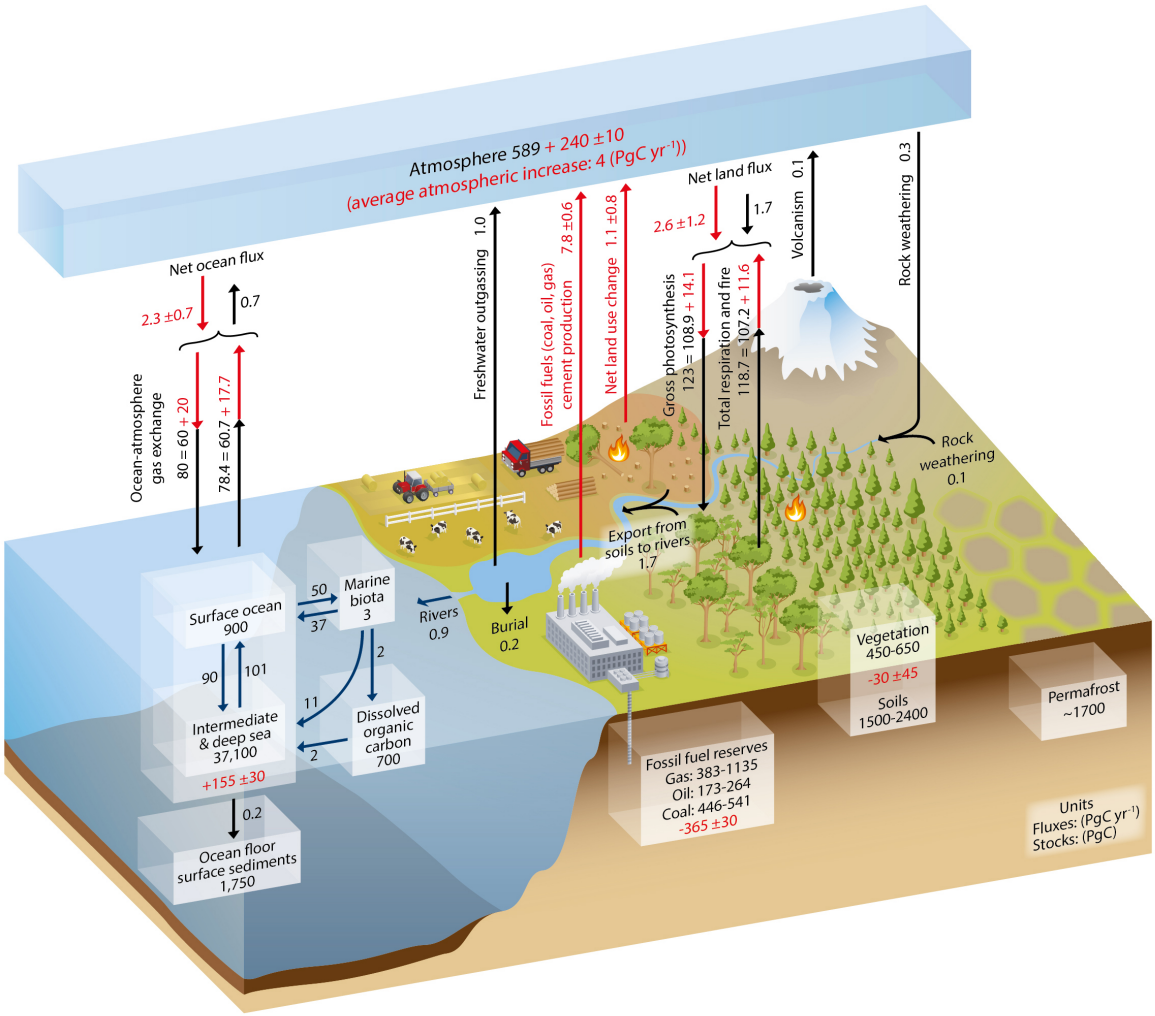

Figure 2.2: Simplified overview of the global carbon cycle. Black numbers indicate the pre-industrial era estimates of the carbon reservoir stocks and fluxes. Red numbers indicate the change in stock or yearly flux since the pre-industrial era. The numbers are given in PgC (1 PgC = 10^{15} gC), and the annual carbon exchange fluxes are given in PgC yr^{-1}. The figure is from IPCC [169].

decomposition). Therefore, a small change in one of these components can have large effects on the net carbon flux, and therefore on the biosphere and atmospheric sink. Because of this, it is essential to study these processes in detail and assess their response to a changing climate.

2.2.2 $\delta^{13}CO_2$ in ecosystems

The most abundant isotopes of CO_2 in nature are $^{12}CO_2$ ($\sim$ 99%) and $^{13}CO_2$ ($\sim$1%). The ratio between these isotopes in nature is usually expressed as:

$$\delta^{13}C(‰) = (\frac{R_{sample}}{R_{VPDB}} - 1) * 1000 \tag{2.1}$$

wherein R_{sample} is the molar ratio of $^{13}C/^{12}C$ and VPDB is a standard ratio of $^{13}C/^{12}C$, namely the Vienna Pee Dee Belemnite laboratory standard (0.0112372) [39, 91].

Stable (carbon) isotope measurements can be used to study ecological and biogeochemical processes in ecosystems [89]. In terrestrial ecosystems, several ecosystem processes within the biosphere have an isotopic preference, causing differences in the $\delta^{13}C$ within plant carbon pools. For example, atmosphere has in general an isotopic signature of approximately -8‰. Photosynthetic fractionation causes the ecosystem pool (soil and vegetation) to be depleted (containing less $^{13}CO_2$) in comparison to the atmosphere. The degree of depletion is dependent on many variables. Spatial or temporal differences in $\delta^{13}C$ in carbon pools can often be explained by environmental factors such as precipitation [14], drought and moisture availability [103, 155, 180, 181], temperature changes [14, 15, 55], change in dominating plant type species (C3 or C4 plant), [50] or human influence [1].

Because of the depleted soil and vegetation carbon pools, decomposition and respiration fluxes are also more depleted. This causes that during daytime, when photosynthesis dominates, the atmosphere becomes relatively enriched in $^{13}CO_2$, and at nighttime, when respiration dominates, the atmosphere becomes relatively enriched in $^{12}CO_2$. A similar pattern is visible on larger scale. Global atmospheric CO_2 levels contain more $^{13}CO_2$ during the northern hemisphere summer than during the southern hemisphere summer: the northern hemisphere contains more land surface which means more photosynthetic activity, causing more $^{12}CO_2$ to be (temporary) stored away in ecosystem carbon during the northern hemisphere summer months. Measuring CO_2 concentration and fluxes in combination with its isotopic components gives the opportunity to study ecosystem carbon production and transport pathways (see Chapter 7).

2.3 Methane (CH_4)

Methane (CH_4) has a relative low average atmospheric concentration of approximately 1803.1$\pm$ 4.8 ppb, but is considered an important greenhouse gas due to its relative high RF (0.48 W m^{-2}) and its high GWP of 72 and 25 over respectively 20 and 100 years [78]. It has been estimated that CH_4 concentrations were around 722 $\pm$ 25 in 1750. Between 2005 and 2011, CH_4 concentrations have increased with 28.6 $\pm$ 0.9 ppb [78]. Increased human activity has led to higher CH_4 concentrations and to increased CH_4 emissions, originating as well from anthropogenic as from natural sources (Figure 2.3). Nowadays 70% of the CH_4 emissions come from anthropogenic sources, and mainly originate from agriculture (rice paddies and wetlands), waste management systems, livestock and fossil-fuel industries, and biomass burning. Natural sources consist of geological sources, anaerobic soils and water areas (peatlands, wetlands, rivers, lakes, oceans), and wild animals [134] (Figure 2.3). The disentangling of methane emissions into anthropogenic and natural sources is difficult due to the many indirect effects which anthropogenic activities

have on natural CH_4 emissions. CH_4 is a reactive gas, with a lifetime shorter than 10 years, which makes its atmospheric concentration very responsive to changes in fluxes [81, 169]. The main sink of atmospheric CH_4 is its oxidation reaction with the hydroxyl radical (OH^-).

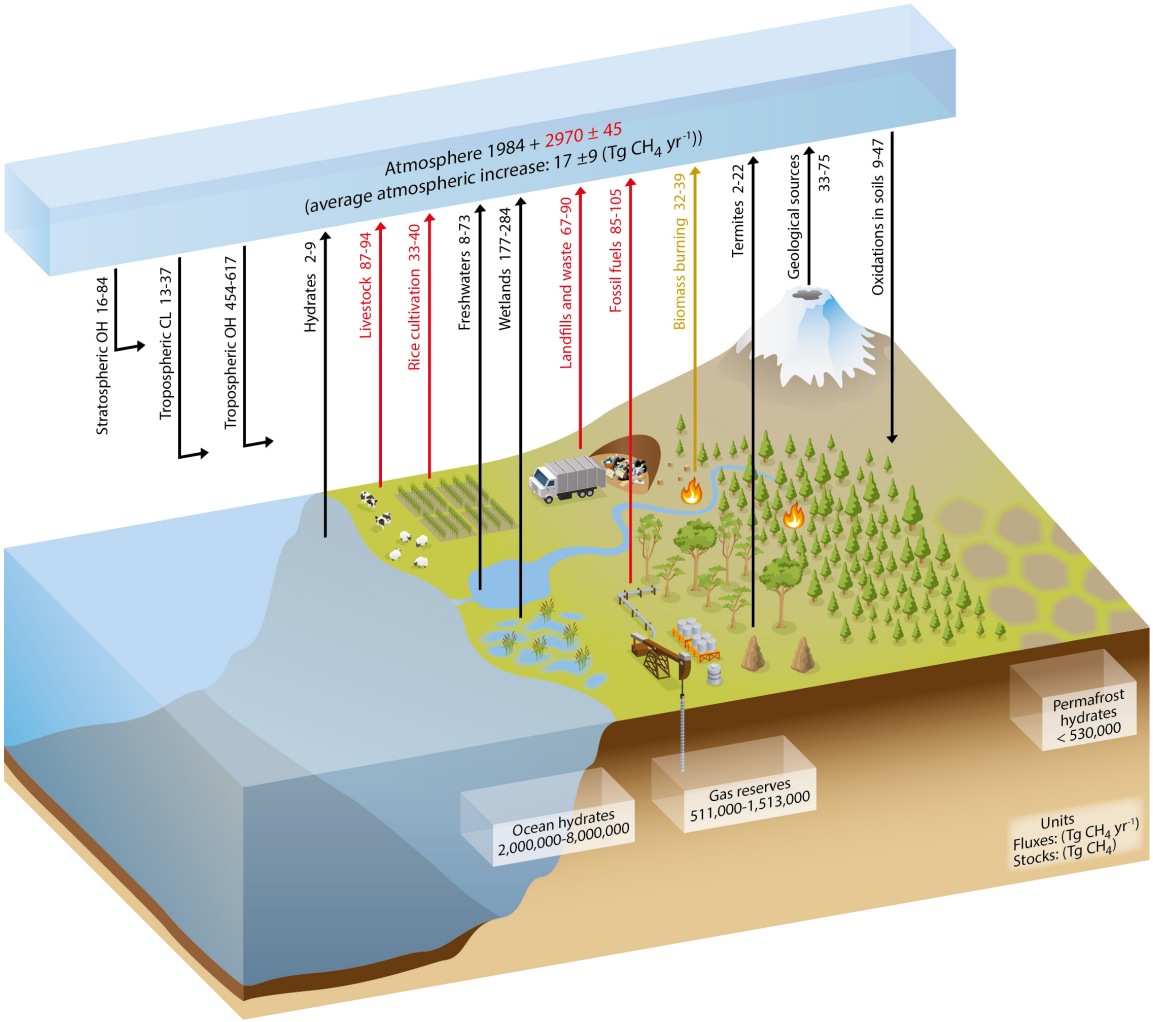

Figure 2.3: Simplified overview of the global CH_4 cycle. Black numbers indicate the pre-industrial era estimates of the reservoir stocks and fluxes. Red numbers indicate the change in stock or yearly flux since the pre-industrial era. The numbers are given in TgC-CH_4 (1 TgC-CH_4 = 10^{12} gC-CH_4), and the annual CH_4 exchange fluxes are given in TgC-CH_4 yr^{-1}. The figure is from IPCC (2013).

Biosphere-atmosphere exchange

In terrestrial ecosystems, highest CH_4 fluxes can be found in (partly) anaerobic ecosystems, such as peatlands and wetlands. The soil CH_4 cycle is closely connected with the soil CO_2 cycle. For example, peatlands and wetlands are known to be able to switch from CO_2 emissions to CH_4 emissions. During anaerobic conditions, production of methane starts, but only after reduction of oxygen (O_2), nitrate (NO_3^-), iron (III) oxide (Fe_2O_3), manganese (IV) oxide (MnO_2), and sulphate (SO_4^{2-}). For this reason, methane production often only starts after prolonged water logging [165]. Methanogens (bacteria) can directly break down carbon (acetate) ($C_2H_3O_2$) to CH_4, which represents 80% of the methane production in wetlands (Eq. 2.2). A smaller percentage of produced CH_4 (10-30%) is because of the reduction of CO_2 to CH_4 (Eq. 2.3) [133].

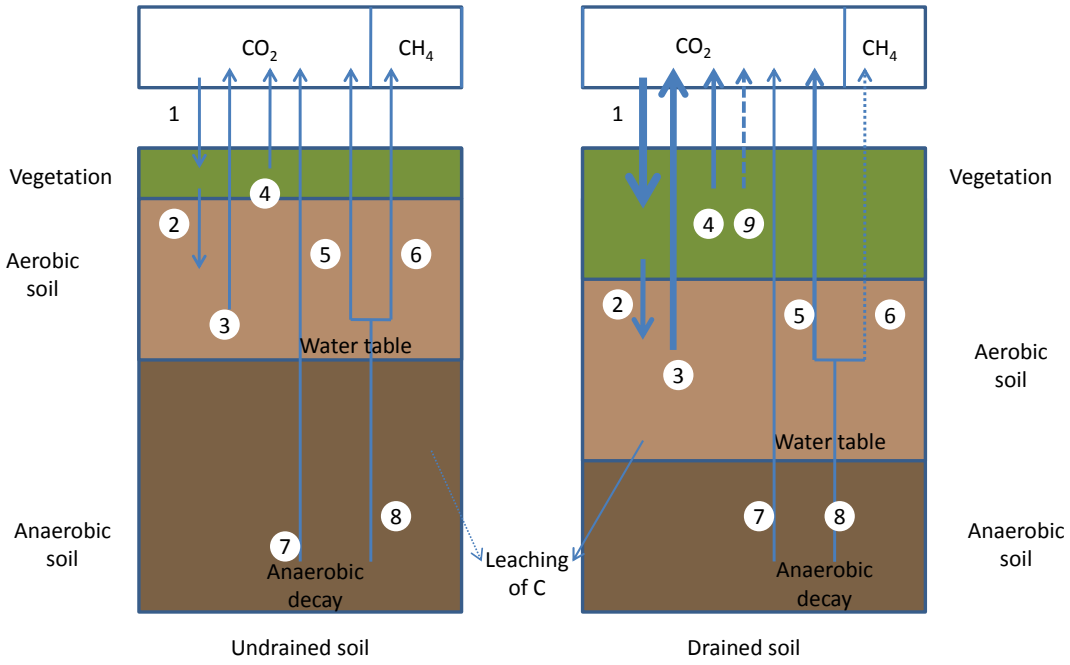

Figure 2.4: Schematic of different CO_2 and CH_4 uptake and production pathways which play a role in peatlands and wetlands. The left figure visualizes a soil profile and its processes under wet (anaerobic) conditions, the right figure visualizes the effects of drainage (lower water table) on the soil profile and its processes. The thicker arrows indicate larger fluxes. The numbers stand for the following processes: 1: photosynthesis, 2: litter production, 3: aerobic decay, 4: respiration, 5: oxidation of CH_4 to CO_2, 6: non-oxidized CH_4, 7: anaerobic decay to CO_2, 8: anaerobic decay to CH_4. The figure is modified from Laine (1996).

$$CH_3COOH \rightarrow CO_2 + CH_4 \tag{2.2}$$

$$4H_2 + CO_2 \rightarrow CH_4 + 2H_2O \tag{2.3}$$

In wetlands, there are three main migration pathways for CH_4: diffusion to the surface, transport by gas bubbles (ebullition), and transport via vascular plants. Methane from soils and wetlands is known for being emitted in pulses [125]. During diffusion, methanotrophic bacteria oxidize a significant part of the CH_4 to CO_2 [81, 133] (Eq. 2.4, pathway 5 in Figure 2.4). The ratio of CH_4 versus CO_2 which leaves the soil surface, is dependent on the length of the gas transport through the aerobic zone: the closer the groundwater level is located to the soil surface, the less CO_2 will be produced; this is visualized by the two different soil profiles which are shown in Figure 2.4.

$$CH_4 \rightarrow CH_3OH \rightarrow HCHO \rightarrow HCOOH \rightarrow CO_2 \tag{2.4}$$

Besides peatlands and wetlands, which are the main natural CH_4 sources, also other smaller sources exist. A debate is ongoing whether plants can emit methane and recently more evidence is found [20, 48, 92, 110]. Also, methane has been named as a product of photo- and thermal degradation [109].

2.4 Nitrous oxide (N_2O)

Nitrous oxide (N_2O) concentrations are variable in space and time, but average levels are found to be approximately 324.3 ± 0.1 ppb, with an increase of 5.24 ± 0.14 ppb between 2005 and 2011 [78]. It is estimated that N_2O concentrations in 1750 were around 270 ± 7 ppb. N_2O is the 3^{rd} most important anthropogenic greenhouse gas in the troposphere: it has an RF of 0.16 W m^{-2}, a GWP of 289 (for 20 years) and 298 (for 100 years), and an atmospheric lifetime of approximately 120 years [59, 78]. The main anthropogenic N_2O sources are fossil fuel burning and the Haber-Bosh process: the artificial nitrogen fixation process [63] (Figure 2.5).

Biosphere-atmosphere exchange
The production and transport of different nitrogen components in the soil-water-atmosphere interface is complex. Atmospheric N_2O is mainly produced as a by-product of nitrification or as an intermediate product of denitrification. Nitrification is an aerobic process, wherein O_2 is used as the electron acceptor. Nitrification is a two-step process wherein first ammonia (NH_4^+) is converted to the intermediate product nitrite (NO_2^-, eq. 2.5), and then converted to the final product nitrate (NO_3^-, eq. 2.6):

$$NH_4^+ \rightarrow NO_2^- \tag{2.5}$$

$$NO_2^- \rightarrow NO_3^- \tag{2.6}$$

The intermediate product NO_2^- can also be used as an electron acceptor in the denitrifying process. Denitrification is an anaerobic process wherein NO_3^- is reduced to the nitrogen gases N_2O or N_2 (eq. 2.7) [10, 63, 165]:

$$NO_3^- \rightarrow NO_2 \rightarrow NO \rightarrow N_2O \rightarrow N_2 \tag{2.7}$$

The ratio between produced N_2 and N_2O highly depends on land use type and precipitation [28, 111]. It has been observed that denitrification activity usually follows the changes in soil respiration; an explanation for this phenomenon could be that respiration consumes the oxygen, and low-oxygen conditions enhance N_2O production [116, 164].

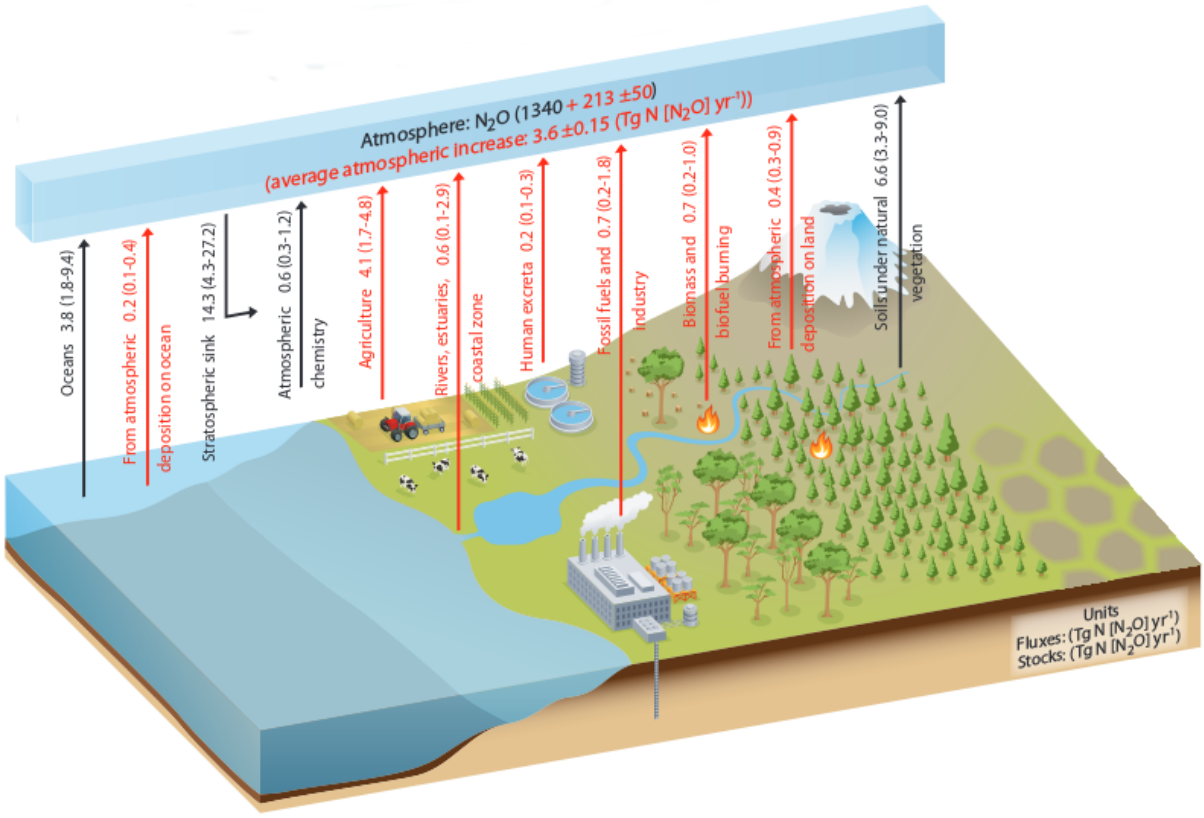

Figure 2.5: Simplified overview of the global sources of N_2O. The black numbers indicate pre-industrial era estimates of the reservoir stocks and fluxes. The red numbers indicate the change in stock or yearly flux since the pre-industrial era. The numbers are given in TgN-N_2O (1 TgN-N_2O = 10^{12} gN-N_2O), and the annual N_2O exchange fluxes are given in Tg N-N_2O yr^{-1}. The figure is from IPCC (2013).

In contrast to CH_4 production, N_2O production can start quite sudden, as soon as O_2 runs out, due to the relative high redox potential. Quantities of emissions are highly dependent on material, environmental and climatic conditions. A recent study found that N_2O can also be produced by plants during UV-exposure [22]. Soil N_2O uptake is also reported, especially in wet conditions, and is suggested to be caused by part of the denitrification process, when N_2O is converted to N_2 [29].

2.5 Carbon monoxide (CO)

Carbon monoxide (CO) has an atmospheric concentration of approximately 60-300 ppb and a mean residence time in the atmosphere of 50 days [160, 169]. Average global CO concentrations have decreased from 2006 to 2010, but it is unclear what causes this pattern [194]. Carbon monoxide does not absorb infrared radiation strongly, and so is not classified as a greenhouse gas. However, CO is the most important sink for the OH^- radical, which serves also as a sink for CH_4. Therefore, an increase in CO emissions leads to less available OH^- to react with CH_4, causing a relative increase in atmospheric CH_4 concentrations. For this reason, CO is called an indirect greenhouse gas. Its indirect RF is estimated to be 0.2 W m^{-2} [78]. Also, CO has an important role in the formation of tropospheric ozone [169].

Natural carbon monoxide emissions originates from: the in-situ oxidation of methane and hydrocarbons, forest fires, ocean emissions, and the degradation of chlorophyll. Anthropogenic carbon monoxide sources are land burning, (incomplete) fossil fuel burning, and deforestation. Natural sinks of carbon monoxide are the oxidation with OH^-, the uptake by the stratosphere, and the uptake by soil and plants [9, 36]. Due to its short residence time, estimates of fluxes and sinks are still unreliable [60].

Biosphere-atmosphere exchange

The role of CO in soils and ecosystems is not well understood. Soils are known for being sources as well as sinks of CO [36]. Most likely, the main cause for soil CO uptake is the oxidation of CO to CO_2 or CH_4 by soil bacteria or soil enzymes [9, 36, 85, 168, 192, 198]. Soil CO consumption is found to be dependent on atmospheric CO concentrations, and the consumption rate is usually expressed in deposition velocity: the uptake rate divided by the atmospheric CO concentration [38, 96]. Soil CO emissions have also been reported and are thought to be of non-biological origin [37, 38]. For example, soil CO emissions were found in peatlands [62] and in arid soils [38]. Living plants are also known to emit a small amount of CO [21, 94, 174]. However, senescent plant material has been shown to emit 5 to 10 times more than photosynthesising leaf material [44, 161, 174]. These fluxes, mostly determined in laboratory studies, were attributed to thermal degradation and, to a larger extent, photodegradation [44, 109, 160, 161].

3 The FTIR-analyzer and different ecosystem flux measurement techniques

Parts of this chapter (§3.4 and §3.5) are modified from:

'The use of FTIR-Spectrometry in combination with different biosphere-atmosphere flux measurement techniques' in 'Towards an interdisciplinary approach in earth system science', p 77-84, Hella van Asperen[1], Thorsten Warneke[1], Justus Notholt[1], Springer International Publishing, 2015.

1) Institute of Environmental Physics, University of Bremen, Otto-Hahn-Allee 1, Bremen, 28359, Germany.

My contributions to this publication are the development and the testing of the described flux measurement set-up, the processing of the flux chamber and the flux gradient measurement data, and the writing of the manuscript.

3.1 Introduction

Earth system sciences embodies the study of the interaction of different earth spheres and aims at a better understanding of the earth as a system. One of the current questions in earth system science research is how biosphere-atmosphere exchange will be affected by the upcoming predicted climate changes. Estimates of (greenhouse gas) fluxes between the biosphere and atmosphere can be obtained via a top-down approach, modeling the exchange based on spatial and temporal concentration-variation in the atmosphere, and by a bottom-up approach, the upscaling of flux estimates, e.g. from field measurements of biosphere-atmosphere gas exchange. Field measurements are of great importance; they provide the opportunity to study greenhouse gas dynamics and its (feedback) mechanics in detail. However, field measurements are labor intensive and often spatially poorly distributed. In-situ high frequency measurement of different (greenhouse) gas concentrations and fluxes are still sparse, especially in remote places, but are of high importance.

The use of FTIR-spectrometry in ecosystem research can contribute to obtaining high frequency in-situ ecosystem gas exchange data, also for remote regions. In this chapter, first the principles of FTIR-spectrometry are described, followed by a detailed description of the use and the practical set-up of the used in-situ FTIR-analyzer. Different types of flux measurement techniques, which are common in ecosystem flux studies, are discussed. Finally, the measurement set-up which was designed and used during this PhD, is described. The measurement set-up which concerns an in-situ FTIR-analyzer connected to flux chambers and a flux gradient technique, is evaluated.

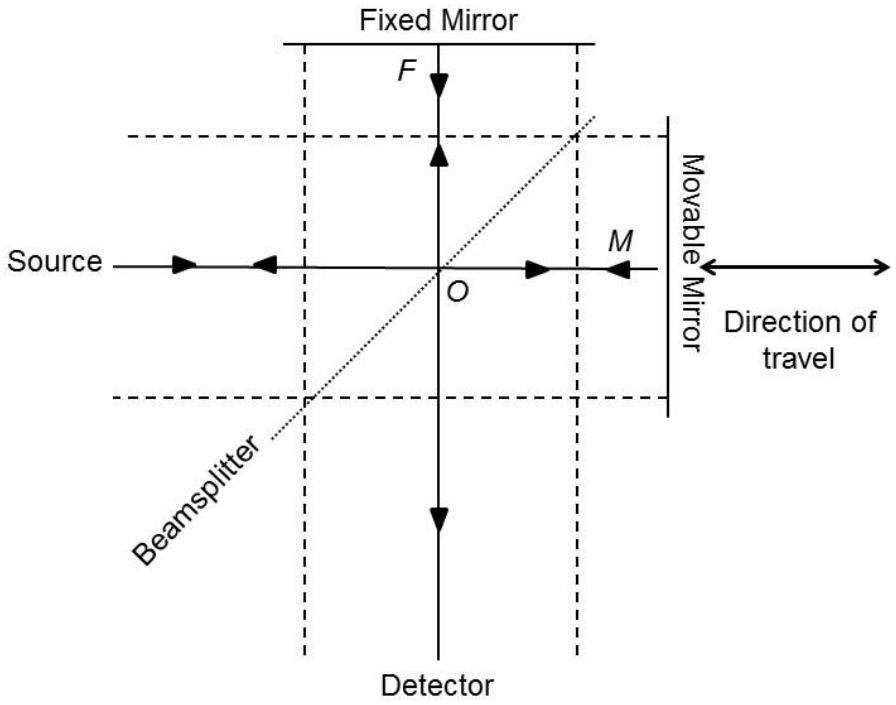

Figure 3.1: Schematic of a Michelson-Interferometer. The figure is modified from Griffith (1986).

3.2 FTIR-spectrometry

FTIR-spectrometry stands for Fourier Transform Infrared-spectrometry. The FTIR-technique is based on the working of a Michelson-Interferometer. A non-dispersive light beam, containing different wavelengths at once, is directed into an interferometer, and focused on a beam splitter. Half of the light beam (beam F) is reflected by the beam splitter, hits a fixed mirror, and is then transmitted through the beam splitter to the detector. The other half of the light beam (beam M) is transmitted by the beam splitter, hits a moving mirror, and then reflected by the beam splitter to the detector (Figure 3.1). If the moving mirror moves with length x, the difference in the light path between beam F and M is 2x. When x increases, more destructive interference occurs, and the intensity of the light beam will decrease. The position of the mirror and the resulting light intensity result in an interferogram. A Fourier transformation is needed to convert the interferogram to an absorption spectrum. Every gas and its isotopic variations has its own unique absorption properties, which can be considered as a fingerprint. From the calculated absorption spectrum, the gas species (absorption wavelengths) and the gas species concentration (absorption intensity) can be derived. The mid-infrared spectrum, approximately 400-4000 cm^{-1}, obtains many spectral lines. Figure 3.2 shows the 2000-4000 cm^{-1} wavelength region, and its absorption features in ambient air [47].

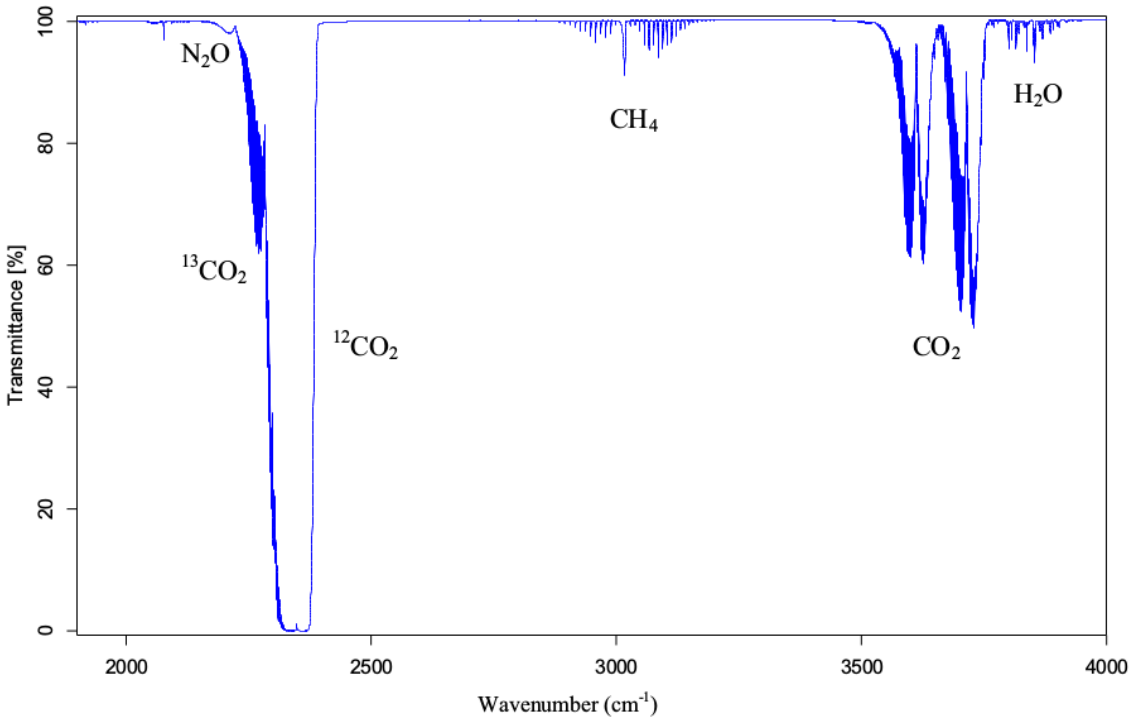

Figure 3.2: Mid-infrared spectrum of ambient air and its main absorption features, as measured by the FTIR-analyzer. The figure is from Deutscher (2009).

3.3 Spectronus: in-situ FTIR-analyzer

The in-situ FTIR spectrometer used for the research described in this thesis, is a 'Spectronus' Trace Gas & Isotope Analyzer, manufactured by Ecotech in Australia, from here on called FTIR-analyzer. The FTIR-analyzer was designed and developed by the university of Wollongong and taken over by Ecotech in 2009. The FTIR-analyzer consists of a 3.5 L white-optics cell, which maximizes the light path to 24 m. The FTIR spectrometer is a Bruker IR-Cube with a thermo-electrically MCT detector (1800-5000 cm^{-1}). Spectra are recorded by OPUS and fitted by MALT5 [70]. Malt5 uses a non-linear least square fitting technique to fit the measured spectra with concentrations. For the fitting, the spectra data base Hitran (HITRAN, 2004) is used [70]. The FTIR-analyzer's precision for 10-minute averaged measurements can be found in Table 3.1.

Table 3.1: FTIR-analyzer's precision for 10-min averaged measurements [69].

Species	**Precision (1, 10 min)**
CO_2	0.02 µmol mol^{-1}
$\delta^{13}CO_2$	0.04 ‰
CH_4	0.2 nmol mol^{-1}
CO	0.2 nmol mol^{-1}
N_2O	0.06 nmol mol^{-1}

The physical dimensions of the FTIR-analyzer are 115 cm x 45 cm x 100 cm, and the instrument weights 117 kg (Figure 3.3). The FTIR-analyzer contains a gas sample handling system,

which can be set up to automatically sample one of the different inlets, lead the air through (or pass by) the dryers and flush, fill and/or empty the cell. This is done by a 12-channel digital IO switching capability for switching 12 (or optionally more) solenoid valves. Also a 8-channel analogue-digital converter for logging the environmental variables is present. The analogue loggers monitors cell temperature and cell pressure, air flow, and room temperature. Figure 3.4 shows the schematic of the FTIR-analyzer and it sample stream handling.

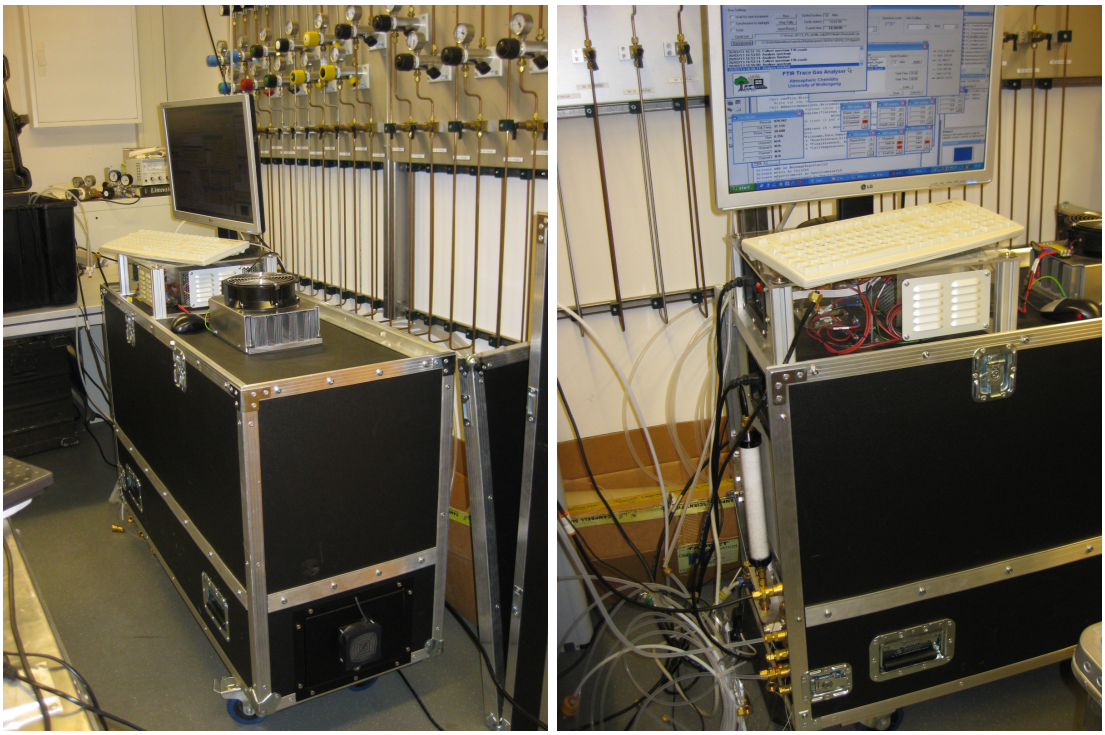

Figure 3.3: In-situ FTIR-analyzer 'Spectronus' during laboratory measurements.

High water levels in the sample cause high absorption at certain wavelengths, thereby loosing part of the sample signal. Therefore, air samples need to be dried before entering the cell. Samples are dried by a Nafion dryer-back flush followed by a chemical dryer, usually filled with Magnesium Perchlorate ($Mg(ClO_4)_2$). Air samples enter via inlet 1, 2, 3 or 4, pass through the dryers and a particle filter, and enter the measurement cell. After the measurement cell, sample air passes a mass flow controller (Kofloc, Japan), and then flows back through the Nafion dryer-back flow, and leaves the instrument via a pump (model MV2, Vaccuband, Germany). The pump can evacuate the cell to below 1 $<$ mb. Cell temperature is kept constant by a thermostat, which is usually set to 30 °C. Measurements were corrected for water vapor, pressure fluctuations, and cross-sensitivities. Pressure sensitivity factors and calibration values can be found in Appendix (§10.2.1). Also, during the different field campaigns, background measurements and a calibration routine were performed frequently. Measurements can be performed in static mode, which means that the measurement cell is closed during analysis, or in flow mode, in which sample air flows through the measurement cell during the analysis.

For the results in this study, CO_2 was retrieved from its spectral lines in the 3600 cm^{-1} region, while its isotope ($^{13}CO_2$) was retrieved from the 2300 cm^{-1} region. From the same region, N_2O and CO are retrieved. Methane is retrieved from the 3000 cm^{-1} region.

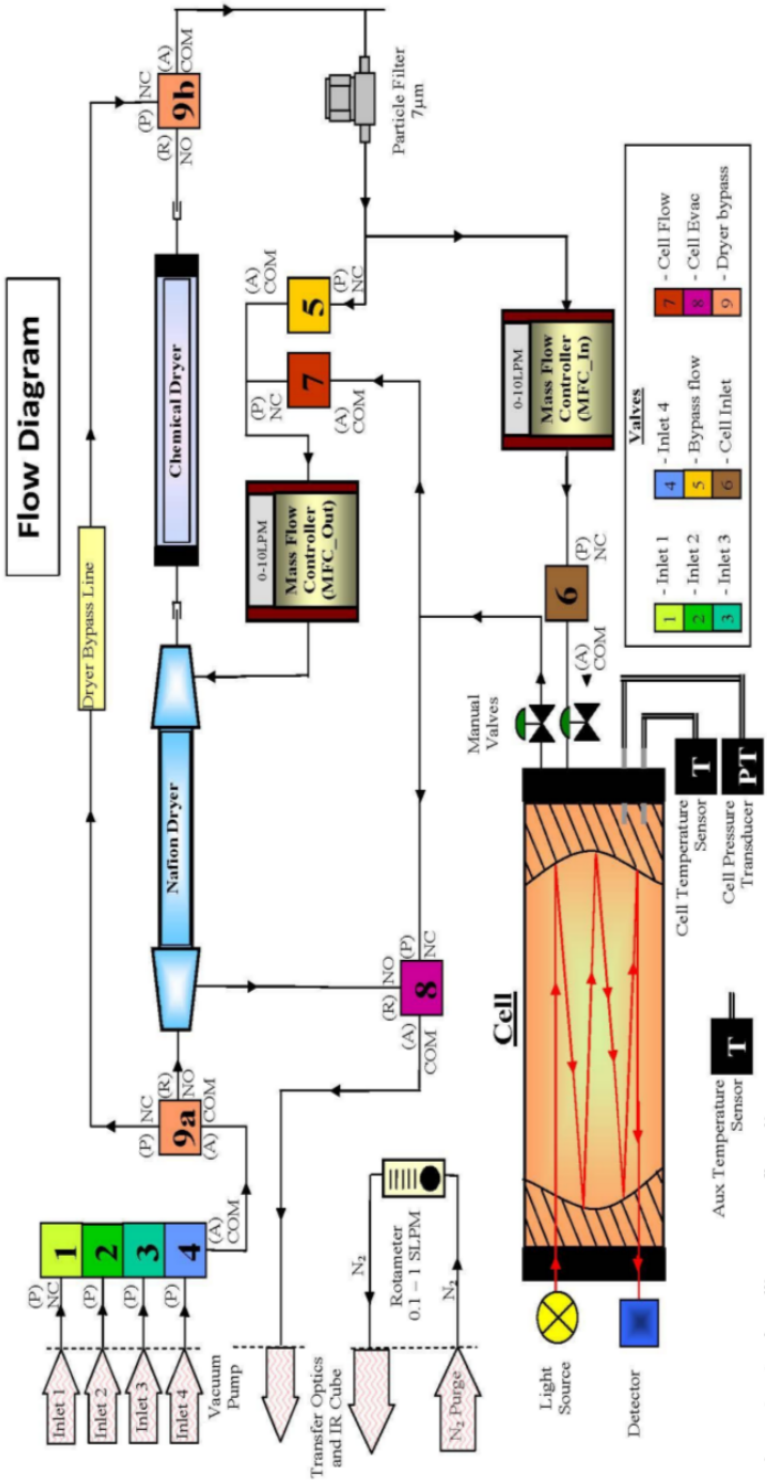

Figure 3.4: Schematic of the gas handling system of the FTIR-analyzer. The valves 1, 2, 3 and 4 control the gas inlets. The sample gas goes through (or passes by) the Nafion dryer and a chemical dryer (valve 9A or 9B), and enters the sampling cell via valve 6. Evacuation of the cell is either via valve 7 (slow evacuation) or via valve 8 (fast evacuation), see also §3.5.1. The figure is from Ecotech (2011).

3.4 Flux measurement techniques

Gas exchange between biosphere and atmosphere can be measured by different flux measurement techniques. Micrometeorological techniques are based on the measurement of the covariance between the vertical air velocity and the concentration of an entity to calculate the flux of this entity. Flux chamber techniques are based on the principle of sealing an area by placing a 'chamber' on a surface, after which chamber fluxes can be derived from the change in gas concentration in the chamber headspace. In Table 3.2, the advantages (underlined) and disadvantages of micrometeorological and flux chamber methods are summarized [42].

Table 3.2: Advantages (underlined) and disadvantages of micrometeorological and flux chamber techniques [23, 57, 127].

	Micrometeorological methods	**Flux chamber methods**
Terrain and conditions	Difficult in hilly terrain Specific atmospheric conditions needed	Possible in all terrains Possible in all weather conditions Suitable for low fluxes
Deployment	Less suitable for low fluxes Technical knowledge required Not labor intensive	Easy in use Labor intensive High precision
Results and representativeness	Demanding data processing Large footprint Suitable for frequent long term measurements	Small footprint Potentially influences fluxes in measured area

3.4.1 Micrometeorological techniques

Several micrometeorological methods exist to quantify biosphere-atmosphere gas exchange [124]. Micrometeorological methods which are related to the research described in this thesis will be discussed.

Eddy covariance technique
Air flow can be considered as a horizontal flow of rotating eddies. Eddies are responsible for the movement of air parcels, each having its own temperature, humidity and concentration. The flux can be considered as the result of these movements on the concentration, e.g. flux can be represented as the covariance of the vertical velocity and concentration of the entity of interest. The eddy covariance (EC) technique uses this covariance between the vertical air velocity and the concentration of an entity to calculate the flux of this entity. This can be done by the following:

$$F = \overline{\rho w s} = \overline{\rho \overline{w} + pw' * \overline{c} + c'} = \overline{pw'c'} \tag{3.1}$$

wherein ρ is the air density, w is the vertical air velocity, and s the concentration of gas of interest per unit mass of air, $\overline{w}$ and $\overline{s}$ are the means, and w' and s' are the deviations from the mean. Averaging periods are usually 30 or 60 min [8].

For EC measurements, fast (>10 Hz) sensors are needed for wind and concentration measurements. Furthermore, measurement of temperature and water vapor are needed to correct concentration measurements for density fluctuations. Fast analyzers for CO_2 and H_2O are since long

available and recent technology developments resulted in fast analyzers for other gases, such as CH_4 and N_2O. However, fast analyzers are expensive and not available for every gas species. Also, many gas species have very low exchange rates, wherefore high quality EC measurements for these gases are difficult [119, 203]. In contrast, the following techniques are suitable for measurement of minor fluxes [71].

Disjunct eddy correlation
Disjunct eddy sampling (D-EC) can as well be applied to the eddy covariance method as well as to eddy accumulation methods. For disjunct eddy correlation measurements, a subset of data points is obtained depending on the speed of the available sensors. The flux can be derived from the covariance of the disjunctly sampled time series.

$$F_c =< w'c >_{disj}= \frac{1}{N}\sum_{i=1}^{N} w_i' * c_i' \tag{3.2}$$

wherein w' and c' are the deviation of the vertical wind speed and concentration respectively, and is N the amount of subsamples, being taken over a certain time [153, 154].

Eddy accumulation
The eddy accumulation technique also uses the covariance of the vertical velocity and concentration of the entity of interest, but does not require fast gas analyzers. It was developed by Desjardin (1973) and was used often afterwards [140, 143, 153]. Eddy accumulation measurements are done by collecting updraft eddies and downdraft eddies in two separate reservoirs. The eddy accumulation technique requires fast air sampling proportionally to the vertical velocity of the air. When the air velocity is positive (w+), a valve opens to the upward-reservoir, when the air velocity direction is negative (w-), a valve opens to the downward-reservoir. After sufficient time, the content of the reservoirs should be proportional to:

$$F = \overline{w^+c} + \overline{w^-c} = (\overline{w^+} + \overline{w^-})\overline{c} + \overline{w^+c'} + \overline{w^-c'} = \overline{w^+c'} + \overline{w^-c'} = \overline{w^-c'} \tag{3.3}$$

wherein w+ is the velocity when the wind direction is upward, w- is the velocity when the wind direction is downward, c+ is the concentration per unit mass of air when the wind direction is upward, and c- is the concentration per unit mass of air when the wind direction is downward [45].

Relaxed and disjunct eddy accumulation
The relaxed eddy accumulation (REA) technique overcomes the need for a fast sampling velocity, by having a constant (relaxed) sampling rate, and the flux can be expressed by:

$$F = \beta * \sigma(C_X^+ - C_X^-) \tag{3.4}$$

wherein β is the semi-empirical coefficient (approx value of 0.56), σ the standard deviation of the vertical wind speed, and C_X^+ and C_X^- the concentrations of the gas in the upward and downward reservoirs [25]. The disadvantage of this method is the dependence on the need to derive an empirical coefficient.

The disjunct eddy accumulation (DEA) has the same principle as the REA technique, but takes samples periodically over larger time intervals (10-60 sec). The grab sample will be stored in the updraft or downdraft sampling container, dependent on the measured direction of the vertical wind velocity, when sampled. This system also allows the use of slower response analytical

sensors [153].

The flux gradient technique
The flux gradient (FG) technique uses the relationship between the gas flux and the atmospheric concentration gradient [71]. The FG technique is based on Fick's law of diffusion, and states that a flux goes from higher concentrations to lower concentrations, with a speed proportional to the concentration gradient and the diffusion coefficient. FG fluxes can be calculated by:

$$F = D\frac{\Delta C}{\Delta z} \tag{3.5}$$

wherein ΔC is the difference in concentration of gas x (mol m^{-3}) at two fixed different inlet-heights (Δz (m)), D is the diffusion coefficient (m^2 s^{-1}), and F the flux (mol m^{-2} s^{-1}). The diffusion coefficient can be parameterized using the data from a sonic anemometer. More information about the parameterization of the diffusion coefficient can be found in §5.2.

Comparison between methods
Previous studies have shown that the eddy covariance method compares well with slower methods such as the flux gradient technique and the relaxed eddy accumulation technique [72]. Important is to filter for the circumstances wherein the slower method is valid. For example, for flux gradient measurements, a minimum wind speed of 1 m s^{-1} is advised [72, 143]. Comparison between the flux gradient technique and the EC method will be discussed in §5.2, comparison between the REA technique and other methods will be discussed in more details in the Appendix (§10.1.2).

3.4.2 Flux chamber techniques

Flux chamber (FC) measurements are based on the principle of sealing an area by placing a 'chamber' on top. All gas exchange in this area will result in a change in chamber air concentrations. There are three main flux chamber designs [148], which are visualized in Figure 3.5.

- **Closed static chamber systems** (non-steady-state)
  In a closed static chamber system, the system is sealed, and air is not circulated. Fluxes are determined by sampling air out of the chamber (one time or multiple times) during flux chamber closure. Samples are analyzed afterwards. The headspace concentration increases during flux chamber closure, influencing the concentration gradient, which can influence the flux (non-steady-state conditions).
  Advantages: measurement device does not have to be on site, not much technical knowledge required.
  Disadvantages: labor intensive, non-steady-state conditions, samples need to be stored, harder to automate.

- **Closed dynamic chamber systems** (non-steady-state)
  In a closed dynamic system, air is being continuously circulated from the flux chamber headspace, to a measurement device and back. The headspace concentration increases during chamber closure, influencing the concentration gradient, which can influence the flux (non-steady-state conditions).
  Advantages: samples are directly analyzed, not-labor intensive.
  Disadvantages: non-steady-state conditions, technical knowledge required.

- **Open dynamic chamber systems** (steady-state)
  In an open dynamic system, air is continuously sampled from the chamber headspace

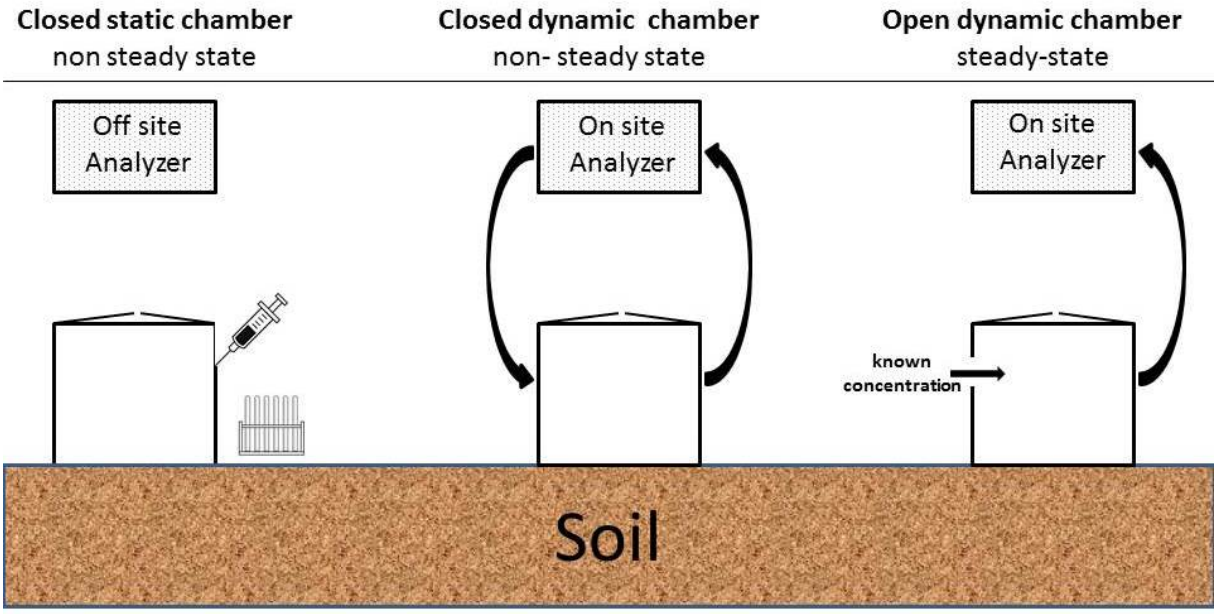

Figure 3.5: Different flux chamber systems: 'closed static chamber', 'closed dynamic chamber', and 'open dynamic chamber'.

but not returned. In this way, if correctly set up, the chamber headspace concentration does not increase so that steady-state conditions remain. However, if incoming flow is wrong/unknown, errors can be induced.
Advantages: samples are directly analyzed, not-labor intensive, steady-state conditions.
Disadvantages: technical knowledge required, precise validation needed.

Comparison between different flux chamber designs

Flux chamber types and usage have been often discussed and evaluated in literature. One of the issues of flux chamber measurements is the degree of flux under- or overestimation. For example, for non-steady-state flux chamber systems, the under/overestimation is quantified to be between -21% to 33% [148]. Underestimation of the flux is caused by the buildup of a gas concentration in the flux chamber headspace, and is especially noticeable when fluxes are high or when flux chambers are closed for longer time periods [84]. Pressure artifacts can be caused by the air pressure in the chamber getting higher than outside the flux chamber, which influences the original flux. Furthermore, a pressure difference can cause existing leaks to grow, or create new leaks. Vents are considered needed in all non-steady-state flux chamber measurements. Leaks cannot be considered as an alternative for venting, because leaks usually provide a shorter pathway for gases than does venting, thereby supporting greater gas loss [84]. While venting is often applied and an accepted method for preventing this bias, also other effects of venting were observed. Conen (1998) stated that in a vented chamber on a less permeable soil, diffusion losses due to the Venturi effect can be larger than soil gas flux into the chamber.

3.4.3 Other techniques

Soil gradient technique

The use of the gradient technique to estimate fluxes is applicable to the atmospheric concentration gradient (see flux gradient technique, §3.4.1), as well as to the soil concentration gradient. For example, by measuring the CO_2 concentration at different points in the soil, a CO_2 gradient can be determined, and the flux can then be calculated using Fick's law of diffusion.

$$F_{CO_2} = -D_s \frac{\Delta C}{\Delta z} \tag{3.6}$$

wherein F_{CO_2} is the CO_2 flux (mol m^{-2} s^{-1}), D_s the CO_2 diffusion coefficient in the soil (m^2 s^{-1}), ΔC the CO_2 concentration (mol m^{-3}), and z the depth (m). This method assumes that diffusion is the main transport of CO_2 in the soil and neglects mass flow or the transport by dissolved CO_2. The diffusion coefficient can either be determined by measurement or can be modeled by the use of soil and environmental variables [173, 178]. D_s can be modeled by:

$$D_s = \xi * D_a \tag{3.7}$$

wherein D_a represents the diffusion coefficient in free air (m^2 s^{-1})), corrected for temperature and pressure, and ξ represents the tortuosity factor, which accounts for the tortuous paths of real pores [173]. D_a can be obtained by correcting the diffusion coefficient at standard conditions by the following equation:

$$D_a = D_{a0} * (\frac{T}{273.15})^{1.75} * \frac{P}{101.3} \tag{3.8}$$

wherein T is soil temperature (K), P is soil air pressure (kPa) and D_{a0} the diffusion coefficient in free air at standard conditions (m^2 s^{-1}, T=273.15 K, P=101.3 kPa). The tortuosity factor can be estimated by:

$$\xi = \frac{\partial^{10/3}}{\phi^2} \tag{3.9}$$

wherein ∂ is the air filled porosity and ϕ is the total porosity [122]. An example of an application of the soil gradient technique can be found in Chapter 7.

NBL technique

The nocturnal boundary layer technique (NBL technique) assumes a well mixed and stable boundary layer at night. With these conditions, the NBL can be considered as a large box sealing a research area wherein gas concentration changes over time are a direct result of gas emissions or gas uptake by the biosphere. The flux can be derived from the following equation [32]:

$$C_{t_o} + \frac{F\Delta t}{z_i} = C(t) \tag{3.10}$$

wherein z_i is the boundary layer height (m), which can be estimated by different techniques, C_{t0} the concentration of the trace gas at a specified start time (mol m^{-3}), C(t) the concentration of the trace gas as the measured time (mol m^{-3}), Δ t the time interval (s), and F the flux (mol m^{-2} s^{-1}). Concentrations do not need to be measured rapidly, which makes it possible to measure with different and/or slower analyzers and therefore do measurements for different gases. The advantage of this method is its sensitivity for trace gas emissions. A disadvantage of the NBL technique is the need for NBL height measurements, which is not common at ecosystem flux

sites. Also, other disadvantages are that possible spatial heterogeneity will not be observed, and stable night conditions are required. An example of a type of NBL technique is described in §5.1.

As sketched in the previous paragraphs, each flux measurement techniques has its advantages, disadvantages and difficulties. To study an ecosystem in spatial and temporal scale, it is advised to combine different flux measurement techniques, so that the different methods can complement each other [127, 171]. An example set-up will be described in §3.5 and results of field experiments combining different flux measurement techniques are shown in Chapter 5, 6, 7 and in the Appendix.

3.5 Description of the experimental field set-up

3.5.1 The sampling manifold

For the field campaigns described in this thesis, we made use of the FTIR-analyzer as described in §3.3. The FTIR-analyzer's cell temperature was set to 30 °C and the N_2 flow to flush the detector was set to 0.2 L min^{-1}, unless mentioned otherwise. To expand the possibilities of the FTIR-analyzer, a small adjustment was made to the instrument: the sampling stream tube between the Nafion dryer and valve 8 was cut and extended to outside the FTIR-analyzer. This outlet was connected to a small pump. The advantage of this new set-up is that a closed flow-mode sampling loop could be created (through valve 1, 6 and 7) but, at the same time, a switch could be made to static sampling with fast evacuation by use of the strong pump (via valve 8). Because of this, and because of the external sampling box, the FTIR-analyzer could simultaneously perform flux gradient measurements as well as closed-loop flux chambers measurements (Figure 3.6).

The sampling manifold was build inside a large suitcase and consists of 2 and 3 way valves and tubing (1/4 inch, material (Dekabon/Synflex) (Figures 3.7 and 3.8). Connections were made by use of Swagelok connectors and SMC pushfits. The programming of the sampling box was done via integration of the manifold into the source code of the FTIR-analyzer's software which is named Oscar, and which is written in Microsoft Visual Basic. The manifold created the possibility to continuously and simultaneously sample and measure different air samples. For example, air from two FG heights was led to the sampling bags (for 30 minutes), while the FTIR-analyzer at the same time analyzed the bag air from the previous 30 minutes. The FTIR-analyzer was set to GMT-time, and the time of the measurements shown in this thesis are as well, unless mentioned otherwise.

The valves ChA and ChB are connected to the outlet of valve 7. If the FTIR-analyzer is running in flow mode, valve ChA and ChB control where the measured sample air is being led to. The valves TR and OP (stands for transparent and opaque) are not meant for air samples but lead pressurized air towards the flux chambers: pressuring one line either opens or closes a flux chamber.

The set-up of the FTIR-analyzer connected to a flux gradient set-up and the two flux chambers is shown in Figure 3.6. A possible sampling schedule is shown in Table 3.3. Within the different field campaigns, the FTIR-analyzer flux measurement set-up has been changed and adapted (see §4.5). Unless mentioned otherwise, the field campaign was set up as described below.

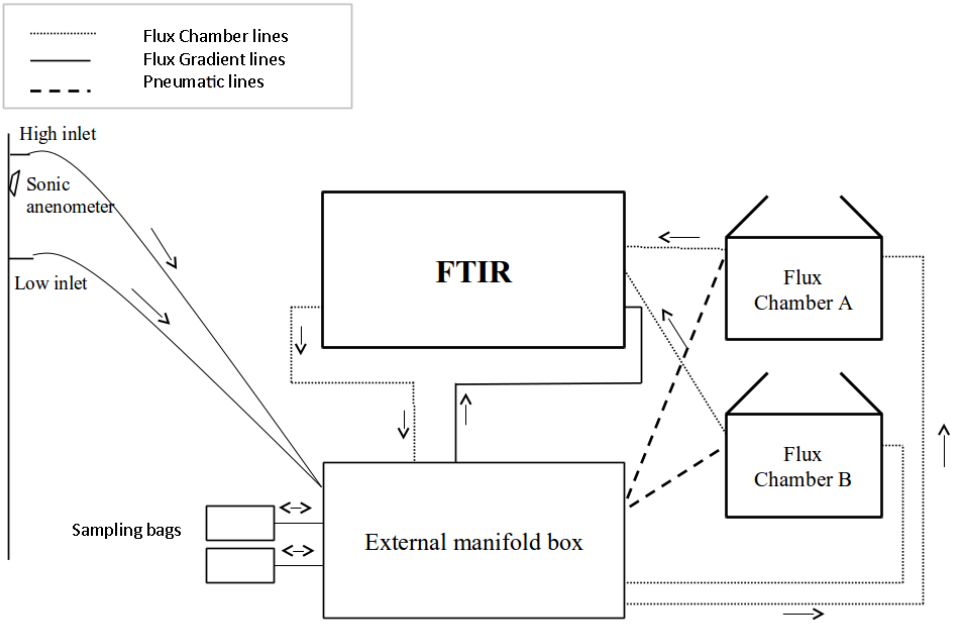

Figure 3.6: Schematic of the measurement set-up which combines two flux measurement techniques: the flux gradient technique and the flux chamber technique.

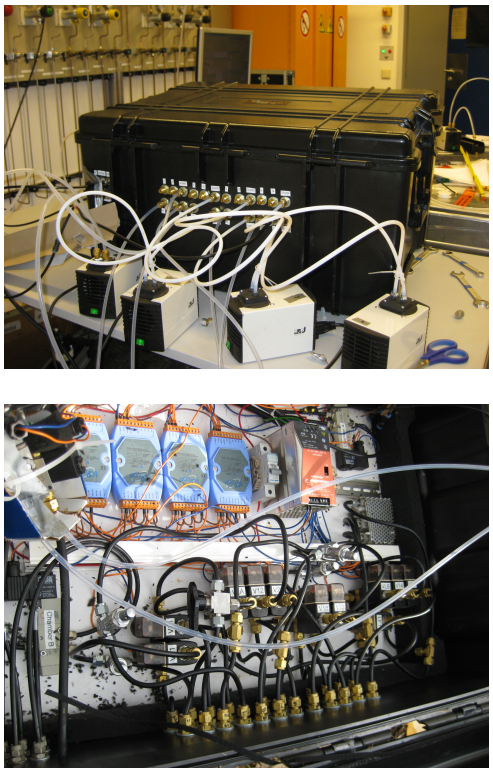

Figure 3.7: Upper figure: the sampling manifold box connected to the pumps (KNF N86KN.18), during the campaign at fieldsite RISØ (see §4.2). Lower figure: the inside of the sampling manifold box.

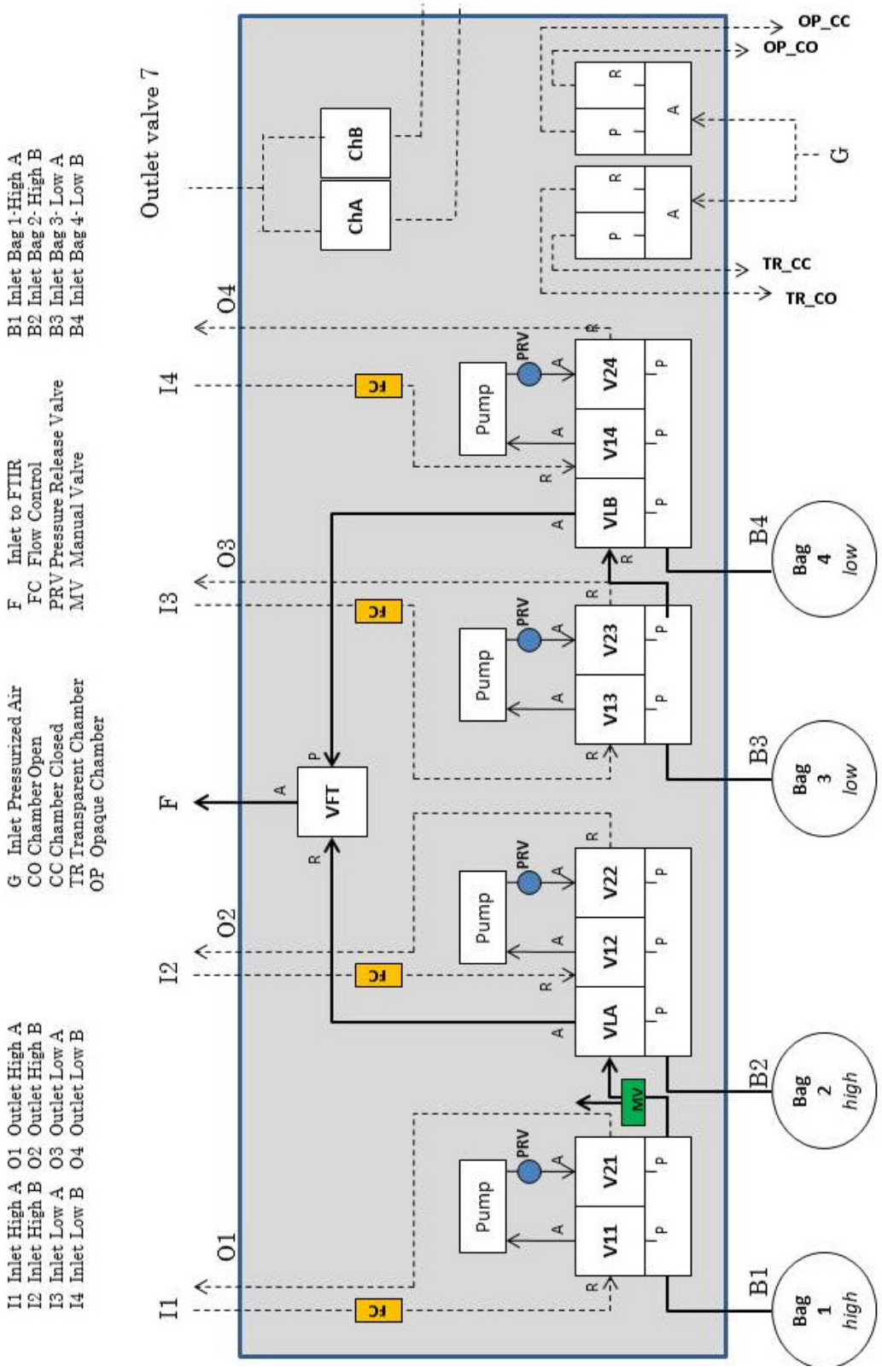

Figure 3.8: Schematic of the valves inside the sampling manifold box.

Table 3.3: Example sampling schedule for the continuous hourly sampling of the flux gradient inlets and the two flux chambers. During the flux gradient bag air analyses, several flush and evacuation cycles inside the FTIR-analyzer were performed. The flux gradient bags are being evacuated simultaneously with the flux chamber air measurements. In this schedule, both flux chambers are connected to inlet 2 of the FTIR-analyzer, however, this can easily be changed to another inlet.

Min	**Actions**	**V11**	**V21**	**V12**	**V22**	**V13**	**V23**	**V14**	**V24**	**VLA**	**VLB**	**VFT**	**ChA**	**ChB**	**OP**	**TR**	**1**	**2**
0-7.5	FTIR-analyzer: Measure bag 2 SB: Fill bag 1&3	0	1	0	0	0	1	0	0	1	1	0	0	1	0	0	1	0
7.5-15	FTIR-analyzer: Measure bag 4 SB: Fill bag 1 & 3 SB: Evac. bag 2	0	1	1	0	0	1	0	0	1	1	1	1	0	0	0	1	0
15-30	FTIR-analyzer: Ch A SB: Fill bag 1& 3 SB: Evac. bag 2 & 4	0	1	1	0	0	1	1	0	1	1	0	1	0	1	0	0	1
30-37.5	FTIR-analyzer: Measure bag 1 SB: Fill bag 2&4	0	0	0	1	0	0	0	1	0	0	0	1	0	0	0	1	0
37.5-45	FTIR-analyzer: Measure bag 3 SB: Fill bag 2&4 SB: Evac. bag 1	1	0	0	1	0	0	0	1	0	0	1	0	1	0	0	1	0
45-60	FTIR-analyzer: Ch B SB: Fill bag 2 & 4 SB: Evac. bag 1 & 3	1	0	0	1	1	0	0	1	0	0	0	0	1	0	1	0	1

3.5.2 The flux gradient measurement set-up

The set-up of the flux gradient technique was varying over the different experiments concerning the FG inlet heights and the sampling times, however, in general the set-up was as follows. Air sampling was done continuously. For 30 minutes per hour, the airflows were directed to air sampling bags, after that the bag inlet was closed until analysis. Before analysis, the measurement cell was evacuated. Afterwards, the cell and sample lines were flushed twice with sample air to avoid contamination with old measurement air. For each air sample, a 3-min spectrum was taken. After analysis, the bags were fully evacuated so that they would be empty at the beginning of the filling cycle. The inlet lines were, if possible, put above and below the on site sonic anemometer, which makes the parameterization of the diffusion coefficient possible [8] (see also §5.2).

The flux gradient technique uses the concentration difference between the two inlet heights to derive the flux (see §3.4.1). During unstable conditions, concentration differences are small and therefore, accurate measurements are necessary. For this reason, sampling lines were regularly checked for leaks and internal gas production. To avoid possible contamination by leaking pumps (see §4.5), during one experiment pumps were placed at the sampling location: if a pump leak would occur, still representative air would be sampled.

3.5.3 The flux chamber measurement set-up

The two flux chambers which were used in the field campaigns (open dynamic chambers, 50 cm $\times$ 50 cm $\times$ 50 cm, produced by Karlsruhe Institute of Technology, Germany) consisted of a stainless steel frame, UV-transparent acrylic sides (Acryl Glass XT solar, 3 mm, UV-transparent) and a vent tube, and were tightened by use of clamps and rubber air strips. Transparency of the acrylic material was measured and reported to be $> 90\%$ in the UV and visible wavelength band (280-700 nm) [150]. Two fans per flux chamber were continuously running, which insured well-mixed headspace air. Air flow from the flux chambers to the FTIR-analyzer was initiated by a membrane pump placed behind the measurement cell (KNF N86KN.18). Automatic chamber closure was made possible by use of a pneumatic system regulated by the valve manifold box (Figure 3.9, right figure). Pressurized nitrogen from a gas bottle (50 L) was connected to inlet G (Figure 3.8) and pressurized either line **TR_CO** or **OP_CO** (chamber open) or **TR_CC** or **OP_CC** (chamber closed). Time of closure was different per field campaign. Gas fluxes were calculated by:

$$F = \frac{VP}{RST}\frac{\Delta C}{\Delta t} \tag{3.11}$$

wherein V is the volume of the chamber (m^3), P the chamber air pressure (Pa), R the gas constant (8.314 m^3 Pa K^{-1} mol^{-1}), S the chamber surface area (m^2), T the chamber air temperature (K) and $\Delta C/\Delta t$ is the gas concentration change over time (mol $mol^{-3}s^{-1}$).

Air flow from the flux chamber to the FTIR-analyzer was started before the flux chamber closure to flush out old air. For flux chamber measurements, 2-min spectra were used. For flux calculations, only the concentration increases from 2 minutes after the chamber closure were used. Concentration increases were checked for non-linear trends and, if observed, not used. Flux standard deviations were derived from the propagated standard deviations of the regression slope.

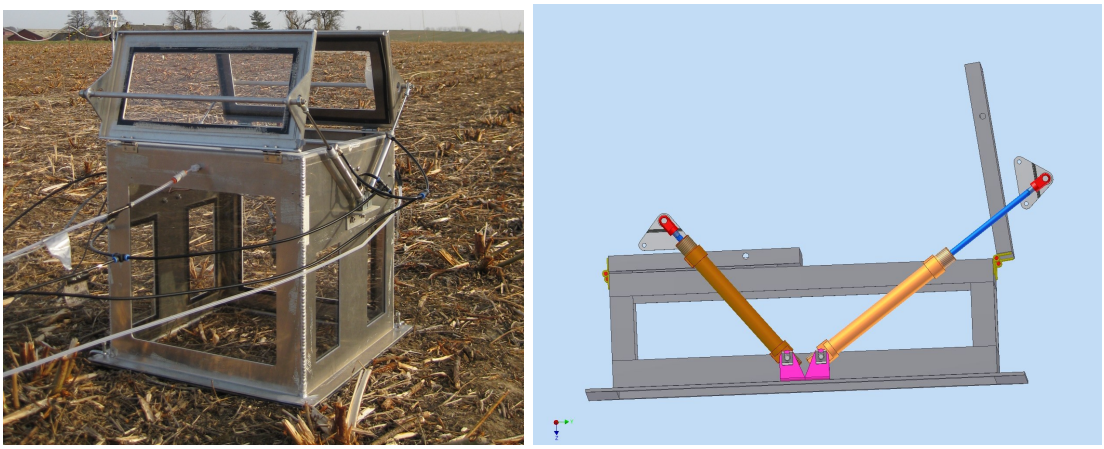

Figure 3.9: Left figure: transparent flux chamber, produced by KIT, during the campaign at fieldsite RISØ (see §4.2). Right figure: schematic of the pneumatic system, which was designed to open or close the flux chamber lids.

3.5.4 Detection limit of the flux measurement set-up

A sensitivity analysis of the set-up for the different flux measurement techniques was performed. For the analysis, data from the campaign at the fielsite Himmelmoor was used (§4.1, §10.3.1). The FTIR-analyzer's measurement precision for 10-minute averaged values is given in Table 3.1. Precisions for spectra with shorter averaging times, such as used in the Himmelmoor field campaign of 2 and 3 minutes, are estimated and shown in Table 3.4.

Measurement of greenhouse gas fluxes by the flux chambers, as well as by the flux gradient technique, are based on concentration differences, where a possible instrumental drift plays a minor role. For reliable flux gradient measurements, a minimum concentration difference of 2σ is needed. Typical diffusion coefficient values under unstable conditions (Obhukov-length < 0, see §5.2) range between 0.1-0.4 $m^2\ s^{-1}\ m^{-1}$ [57]. For reliable flux chamber measurements, also a minimum difference of 2σ between measurements is required. Minimum detectable fluxes for the flux gradient technique (3 min-spectra) and for the flux chamber technique (2 min-spectra) are given in Table 3.4.

Increasing the time per spectrum decreases the required minimum concentration difference and could be considered in small magnitude flux ecosystems. Increasing the sensitivity of the flux gradient method for low fluxes can be done by increasing the inlet-height difference, which will result in higher concentration differences. However, a too large distance between the inlets may lead to a different footprint per inlet (e.g. measuring different types of soil, ecosystems or environmental conditions). Also, the lower inlet position should be higher than nearby vegetation or other disturbances.

Table 3.4: Estimated minimum detectable fluxes for the described measuremen set-up, based on the FTIR-analyzer's precision. For the flux gradient technique, the following is assumed: a diffusion coefficient of 0.1 m^2 s^{-1}, a Δz of 1.5 m, and a spectra time of 3 minutes. For the flux chamber technique, a spectra time of 2 minutes is assumed.

	FTIR-analyzer's precision (1δ, 10 min)	**Estimated FTIR's precision (1δ) for 3 & 2 min spectra**	**Minimum detectable flux flux gradient method**	**Minimum detectable flux flux chamber method**
CO_2	0.02 µmol mol^{-1}	0.04 & 0.05 µmol mol^{-1}	0.2 µmol m $^{-2}$ s^{-1} 9.7 µg m $^{-2}$ s^{-1}	0.003 µmol m $^{-2}$ s^{-1} 0.12 µg m $^{-2}$ s^{-1}
CH_4	0.2 nmol mol^{-1}	0.36 & 0.45 nmol mol^{-1}	2.0 nmo m $^{-2}$ s^{-1} 35.6 ng m $^{-2}$ s^{-1}	0.09 nmol m $^{-2}$ s^{-1} 1.3 ng m $^{-2}$ s^{-1}
CO	0.2 nmol mol^{-1}	0.36 & 0.45 nmol mol^{-1}	2.2 nmol m -2 s^{-1} 62.2 ng m $^{-2}$ s^{-1}	0.3 nmol m $^{-2}$ s^{-1} 7.6 ng m $^{-2}$ s^{-1}
N_2O	0.06 nmol mol $^{-1}$	0.11 & 0.13 nmol mol $^{-1}$	0.67 nmol m $^{-2}$ s^{-1} 29.4 ng m $^{-2}$ s^{-1}	0.02 nmol m $^{-2}$ s^{-1} 0.02 ng m $^{-2}$ s^{-1}

4 Description of the field experiments

Four main field campaigns, wherein the FTIR-analyzer was combined with different types of ecosystem flux and concentration measurement techniques, have been performed during the PhD. These field campaigns were funded by InGOS (Integrated non-CO_2 Greenhouse gas Observing System, see Chapter 5 and Acknowledgements) and were directed to the objective of InGOS to assess the use of the FTIR-analyzer for biosphere-atmosphere exchange studies. Furthermore, the field campaigns were designed to study different types of ecosystem processes.

The first three field campaigns, described in §4.1, §4.2 and §4.3, were focused on the measurement of biosphere-atmosphere exchange fluxes. The first field campaign was performed in the peatland Himmelmoor (Quickborn, Germany) in the summer and fall of 2012 (§4.1). The second field campaign was performed in a willow field after harvest at RISØ (Roskilde, Denmark) in April 2013 and was part of a collaborative InGOS N_2O flux chamber intercomparison campaign (§4.2). The third and fourth field campaign have been performed in the region of Viterbo (Italy) in the summer and autumn of 2013. The third campaign was especially set up to study abiotic degradation fluxes in an arid ecosystem (§4.3). The last field campaign concerned an experiment with continuous multiple-inlet concentration measurements to study the storage component of the eddy covariance method (§4.4).

Data from the different campaigns is presented in different parts of this thesis (Chapter 5, 6, 7 and the Appendix). To avoid double descriptions in this thesis, all fieldsite information and details concerning the FTIR-analyzer and its experimental set-up, are described in this chapter. Possible scientific background of experiments is given where the results are presented.

4.1 The fieldsite Himmelmoor

4.1.1 Motivation and objectives

The field experiment in peatland Himmelmoor was the first field campaign performed during the PhD, and took place in the summer and fall of 2012. One of the aims of this experiment was to test and improve the set-up, which was described in §3.5. The second aim was to study the process of photodegradation: the direct breakdown of organic matter by radiation. The fieldsite Himmelmoor has large not-vegetated areas with organic matter at the surface and would therefore be an interesting location to study photodegradation fluxes. For more information on photodegradation, see Chapter 6. During the experiment, continuous improvements have been applied to the field set-up but also several errors have been discovered, wherefore not all data from this field experiment can be used. In this thesis, the field campaign will be referred to as 'Himmelmoor' and data from the campaign can be found in the Appendix (§10.3.1).

4.1.2 Fieldsite

The peatland Himmelmoor is situated 3 km west of the village of Quickborn (Schleswig-Holstein, Germany). The climate in this region is classified as Dfb (hemiboreal climate [100]), with an average annual temperature of 8.3 °C and an average precipitation of 767 mm. Himmelmoor is the

largest raised (rain-fed) heavily degraded bog in the state of Schleswig-Holstein (605 hectares). It is expected that at some places, the peat was up to 10 meters deep, now the maximum depth is approximately 2 meters. Since 1920, peat is being excavated by Torfwerk Quickborn (Torfwerk Enfeld Carl Hornung Werk Quickborn). In 2008, the company started to stepwise restore the peatland and bring it back to its natural state by rewetting the area. All excavation activities have to be ended in 2020. Figure 4.1 shows an overview of the peatland with the different phases of the rewetting indicated. The vegetation in the fieldsite Himmelmoor in the rewetted parts mostly consist of different types of Sphagnums mosses (*S. angustifolium, S. fimbriatum, S. rubellum, S. imbricatum, S palustre*), trees (*salix, Betule pubescens*) and grasses (*Eriophorum, Molina caerulea*). The active excavations areas are without vegetation.

The fieldsite Himmelmoor is an experimental site managed by the University of Hamburg and eddy covariance measurements are performed since 2011. The fieldsite also functions as a test site for the company LI-COR (Lincoln, Nebraska, USA). Continuous EC measurements of scalars and energy fluxes are performed (LI-7700 for Methane, LI-COR, Lincoln, Nebraska, USA; LI-7200 for CO_2/H_2O, LI-COR, Lincoln, Nebraska, USA; Windmaster Pro sonic anemometer, Gill, Hampshire, UK.)

4.1.3 Field experiment

- **Start experiment**: 31 July 2012
- **End experiment**: 1 December 2012
- **Usable data**: 4 August-16 November

- **Persons involved**: Lars Kutzbach, David Holl, Norman Rüggen, Christian Wille (University of Hamburg, Germany); Hans Czerwonka, Klaus-Dieter Cherwonka (Torfwerk Einfeld Carl Hornung); Hella van Asperen, Thorsten Warneke (University Bremen, Germany)

The set-up of the field experiment in Himmelmoor was mainly as described in §3.5. The FTIR-analyzer, the sampling box, an uninterruptible power supply (UPS), and a ventilator were placed in a wagon in the middle of the fieldsite (Figure 4.1, upper left picture in Figure 4.2). The flux gradient tower was placed in the rewetted area, approximately 35 meters away from the wagon (light green zone in Figure 4.1). The location of the tower was still dry at the beginning of the experiment, but was flooded at the end of the experiment (upper right picture in Figure 4.2). The FG inlet heights were at 0.55 and 1.95 m. The sonic anemometer was placed at 1.85 m. Air from the FG system was let via PTFE tubing (length of sampling line approximately 45 meters) to the FTIR-analyzer. Air was continuously being sampled and led to one pair of FG sampling bags (non-transparent wine bags, 10 L) for 30 min, after which the inlet flow was directed to the other pair of sampling bags for 30 min. Analysis of the two bags was done within 15 minutes: the measurement cell was evacuated (2 min, untill around 1 mb), filled (2 min), and analyzed (3-min spectra, static mode). When both bags were analyzed, the bags were evacuated to be prepared for the next filling phase. The other 15 minutes were used by the FTIR-analyzer to analyze one of the flux chambers. In the next half hour, the remaining 15 minutes were used to analyze the other flux chamber. For an overview of the sampling schedule, see Table 3.3.

The flux chambers were first placed on the dry wall between two rewetted areas on a distance of approximately 40 meters from the FTIR-analyzer (Figure 4.1). Both flux chambers were connected in a closed loop to the FTIR-analyzer by PTFE tubing; the lines from and to the flux chambers were between 57 and 78 m. Air from the flux chambers was circulated and measured

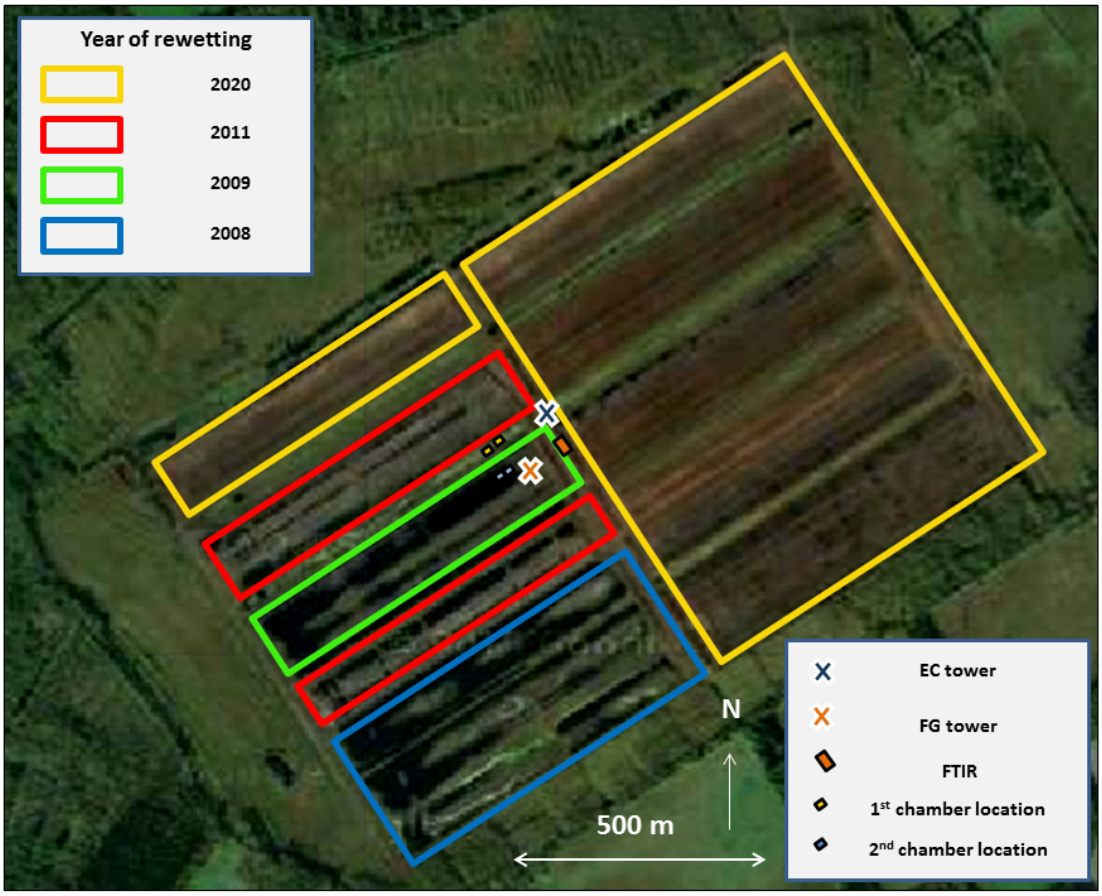

Figure 4.1: Aerial photograph of the fieldsite Himmelmoor. The different colors indicate the different starts of the rewetting phases (see legend). The two flux chambers have been positioned for approximately 8 weeks at chamber position 1, followed by approximately 5 weeks at chamber position 2. The aerial photograph is from Google (2015).

for 14 minutes, by taking seven 2-min spectra (flow mode). The flux chambers were closed after the first measurement. On 16 August, one chamber (chamber A) was covered with aluminum foil for the photodegradation experiment. Between 25 September and 4 October both flux chambers were sealed (closed at bottom by aluminum foil) to test the flux chamber and sampling lines for internal CO and CO_2 production. Only minor CO production was found, results can be found in the Appendix (§10.2.3).

From 4 October to 15 November, a second location, in the rewetted area next to the FG tower, was measured by the flux chambers, which were now both transparent. After 15 November, the flux chambers were placed in the fully flooded area on top of vegetation and on the east side of the FTIR-analyzer (yellow zone in Figure 4.1). Also, the chamber lines have been connected to a floating chamber (lower left picture, Figure 4.2, for results, see §10.3.1). During the experiment, flux chamber and FG sampling lines have been tested for leaks. Halfway the experiment, when cold temperatures caused condensation in the sampling lines, the lines were raised to 1 m by use of metal sticks. N_2 for flushing of the detector and for the pneumatic flux chamber opening originated from two pressurized gas bottles (50 L), placed below the wagon (lower right picture, Figure 4.2).

Figure 4.2: Pictures of the measurement set-up at the fieldsite Himmelmoor. Upper left: the view of the set-up in the rewetted area (light green zone, Figure 4.1); upper right: the FG tower in the rewetted area; at the end of the experiment, the FG tower was inside a water pond. Lower left: picture of the floating chamber experiment (see §10.3.1), lower right: the wagon wherein the FTIR-analyzer, the UPS and sampling box were placed.

4.2 The fieldsite RISØ

4.2.1 Motivation and objectives

The following campaign was directed towards the InGOS project work package task 13.2 (see Chapter 5), and was coordinated by RISØ (Roskilde, Denmark). The goals of the campaign were a) to compare different flux measurement set-ups which are in use by different institutes, b) to gain more knowledge on the errors related to N_2O flux chambers, and c) to be able to provide methods to control them. Therefore, different working groups were invited to participate in the field campaign, by bringing their own flux chambers and analyzers. To assure the presence of major N_2O fluxes, the fieldsite was fertilized before the start of the campaign. A second objective, not related to the InGOS intercomparison campaign, was to further test the set-up, which was described in §3.5, and to implement the improvements which were developed after the field campaign 'Himmelmoor' (see §4.5). In this thesis, the field campaign will be referred to as 'RISØ' and data from the experiment can be found in §5.1, §5.4 and in the Appendix (§10.1.1, §10.2.3 and §10.3.2).

4.2.2 Fieldsite

- **Start experiment**: 15 April 2013
- **End experiment**: 27 April 2013
- **Usable Data**: 15-27 April 2013

- **Persons involved**: Per Ambus, Mette S. Carter, Andreas Ibrom, Kim Pilegaard (RISØ, Denmark); Werner Kutsch, Christian Brümmer, Jeremy Smith, Bjarne Lyshede, Dirk Lempio, Jean-Pierre Delorme (Thünen Institute, Germany); Rainer Gasche, Georg Willibald, Robin Arnold, Eugenio Díaz-Pinés (KIT, Germany); Hella van Asperen, Thorsten Warneke (University Bremen, Germany)

The field campaign took place on an experimental fieldsite of RISØ, 5 km north of the city of Roskilde. The climate in this region is classified as Dfb (hemiboreal climate [100]), with an average annual temperature of 8.3 °C and average precipitation of 604 mm. The fieldsite is a willow plantation since 2010 (*Salix triandra x S. viminalis & Salix schwerinii x S. viminalis x S. vim.*), covers 10 ha and is established on a fertile loamy sand soil. Fertilization took place in 2011 (slurry fertilization 81 kg N ha^{-1}), and willows were harvested in February 2013. The fieldsite was fertilized again in April 2013, right before the start of the experiment with 120 kg N-PK ha $^{-1}$.

4.2.3 Field experiment

The set-up at the fieldsite RISØ was mainly as described in §3.5. The FTIR-analyzer, the sampling box and the UPS were placed in an air-conditioned measurement truck of Karlsruhe Institute of Technology (KIT). The N_2-flow for flushing the detector and for the pneumatic chamber system was provided by KIT, and was produced by a nitrogen gas generator.

The flux gradient inlets were at the EC tower of RISØ at approximately 30 m distance from the FTIR-analyzer and inlets were at 0.42 and 2.42 m height. The sonic anemometer and CO_2 analyzer (Gill HS and LI-7200) were also placed at 2.42 m height. The sampling schedule was different than described in §3.5 (Table 3.3): instead of two, only one hourly 30-min averaged flux gradient measurement was performed. Therefore, air was not continuously sampled: only for 30 min per hour the air was led and stored in sampling bags. After sampling, 20 minutes was planned for the full analysis of both bags, which included evacuation of the cell (2 min, untill approx 1 mb.), flushing of sampling lines and cell (15 sec), evacuation of the cell (2 min, until approx 1 mb.), filling of the cell (2 min), and stabilization of the cell (30 sec), followed by the analysis (3-min spectra, static mode). After the analysis, the bags were evacuated to be prepared for refilling.

Flux chambers were both sampled for 20 minutes. Nine 2-min spectra were taken (flow mode) and chamber closure was after the 2^{nd} measurement. Flux chambers were placed close to other flux chambers (see Figure 10.2) and to each other (± 4 m). Extra soil collars, brought by KIT, were installed and were used in the second half of the experiment for the study which is described in §5.4. On 19 April, chamber A was covered with aluminum foil for a short photodegradation experiment. On 22 April, chamber B and all other transparent flux chambers of the intercomparison campaign were also covered with aluminum foil to avoid high temperatures inside the chambers. More details about the other flux chambers can be found in §10.1.1.

4.3 The fieldsite Rocca4

4.3.1 Motivation and objectives

The field campaign in the arid grassland Rocca4 (Italy) was performed in the summer of 2013 and was a result of a collaboration between University of Bremen and University of Tuscia (UNITUS) and directed towards the InGOS project work package task 13.2, in which University of Bremen and UNITUS were both collaborators. The main aim of this experiment was to study the process of photodegradation: the direct breakdown of organic matter by sunlight. The fieldsite, Rocca4, is very suitable for abiotic degradation studies due to its sunny conditions, its arid climate and its available dry organic matter on the surface. A second aim of this experiment was to study the possible geological fluxes by use of isotopic measurements. In this thesis, the field campaign will be referred to as 'Rocca4' and data from the experiment can be found in §5.2, Chapter 6, Chapter 7 and in the Appendix (§10.2.3, §10.3.3).

4.3.2 Fieldsite

The field experiment was performed at an experimental station named Rocca4 (IT-Ro4), which is managed by the University of Tuscia (UNITUS). The fieldsite is a grassland (harvested cropland, approximately 250 m by 450 m, lat 42.37 N, long 11.92 E, 147 m, a.s.l.), in the province of Viterbo, Italy. The climate in this region can be classified as Csa (Mediterranean) [100], with a typical drought period covering approximately 2 months during summer (July–August). Mean annual temperature is 14°C and annual rainfall is 755 mm. The underlying material is tuff, soil texture is clay loam and soils are classified as Eutric Cambisol. Yearly, the fieldsite is ploughed to a depth of 20 or 50 cm. Just before the experiment, oat and vetch were cultivated. During the experiment, vegetation was not managed and was a mix of invasive species such as *Amaranthus retroflexus*, *Chenopodium* spp., *Conyza canadensis*, *Artemisia vulgaris*, *Cirsium* spp., *Mercurialis annua* and *Polygonum* spp. At the beginning of the experiment, most vegetation was dried out, however, patches of active vegetation were observed. Temperature and rainfall during measurements were representative for the period (hot and dry) (Figure 6.3), however, the preceding spring had been cold and rainy in respect to the average.

Continuous EC measurements of scalars and energy fluxes are performed (LI-7500 open path analyzer, LI-COR, Lincoln, Nebraska, USA; Windmaster Pro sonic anemometer, Gill, Hampshire, UK) along with meteorological and environmental measurements (CNR-1, Kipp & Zonen, Delft, the Netherlands; soil water content, CS616, Campbell Scientific, North Logan, USA; soil temperature, CS107, Campbell scientific, North Logan, USA; soil heat flux, HFT3 Soil Heat Flux Plate, Campbell scientific, North Logan, USA).

4.3.3 Field experiment

- **Start experiment**: 15 July 2013
- **End experiment**: 11 September 2013
- **Usable data**: 4 August-11 September 2013

- **Persons involved**: Dario Papale, Giacomo Nicolini, Simone Sabbatini, Tommaso Chiti, Alessio Boschi, Michele Tomassucci (UNITUS); Hella van Asperen, Thorsten Warneke (University Bremen, Germany)

The set-up in Rocca4 was mainly as described in §3.5. The FTIR-analyzer, an air conditioning and an UPS were placed in a metal housing, which was packed in white styrofoam to increase

Figure 4.3: Pictures of the fieldsite Rocca4. Left figure: an overview of the fieldsite Rocca4, with in the front the two flux chambers, and in the back the EC tower and the metal housing. Right figure: the EC tower with the FG inlets and the small pumps at 1.30 and 4.10 m. The fence is against cattle, which usually graze in this fieldsite.

its albedo (Figure 4.3). The N_2-flow for flushing the detector and for the pneumatic chamber closing system originated from two 50 L bottles, positioned outside the housing. Due to lack of space, the sampling box was also placed outside, under a small plastic cover. During this experiment, on 2 August, the FTIR-analyzers cell temperature was changed to 35 °C.

The flux gradient inlets were at the EC tower of UNITUS and at 1.30 and 4.10 m height. The EC measurements were performed at 3.30 m. Just as in the campaign at RISØ, only one 30 min averaged FG measurement was performed per hour. However, the sampling flow was continuous to avoid accumulation of air in the sampling box and lines. Furthermore, sample lines for the experiment were of stainless steel material (Swagelok, 1/8 inch) to avoid internal CO production (see §4.5). Also, the pumps were replaced by smaller pumps (KNF-N86KNDCB and were placed at the sampling location in the tower; if the pumps would start to leak, they would be surrounded by measurement air, and the sampled air would therefore be diluted by a similar gas mixture (see §4.5). Ten minutes per bag was available for analysis, which included flushing of sampling lines and cell (15 sec), evacuation of the cell (2 min, until approx 1 mb.), filling of the cell (2 min), and stabilization of the cell (30 sec), followed by the analysis (3-min spectra, static mode). After analysis, the bags were evacuated to be prepared for refilling.

The flux chambers were both sampled for 20 minutes. Nine 2-min spectra were taken (flow mode) and flux chamber closure was after the 2^{nd} measurement. For chambers, stainless steel sampling lines could not be used due its small diameter which causes a too large pressure drop (distance to chambers was more than 40 m). However, before the start of the chamber measurement, the air between the flux chamber and the FTIR-analyzer was already circulating for 2 minutes, to flush out the old sampling air. Also, to avoid contamination with 'old' air, the first 4 minutes of the flux chamber measurements were not used. Flux chamber lines were covered with aluminum foil or placed within a plastic tube to be protected against the sun and animals. Instead of two, now six soil collars were inserted on 15 July 2013. The two flux chambers were exchanged between the different collar locations (visualized with colors in Figure 4.4). One chamber (chamber B) was made opaque on 5 August. It is expected that on 8 August a leak has formed in this chamber. Measurements from this chamber after 8 August are not used for further analyses. Flux chambers were tested for internal CO and CO_2 production on 19 August:

Figure 4.4: Aerial photograph of the fieldsite Rocca4. Figure upper left: overview of the fieldsite Rocca4. The black open square indicates the fence around the EC tower (see Figure 4.3) and the blue square is the location of the metal housing of the FTIR-analyzer. The aerial photograph is from Google (2015). Figure right below: zoom in on the position of the flux chambers which were positioned west of the EC tower. The color of the squares indicate the following: power supply = black square, pos. 1 = yellow, pos. 2 = purple, pos. 3 = red, pos. 4 = blue, pos. 5 = green, pos. 6 = orange. The positions 1 and 4 were bare soil locations.

minor CO production was found (see §10.2.3), data shown in this thesis is not corrected for this. At two soil collar locations (position 1 and 4), all above ground organic material was removed to create 'bare soil'-locations.

On 12 August, a Los Gatos instrument (CO_2 isotope analyzer), measuring CO_2 and $\delta^{13}CO_2$ was placed alongside the FTIR-analyzer. The sampling box was programmed so that the remaining FG sample bag air was led for 3 minutes to the Los Gatos instrument to be analyzed. Also, during flux chamber measurements and closure, the Los Gatos instrument measured the same chamber air. To make this possible, the closed loop of the FTIR-analyzer was changed: measured FTIR-analyzer-air was not led back to the flux chamber and the inlet was used for the Los Gatos measurements (Figure 4.5). The flux calculations were corrected for this. Concentration and flux measurements of the Los Gatos are not shown in this thesis.

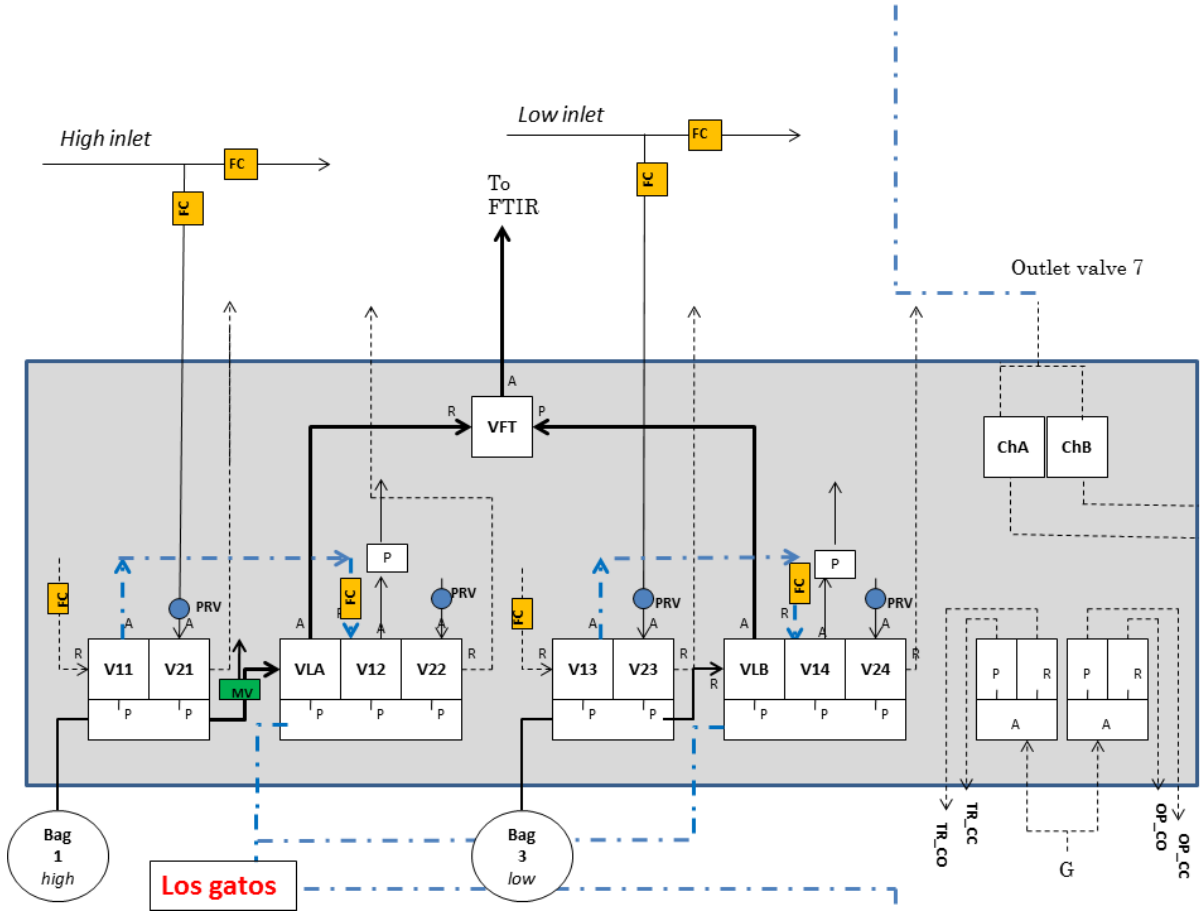

Figure 4.5: Schematic of the sampling box set-up for connecting the Los Gatos instrument during the campaign at fieldsite Rocca4. The measured flux chamber air was not led back to the flux chambers, and the flux chambers could therefore simultaneously be measured by the FTIR-analyzer and the Los Gatos instrument. The FG bag air was led to the Los Gatos instrument after the FG bag air was sampled by the FTIR-analyzer. To lead bag 1 air to the Los Gatos instrument, valves V11 and V12 were activated. To lead bag 3 air to the Los Gatos instrument, valves V13 and V14 were activated. To lead flux chamber A air to the Los Gatos instrument, valve ChA was activated. To lead flux chamber B air to the Los Gatos instrument, valve ChB was activated. The blue dotted lines indicate the air flows to the Los Gatos instrument.

4.4 The fieldsite Poplar

4.4.1 Motivation and objectives

The following field campaign was focussed on the measurement of the eddy covariance storage component. The aim of the field campaign was to study the horizontal and vertical concentrations of different gases within a canopy during non-turbulent conditions, with the goal to improve estimates of the EC storage term. In this thesis, the field campaign will be referred to as 'Poplar' and data from the experiment can be found in §5.3 and in the Appendix (§10.3.4).

4.4.2 Fieldsite

The field experiment took place in a poplar plantation 10 kilometers east of the city of Viterbo. The climate in this region is Csa (Mediterranean) [100], with a typical drought period covering approximately 2 months during summer (July–August). The type of soil is a Chromic Luvisol [87]. Mean annual temperature is 14°C and annual rainfall is 755 mm. Poplar tree rows (*Populus nigra*) were spaced 2.5 m apart and 0.75 m between each other. At time of the experiment, poplar trees were 7 meters high. The poplar plantation is harvested every two years. An anemometer (Gill R3) was placed above the canopy at 9.5 m. Eddy covariance measurements were performed at a poplar plantation close by.

4.4.3 Field experiment

- **Start experiment**: 26 September 2013
- **End experiment**: 29 October 2013
- **Usable data**: 1-29 October 2013

- **Persons involved**: Dario Papale, Giacomo Nicolini, Simone Sabbatini, Tommaso Chiti, Alessio Boschi, Michele Tomassucci (UNITUS); Hella van Asperen, Thorsten Warneke (University Bremen, Germany)

Since the goal of this experiment was to measure gas concentrations instead of gas fluxes, the set-up is different than in the other field experiments (Figure 4.6). The FTIR-analyzer was placed in the air-conditioned metal housing, which was located between two lines of poplar trees, 40 meters away from the poplar plantation outer borders (Figure 4.8). The N_2-flow for flushing the detector originated from a 50 L bottle, positioned outside the housing. The sampling box was also placed outside, under a small plastic cover. During this experiment, the FTIR-analyzer's cell temperature was set to 35 °C.

12 air inlets were distributed in the poplar plantation: 6 inlets were distributed in a vertical plane, 6 inlets were distributed in a horizontal plane at 90 cm (Figures 4.7 and 4.8). All 12 inlets were measured every 1.5 hours, the FTIR-analyzer needed 7.5 min per inlet: evacuating of the cell (15 sec), flushing of sampling line and cell (15 sec), evacuating of the cell (2 min untill approx. 1 mb), filling of the cell (2 min), settling of the cell (30 sec), followed by the measurement (3-min spectra, static mode).

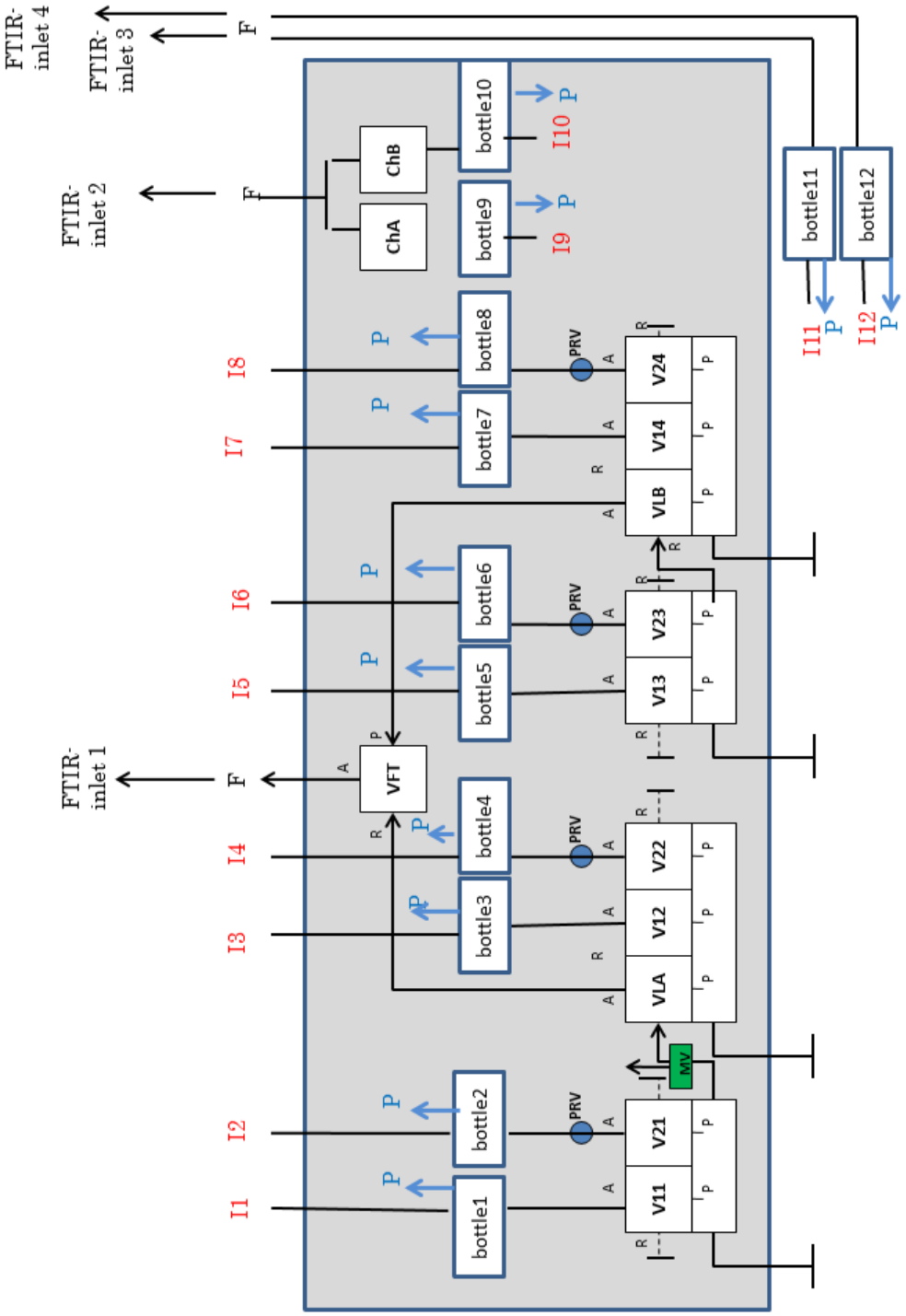

Figure 4.6: Sampling box set-up for the fieldsite Poplar, designed for 12-inlets concentration measurements. For the experiment, the use of buffer volumes (bottles) was planned to increase the sample's representativeness. However, for practical reasons, the buffer volumes were removed in the final set-up.

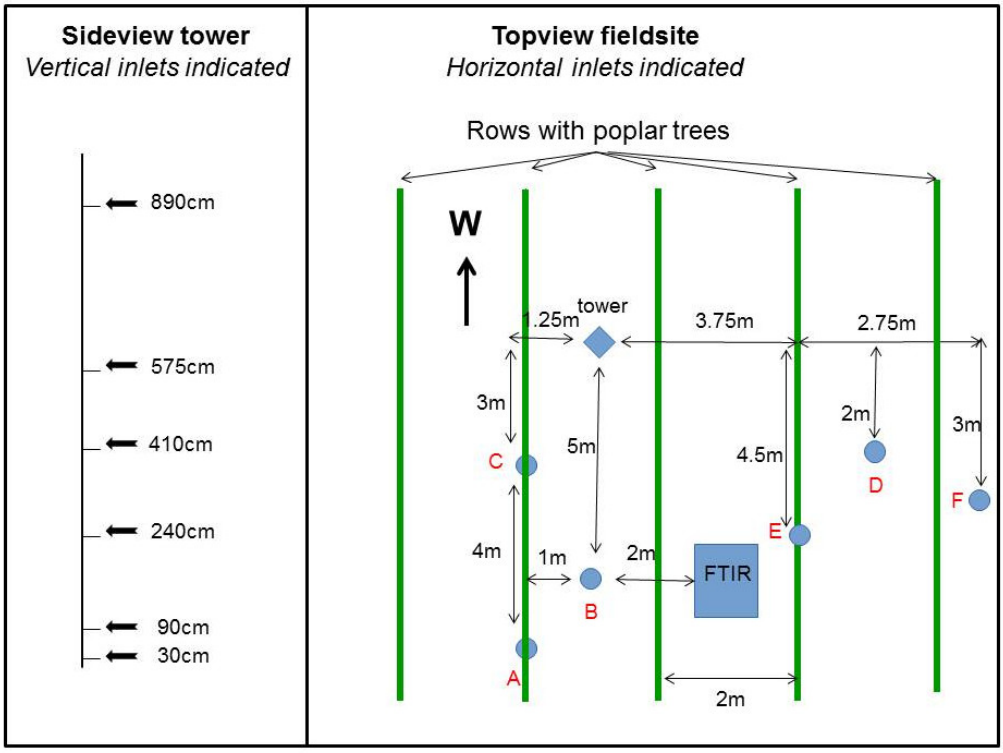

Figure 4.7: The field experiment set-up at the fieldsite Poplar. The left part of the figure shows the vertical distribution of the inlets, which were positioned at the tower. The tower can be seen in Figure 4.8. The right part of the figure shows the top view of the fieldsite Poplar, with the tower and the horizontal inlets indicated.

Figure 4.8: Pictures of the set-up at the fieldsite Poplar. Left figure: the tower with the vertical inlets was positioned between two poplar tree lanes. Right figure: the metal housing of the FTIR-analyzer was placed between two poplar tree lanes.

4.5 Evaluation and development of the experimental field set-up

During the different field campaigns which have been performed during the PhD, several minor and major adjustments have been made to improve the set-up of the FTIR-analyzer and the flux measurements. In this paragraph, the problems per field campaign and the applied solutions will be described.

4.5.1 The fieldsite Himmelmoor

Several shortcomings have been detected during and after the field experiment in Himmelmoor. First of all, the temperatures inside the flux chambers were not recorded, while internal temperature measurements are essential when studying respiration and degradation processes, and similarity with outside temperatures cannot be assumed. Furthermore, the measurement schedule caused the FTIR-analyzer to be unstable at time of the start of the measurement (cell pressure and cell temperature were not settled because of the quick filling of the cell). Possibly also the fact that the FTIR-analyzer was placed in a location with large temperature fluctuations can have caused unstable behavior of the FTIR-analyzer. Most important was the discovery that the used pumps had degraded strongly during or before the experiment which caused a strong leak in several parts of the measurement set-up; this finding was unexpected since these type of pumps are commonly used in ecosystem research. For the flux gradient measurements, which results are based on small concentration differences, this meant that the quality of the data could not be assured and the flux gradient data can probably not be used.

4.5.2 The fieldsite RISØ

After evaluation of the field campaign 'Himmelmoor', two temperature sensors were acquired and installed inside the flux chambers. The amount of measurements per hour was reduced to be able to create more time for flushing of the sampling lines and measurement cell, and to have more time for cell pressure and cell temperature stabilization. However, because of the longer measurement time required per sample, FG measurement frequency went down from two to one measurement per hour. Furthermore, it was expected that the environment of the FTIR-analyzer (air conditioned room) also caused the FTIR-analyzer to perform more stable.

Pumps were tested before the experiment but showed major leaks within the first week of the field campaign, wherefore FG flux data again could not be used. Also, some PTFE sampling lines showed high internal CO production, possibly caused because of solar radiation exposure (§10.2.3). The CO production was especially visible because the sample air inside the FG sampling lines was not moving for 30 min per hour due to the reduced sampling frequency. Animals in the field caused leaks within a day, wherefore it was decided to raise all sampling lines above the soil surface.

4.5.3 The fieldsite Rocca4

After the problems at RISØ, several major improvements were made before the start of this experiment. The pumps, which caused problems during the first two experiments, were replaced by smaller pumps, more suited for the required small sampling flow. Also, the problem of internal CO production was avoided by changing sampling line material to stainless steel and by keeping the sampling lines constantly flushed. Also, the pump location was changed to the sampling position in the tower, so that a possible leak would only result in contamination with

similar sampling air. Stainless steel lines were not used for flux chamber measurements. Stainless steel tubing of 1/4 inch is unpractical for field applications (unbendable and heavy), so 1/8 inch lines are used. However, the required flow rate of 1 liter per min is too high for such a diameter for long distances. However, flux chamber measurements are less sensitive to possible small PTFE line contaminations, because of the usual large concentration differences which are being measured in the flux chambers. To reduce possible CO production in the lines, the flux chamber sampling lines were covered by dark plastic tubing or aluminum foil.

The main problem during this campaign was the extreme temperature conditions. While the use of styrofoam and air conditioning helped, still temperature problems occurred. Chemical dryers needed to be changed frequently (>2 times a week), most likely due to the high water content of the warm sampling air. The raising of the cell temperature to 35 °C helped a little. When the chemical dryer was exchanged, measurements and air flows were stopped, causing condensation in the instrument and lines. After the exchange of the dryer, water levels in the instrument remained high (>20 ppm) for several hours, which is long in comparison to the exchanging frequency (3 days). Future campaigns in similar conditions need to consider longer or multiple chemical dryers to limit the amount of system disturbances.

4.5.4 The fieldsite Poplar

During the field experiment Poplar, two minor experimental problems have been encountered. Due to the varying length of the sampling lines and the varying resistance of the chemical dryer material, cell pressure was fluctuating (between 700-1000 mb) over the different measurements. For possible future field experiments, a different type of chemical dryer needs to be used and longer cell filling times need to be considered. To correct the data for the pressure fluctuations, pressure sensitivities were determined (§10.2.2) and corrections have been applied.

Animals were the second problem encountered at the fieldsite Poplar. Bugs climbed into the sampling box and clogged the lines and valves. The sampling box and valves needed to be flushed several times with pressurized air to remove all animals. More serious were the mice who crawled into the lower part of the FTIR-analyzer and chewed on its electronics. For follow up experiments, an idea would be to raise the FTIR-analyzer from the floor and to close the FTIR-analyzer openings completely.

4.5.5 General considerations for future field campaigns

Speed of sample gas handling within the measurement cycle is important: reserving more time for the flushing of the sampling lines and the cell minimizes the risk of polluting the sample air with the accumulated air from the lines and sampling box. Also, creating more time for settling of the cell after filling creates more constant measurement conditions (constant cell temperature and cell pressure). For the field experiments in this PhD, extra time was gained by reducing the amount of FG measurements. The decision to miss one FG measurement instead of one chamber measurement was made for two experiments (in RISØ and Rocca4), because of the important role the flux chamber measurements played in these field campaigns. For possible upcoming new campaigns, this decision needs to be reconsidered.

Leaking pumps can cause major problems, especially for FG measurements, wherein accuracy is important to correctly detect the small atmospheric concentration differences. The larger pumps, which were described in §3.5, are commonly used in ecosystem research, hence this degradation of the pumps was unexpected. Hypothesized is that by reducing the pumps inflow

(flow rate of pump exceeded required flow rate by factor of 10), an underpressure inside the pump occurs, which easily results in leaks. Therefore, it is advised to use smaller pumps from which the maximum flow rate lays closer to the required sampling flow rate. Also, it is advised to place pumps on the sampling location: a possible leak would then cause a pollution of the sample air by similar air.

The use of PTFE sampling lines can give problems because of internal CO production, which is especially problematic for FG measurements, where small concentration differences can disturb the correct measurement of small atmospheric concentration gradients. By replacing the PTFE sampling lines with stainless steel sampling lines and by continuously flushing the flux gradient lines, also when not sampled, the risk of contamination is reduced. A disadvantage of the stainless steel lines is that the 1/4 inch diameter lines are too unpractical for field experiments, wherefore 1/8 inch diameter lines need to be used, which are not suitable for larger flow rates, such as required for the flux chamber measurements. To reduce the risk of CO production in the PTFE sampling lines of the flux chamber systems, the lines can be covered by plastic tubing or aluminum foil.

Lifting of the sampling lines is advised for multiple reasons. Temperature fluctuations are the strongest at the surface and can cause condensation in the sampling lines. Also, animals such as mice or bugs, can cause leaks or clogging of the sampling lines. Lifting of the FTIR-analyzer is also advised in colder field experiments, when the FTIR-analyzer's internal heat can attract mice and other animals to inhabit the internal compartment.

A final remark concerns the environment and measurement conditions of the FTIR-analyzer. During the field campaigns and the data processing, it has been recognized that variation in the FTIR-analyzer's environmental variables causes the largest uncertainty during data processing. To assure that all variation in the measurement data is caused by natural causes, it is vital to keep the FTIR-analyzer as stable as possible. Small details such as similar final cell pressure and temperature for all measurements is essential, but also similar length and material of sampling lines should be considered. Furthermore, the use of an air conditioning to further stabilize the FTIR-analyzer's environment is recommended.

5 Evaluation of the FTIR-analyzer for ecosystem flux measurements

The evaluation of the use of the FTIR-analyzer for flux measurements is part of the infrastructure project InGOS. InGOS stands for Integrated non-CO_2 Greenhouse gas Observing System and is an EU funded Integrating Activity (IA) project. InGOS supports, integrates and extends the observing capacity of Europe for non-CO_2 greenhouse gases. The project involves 38 partners from different European countries and is coordinated by the Energy Research Center Netherlands (ECN). The focus of InGOS on non-CO_2 greenhouse gases is chosen because of the realization that emissions and behavior of these gases are still very uncertain and it is unknown how future climate change will feedback into the terrestrial coupled emissions. The project works on the following topics: standardizing the measurements, strengthening the existing observation sites, capacity building in new member states, and supporting other networks already in place such as ICOS (Integrated Carbon Observation System). InGOS is divided into different work packages involving different institutes. Within the work packages, specific tasks are described and led by one or more institutes. Work package 13 concerns 'Infrastructure Development' and focuses on the testing and the further development of new techniques to monitor the atmospheric concentration, the fluxes and the behavior of non-CO_2 greenhouse gases. The work package is split into different tasks. Work in this PhD was partly directed to the goals and objectives of task 13.2: combine the FTIR-analyzer with micrometeorological techniques for multi-species biosphere-atmosphere exchange flux measurements.

In this chapter, the use of the FTIR-analyzer for different types of flux measurement techniques is assessed by the use of different case studies, with the aim to explore the possibilities of using an FTIR-analyzer for ecosystem research. Different projects are presented wherein the main part of the research was conducted by me. Other case studies, in which I was involved as a collaborator, are shown in the Appendix (§10.1).

During the field campaign 'RISØ' (field experiment described in §4.2), three case studies have been performed. §5.1 evaluates the use of a new boundary layer technique, wherein the correlation between atmospheric N_2O and CO_2 concentration-changes was used to derive N_2O fluxes from EC CO_2 fluxes. §5.4 shows a case study, in which the FTIR-analyzer was used to study different N_2O production pathways by means of an experiment wherein ^{15}N-spiked fertilizer was used. The third case study is presented in the Appendix (§10.1.1); here the set-up and the preliminary results of a N_2O flux chamber intercomparison campaign are shown and discussed.

During the field campaign 'Rocca4' (field experiment described in §4.3), a case study was performed, wherein flux gradient measurements with an FTIR-analyzer were compared to EC measurements and the parameterization of the flux gradient diffusivity coefficient was assessed. The results of this case study are shown in §5.2.

During the field campaign 'Poplar' (field experiment described in §4.4), a case study was performed, in which the FTIR-analyzer was used to study the storage term of EC measurements inside a poplar plantation. The results of this case study are shown in §5.3.

5.1 Assessment of N_2O flux estimations by the ratio-boundary layer technique

5.1.1 Introduction

Measuring N_2O fluxes at ecosystem scale can be challenging due to the usual low N_2O production rates and background concentrations. Flux chambers can be used to measure N_2O production and can be considered representative if a) multiple flux chambers are available, b) the ecosystem is homogeneous and, c) vegetation is low. However, as shown in §10.1.1, the true determination of absolute N_2O fluxes is difficult, even with multiple flux chambers measuring simultaneously. Therefore micrometeorological methods, such as the eddy covariance method, the flux gradient technique or the relaxed/adjunct eddy correlation/accumulation technique, which all have a large footprint, are desired (§3.4.1).

A disadvantage of the eddy covariance method for flux determination is the required high measurement frequency and precision. N_2O analyzers which fulfill these requirements are commercially available but still under development [83, 151]. Micrometeorological methods perform best under unstable conditions with high turbulence. However, during the night, the surface often becomes cooler than the atmosphere causing a thermal layering of the lower atmosphere. The thermal layering disables air parcels to be displaced, resulting in a so called nocturnal boundary layer (NBL) (Figure 5.1, [170]). During these stable conditions, micrometeorological techniques perform less good and therefore, for measuring ecosystem fluxes with high precision and a large footprint under low wind speed conditions, the use of a different method is suggested.

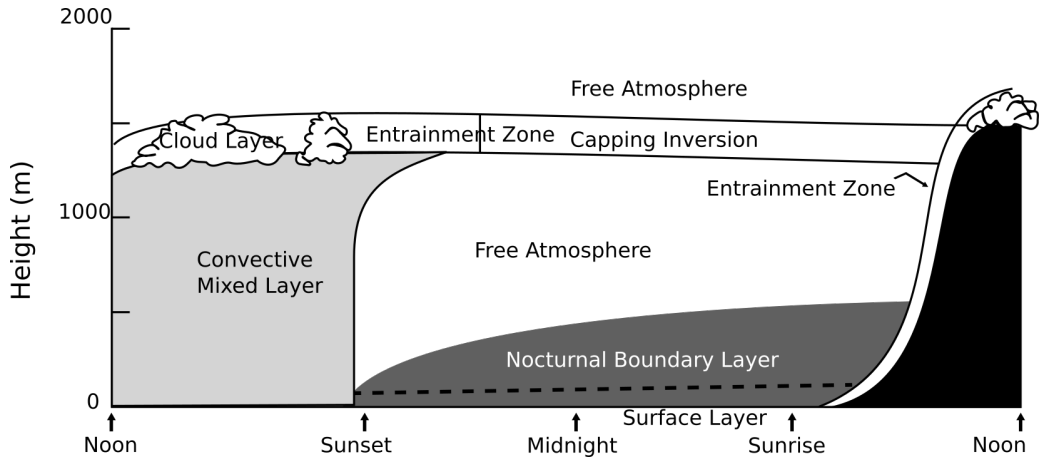

Figure 5.1: Schematic of the daily buildup of the nocturnal boundary layer. During the day, unstable conditions cause the lower atmosphere to be well mixed (convective mixed layer). At sunset, the atmospheric conditions become stable and a nocturnal boundary layer is formed. More information about the stability of the atmosphere can be found in §5.2.2. The figure is modified from Stull (2000).

An approach to estimate the nighttime ecosystem fluxes without a micrometeorological technique is by the nocturnal boundary layer technique (NBL technique). The NBL technique was first described by Denmead (1996), and has been applied in different studies [32, 43, 139]. The NBL

technique assumes that the nocturnal boundary layer is acting as a lid which traps the gases which are respired by the ecosystem (Figure 5.1). By means of the NBL technique, fluxes can be calculated as follows [32]:

$$C_{t_o} + \frac{F\Delta t}{z} = C_{t_1} \tag{5.1}$$

wherein C_{t_o} is the concentration of the trace gas at a specified start time (mol m^{-3}), C_{t_1} the concentration of the trace gas as the measured time (mol m^{-3}), Δt the time interval (s), z the NBL height (m) and F the flux of the trace gas (mol m^{-2} s^{-1}). For use of this method, it is necessary to know the NBL height. The NBL height has to be either measured (by radiosonde) or modeled. The technique cannot account for small spatial variation which often happens close to the surface, but has shown to give valid estimates when compared to other flux methods [43, 53, 139].

The disadvantage of the NBL method is the need to measure or estimate the NBL height. This introduces high uncertainties and most flux ecosystem sites do not have the equipment to determine the NBL height. Here we present a flux measurement technique called the ratio-nocturnal boundary layer (R-NBL) technique, which is based on the concept of the simultaneous measurement of atmospheric concentrations of gas X and gas Y, and of fluxes of gas X by the EC method [68, 107]. The aim of this study is to evaluate the performance of the R-NBL technique during a case study and assess the applicability of the method for ecosystem flux sites.

5.1.2 Ratio-nocturnal boundary layer method

In contrast to the NBL method, the R-NBL technique does not require knowledge of the NBL height. For the determination of the flux of gas Y, the R-NBL method only requires eddy covariance measurements of gas X, concentration measurements of gas X and concentration measurements of gas Y (gas of interest). Furthermore, the ecosystem needs to be homogeneous and gas X and gas Y should originate from sources which are spatially and temporary correlated. If this is the case, a same ratio between the gas concentration X and the gas concentration Y can be assumed as between the flux of gas X and the flux of gas Y. With this ratio, the estimated gas flux for Y can be derived from the EC flux of gas X. For the following case study, we use EC CO_2 measurements (gas X) to study the gas of interest N_2O (gas Y). The ratio between the fluxes of FN_2O/ FCO_2 can then be written as:

$$\frac{F\mathrm{N_2O}}{F\mathrm{CO_2}} = \frac{\frac{\Delta \mathrm{N_2O}}{\Delta t} * V * A^{-1}}{\frac{\Delta \mathrm{CO_2}}{\Delta t} * V * A^{-1}} = \frac{\frac{\Delta \mathrm{N_2O}}{\Delta t}}{\frac{\Delta \mathrm{CO_2}}{\Delta t}} = \frac{\Delta \mathrm{N_2O}}{\Delta \mathrm{CO_2}} \tag{5.2}$$

which can be rewritten to:

$$F_{\mathrm{N_2O}} = \frac{\Delta \mathrm{N_2O}}{\Delta \mathrm{CO_2}} * F_{\mathrm{CO_2}} \tag{5.3}$$

wherein F_{CO_2} is the CO_2 flux (mol m^{-2} s^{-1}), F_{N_2O} is the N_2O flux (mol m^{-2} s^{-1}), $\frac{\Delta CO_2}{\Delta t}$ is the change in CO_2 concentration over time (mol m^{-3} s^{-1}), $\frac{\Delta N_2O}{\Delta t}$ is the change in N_2O concentration over time (mol m^{-3} s^{-1}), V the considered volume (m^3), and A the considered area (m^2). The boundary layer height z (m) can be defined as: z=V/A. As can be seen in equation 5.3, the R-NBL technique can estimate N_2O fluxes without knowledge of the NBL height 'z' or the area 'A'. A schematic figure of the R-NBL technique is shown in Figure 5.2.

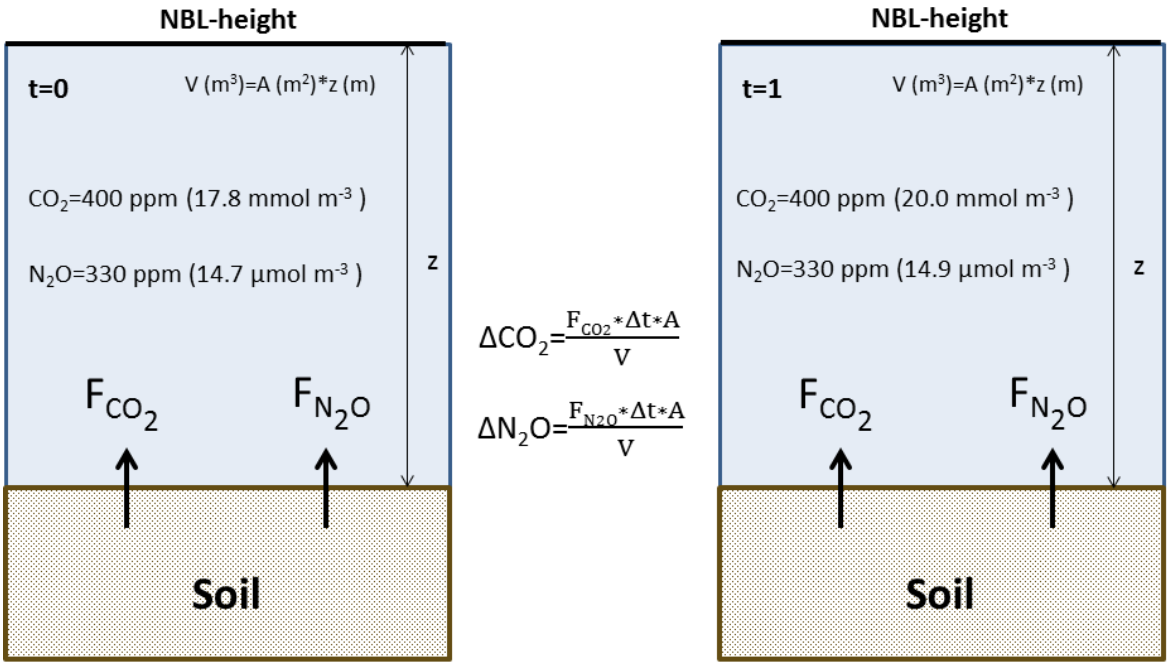

Figure 5.2: Visualization of the functioning of the R-NBL technique. The fluxes of both gases should originate from sources which are temporary and spatially correlated, and therefore the terrain should be homogeneous. For the gas concentrations in this picture, the ratio $\Delta N_2O/\Delta CO_2$ is 0.10. The 'A' stands for the considered area (m^2), the 'z' for the boundary layer height (m), and the 'V' for the considered volume (m^3).

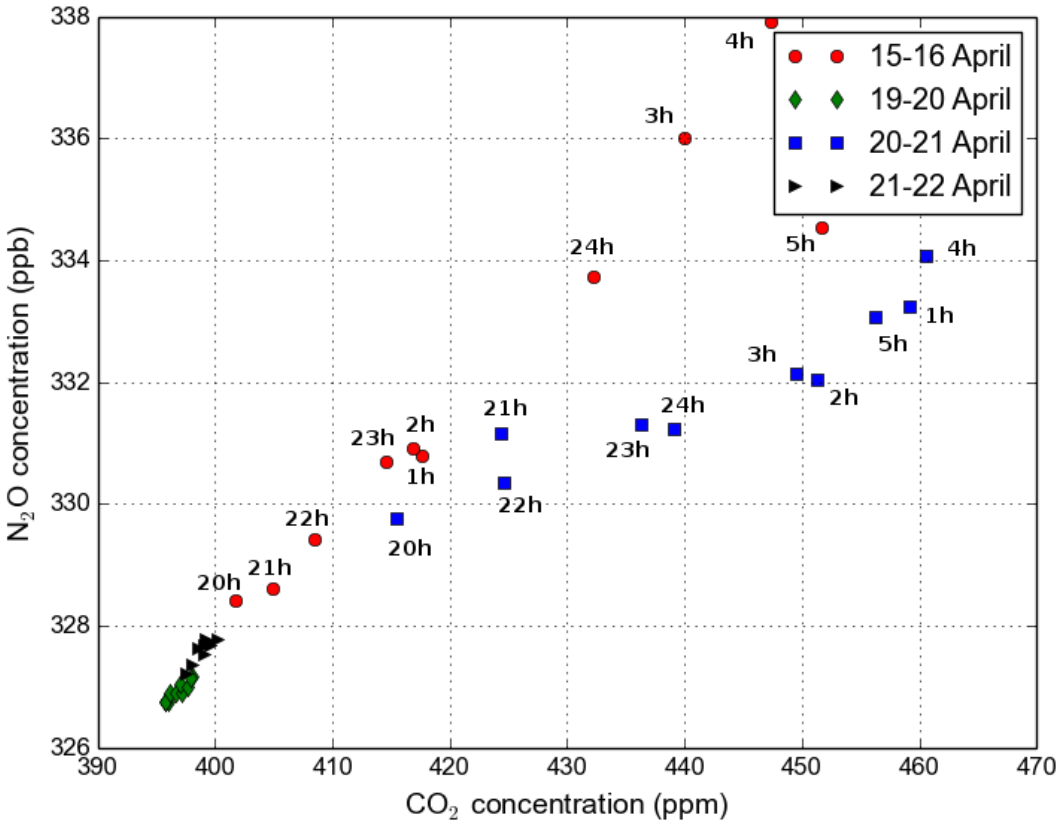

Figure 5.3: Atmospheric CO_2 concentrations versus atmospheric N_2O concentrations for four individual nights measured at 2.42 m, between 20 h and 5 h. The nights of 15-16 April and 20-21 April were nights with low wind speed (approx. 1 m s^{-1}, Figure 5.5), while the nights of 19-20 and 21-22 were nights with higher wind speed (approx. 2-6 m s^{-1}, Figure 5.5). For visualization purposes, the concentrations are given in ppb and ppm.

Case study for R-NBL technique

The case study for the R-NBL technique was performed on the field data obtained during the campaign at the fieldsite RISØ, details about this campaign can be found in §4.2. At this fieldsite, we expect that N_2O and CO_2 concentrations are spatially and temporary correlated; both gases are expected to be only produced by the soil (no trees or vegetation on site), for both gases only production is expected and, in this homogeneous fertilized fieldsite, a similar production ratio between N_2O and CO_2 can be expected. The determination of the concentration change source area will be discussed in §5.1.3.

Atmospheric CO_2 concentrations versus atmospheric N_2O concentrations during four different nights are shown in Figure 5.3. Correlation analyses between ΔCO_2 and ΔN_2O were performed for 3 hour periods at night, measured at 2.42 m height. Table 5.1 shows the individual determined ratios and their correlation coefficients for the 2.42 m height. If a good correlations was found ($R^2 > 0.8$), the ratio $\Delta N_2O/\Delta CO_2$ was used to derive F_{N_2O} from measured EC CO_2 fluxes. Estimated fluxes are shown in Figure 5.4.

Table 5.1: ΔN_2O (ppb)/ΔCO_2 (ppm) for 3 hour-periods for concentrations measured at 2.42 m, 21 h stands for 20-22 h period.

	21 h		**22 h**		**23 h**		**0 h**		**1 h**		**2 h**		**3 h**		**4 h**	
Date	ratio	R^2	ratio	R^2	ratio	R^2	ratio	R^2	ratio	R^2	ratio	R^2	ratio	R^2	ratio	R^2
15-16	0.15	0.90	0.21	0.98	0.18	0.98	0.18	0.98	0.19	0.98	0.23	0.98	0.22	0.98	−0.08	0.08
16-17	0.92	0.81	0.56	0.83	0.23	0.98	0.22	0.85	0.22	0.81	0.12	0.98	0.1	0.71	0.15	0.30
17-18	0.32	0.18	0.43	0.96	0.29	0.96	0.28	0.98	0.22	0.96	−0.02	0.03	0.1	0.71	0.09	0.50
18-19	0.02	0.01	0	0.06	−0.18	0.44	0.25	0.79	0.1	0.48	−1.69	0.98	0.22	0.62	0.31	0.98
19-20	0.05	0.61	0.46	0.98	0.14	0.59	-0.01	0.96	0.02	0.01	−0.05	0.04	0.10	0.30	0.45	0.98
20-21	0.11	0.66	0.45	0.35	0.06	0.94	0.09	0.98	0.09	0.98	0.12	0.94	0.15	0.88	0.17	0.98
21-22	0.31	0.98	0.23	0.72	0.15	0.19	0.45	0.85	−0.27	0.94	0.13	0.79	0.22	0.92	0.07	0.52
22-23	0.09	0.67	0.08	0.44	0.1	0.92	−0.07	0.88	−0.03	0.76	0.026	0.36	0.11	0.81	0.12	0.90
23-24	0.11	0.96	0.19	0.94	0.14	0.98	0.04	0.17	−0.17	0.36	0.11	0.49	−0.02	0.12	0.21	0.26
24-25	0.15	0.98	0.14	0.77	−0.03	0.05	0.61	0.92	0.51	0.98	−0.21	0.12	−0.12	0.71	−0.03	0.33
25-26	-	-	-	-	-	-	0.19	0.98	−0.02	0.00	−0.14	0.92	0.96	0.87	1.06	0.90
26-27	−0.01	0.98	0.12	0.71	0.22	0.85	−0.07	0.07	0.01	0.02	0.13	0.98	0.12	0.76	0.14	0.98

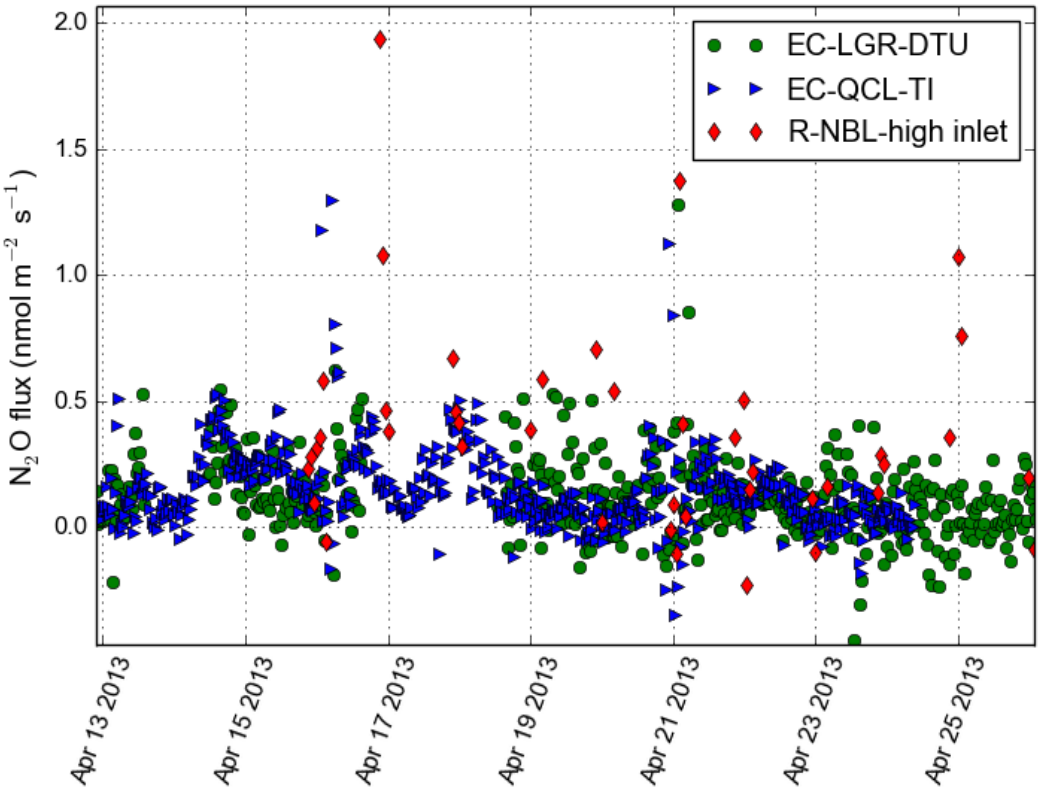

Figure 5.4: Measured eddy covariance fluxes and estimated R-NBL N_2O fluxes. The green circles indicate eddy covariance N_2O fluxes, as measured by DTU-RISØ (instrument: Los Gatos CO_2 analyzer) and the blue triangles indicate eddy covariance N_2O fluxes, as measured by the Thünen Institute (instrument: QCL Aerodyne). Red diamonds show the N_2O fluxes as estimated by the R-NBL technique based on concentration changes at the 2.42 m inlet. More information about the used eddy covariance systems of the different institutes can be found in §4.2 and §10.1.1.

5.1.3 Source area determination

Homogeneity in the source area of the concentration and the eddy covariance measurements is important for the R-NBL method. For EC flux measurements, the source area is called a footprint and it represents the area where x% of the measured fluxes originate from. For R-NBL concentration measurements, we will keep calling it the source area, to avoid confusion with the EC footprint. The source area of the R-NBL method represents the area where the measured concentration changes are originating from. The size of a footprint or source area is dependent on different factors such as measurement height, wind speed and atmospheric stability, and many different concentration and flux footprint models exist [24, 82, 97, 99, 163, 184]. In general, concentration source areas tend to be larger than EC flux footprints [184]. For this experiment, no concentration source area model was available. By means of the wind speed, the wind direction and a map of the fieldsite (Figure 5.7), the source area was roughly estimated, and the assumption that the area is homogeneous (with respect to the N_2O-CO_2 flux ratio) was assessed.

Figure 5.5 shows the wind speed and wind direction during the experiment. As can be seen, the wind direction and wind speed vary largely between the different nights. Figure 5.6 shows a wind rose of the nighttime wind speeds (20 h - 5 h, wind speed indicated by different colors) and wind direction. The length of the bars indicate the frequency of occurrence during the field campaign. The figure shows that nighttime winds mostly originate from the NW or the SW direction, and that the wind speed is not directly related to the wind direction. An exception is the wind direction originating from E to SE, which showed very low wind speeds during the field campaign.

The maximum extent of the source area was calculated by multiplying the considered concentration correlation time span with the average wind speed (m s^{-1}). In general, nighttime wind speed ranged between 1 and 6 m s^{-1}. A concentration change measurement over a 3 hour-interval will result in a 'maximum extent of the source area'-estimate of approximately 10 kilometers during low wind speed-nights (1 m s^{-1}), and up to 65 kilometers during nights with high wind speed (6 m s^{-1}). Unfortunately, since too few data points are available to correlate wind speed, wind direction and quality of N_2O-CO_2 correlation, it is not possible to assess the suitability of the R-NBL's source area per wind direction in detail.

The R-NBL method was expected to perform better during nights with low wind speeds when the boundary layer is stronger and shallower, and when a smaller source area was foreseen: a smaller source area would mean a relative larger contribution of the fertilized fieldsite. Also, a smaller source area is easier to check for possible disturbing features. Low nighttime wind speed was observed during the night of 15-16 April, originating from SW-NW (210-340°) and showed strong N_2O-CO_2 concentration correlations. Low nighttime wind speed was also observed during the night of 20-21 April and also resulted in strong N_2O-CO_2 concentration correlations, but only after wind direction turned from 160° (SSE) to 80-130° (SE to E) (Table 5.1, Figure 5.5). Possibly, wind originating from 160° (SSE) brought air from the city of Roskilde (Figures 5.6 and 5.7). A similar weak relationship was found during a night with higher wind speed (approx. 5 m s^{-1}) when air originated from the village of Vedelev (SW). In general, during nights with low and high wind speed, stronger correlations were found when wind originated from the direction 250-300° (W-NW) (nights of 15-16, 19-20, 23-24, 24-25 April). This wind direction mainly brings air from agricultural regions and the fjord.

It should be considered that for most nights a source area of more than 10 kilometers was expected which means that very different land use types were inside the R-NBL's source area,

and that even during low wind speed conditions the fertilized fieldsite is only a very small part of the source area. Therefore, the presented R-NBL N_2O flux data does not solely represent the fertilized fieldsite. The EC footprint is expected to be much smaller than the R-NBL source area, wherefore similarity in the flux method's source areas can not easily be assumed. However, still quite some nights occurred wherein the CO_2 concentration change could be correlated to the N_2O concentration change, and where the estimated R-NBL N_2O flux agreed well with the EC N_2O measurements. Expected is that, in absence of strong source area/footprint disturbances (cities, villages), the N_2O and CO_2 emissions mostly originate from the surrounding agricultural lands. As it has been observed that N_2O fluxes (denitrification) usually follow CO_2 fluxes (soil respiration), a similar N_2O-CO_2 production can therefore be expected [116, 164]. The influence of the fertilized fieldsite, from where a different N_2O-CO_2 emission ratio can be expected in comparison to its surroundings, is expected to be larger for the EC fluxes than for the R-NBL fluxes. Since it is expected that the fertilized fieldsite has very irregular N_2O fluxes (see §10.1.1), the difference in fieldsite's influence could explain the discrepancy between the method's fluxes, which was seen for some nights during the field campaign (Figure 5.4).

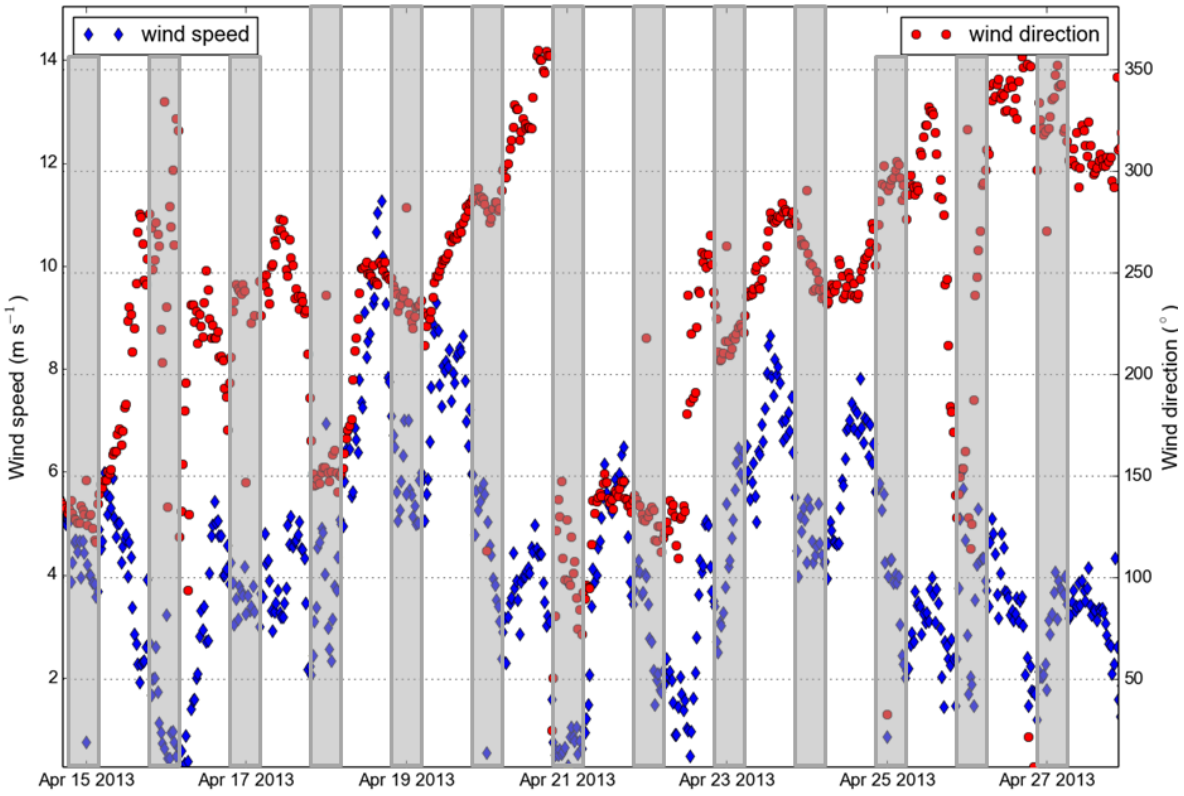

Figure 5.5: Nighttime (20-5 h) wind speed (blue circles in m s^{-1}) and wind direction (red diamonds) during the field campaign at the fieldsite RISØ. The vertical gray blocks indicate the nighttime.

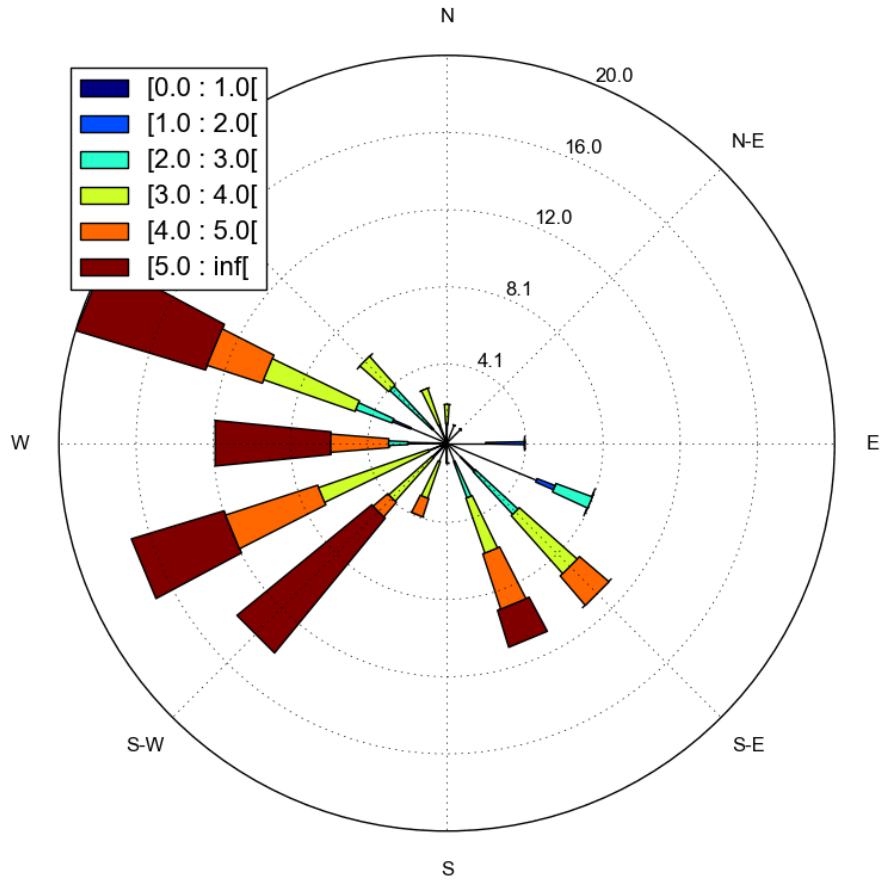

Figure 5.6: Nighttime wind speed (20-5 h, wind speed indicated with color) and wind direction during the field campaign at the fieldsite RISØ. The length of the bars indicate the frequency of occurrence of the wind direction: N = 0°, NE = 45°, E = 90°, SE = 135°, S = 180°, SW = 225°, W = 270° and NW = 315°.

5.1.4 Discussion

Performance of ratio-NBL methodology

Figure 5.4 shows the determined N_2O fluxes, derived using the R-NBL technique. Estimated fluxes have a magnitude of approximately of 0.2 nmol m^{-2} s^{-1}. As part of the N_2O intercomparison campaign (§4.2), micrometeorological (EC) N_2O fluxes were measured by different institutes; their measured fluxes are shown in Figure 5.4. The comparison with these measurements shows that most N_2O flux peaks, which were seen by the micrometeorological methods, were also observed by the ratio-NBL technique. The temporary higher fluxes in the nights of 16-17 and 20-21 April, measured by the EC systems, were also observed by the ratio-NBL technique, although were less consistent (Figure 5.4). However, the clear N_2O flux peaks observed by the R-NBL method (in the nights of 16-17 April and 24-25 April), were not seen by any of the EC methods and could not be related to a specific wind direction (Figure 5.4).

Figure 5.7: Aerial photograph of the fieldsite RISØ and its environment. The aerial photograph is from Google (2015). The R-NBL measurement location is indicated with a red dot. The wind directions are indicated by the red lines which represent a 2 km radius. The city of Roskilde is 2 km south of the measurement site.

Detection limit
The detection limit of the ratio-NBL method is mostly determined by the height and stability of the NBL layer: the shallower the NBL layer, the clearer the increase in gas concentrations, and the lower the detection limit. The detection limit for the EC measurement method, which is around 0.5 μmol m^{-2} s^{-1} for CO_2, might play a role when CO_2 fluxes become very small. To estimate a detection limit for a typical night during our case study, the following is assumed.

Some nights with a weak boundary layer showed an atmospheric CO_2 concentration increase of 10 ppm over the whole night, originating from a 1 μmol m^{-2} s^{-1} CO_2 flux (EC flux at night, not shown). This 10 ppm increase was accompanied by a 2 ppb increase in atmospheric N_2O concentrations, which gives a flux estimate of 0.2 nmol N_2O m^{-2} s^{-1}. Some nights with a stronger stable boundary layer showed an atmospheric CO_2 concentration increase of 50 ppm, originating from a 1 μmol m^{-2} s^{-1} CO_2 flux (EC flux at night). This 50 ppm increase is accompanied by a 10 ppb increase in atmospheric N_2O concentrations, which also results in a flux estimate of 0.2 nmol N_2O m^{-2} s^{-1}.

As described in §3.5.4, the minimum N_2O concentration difference (between the two inlets) which can be measured significantly is equal to two times the FTIR-analyzers precision (2σ), which is 0.22 ppb (Table 3.4). If, under a weak stable boundary layer, 0.22 ppb is the minimal atmospheric concentration increase over night, the detection limit of this method would be 0.02 nmol N_2O m^{-2} s^{-1}. If, under a strong stable boundary layer, 0.22 ppb is the minimal atmospheric concentration increase over night, the detection limit of this method would be 0.004 nmol N_2O m^{-2} s^{-1}. It should be considered that in this example the increase over the whole night is taken. When increasing temporal resolution, the detection limit will go up.

5.1.5 Conclusion

In this paragraph we showed that, by use of the R-NBL method, only EC CO_2 measurements and atmospheric concentration measurements of CO_2 and N_2O were needed to be able to estimate ecosystem N_2O fluxes. The case study showed that the estimates agreed well with the N_2O fluxes measured by the different EC systems. It is expected that the R-NBL source area can be very large, especially in windy conditions, wherefore the source area is almost never fully homogeneous. Future studies might consider filtering for high wind speed [107]. For the R-NBL method, the smaller EC footprint should be similar to the larger the R-NBL source area. Analysis of the source area showed that the method is sensitive to the presence of anthropogenic features in its footprint. Assessment of the detection limit showed that the method is capable of measuring very small fluxes of down to 0.004 nmol N_2O m^{-2} s^{-1} if the conditions are suitable, which is lower than reached by other flux measurement methods, besides the flux chamber technique [146].

Ecosystem flux sites usually already perform EC CO_2 flux and atmospheric CO_2 concentration measurements. The R-NBL method is therefore easily added to a flux measurement site and especially very well suited for flat homogeneous terrains. Suitable landscapes could be a large flat agricultural fields, wetlands or tundra steppe, where simultaneous and homogeneous emission of N_2O, CH_4 and CO_2 can be expected and no vertical variation in form of trees or hills are usually present.

5.2 Evaluation of the flux gradient technique

5.2.1 Introduction

The flux gradient (FG) technique is one of the micrometeorological methods which does not require fast concentration measurements (> 10 Hz) and can therefore be used for many different gases for which no fast analyzers are available. As described in §3.4.1, the flux gradient technique uses the relationship between the gas flux and the atmospheric concentration gradient: by use of a diffusion coefficient, a relationship between the concentration gradient and the actual flux is established:

$$F = D\frac{\Delta C}{\Delta z} \tag{5.4}$$

wherein ΔC is the difference in concentration of gas x at the z-heights (mol m^{-3}), Δz the height difference between the two different inlets (m), D is the diffusion coefficient (m^2 s^{-1}), and F the flux (mol m^{-2} s^{-1}).

The determination of the diffusion coefficient, also called the eddy diffusivity, can be done by different methods. One method is to measure the flux of an entity by the EC technique and, at the same time, monitor the concentration gradient ($\frac{\Delta C}{\Delta z}$) of the same entity. The diffusion coefficient can then directly be calculated by dividing the gas flux by the gas concentration gradient, resulting in the diffusion coefficient D (Eq. 5.4). Another method is an empirical parameterization of the diffusion coefficient. For a correct parameterization, knowledge of the state of the atmosphere and details of the measurement set-up and fieldsite are needed.

In this paragraph flux gradient CO_2 fluxes from the fieldsite Rocca4, calculated with the different diffusion coefficients determination methods, are shown and compared to EC CO_2 fluxes. The aim of this study is to assess the performance of the both 'diffusion coefficient'-obtaining methods and to improve the parameterization of the diffusion coefficient for our specific fieldsite. Furthermore, a new approach which combines the strong points of both 'diffusion coefficient'-obtaining methods, is described.

5.2.2 Parameterization of the diffusion coefficient

In literature, the common parameterization of the diffusion coefficient is:

$$D = \frac{k * zmean * u^*}{\Phi} \tag{5.5}$$

wherein D is the diffusion coefficient (m^2 s^{-1}), k the vonKarman constant (-), zmean the effective height ($\sqrt{z1 * z2}$, wherein z1 and z2 are the individual inlet heights (m)), u^* the friction velocity (m s^{-1}) and Φ a dimensionless constant (-). The vonKarman constant is a dimensionless constant and has a value of 0.35 or 0.4 [57, 157]. The friction velocity u^* (also known as shear velocity), characterizes the shear at the boundary, to quantify the true velocity in comparison to the shear between layers of the horizontal flow. The friction velocity can be calculated from the wind components measured by a sonic anemometer.

$$u^* = (|\frac{\tau}{\varrho}|)^{1/2} \tag{5.6}$$

in where ϱ is the air density and τ is the Reynolds stress, which can be defined:

$$\tau = \varrho * \overline{u_i' * u_j'} \tag{5.7}$$

The diffusion coefficient is parameterized according to the stability of the atmosphere. At ecosystem level, daytime conditions are usually unstable with no vertical thermal layering: warm air particles at the surface will rise and will be pushed forward because they remain warmer than its surrounding. Nighttime conditions are usually stable: due to thermal layering, an air parcel being displaced will move back to its original position, wherefore the mixing between different atmospheric layers is low. Sometimes also neutral conditions occur, which means that a displaced air parcel has the same temperature as its surrounding wherefore it is neither pulled back or pushed forward.

The degree of stability can be quantified by use of the Obukhov-length, which relates dynamics, thermal processes and buoyancy processes. The Obukhov-length represents the heights of an air column wherein the production or loss of turbulent kinetic energy is equal to the dynamic production of turbulent kinetic energy [57]. The Obukhov-length can be calculated by [57]:

$$L = -\frac{u*^3}{k * \frac{g}{\theta} \frac{Q_H}{c_p * \varrho}} \tag{5.8}$$

wherein c_p is the specific heat capacity (for dry air=1004 J kg^{-1} K^{-1}), ϱ is the moist air density (kg m^{-3}), θ the virtual temperature (K), u* is the friction velocity (m s^{-1}), k the vonKarman-constant (-), g gravitational acceleration constant (9.8 m s^{-2}), and Q_H the virtual sensible heat flux (J m^{-2} s^{-1}). Whether L is negative or positive is defined by the heat flux. If the heat flux is positive (surface warmer than air), the vertical turbulent energy increases, associated with a positive buoyancy (unstable conditions). If the heat flux is negative (surface colder than air), the vertical turbulent energy decreases, associated with a negative buoyancy (stable conditions).

The degree of stability is estimated by the parameter 'zeta':

$$zeta = \frac{(z - z_0)}{L} \tag{5.9}$$

wherein z is the measurement height (z_{sonic} for EC measurements or zmean (effective height) for flux gradient measurements) and z_0 the displacement height, which is the distance above the ground at which the wind speed profile is zero. The displacement height is usually 2/3 of the canopy height.

Stable conditions
If zeta is positive, the atmosphere is stable and vertical transport is limited because of thermal layering. The Φ in Equation 5.5 has been parameterized by:

$$\Phi = 1 + 4.7 * zeta \tag{5.10}$$

or by:

$$\Phi = 1 + 6 * zeta \tag{5.11}$$

or by:

$$\Phi = 1 + 7.8 * zeta \tag{5.12}$$

The above mentioned parameterizations are from Roedel (1992), Businger (1971), and Hogstrom (1989), but many similar parameterizations exist.

Unstable conditions
If zeta is negative, the atmosphere is unstable and vertical transport is not limited because of thermal layering. The Φ in Equation 5.5 has been parameterized by:

$$\Phi = (1 - 15 * zeta)^{-0.25} \tag{5.13}$$

or by:

$$\Phi = (1 - 19.3 * zeta)^{-0.25} \tag{5.14}$$

or by:

$$\Phi = (1 - 12 * zeta)^{-0.25} \tag{5.15}$$

The above mentioned parameterizations are from Roedel (1992), Foken (2008), and Hogstrom (1989), but many similar parameterizations exist.

Neutral conditions
Neutral conditions are defined when the Obukhov-length is very large and zeta approaches zero (zeta between -0.05 and 0.05). For neutral conditions, only one parameterization has been found in literature [157].

$$\Phi = 1 \tag{5.16}$$

Different criteria exist for stable, neutral and unstable conditions [57]. During this case study, several combinations were tried and different classifications for stable, unstable and neutral conditions were used. For simplification, this paragraph will just show the results of the 7 different parameterizations which were described before (Eq. 5.10-5.16).

5.2.3 Parameterization of the diffusion coefficient for the fieldsite Rocca4

During the field campaign in Rocca4, flux gradient inlets were at 1.30 and 4.10 m height and installed at the same tower as the sonic anemometer (3.5 m height). Displacement height was set to 0.1 m, zmean was 2.19 m and Δz was 2.8 m. L and $u*$ were taken as processed by the LI-COR processing software EddyPro ® (LI-COR, Lincoln, NE, USA). For the VonKarman-constant, 0.4 was chosen [25]. FG fluxes were calculated using the different diffusivity coefficient-parameterizations (Eq. 5.10-5.16), and the performance of the different parameterizations for our field measurements was investigated.

Figure 5.8 shows typical Obukhov-length values during the day. Neutral conditions (-70 > L or L > 70) occurred sometimes in the early morning and the late afternoon. Stable conditions (L > 0) usually occurred between 19 h and 6 h. Unstable conditions (L < 0) usually occurred between 7 h and 18 h. As can be seen in Figure 5.8, all used diffusion coefficient parameterizations from literature for stable conditions (nighttime) underestimated the flux; the EC method observed higher respiration fluxes than the FG method. During unstable conditions (daytime), the difference was even larger: the EC method observed higher photosynthesis fluxes than the flux gradient system. Changing the VonKarman constant to 0.35 did not change this outcome.

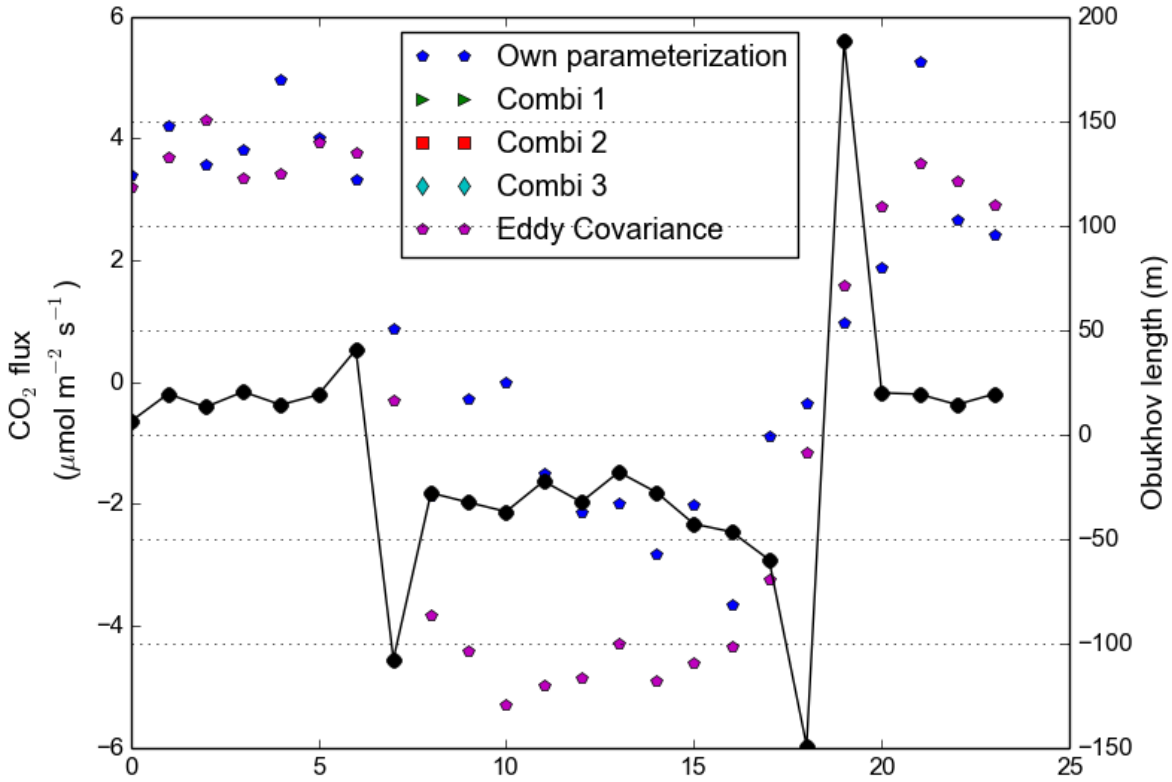

Figure 5.8: Averaged eddy covariance and flux gradient measurements during the field campaign at the fieldsite Rocca4. The values on the left axis show the CO_2 fluxes as calculated by use of the different parameterizations; Combi 1 stands for Eq. 5.10 and Eq. 5.13 for stable and unstable conditions respectively; Combi 2 stands for Eq. 5.11 and Eq. 5.14 for stable and unstable conditions respectively; and Combi 3 stands for Eq. 5.12 and Eq. 5.15 for stable and unstable conditions respectively. The fluxes calculated with the own parameterization are shown as blue pentagons. The values on the right axis show typical Obukhov-length values (black circles and line) with positive stable conditions during the night, and negative unstable conditions during the day.

Own parameterization

To fit the FG CO_2 measurements to the measured EC CO_2 fluxes, different own parameterizations were tried. The following parameterizations fitted best to the measured EC CO_2 fluxes:

For neutral conditions: Equation 5.5 with Φ=1

For stable conditions: Equation 5.5 with Φ=1

For unstable conditions: Equation 5.5 with

$$\Phi = (1 - 15 * zeta)^{-1.1} \tag{5.17}$$

Results from the old and the new parameterization of FG diffusion coefficient in comparison to EC fluxes are shown in Figure 5.8 and Figure 5.9. While still the parameterization does not cover all variation which is observed by the EC method, it manages to capture the general flux magnitudes, and is improved in comparison to the parameterizations from literature.

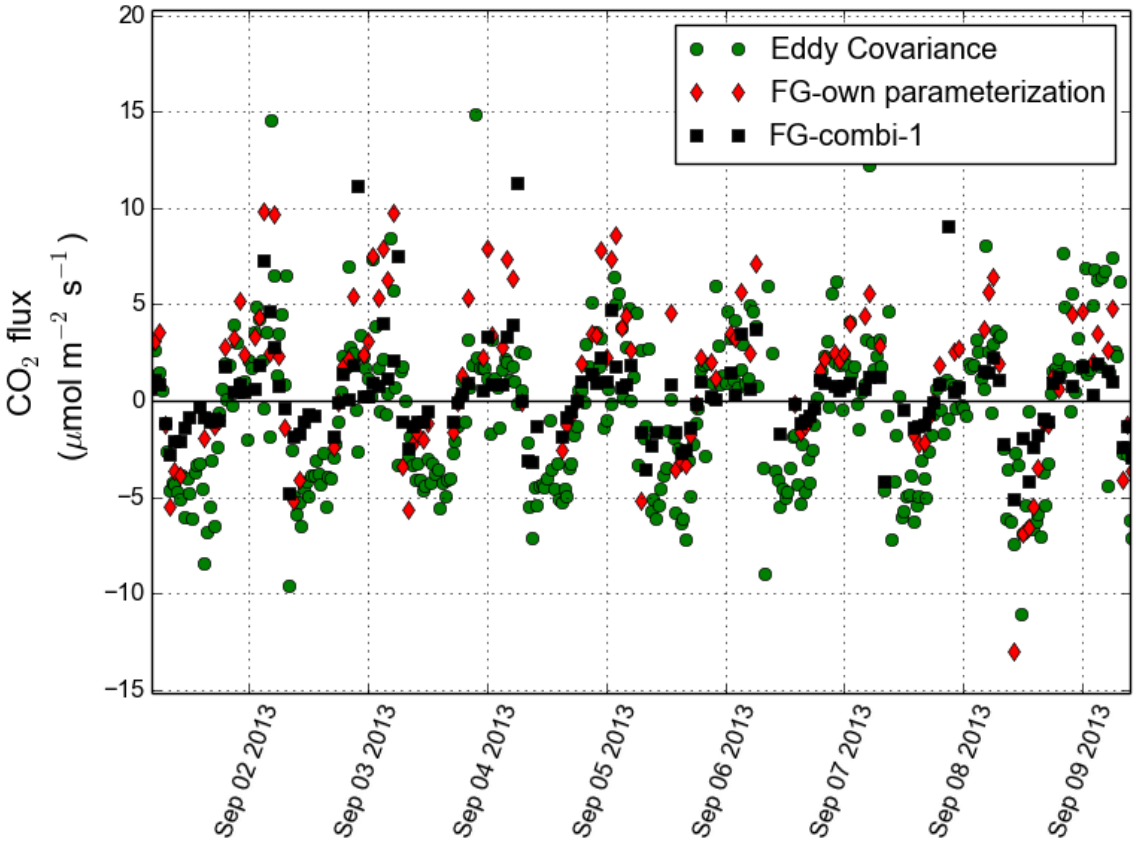

Figure 5.9: Eddy covariance and flux gradient measurements for one week during the field campaign at the fieldsite Rocca4. The eddy covariance measurements are shown as green circles, the FG fluxes calculated with the parameterization from Combi 1 (Eq 5.10 and 5.13) are shown as black squares, and the fluxes calculated with the own parameterization are shown as red diamonds.

Flux gradient technique applied to other gases

With the own parameterization, with Φ=1 for neutral and stable conditions, and equation 5.17 for unstable conditions, fluxes for other trace gases which were measured by the FTIR-analyzer could be calculated. As described in §3.5.4, a minimum concentration difference between the inlets of 2σ is needed. This means that a minimum difference of 0.08 ppm for CO_2, 0.72 ppb for CO, 0.72 ppb for CH_4, and 0.22 ppb for N_2O is required (Table 3.4). Figure 5.10 shows the average concentration difference per hour for CH_4 and N_2O, a positive number means an upward flux. As can be seen in Figure 5.10, daytime FG concentration differences for N_2O are too small to be considered significant and no clear pattern could be observed. Expected is that fluxes are too small to be detected by the flux gradient method. This hypothesis is confirmed by flux chamber measurements, which are shown in the Appendix (§10.3.3). For CH_4, FG differences were often larger than the minimum required difference, but no clear daily pattern was observed and we expect that natural atmospheric concentration variation causes the observed pattern. The CO concentration differences between the FG inlets were most of the time higher than the required minimum difference, and the flux gradient technique could be used. Results from FG CO measurements are shown in Figure 5.10 (lower figure) and in Chapter 6.

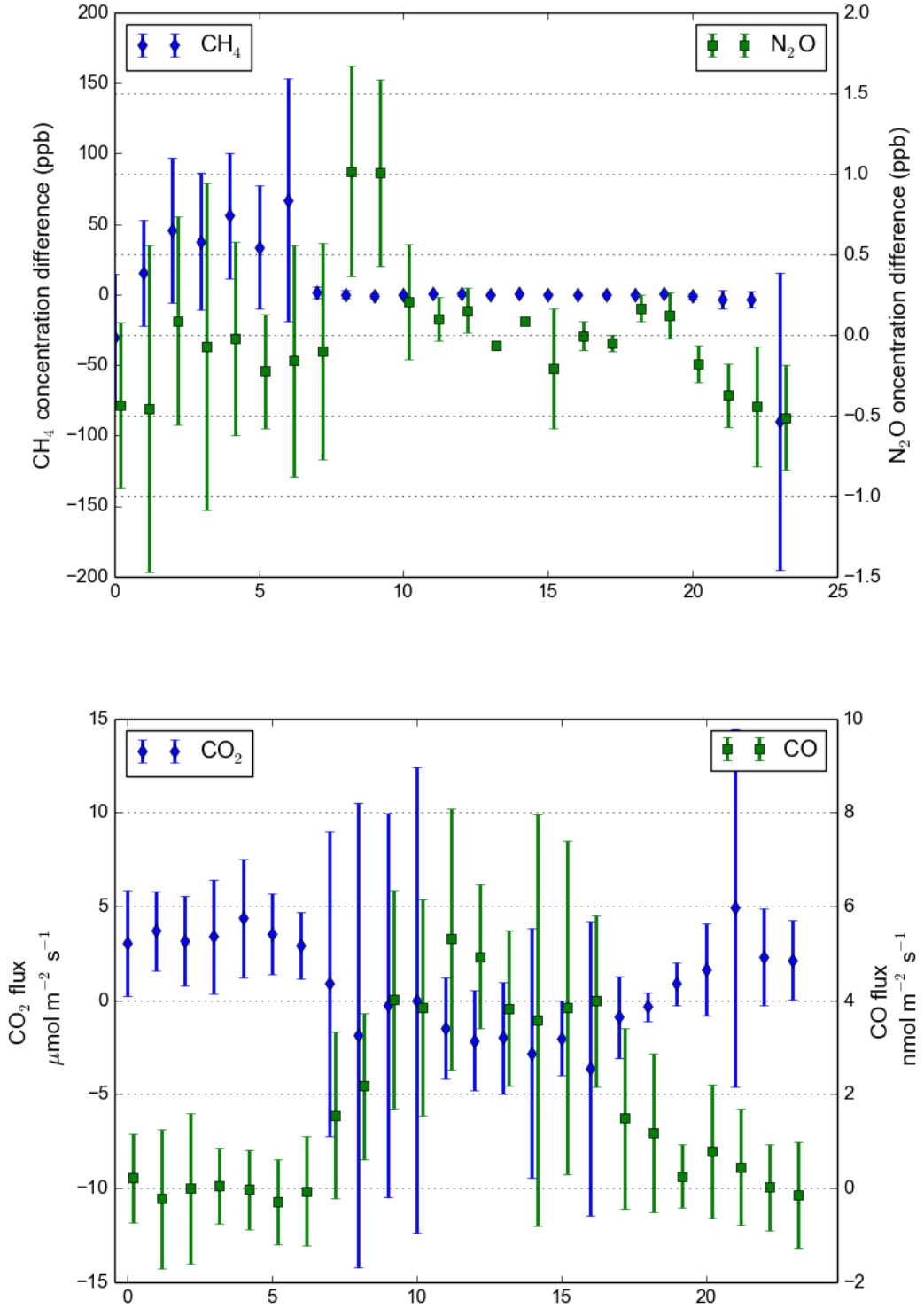

Figure 5.10: Flux gradient concentration differences for CH_4 and N_2O at the fieldsite Rocca4. Upper figure: the 10-day average concentration FG inlet difference per hour for CH_4 and N_2O concentrations, a positive difference indicates an upward flux. For the FG CH_4 and N_2O measurements, the FG inlet differences were mostly lower than the minimum required FG inlet concentration difference (see text). Lower figure: the FG CO and CO_2 fluxes calculated with the own diffusion coefficient parameterization.

5.2.4 Conclusion

Different studies have used the flux gradient method to measure ecosystem fluxes [71, 143]. Some studies used the direct parameterizations from literature to determine the FG fluxes. The assessment shown in this paragraph indicates that parameterizations from literature can consistently under or overestimate fluxes, in comparison to EC fluxes (Figure 5.8 and 5.9).

Another method to determine the diffusion coefficient value, is to directly divide EC CO_2 fluxes by the CO_2 concentration gradient. This value can then be applied to other gas concentration gradients. However, as can be seen in Figure 5.9, EC CO_2 fluxes can contain unexpected, noise-related peaks. Directly deriving the diffusion coefficients from the EC measurements can introduce noise into the FG measurements of the other gases.

In this assessment, we used a combination of the both methods. The diffusion coefficient was parameterized by empirical relationships as can be found in literature and checked with the on site EC CO_2 measurements. If a discrepancy was found, the empirical literature relationship was adapted, resulting in a fieldsite-specific parameterization. With this approach, it can be checked if the diffusion coefficient value is close to the real diffusion coefficient value, without introducing noise from the high frequency EC measurements.

Based on this study, it is advised to have EC measurements alongside FG measurements so that the parameterization of the diffusion coefficient can be checked. With the combination of the flux gradient and the eddy covariance method, many different gases can be measured reliably with the relative simple FG method.

5.3 The use of the FTIR-analyzer to quantify the storage component in forest ecosystems

5.3.1 Introduction

The eddy covariance method is commonly used to quantify the gas exchange between the biosphere and the atmosphere and also often used in forest ecosystems. In forest ecosystems, the EC measurements are performed above the canopy. In steady-state conditions (daytime), mixing is strong and fluxes originating from the surface will reach the EC measurement height. Flux measurements performed at EC height are therefore considered to be representative for forest fluxes [23]. However, when turbulent mixing is low and thermal stratification occurs (nighttime: low wind, high canopy, nocturnal boundary layer), not all surface fluxes will (directly) reach the EC measurement height and steady-state conditions can not be assumed. During these conditions, gases are accumulating in the boundary layer and a strong concentration gradient can be observed, especially close to the surface [197]. When turbulent conditions return, these gases are 'flushed out' in a relative short timespan. It is difficult to quantify the 'flushing' of the canopy storage layer by the EC method. For accurate estimates of the net carbon exchange, a correction term to EC measurements needs to be applied: the storage term. The storage term represents the buildup of the gas of interest between the ground and the point of measurement that is unaccounted for by EC measurements [8, 40].

The storage term can be modeled and depends on atmospheric pressure, temperature, canopy structure and, most importantly, concentration measurements of the gas of interest along one or more vertical profiles including at least one point above the canopy and two points within the canopy [135, 197]. Sometimes, flux sites do not have additional concentration measurements within the canopy and therefore, for storage term estimation, only use concentration measurements at EC measurement height [135]. Other flux sites measure the concentration gradient but remain unaware of spatial (horizontal and vertical) variation due to a limited amount of measurement points.

A field experiment was set up in a poplar plantation, where continuous EC measurements (in a neighboring field) are ongoing since July 2011. In this experiment, concentrations inside the canopy were continuously measured and sample inlets were distributed in a horizontal and vertical plane (12 inlets in total, Figure 4.6 and 4.7). In the horizontal plane, inlets were positioned at 90 cm height and some inlets were placed in line with the poplar trees, while others were placed in the middle of the poplar tree lines. For more details on the field experiment and the fieldsite, see §4.4.

The goal of this field experiment was to study the distribution and behavior of the different gases (CO_2, CO, N_2O, CH_4, and $\delta^{13}CO_2$) within the canopy, especially during nighttime. The aim was to assess the spatial and temporal concentration variability within the canopy, to discuss the consequences of this variability for the estimation of the storage term, and to evaluate the advantages of adding different types of concentration measurements (by the FTIR-analyzer) to a forest ecosystem flux site.

5.3.2 Results

An overview of the concentration data of the campaign at the fieldsite Poplar plantation can be found in Appendix (§10.3.4). In this paragraph, general patterns will be shown and preliminary results are discussed.

Vertical profile

The concentration profiles for the different gases for a typical day and night are shown in Figure 5.11. Turbulent conditions during the day cause concentrations of all gases to be homogeneous throughout the canopy (solid lines in Figure 5.11). During the night, the concentration patterns are very different (dashed lines in Figure 5.11). For CO_2, a clear concentration buildup close to the soil surface can be observed, and CO_2 concentrations follow a logarithmic profile. Nighttime CH_4 concentrations are much higher than daytime concentrations with daily differences of approximately 1000 ppb in all layers of the canopy. Nighttime CH_4 concentrations do not show a distinct vertical pattern, indicating the absence of a strong uptake or emission point source in the canopy. CH_4 is either equally produced throughout the canopy, or transported by advection from elsewhere in the nocturnal boundary layer. CO concentrations at night show a strong decrease close to the soil surface, possibly indicating the uptake of CO by the soil. Soil CO uptake is common, especially at night when the process is less buffered by possible thermal degradation CO fluxes [36, 183]. The nighttime vertical N_2O profile shows higher concentrations close to the soil surface, which could point at production at the surface. However, not every night showed this logarithmic shape and some nights even showed lower N_2O concentrations in comparison to daytime concentrations, indicating that, most likely, changes in N_2O concentrations are caused by sources from outside the canopy. Therefore, analysis of wind direction in relation to N_2O and other gas concentrations could be useful. Figure 5.12 shows the concentrations of three different heights during a part of the experiment.

Horizontal variation

Figure 5.13 shows the gas concentrations measured at the horizontal inlets (for an overview of the position of the inlets, see Figure 4.7). During the day, CO_2 concentrations varied less than 4 ppm, but during the night, differences up to 70 ppm were observed. Inlets showing higher CO_2 concentrations often showed deviating CO_2 concentrations for longer times (inlet E during 13-16 October (not shown) or inlet A and B during 19-22 October), possibly indicating a temporary more suitable soil respiration environment, which can be caused by changes in soil fauna, moisture content or organic matter availability. For N_2O, concentration differences between the horizontal inlets were usually around 0.5 ppb, and went up to maximum 4 ppb during some nights, which is similar to differences observed in the vertical plane. CO concentrations were well mixed during daytime (less than 2 ppb differences between inlets), but showed up to 40 ppb differences during nighttime. Daytime CH_4 concentrations were also well mixed (less than 20 ppb differences between inlets), but differences of up to 700 ppb have been observed during nighttime. The inlets placed in line with the poplar trees (inlet A, C and E) showed no consistent higher or lower concentrations in comparison to the inlets in the middle of the poplar tree lanes.

Figure 5.14 shows the average concentrations (over all horizontal inlets) for one week during the campaign. For all gases and positions, similar temporal concentration patterns were found. CO_2 concentrations increased during the night, most likely as a result of dominating respiratory fluxes and low atmospheric mixing conditions. The dominating respiratory fluxes are also visible in the $\delta^{13}CO_2$ pattern, which shows more depleted values during nighttime. The temporal daily patterns for CH_4 and N_2O were less clear: slightly higher concentrations at night were observed in comparison to daytime values, most likely caused by the low atmospheric mixing at nighttime. CO concentrations showed a very interesting pattern with peak concentrations in the early morning (6:00) and late afternoon (18:00). It is not known what causes this pattern, but a hypothesis is that the CO concentrations are determined by biological soil uptake and

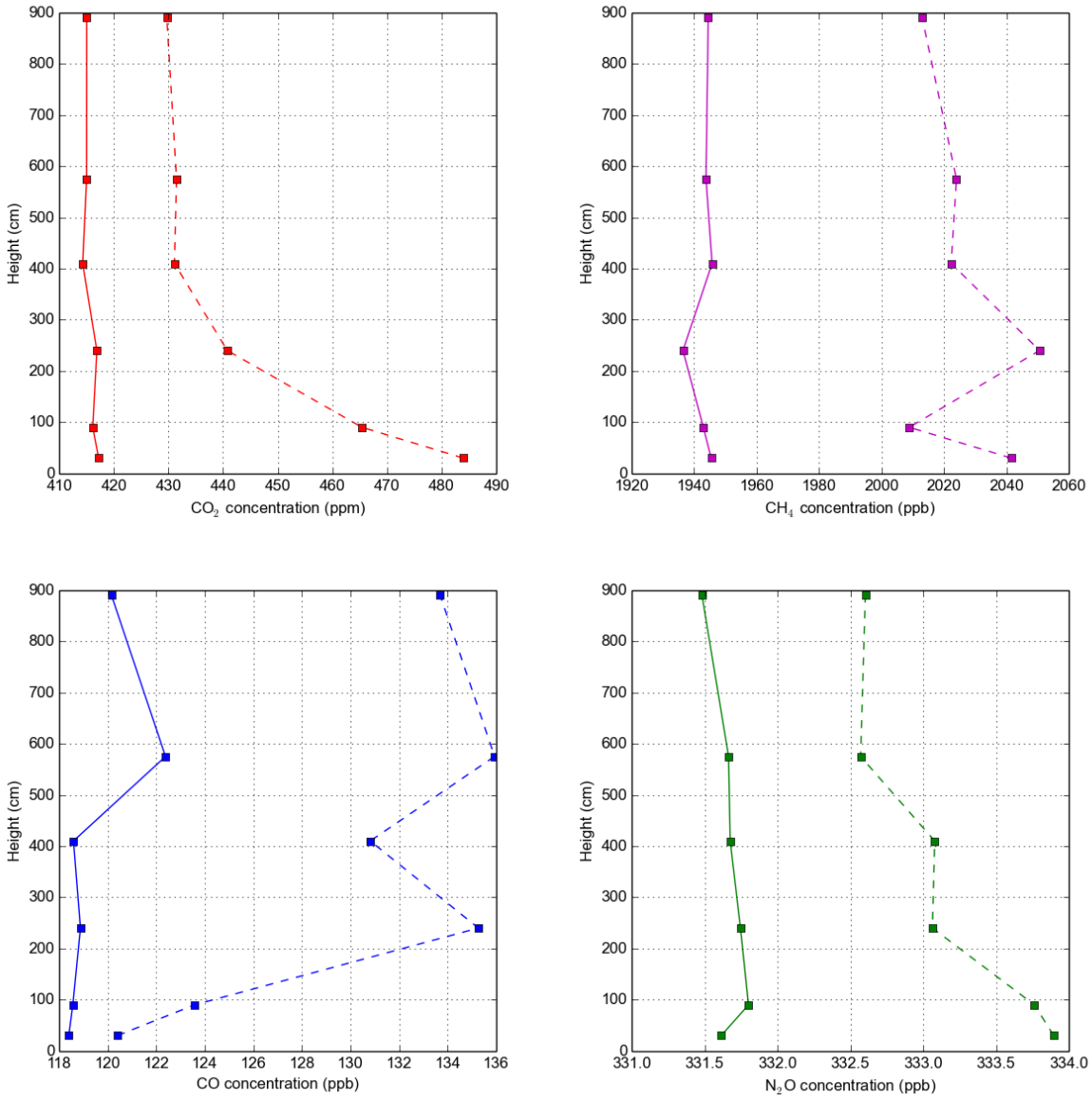

Figure 5.11: Vertical concentration profiles in canopy during day and night, during the field campaign at the fieldsite Poplar. The solid lines show example gas concentrations during daytime (23-10-2013 13:00), the dashed lines show example gas concentrations during nighttime (23-10-2013 23:00).

abiotic soil CO emission. During the night, the processes are close to equilibrium, but in the morning when temperatures rise, the thermal degradation fluxes become larger. The fact that CO concentrations drop after the peak at 6:00, can possibly be explained by the mixing conditions of the atmosphere. The expected increase in CO, without mixing, is indicated in Figure 5.14.

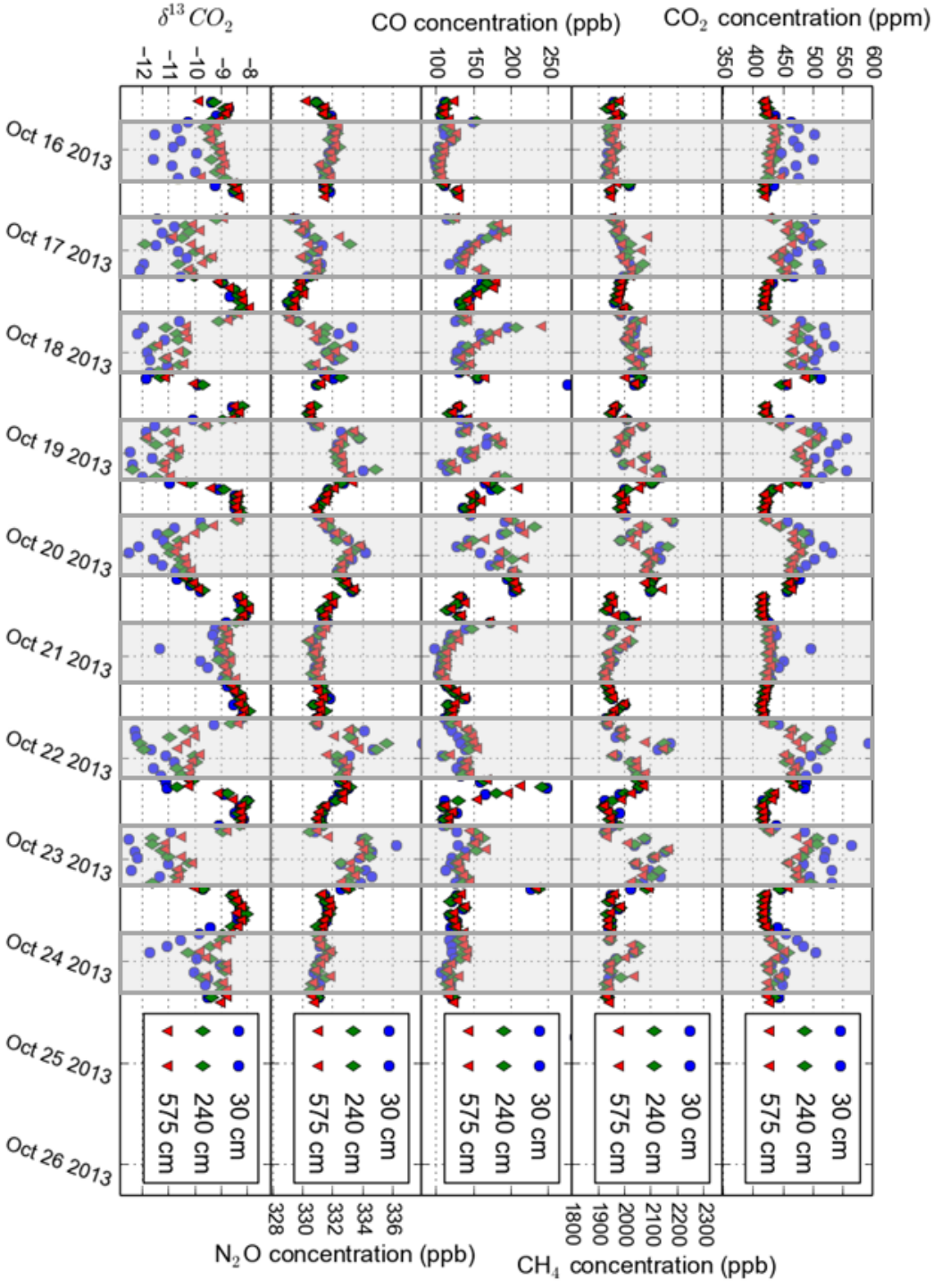

Figure 5.12: Vertical concentration measurements in the canopy, during the field campaign at the fieldsite Poplar. The gas concentrations for the inlet heights 30, 240 and 575 cm for several days are shown. The gray areas indicate nighttime (20 -5 h). More concentration data can be found in §10.3.4.

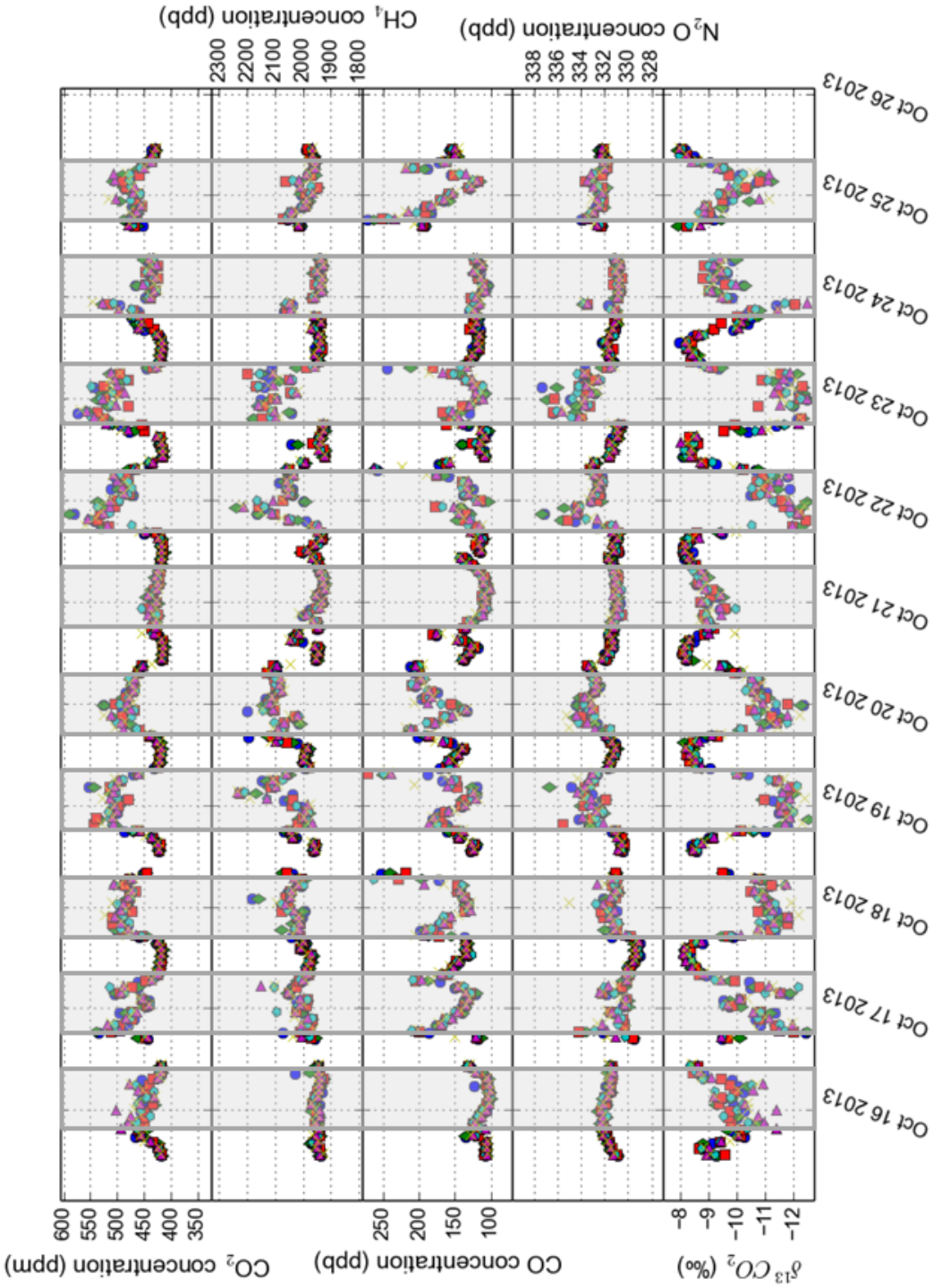

Figure 5.13: Horizontal concentration measurements, during the field campaign at the fieldsite Poplar. The colors indicate the following positions: blue circles = inlet A, green diamonds = inlet B, red squares = inlet C, light blue pentagons = inlet D, purple right triangle = inlet E, yellow cross = inlet F (see schematic in Figure 4.7). The gray areas indicate nighttime (20 -5 h). More concentration data can be found in §10.3.4

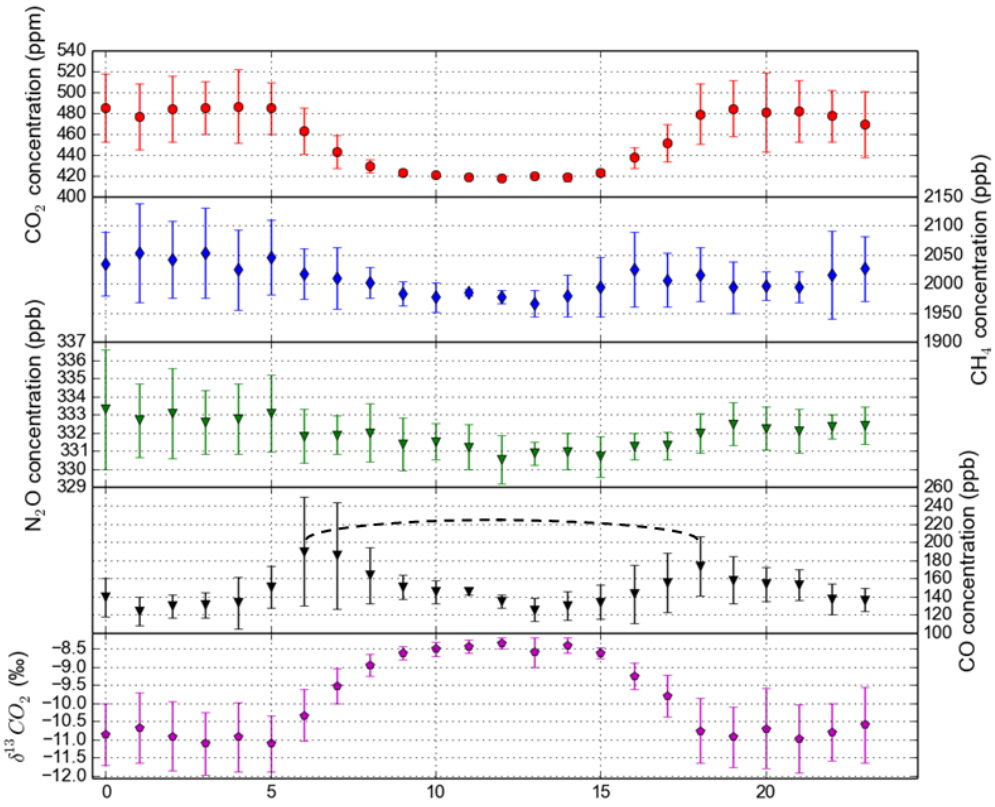

Figure 5.14: Averaged horizontal concentrations measured at 90 cm between 14-19 October. The black dashed line indicate expected CO concentrations (because of increased thermal degradation fluxes) if daytime atmospheric mixing would not occur.

Correlations of the gases in the vertical profile

Figure 5.15 shows the measured CO_2 concentrations at different heights versus the CH_4, N_2O and CO concentrations. A possible correlation would indicate similarity in diurnal cycle and would indicate sources which respond similar to an environmental variable such as temperature, moisture, pressure etc. The clearest correlation was found between N_2O and CO_2 concentrations at 240 cm during the night: for most nights a 10 ppm CO_2 concentration increase was accompanied by a 0.5 ppb N_2O concentration increase, pointing at very low N_2O fluxes. An increase in N_2O is most likely caused by small soil N_2O fluxes. A large part of the CO_2 production at night originates from soil respiration. Both fluxes therefore might have a shared dependency on variables such as soil temperature and moisture. However, for CO_2 also sources and sinks higher in the canopy are expected, wherefore not a strong correlation between these gases can be assumed.

The correlation between CO_2 and CH_4 concentrations is not strong, most likely due to the irregular behavior of the CH_4 concentrations, which is not fully understood. For CO concentrations, only a very weak ($R^2 = 0.20$ at 8.90 m) concentration correlation to CO_2 concentrations was found, and no correlation at the surface. This can be explained by the fact that, close to the surface, CO_2 and CO concentrations are dependent on very different (opposite) processes (CO_2 production and CO uptake by soil microbes).

In general, gas concentration correlations between CO_2 and the gases CH_4, N_2O and CO within the canopy were not strong, most likely due to the different type (uptake or emission) or location of production processes. Assuming similar behavior for different gases within the canopy for estimation of the storage component might therefore lead to incorrect estimates.

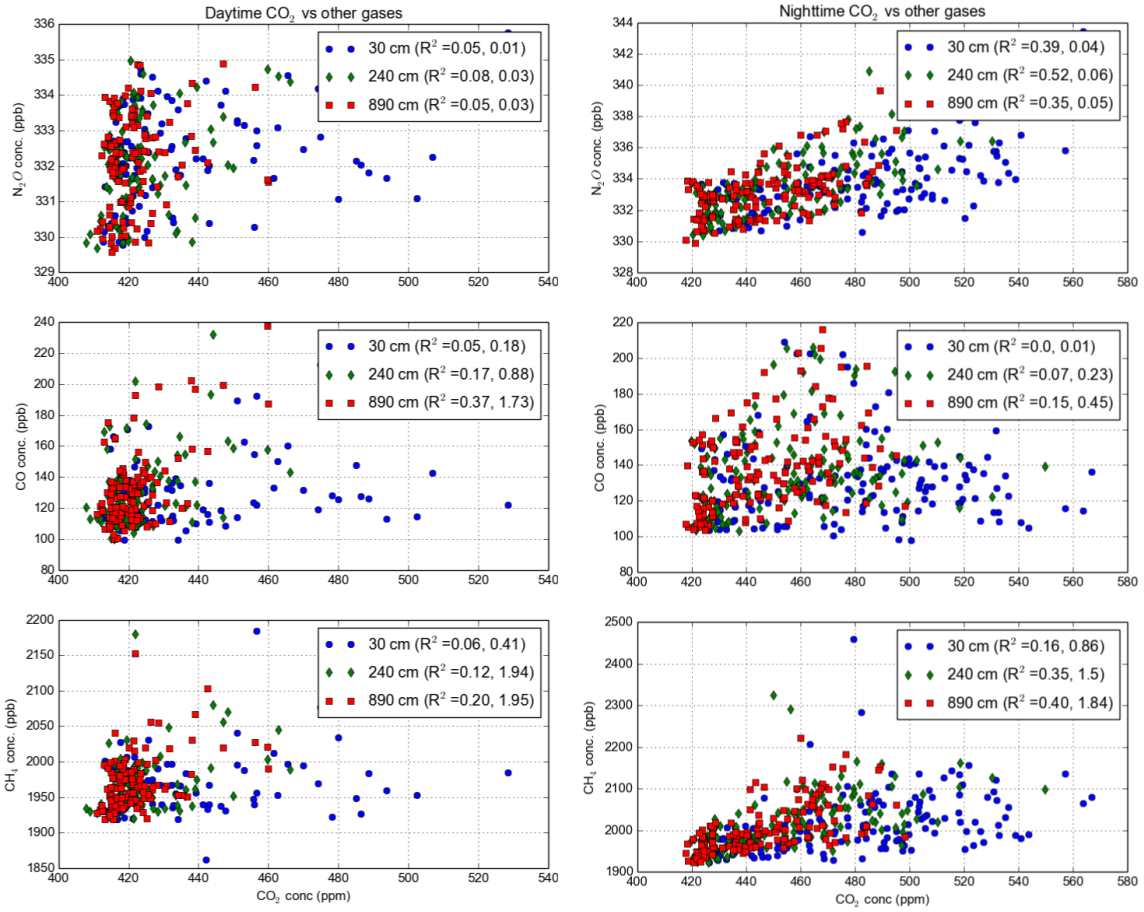

Figure 5.15: Correlation between the concentrations of different gases versus the CO_2 concentration. The daytime values (left figures) are measured between 10-18 h and the nighttime values (right figures) are measured between 20-5 h.

$\delta^{13}CO_2$ and Keeling plot intercepts

Figure 5.16 shows $\delta^{13}CO_2$ values at different heights for 6 days during the experiment. During the day (7-18 h), turbulent conditions in the atmosphere also cause mixing within the canopy and, just as observed in the concentration profiles (Figure 5.11), the measured $\delta^{13}CO_2$ value is similar values over all heights. During the night (18-6 h), a boundary layer builds up and, as can be seen in Figure 5.11, CO_2 concentrations buildup close to the surface. The added CO_2 originates from soil and ecosystem respiration and therefore is more depleted than the atmospheric CO_2, which is visible in Figure 5.16. During boundary layer buildup, a Keeling plot can be created to determine the $\delta^{13}CO_2$ value of the respiration. For more information on the use of Keeling plots, see Chapter 7. Per inlet and per night a Keeling plot has been created. Keeling plot intercepts, derived from plots with $R^2 > 0.90$, are shown in Figure 5.17 and Figure 5.18. On 5 October, a period of rain started (black diamonds, Figure 5.17), which seems to coincide with the drop in respiratory $\delta^{13}CO_2$ values. Further analysis of wind, precipitation and temperature patterns could show whether environmental drivers might be the cause of the temporal variation in the respiratory $\delta^{13}CO_2$ value. In Figure 5.18, no clear spatial or temporal pattern could be distinguished. Averaging all intercept values, based on plots with $R^2 > 0.985$, resulted in the values which are displayed as black triangles (Figure 5.18). Inlets closer to the soil surface showed slightly more depleted intercept values. Lower inlets are more influenced by soil respiration while higher inlets are more influenced by tree respiration. Soil respiration being more depleted than tree respiration could explain such a pattern.

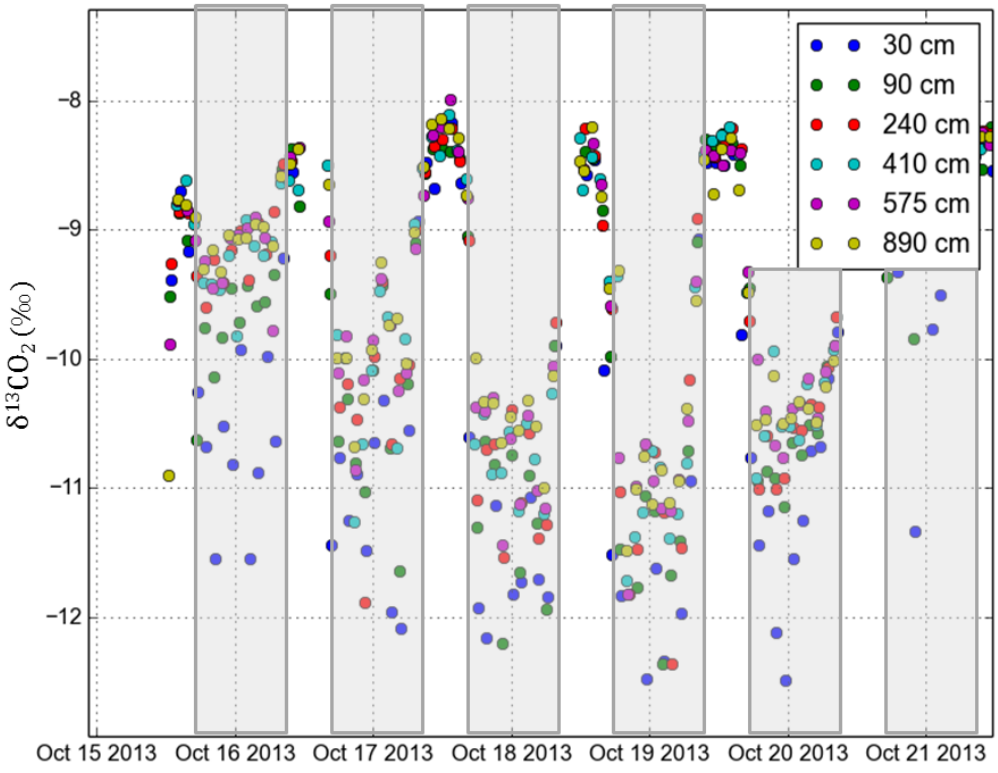

Figure 5.16: Atmospheric $\delta^{13}CO_2$ values measured at the different heights for 4 days during the campaign at fieldsite Poplar. The gray blocks represent nighttime.

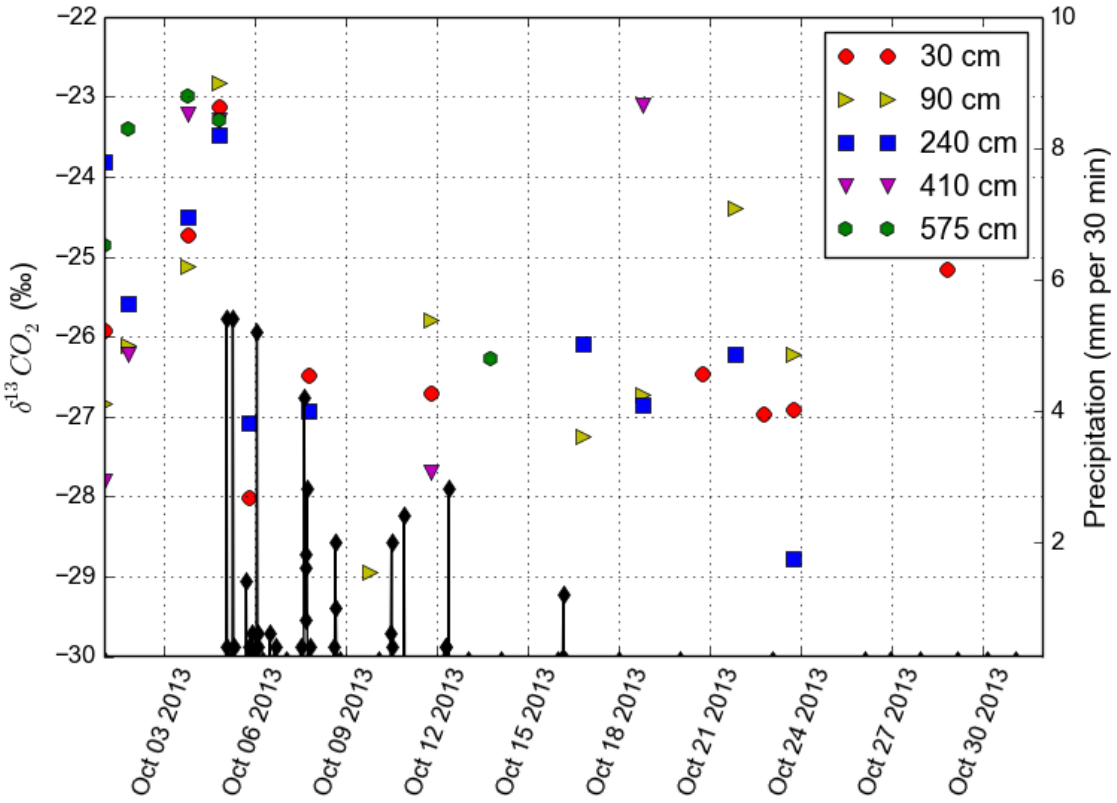

Figure 5.17: Keeling plot intercepts per height ($R^2 > 0.95$) over time, the black diamonds indicate precipitation. A decrease in respiratory $^{13}CO_2$ values is visible after 5 October, coinciding with the start of a period of rain.

5.3.3 Conclusion

$\delta^{13}CO_2$ measurements showed a clear respiratory signal during the night. By means of Keeling plots, the $\delta^{13}CO_2$ value of the respiratory flux could be estimated. A possible relationship between precipitation and respiratory $\delta^{13}CO_2$ value was observed. Possibly, by measuring $\delta^{13}CO_2$ values over longer time scales and under different conditions (temperature, drought, wind, precipitation), more detailed information can be obtained about the fractionation processes within the canopy under different circumstances.

Vertical concentration buildup during non-turbulent (nighttime) conditions was different per gas: CO_2 concentrations showed a logarithmic shape, indicating sources at or close to the soil surface. Also for N_2O concentrations a logarithmic shape could sometimes be observed, however not for all nights. CO concentrations were rather homogeneous in the vertical plane, except for the lowest inlets where lower concentrations were observed, pointing at CO uptake. CH_4 concentrations showed no clear vertical pattern; the highest concentrations were observed at the higher inlets as well as at the lower inlets.

Spatial heterogeneity in the horizontal plane was existent but irregular and without a clear spatial pattern. Horizontal differences for N_2O were very small (less than 4 ppb, also during

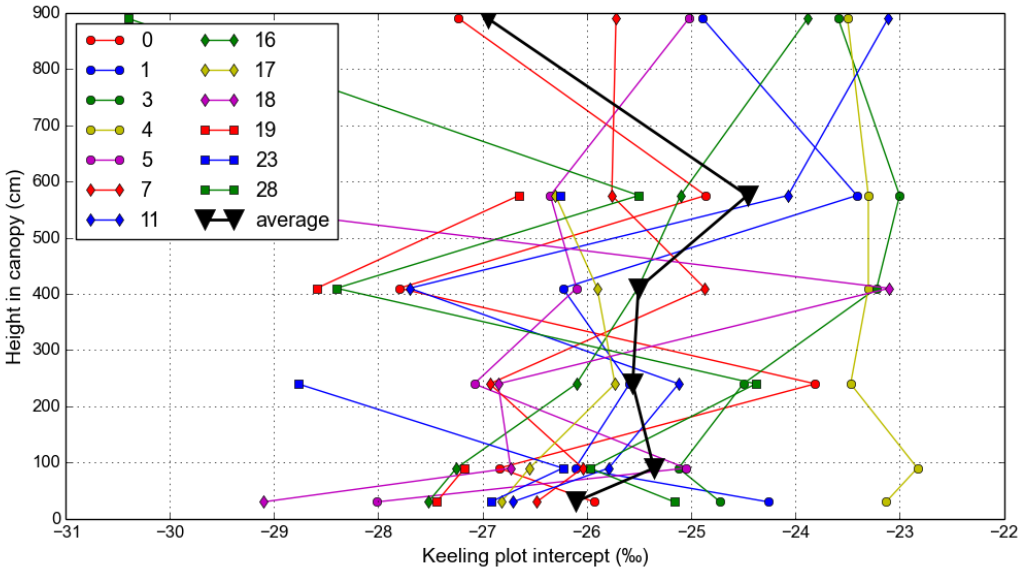

Figure 5.18: Keeling plot intercepts derived from the gas concentrations measured at the different heights and during the different nights between 20 h and 5 h, with $R^2 > 0.90$. The numbers in the legend indicate the date in October. The bold black line indicates the average of the measurements (with $R^2 > 0.985$) for the different heights.

nighttime). Expected is that a change in N_2O inside the canopy is caused by advection, which could explain the homogeneity of the concentrations inside the canopy. The other gases showed much larger variations during nighttime, indicating uptake or production processes inside the canopy: for CO_2, CH_4 and CO respectively differences up to 70 ppm, 700 ppb and 20 ppb were observed within 10 meters, thereby exceeding the vertical concentration variation. No clear differences were found between inlets placed in line with the poplar trees in comparison to inlets placed between the poplar tree lines.

The addition of concentration measurements by an FTIR-analyzer to an EC forest flux site provides valuable information about the concentrations, spatial distributions and cross-concentration correlations of different (greenhouse) gases in the canopy under non-turbulent conditions. This data shows that assuming a homogeneous storage layer can cause a large underestimation of the storage flux when measured too far above the surface. More horizontal concentration measurements over a larger horizontal scale are necessary to test whether horizontal variation can be quantified, and to be able to decide if additional horizontal measurements within the canopy are valuable. However, more importantly, it is unclear if and how the large horizontal concentration differences, which were observed at 90 cm, can be propagated to the other heights. For a future experiment, multiple vertical concentration profiles need to be measured to assess the horizontal spatial variability of the vertical profile.

5.4 The use of the FTIR-analyzer to study N_2O production pathways

5.4.1 Introduction

Atmospheric N_2O concentrations have been increasing as a result of human activities. The emissions from agricultural soils are one of the largest sources of atmospheric anthropogenic N_2O (approximately 60%, Figure 2.5). Agricultural soils produce N_2O via different pathways, as visualized in Figure 5.19. Production of N_2O in soil and water is mostly by nitrification and denitrification.

Nitrification is the aerobic microbial oxidation of ammonium (NH_4^+) to nitrate (NO_3^-). In (partly) anaerobic conditions, when oxygen is limiting, NO_2^- can be used as an alternative electron acceptor (instead of O_2) and N_2O is produced (Figure 5.19); this process is called nitrifier denitrification. Denitrification is the anaerobic microbial reduction of nitrate to ao N_2O. In general in agricultural soil, denitrification is the major source for N_2O production (Figure 2.5) [172].

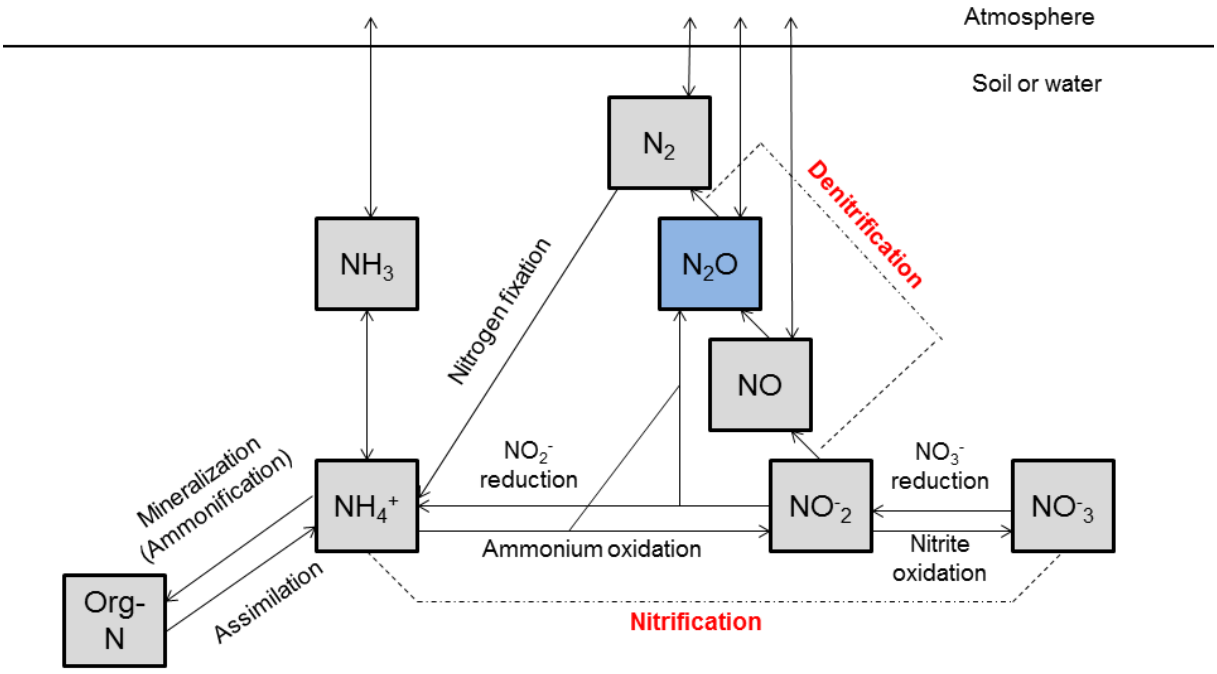

Figure 5.19: Simplified schematic of the nitrogen cycling between soil, water and atmosphere: NH_3 is called ammonia, NH_4^+ is called ammonium, NO_2^- is called nitrite, and NO_3^- is called nitrate. The figure is modified from Galloway (2005).

Agricultural crops can take up nitrogen in different forms. For fertilization purposes, nitrogen is often added as nitrate (NO_3^-) or ammonium (NH_4^+). Each fertilizer has its advantages and disadvantages.

Nitrate is easier taken up by crops, in comparison to ammonium, and also has the advantage of being negatively charged, which enhances the uptake by plants of positive nutrients such as magnesium (Mg^+), calcium (Ca^+) and potassium (K^+). Also, it is highly soluble in water wherefore it distributes easily through the soil. Its solubility can also be a disadvantage since it causes leaching from the root zone to deeper layers and/or the groundwater, especially in wet conditions or after precipitation events. During anaerobic (wet) conditions, denitrification goes faster and part of the fertilizer-nitrogen will be 'lost' to the atmosphere via NO, N_2O and N_2 emissions [186].

Ammonium is less easily taken up by plants. Also, because of its positive charge, most of it is adsorbed by negatively charged clay molecules. Because of this, ammonium is less available for crops, but also less sensitive to leaching. Part of the ammonium is directly taken up by plants, but most of the not-bound ammonium is transformed intro nitrate (via nitrification) and then taken up. In general, fertilizer containing ammonium releases its nitrogen to crops slower, making it a longer-lasting fertilizer in comparison to nitrate. However, a large disadvantage of the use of ammonium is the volatilization of ammonia (NH_3), which can be produced from ammonium (NH_4^+). Also, ammonium addition can results in N_2O emission during the nitrification process (nitrifier denitrification). Therefore, nitrogen losses to the atmosphere can be large when using ammonium-based fertilizer [186].

Flux chamber and micrometeorological techniques are able to quantify N_2O emissions but cannot identify which processes are the cause for the N_2O production. Especially for agricultural studies, the question by which pathway the N_2O is produced is interesting, since it can reveal the nitrogen-use efficiency of different type of fertilizers. The use of a ^{15}N-labeled fertilizer can be applied to study nitrogen cycling patterns and can be used to assess the efficiency of the different fertilizers [144].

In this paragraph, an experiment is described wherein the FTIR-analyzer was connected to two flux chambers. Soil inside the flux chambers was fertilized by two different types of fertilizer: one ^{15}N-spiked nitrate-based (KNO_3) fertilizer and one ^{15}N-spiked ammonium-based (NH_4Cl) fertilizer. The goal was a) to assess whether it is possible to retrieve N_2O isotopologues and isotopomers by use of the FTIR-analyzer and b) to compare the nitrogen losses to the atmosphere by soil N_2O fluxes of a nitrate- and ammonium-based fertilizer, by use of a ^{15}N-labeling-technique.

5.4.2 The ^{15}N-labeling experiment

The measurements were performed during the N_2O flux chamber intercomparison campaign at RISØ; the FTIR-analyzer and flux chambers set-up description can be found in §4.2 and more details on this experiment can be found in §10.1.1. For this experiment, two additional soil collars were used. Measurements were alternating between the ^{15}N-labeling experiment and the intercomparison campaign wherefore the measurement frequency is varying. The nitrate-based fertilization solution was made as follows: 0.7328 gram KNO_3 (0.00724 mol N) was dissolved in 250 ml distilled water. 10% of the added N was ^{15}N, wherefore 6.517 mmol is ^{14}N-KNO_3 and 0.724 mmol is ^{15}N-KNO_3. The ammonium-based solution was made as follows: 0.3818 gram NH_4Cl (0.007125 mol N) was dissolved in 250 ml distilled water. 10% of the added N was ^{15}N, wherefore 6.4123 mmol is ^{14}N-KNO_3 and 0.7125 mmol is ^{15}N-KNO_3. The nitrate-solution was added to chamber A, and the ammonium-solution was added to chamber B.

The measurements of the additional soil collars started on 22 April 2013 and the fertilizer was added on 24 April 2013: at 9:15 the nitrate-based fertilizer was added to the soil of chamber

A, and at 9:35 the ammonium-based fertilizer was added to the soil of chamber B. Fertilizer addition was performed 10 minutes before flux chamber closure. Additionally, air samples for GC analyses were taken from the sampling line between the chamber and the FTIR-analyzer by use of a syringe.

Standard retrieval settings of the FTIR-analyzer do not include the measurement of isotopes of N_2O. Additional analyses were performed by David Griffith (University of Wollongong, [68]) to retrieve N_2O isotopologue and isotopomer concentrations [68]. The details of the methodology for this retrieval can be found in Phillips (2013) and its complementary materials. Concentrations of $^{15}N^{15}N^{16}O$ were too small and are not considered in this paragraph [68].

5.4.3 Results

General flux patterns

Figure 5.20 shows the measured total N_2O fluxes during the RISØ intercomparison campaign: the red diamonds and the blue squares indicate measurements performed as part of the intercomparison campaign and the purple circles and the black pentagons indicate measurements from locations where ^{15}N-labeled fertilizer was applied on 24 April. The figure shows that, immediately after fertilization, the N_2O fluxes in chamber A, where nitrate-based fertilizer was applied, increased. Afterwards, N_2O fluxes decreased back to normal levels (in comparison to 23 April) within 3 hours. No response was visible in chamber B where fluxes showed a similar daily pattern as before the fertilization. N_2O fluxes at the end of the experiment, on 26 and 27 of April, were higher in comparison to the days before, but are still small in comparison to fluxes measured in the beginning of the experiment at other locations in the field (Figure 5.20, upper figure).

N_2O isotopologues and isotopomers

Figure 5.21 shows the individual concentrations of the different isotopomers of $^{15}N_2O$ in the different chambers. Figure 5.22 shows the N_2O concentration increase (in ppb per minute) per isotopomer and per chamber, based on linear regression. Figure 5.23 shows the calculated N_2O fluxes of the different N_2O isotopologues and isotopomers. Fluxes based on linear regression coefficients lower than 0.6 ($R^2 < 0.6$) are not shown.

5.4.4 Discussion

Concentration and fluxes before ^{15}N-labeled fertilization experiment

The chamber locations which were used for the ^{15}N-labelling fertilization experiment were located in a fieldsite which was also fertilized in the beginning of April, as part of the N_2O flux chamber intercomparison campaign (for details, see §4.2 and §10.1.1). While having received the same treatment as other field locations, the N_2O fluxes measured on 22 and 23 April were much lower in comparison to fluxes measured in other places of the field (Figure 5.20). However, as also discussed in §10.1.1, it is expected that small scale spatial variation can play a major role in N_2O flux variations. Retrieval of the $^{15}N_2O$ isotopomer concentrations resulted in concentration measurements of around 1 to 1.5 ppb (before the fertilization). Concentrations during flux chamber closure before fertilization did not consistently change wherefore individual $^{15}N_2O$ isotopomer fluxes could not be calculated and expected is that these fluxes were below the detection limit.

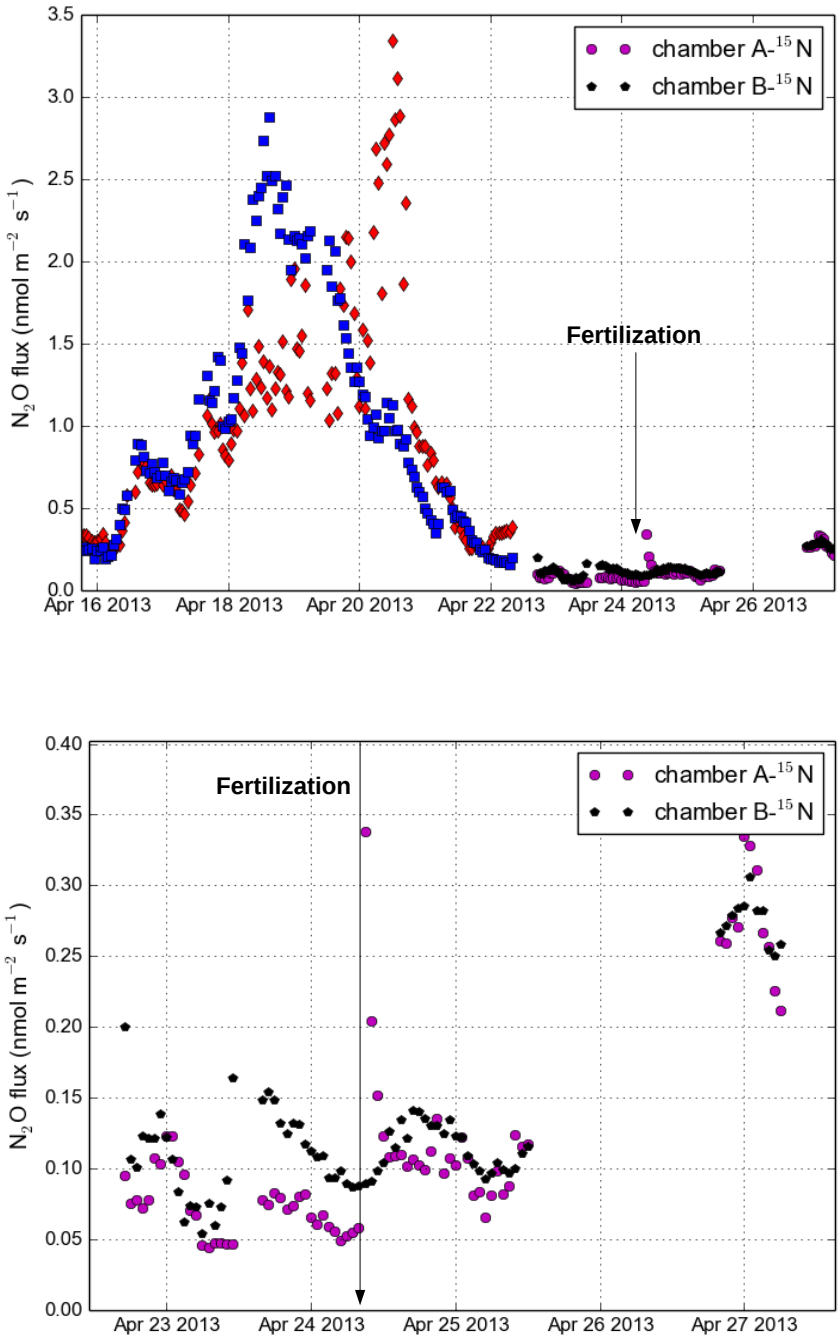

Figure 5.20: Flux chamber fluxes from the ^{15}N-labelling fertilization experiment. Upper figure: the N_2O fluxes during the RISØ intercomparison campaign. The red diamonds and the blue squares are the fluxes from the locations which were not fertilized with ^{15}N-spiked fertilizer. The purple circles are the fluxes from the location with nitrate-based (KNO_3) fertilizer, the black pentagons are the fluxes from the location with ammonium-based (NH_4Cl) fertilizer. The shown fluxes are the total non-isotope specific N_2O fluxes. The fertilization event is indicated with the black arrow. Lower figure: zoom in on the ^{15}N-labelling fertilization-part of experiment. Fertilization took place on 24 April at 9:15 (chamber A) and at 09.35 (chamber B). On 25 April, there was a precipitation event. The fertilization event is indicated with the black vertical arrow.

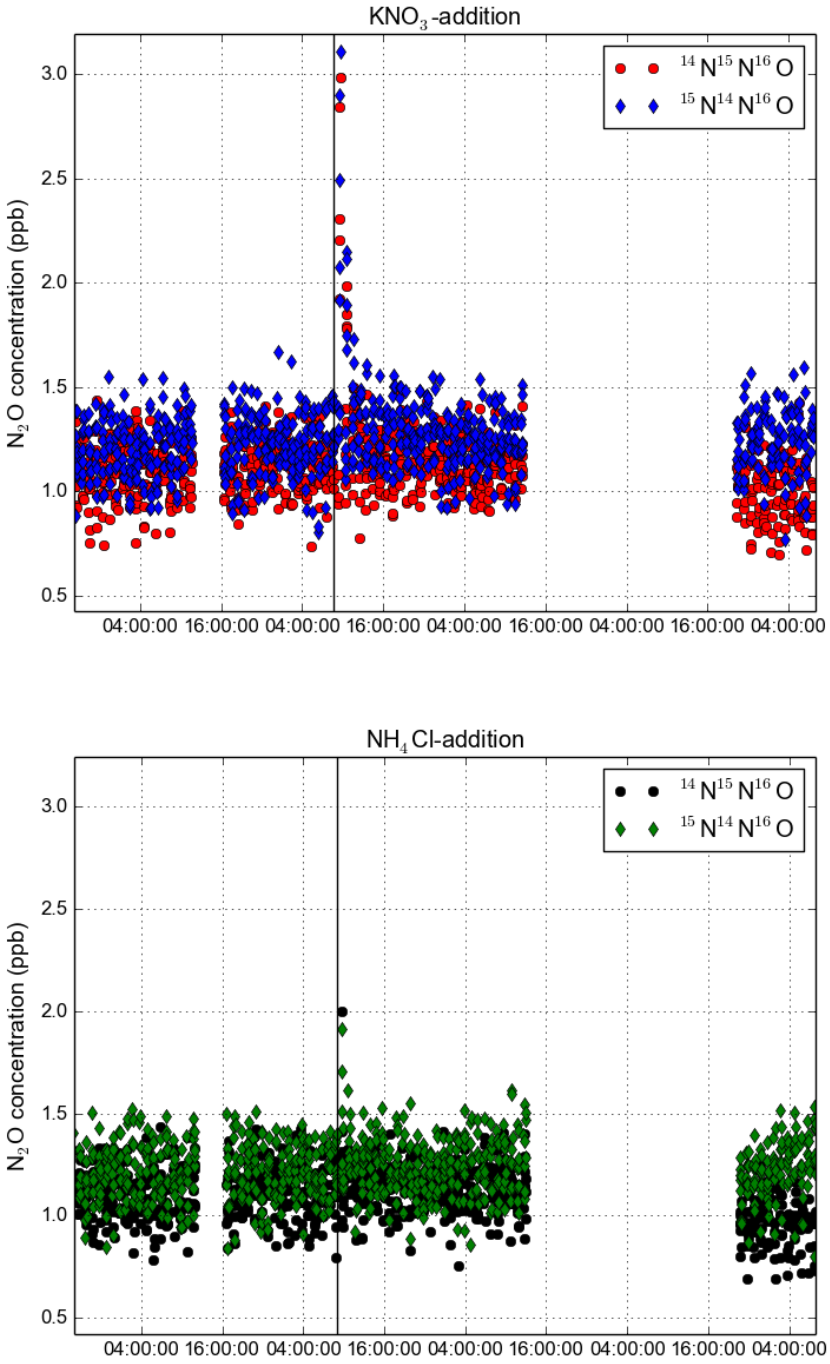

Figure 5.21: Upper figure: the concentrations of the different $^{15}N_2O$ isotopomers in chamber A (KNO_3-based fertilized); the fertilization event is indicated by the black vertical line. Lower figure: the concentrations of the different $^{15}N_2O$ isotopomers in chamber B (NH_4Cl-based fertilized); the fertilization event is indicated by the black vertical line.

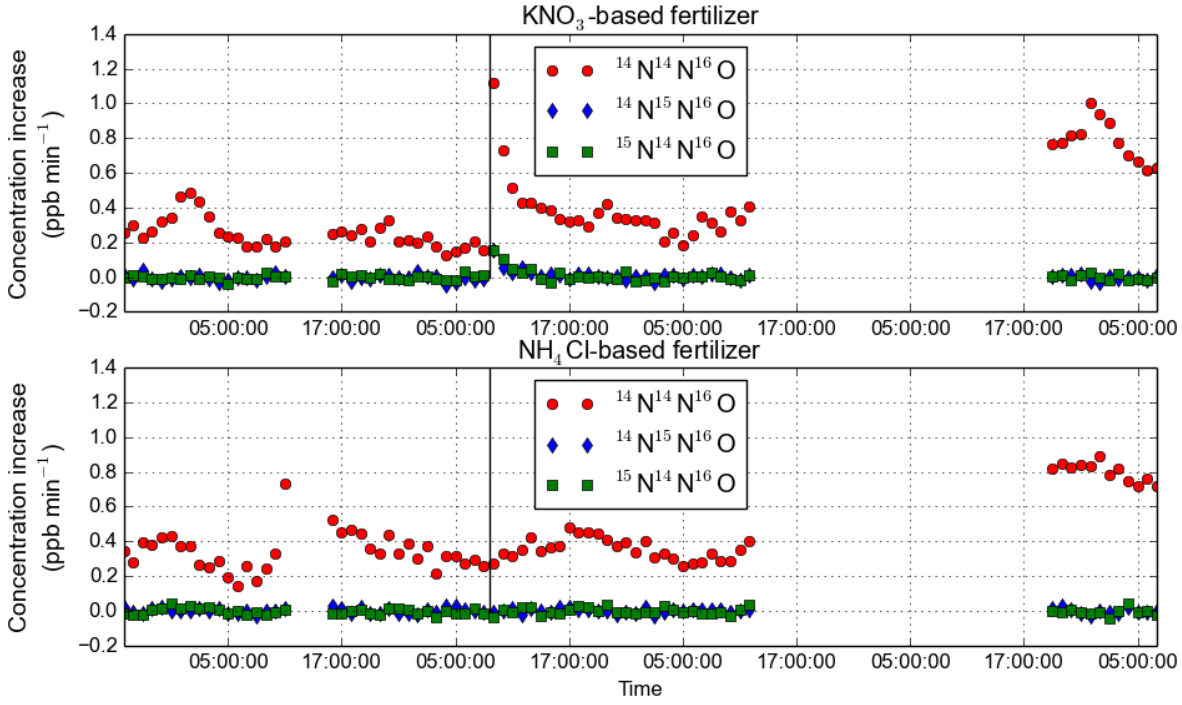

Figure 5.22: Upper figure: N_2O increase (ppb per minute) during the 10 min-chamber closure in chamber A (KNO_3-based fertilized). Lower figure: N_2O increase (ppb per minute) during the 10 min-chamber closure in chamber B (NH_4Cl-based fertilized). The fertilization event is indicated by the black vertical line.

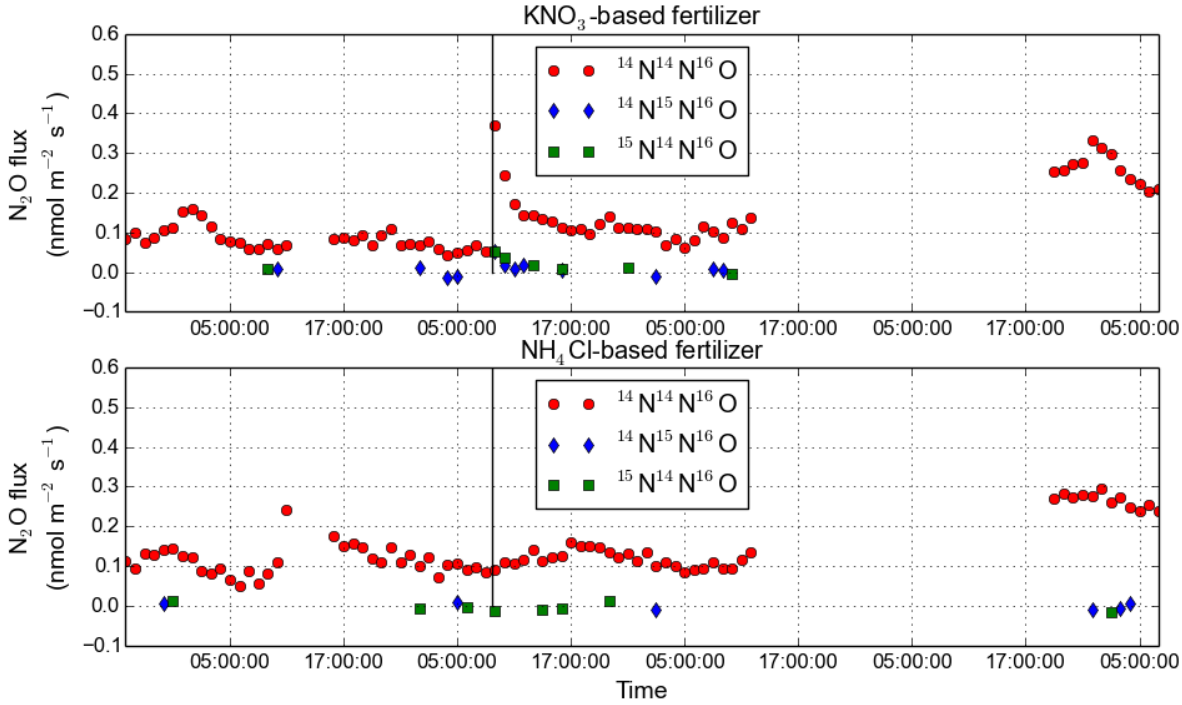

Figure 5.23: Upper figure: N_2O flux (in nmol m^{-2} s^{-1}), when the R^2 of the linear regression was > 0.60 in chamber A (KNO_3-based fertilized). Lower figure: N_2O flux (in nmol m^{-2} s^{-1}) when the R^2 of the linear regression was > 0.60 in chamber B (NH_4Cl-based fertilized). The fertilization event is indicated by the black vertical line.

Concentration and fluxes after ^{15}N-labeled fertilization experiment
Chamber A received nitrate-based fertilization on 24 April at 09:15 and chamber closure was between 09:23 and 09:37. After fertilization, the chamber immediately showed higher N_2O fluxes. The most abundant isotope $^{14}N^{14}N^{16}O$ showed fluxes of 0.38 nmol m^{-2} s^{-1}, and an average flux of 0.236 nmol m^{-2} s^{-1} was estimated for the first 3 hours. The isotopomers of $^{15}N_2O$ showed very similar fluxes right after fertilization with an estimated average flux of 0.032 nmol m^{-2} s^{-1} during the first 3 hours. The estimated flux ratio $^{14}N_2O$:$^{15}N_2O$ is therefore 20% vs 80%. It is unknown whether the fact that the applied ratio (10% vs 90%) is different from the observed ratio, is due to the measurements precision or due to a fractionation process. The estimated cumulative ^{15}N-N_2O flux is 690 nmol m^{-2} per 3 hours (0.032 x 60 x 60 x 3 x 2). So, of the 724 mmol added ^{15}N, approximately 1% is emitted back to the atmosphere within the first 3 hours. After these 3 hours, isotopomer fluxes seem to return to pre-fertilization values. However, when studying the isotope $^{14}N^{14}N^{16}O$, it seems that enhanced fluxes appear longer. This means that either the $^{15}N_2O$ fluxes decreased faster or that, after the three hours, these fluxes went below the detection limit.

Chamber B received ammonium-based fertilization on 24 April at 09:35 and chamber closure was between 09:43 and 09:57. No higher N_2O fluxes were observed after fertilization. However, the chamber headspace ^{15}N-N_2O isotopomer concentrations before chamber closure were higher than before the fertilization and went down during chamber closure. It could be that during the 8 minutes before chamber closure already N_2O fluxes occurred, resulting in higher headspace concentrations. However, it is unclear if and why the N_2O fluxes went down so quickly and why the ^{15}N-N_2O isotopomer concentrations (not the total concentrations) in the chamber (during chamber closure) went down.

Higher fluxes in both chambers were observed in the end of the experiment, possibly caused by the rain event of 25 April. A previous study has shown that rain can have positive effects on N_2O production for more than 10 days [144]. Our experiment is too short to assess the long term effect of the rain. Concentration measurements of isotopomers after the rain event showed slightly lower concentrations for the isotopomer $^{14}N^{15}N^{16}O$ in both chambers, in comparison to the $^{15}N^{14}N^{16}O$ isotopomer. However, during chamber closure, no clear difference in fluxes was found. A theory is that both isotopomer fluxes were too low to be detected, but that the isotopomer $^{15}N^{14}N^{16}O$ flux is slightly higher, which can result in consistent higher chamber headspace concentrations.

Based on this very brief experiment, it seems that nitrogen-fertilization with a nitrate-based fertilizer results in a nitrogen loss via N_2O production of almost 1% already in the first 3 hours after fertilization. It is unclear how much is lost via different forms of nitrogen emission, and how much is emitted after the 3 hour period (since the labeled ^{15}N-N_2O fluxes went below the detection limit). Nitrogen-fertilization with an ammonium-based fertilizer did not result in an immediate increase in N_2O fluxes. This could indicate a more efficient use of nitrogen by the soil, which can be expected based on its characteristics (see §5.4.1). However, results might be very different if measurements were performed in wetter conditions. Also, the loss of nitrogen via volatilization of NH_3 was not monitored. So far, samples which were taken for GC measurements have not yet been analyzed.

5.4.5 Conclusion

In this experiment, the use of the FTIR-analyzer to study N_2O emissions of different nitrogen fertilizers, was assessed. Concentrations of $^{15}N_2O$ isotopomers could be obtained by an adapted spectral retrieval, and concentrations between 1-1.5 ppb were found. Fluxes of $^{15}N_2O$ isotopomers were too low to be detected, except right after the ^{15}N-labeled fertilization. The nitrate-fertilization caused a peak emission but fluxes returned to original levels within 3 hours. It is estimated that almost 1% of the added N-NO_3^- is emitted as N_2O right after the fertilization. The ammonium-based fertilization did not result in enhanced N_2O emissions, most likely due to its quick adsorption to soil clay particles. Results of this experiment could have been very different if fertilization was performed in wetter conditions, which enhances volatilization of NH_3 (derived from ammonium), but also increases leaching and denitrification of NO_3^-.

In this paragraph, we have shown that the FTIR-analyzer can measure $^{15}N_2O$ concentration and fluxes, and that it can be used to study the nitrogen losses of different type of fertilizers. For future ^{15}N-labeling studies, it is advised to increase the amount of ^{15}N-labeled fertilizer and increase the length of the measurement campaign, so that fertilization effects are stronger and long term fertilization effects can be studied [144].

5.5 Conclusion

The research performed during this PhD was partly directed to one of the goals of the InGOS infrastructure project, namely combining the FTIR-analyzer with micrometeorological techniques for biosphere-atmosphere gas exchange measurements. During the PhD, several field experiments have been performed wherein the FTIR-analyzer was combined with different types of micrometeorological techniques. In this chapter, we have explored the possibilities of the set-up for other type of flux methodology- or ecosystem research related questions.

In §5.1, the application of the new ratio-nocturnal boundary layer (R-NBL) technique is presented. If an ecosystem is homogeneous and an eddy covariance system is available, fluxes of different gases can be derived from concentration measurements without knowledge of the boundary layer height. In our case study at the fieldsite RISØ, we measured N_2O fluxes of approximately 0.2 nmol m^{-2} s^{-1}, which was of a similar magnitude as fluxes measured by the on site EC method. Analysis of the source area showed that the method is suitable when the source area does not include cities, villages or roads. Under suitable conditions (stable boundary layer, homogeneous footprint), the detection limit of the R-NBL method was estimated to be 0.004 nmol m^{-2} s^{-1}, which is lower than reached by most other flux measurement techniques. Using an FTIR-analyzer in combination with the R-NBL technique enables the study of different gas fluxes simultaneously.

In §5.2, the parameterization of the diffusion coefficient, required for the flux gradient technique, has been studied. For FG measurements performed at Rocca4, we found that parameterizations from literature largely underestimated CO_2 fluxes, in comparison to eddy covariance measurements. A new method to derive diffusion coefficient values, which is based on as well EC measurements as on an empirical parameterization, was presented and resulted in a fieldsite specific parameterization. The results showed that the newly derived diffusion coefficients results in FG fluxes which are close to EC measurements. This approach in combination with the FTIR-analyzer enables reliable flux gradient measurements for multiple gases.

In §5.3, the use of the FTIR-analyzer for the continuous measurement of multiple concentrations inside a forest canopy was presented. The results showed that spatial variation inside a canopy is large. The vertical nighttime CO_2 concentration buildup showed a clear logarithmic pattern. Less clear vertical patterns for the other gases were observed. Horizontal variation was found to be larger than vertical variation: nighttime concentration differences could be up to 4 ppb (for N_2O), 40 ppb (for CO), 700 ppb (for CH_4), and 70 ppm (for CO_2), within 10 meter distance. For the determination of the storage component for EC measurements, multiple vertical concentration profiles need to be measured to check whether horizontal variation is consistent for all heights.

In §5.4, a ^{15}N-labeling experiment was presented with the aim to study different N_2O production pathways in an agricultural field. ^{15}N-labeled nitrate- and ammonium-based fertilizer was applied to soil in the flux chambers, and individual concentrations and fluxes of N_2O isotopologues and isotopomers were measured every hour. The results showed that the FTIR-analyzer was capable of measuring different isotopologues and isotopomers of N_2O at low concentrations (1 ppb). The fertilization experiment showed the fast and large loss of nitrogen by N_2O emissions to the atmosphere after application of the nitrate-based fertilizer, in comparison to the ammonium-based fertilizer.

In summary, the use of an FTIR-analyzer for ecosystem flux measurements has enabled us to test and improve existing and new flux measurement methodologies. The advantage of using the FTIR-analyzer for this purpose is the flexibility of the system wherefore many types of research set-ups are possible. The simultaneous measurement of multiple gas species (CO_2, N_2O, CH_4, CO and $\delta^{13}CO_2$) provides the opportunity to study different gases, to assess inter gas species relationships, and to explore new fields in ecosystem science. In conclusion, the addition of an FTIR-analyzer to ecosystem flux sites can provide valuable data with the possibility to improve the existing flux measurement set-up, and enables to explore the study of different ecosystem processes.

6 The role of photo and thermal degradation in an arid ecosystem

Parts of this chapter are modified from the following manuscript:

'The role of photo- and thermal degradation for CO_2 and CO fluxes in an arid ecosystem', Hella van Asperen[1], Thorsten Warneke[1], Simone Sabbatini[2], Giacomo Nicolini[2,3], Dario Papale[2], Justus Notholt[1], Biogeosciences, 12, 4161-4174, doi:10.5194 bg-12-4161-2015.

1) Institute of Environmental Physics, University of Bremen, Otto-Hahn-Allee 1, Bremen, 28359, Germany.
2) Department for innovation in biological agro-food and forest systems, University of Tuscia, via S. Camillo de Lellis s.n.c., 01100 Viterbo, Italy.
3) EuroMediterranean Center on Climate Changes – Impacts on Agriculture, Forest and Natural Ecosystem Division (IAFENT), 01100 Viterbo, VT, Italy.

My contributions to this publication are the design, the preparation and the set-up of the field experiment concerning the FTIR-analyzer connected to the flux gradient and the flux chamber method, the design and execution of the laboratory experiment, the data processing and analyses of the flux gradient and the flux chamber concentration and flux data, and the writing of this manuscript.

6.1 Introduction

CO_2 is the main carbon species being exchanged between biosphere and atmosphere and the most important anthropogenic greenhouse gas. CO is a less abundant non-greenhouse gas but considered important in the climate debate due to its oxidation process with atmospheric OH^- [169]. Yearly, terrestrial ecosystems exchange approximately 120 Pg of carbon with the atmosphere [169]. Arid ecosystems account for approximately 40% of land area and 20% of the soil carbon pool but are still an unknown factor in climate models [105]. In recent studies, the possible importance of abiotic degradation for arid regions, such as photo- and thermal degradation, has been recognized [4, 93, 159].

6.1.1 Ecosystem CO_2 fluxes; photo- and thermal degradation

Photodegradation is the direct breakdown of organic matter by radiation. Photodegradation is known to be an important pathway in aquatic ecosystems [201]. Recently, the possible importance of photodegradation in terrestrial ecosystems has been suggested [4, 17, 61, 159]. Photodegradation can play an important role in arid ecosystems, where microbial decomposition is restricted [4, 17, 109, 113, 176]. Rutledge (2010) estimated that in arid ecosystems 19% of the annual CO_2 flux is induced by photodegradation and, in dry summer conditions, even 92% of

daytime CO_2 emissions can be attributed to this process.

Photodegradation is attributed to UV as well as visible radiation [4, 17, 19]. The biochemical mechanisms behind photodegradation-induced carbon fluxes are not clear; it is proposed that solar radiative energy breaks down the bonds of carboxyl, directly producing CO_2 and other gas species [109]. It has been hypothesized that rates of photodegradation depend on plant and litter tissue type: lignin, one of the most recalcitrant tissue in plant material (to microbial decomposition), is expected to be most sensitive to photodegradation [3, 93]. However, while studies reporting photodegradation are multiple, recent studies, aiming to further investigate the process, were unable to observe the effects of photodegradation [95, 106, 182]. A reason for this discrepancy has not yet been found [95, 106, 175, 182]. It is important to notice that in literature, the term photodegradation is sometimes also used for the indirect effects of radiation on decomposition. One example is microbial facilitation: radiation breaks down organic compounds into smaller molecules, which are then more easily degradable for microbes. For a review on studies done on photodegradation, please see King (2012).

A less studied abiotic degradation pathway is thermal degradation, the temperature-dependent degradation of carbon in the absence of radiation and possibly oxygen [44, 109, 161]. However, photodegradation is considered the more dominant abiotic CO_2 producing process [109]. Besides CO_2, CO and CH_4 are also reported as products of photo- and thermal degradation [44, 109, 161, 174, 185].

6.1.2 Ecosystem CO fluxes; photo- and thermal degradation

The role of CO in soils and ecosystems is not well understood. Soils are known for being sources as well as sinks of CO [36]. Most likely, the main cause for soil CO uptake is the oxidation of CO to CO_2 or CH_4 by soil bacteria or soil enzymes [9, 36, 85, 168, 192, 198]. Soil CO consumption is found to be dependent on atmospheric CO concentrations and the consumption rate is usually expressed in deposition velocity: the uptake rate divided by the atmospheric CO concentration [38, 96].
Soil CO emissions have also been reported and are thought to be of non-biological origin [37, 38]. For example, soil CO emissions were found in peatlands [62] and in arid soils [38]. Living plants are also known to emit a small amount of CO [21, 94, 174]. However, senescent plant material has been shown to emit 5 to 10 times more than photosynthesising leaf material [44, 161, 174]. These fluxes, mostly determined in laboratory studies, were attributed to thermal degradation and, to a larger extent, photodegradation [44, 109, 161].

6.1.3 Measurement of photo- and thermal degradation

Studying photodegradation is difficult due to the multiple (indirect) effects radiation has on total biological decomposition. For example, UV-radiation is known to inhibit microbial processes, to change (senescent) tissue chemistry and to alter the dominating microbial and fungal communities, thereby affecting microbial decomposition rates in both directions [58, 166, 193, 201]. Differentiating photodegradation-induced fluxes from biological sources in field experiments can be achieved by the comparison of different flux measurement techniques such as eddy covariance (EC) measurements vs. flux chamber measurements and/or soil gradient measurements, in that one method does not receive solar radiation [159]. This approach requires that the areas or footprints sensed by the different techniques are fully homogeneous, which is not often the case and hard to validate. To study the effects of photodegradation (in field or laboratory), radiation filters can also be used to expose samples to different types or amounts of radiation [17, 109, 113].

Studying the role of thermal degradation-induced carbon fluxes is challenging, especially for CO_2 due to the accompanying effect temperature has on microbial decomposition. To study thermal degradation-induced CO_2 production, microbial decomposition should be absent, which can only be achieved in laboratory studies [109]. Previous field and laboratory studies on the role of direct or indirect abiotic degradation report very contrasting results [93, 95, 106, 109, 159, 182]. More specific studies are thus needed to better understand this process and its role in the carbon cycle. In this chapter, I present the results of field and laboratory measurements aimed to evaluate the role of direct photodegradation and thermal degradation in an arid ecosystem.

6.2 Materials and methods

6.2.1 Field experiment

We performed a field experiment in a grassland (IT-Ro4, harvested cropland). An FTIR-analyzer was connected to a flux gradient set-up and to two flux chamber systems. Details about the FTIR-analyzer can be found in §3.3, details about the set-up can be found in §3.5 and §4.3.3. Information about the flux gradient technique can be found in §3.4.1 and §5.2. Information about the flux chamber technique can be found in §3.4.2. General information about the field-site can be found in §4.3.

Measurement of photo and thermal degradation
When homogeneity in footprint can be assured, micrometeorological and FC methods can be compared and used to study the role of photodegradation. Flux chambers can be shielded from incoming radiation, preventing photodegradation-induced carbon production, while micrometeorological methods capture all fluxes. Comparing the two methods therefore gives an indication of the presence and the magnitude of photodegradation-induced carbon fluxes [159]. The use of this method was planned for our field experiment, but could not be applied due to lack of conformity between flux methods footprints, because of sparse photosynthetically active vegetation present in the footprint of the FG technique, causing the methods to be incomparable.

To study photodegradation, two different flux chambers, one with and one without solar radiation exposure were used. During this experiment, the flux chambers were measuring six fixed chamber locations; chambers were manually moved every few days. One flux chamber was made opaque by the use of light excluding aluminum foil (on 5 August). On the days before (28 July–5 August), all positions were compared by measuring the locations with transparent chambers. On 3–5 August, the same locations were measured (with transparent chambers) as on 5–8 August, when one of the two chambers was covered. Both locations showed very similar CO_2 and CO flux patterns. Unfortunately, on 8 August, a leak formed in the opaque chamber system, therefore direct comparison between the two treatments is limited to 3 days. Flux measurements made by the opaque chamber after 8 August are not shown. With blank measurements, the flux chambers were tested for internal CO_2 and/or CO production. No CO_2 production was found. Minor CO production was found during the day, negligible in comparison to field CO production: values presented in this paper are not corrected for this.

Studying thermal degradation-induced CO_2 production in the field is not possible due to the simultaneous temperature response of biological CO_2 production. For CO, no temperature-dependent biological CO production is expected, wherefore measurement of thermal degradation-induced CO production in the field is possible. To study the role of thermal degradation in field

CO exchange, chamber temperature sensors were installed, measuring air temperature every minute.

6.2.2 Laboratory experiment

Two different laboratory experiments were performed to study photo- and thermal degradation. Grass samples (senescent above ground grass material, mix of species as described in §4.3.2, pieces between 20–80 cm, not ground) for the laboratory experiment were taken from the field-site. Mixed soil material samples were taken from the upper 3 cm of the soil, soil samples were not sieved. Both sample types were dried at 35 °C for 72 h, to assure microbial activity to be negligible [109].

Photodegradation of senescent grass material was studied with a system consisting of a metal cylinder, inner diameter 6.5 cm, height 25 cm, area 33 cm^2, with an acrylic cap, which could be closed by screws. Transmittance of cap was measured and was 0.2 (250 nm), 6.1 (260 nm), 35.9 (270 nm), 73.9 (280 nm), 89.6 (290 nm) and approximately 94% for larger wavelengths. The cylinder was placed beneath a UV-A and UV-B source (manufacture instrument: Isitec GmbH, Bremerhaven; UV-A lamp: Philips TL 60W/10R (peak emission at 375 nm), UV-B lamp: Philips TL 40W/12RS (peak emission at 310 nm)). Radiation intensities at the sample location were quantified by use of an OceanOptics USB 2000 spectrometer with an optical fibre patch cord (P200-2-UV/VIS) and by an ILT-1700 research radiometer with accompanying optical filters and are reported as comparison to natural radiation measured with the same instruments (determined in summer in Northern Germany, midday, no clouds, pointed at sun). Instrument radiation in the UV-A wavelength band 360–400 nm was measured to be 1.6 times higher than natural radiation, with the peak emission being at 375 nm (2.9 times natural radiation). Instrument radiation in the wavelength band 200–320 nm was measured to be 2.9 times higher than natural radiation, with the peak emission being between 290 and 310 nm (7.7 times natural radiation). During the experiment, different samples (empty cylinder, 2 gram-sample and 4 gram-sample) were exposed to different types/amounts of radiation (no radiation, UV-A and/or UV-B radiation). Grass in the cylinders was positioned so that at least 80% of the surface bottom was covered with grass material. During the experiments, air was continuously circulated from the cylinder to the FTIR-analyzer and measured once per minute; emissions were derived from the measured concentration changes. Cylinder temperatures were monitored by an internal temperature probe (GTH 175/PT, Greisinger Electronics) and remained constant over the experiments (21, sd 0.15 °C). Every treatment was performed for 30 min and was duplicated.

To study thermal degradation, a glass flask (inner diameter 6.7 cm, height 6 cm) was placed in a closed loop with the FTIR. For this experiment, only glass and stainless steel materials were used. 4 grass samples of 2 grams and 4 soil samples of 30 grams were taken. The grass sample was distributed equally in the flask. The soil sample was not sieved and filled approximately 1 cm (height) of the glass flask. The samples were heated in temperature steps of 5 °C (20–65 °C) by use of a controlled temperature water bath. Temperature time steps were 20 min. During the experiments, air was circulated from the glass flask to the FTIR-analyzer and measured once per minute. After approximately 3 min, a stabilization in the CO production could be observed. Emissions were derived from the measured concentration changes. Glass flask air temperatures were manually measured to check if water bath temperature was representative for grass and soil material temperatures; after 5 min, the glass flask air temperature had reached the same temperature as the water. All experiments were performed in duplicate and in dark conditions.

In the results sections, the given regression coefficients from polynomial fits are the explained sum of squares divided by the total sum of squares.

6.3 Results

During the field campaign (3 August–11 September 2013), total precipitation was 1.5 mm and air temperatures ranged between 13 and 43 °C (see Figure 6.3). Soil water content, measured at 10 cm depth was 18% (VWC) and decreased less than 1% over the experiment.

6.3.1 CO_2 and CO flux measurements

FG measurements were performed at the same point as where the EC measurements took place (measurement height at 3.5 m). During day time, footprint analysis showed that 90% of the source area of the EC signal came from the grassland area within 150 m. Since the FG method is measuring at the same location and height, it is expected that daytime FG fluxes mainly originate from the grassland area as well. During nighttime, footprint analysis showed fluxes mainly originating from outside the grassland. FG CO_2 fluxes are shown in Figure 6.1. FG CO_2 fluxes agreed well with EC fluxes and ranged between -7 and 8 μmol m^{-2} s^{-1} (Figure 6.1).

FG CO uptake (up to 1 nmol m^{-2} s^{-1} and emission (on average 2 nmol m^{-2} s^{-1}) at night were measured (Figure 6.2). During the day, large ($\geq$ 10 nmol m^{-2} s^{-1}) CO emissions were recorded (Figure 6.2). Based on the 31 days of FG measurements, on average net 150 μmol CO m^{-2} per day was estimated to be emitted. FC CO_2 and FC CO fluxes of the transparent flux chamber can be seen in Figure 6.3, rain events and incoming solar radiation are indicated. FC CO_2 fluxes showed a diurnal pattern with small emissions at night (1 μmol m^{-2} s^{-1}) and higher emissions during the day (up to 8 μmol m^{-2} s^{-1}). Large rain events on 20 and 27 August (6.6 and 2 mm) caused a short increase in chamber CO_2 fluxes. Locations without organic surface material (indicated as bare soils in Figure 6.3) showed slightly lower CO_2 and CO fluxes.

At night, CO uptake of maximum 0.8 nmol m^{-2} s^{-1} was observed. During the day, emissions up to 3 nmol m^{-2} s^{-1} were observed. Over the course of the experiment, nightly CO uptake was continuously decreasing. The rain events caused a clear increase in nightly CO uptake, after which the decreasing continued (Figures 6.2 and 6.3). Based on 36 days of FC measurements, on average net 30 μmol CO m^{-2} per day was estimated to be emitted.

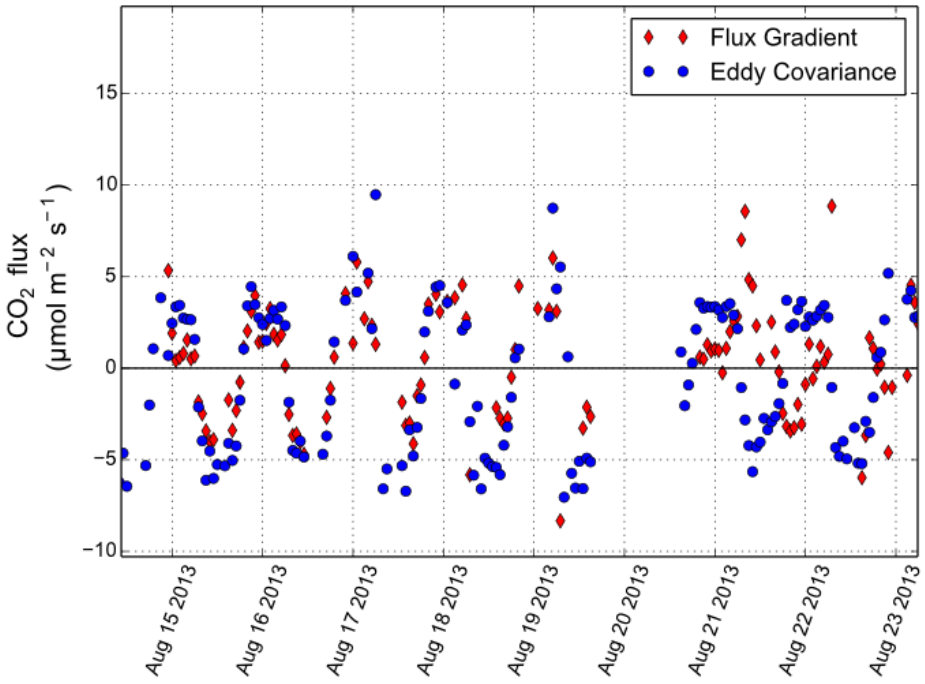

Figure 6.1: Eddy covariance and flux gradient CO_2 measurements over 8 days in August. A large rain event took place on 20 August.

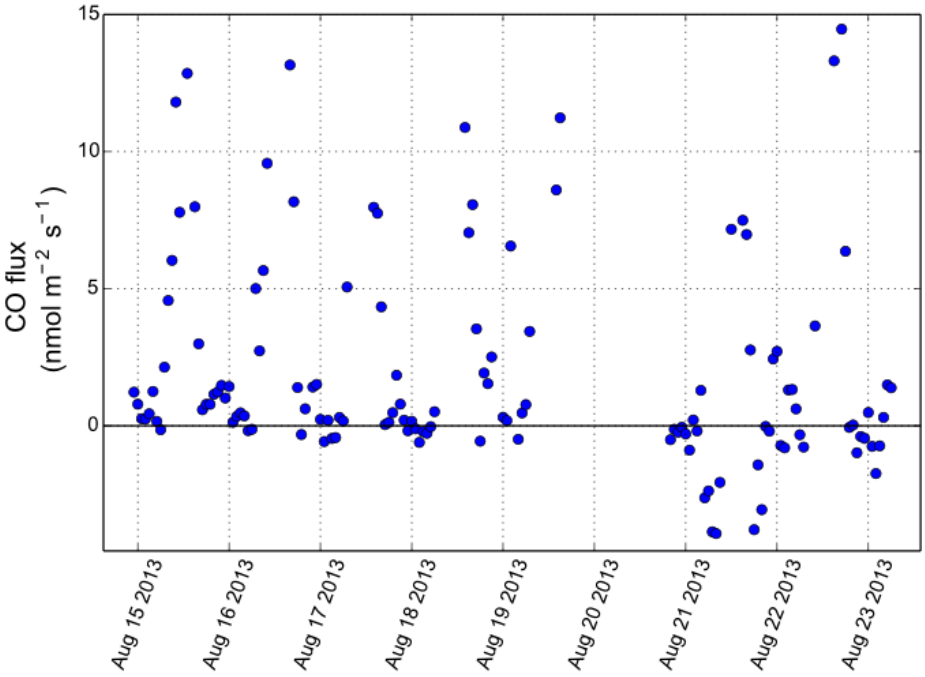

Figure 6.2: Flux gradient CO measurements over 8 days in August. A large rain event took place on 20 August.

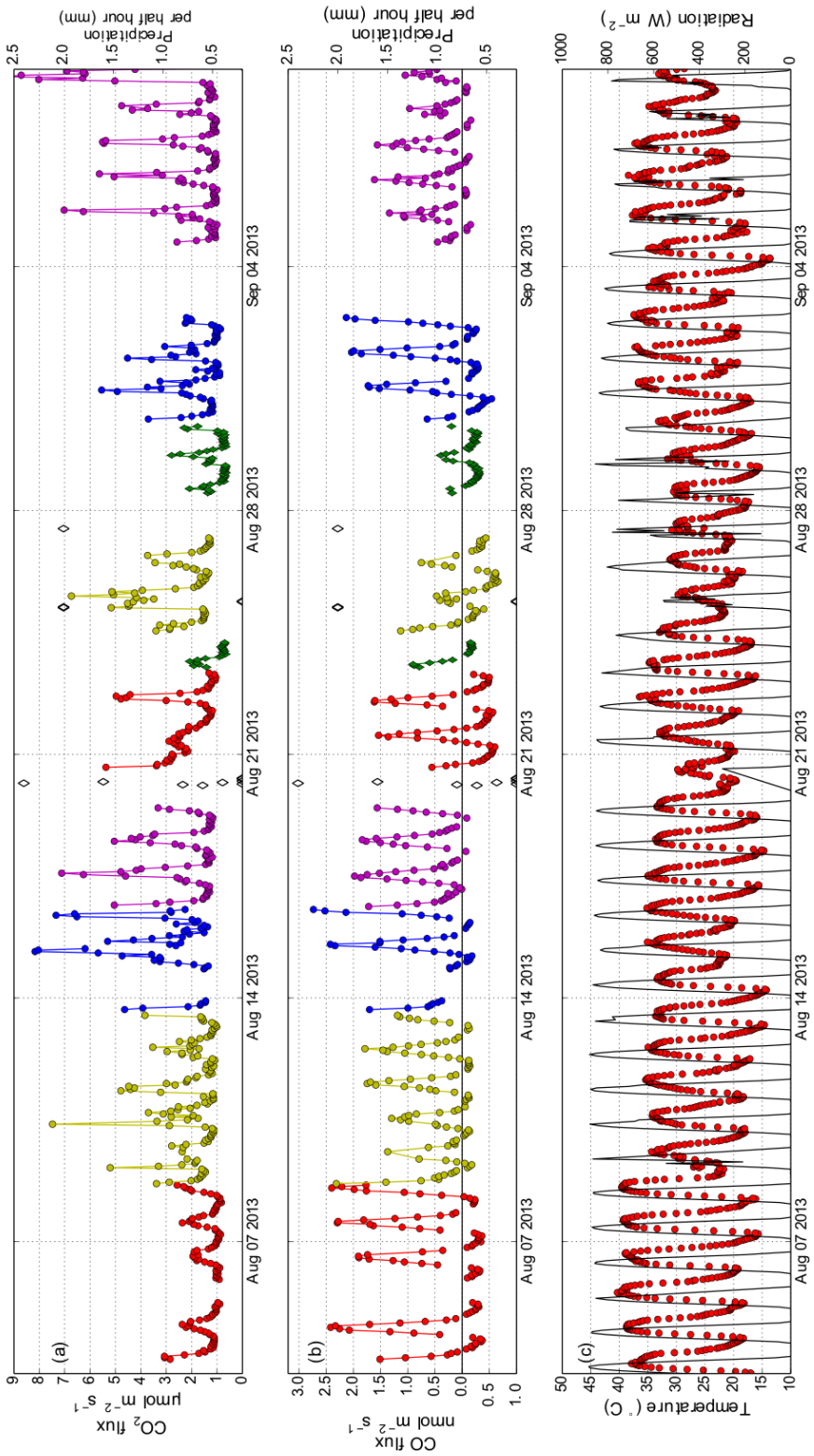

Figure 6.3: **(a, b)** Chamber CO_2 and CO fluxes (error bars with SD of flux are included but not visible due to low value) during the field experiment, different colors indicate different soil collar locations. The two bare soil locations (soils without organic surface material) are both presented with green diamonds. Rain events (open diamonds) are indicated. Presented data are from transparent flux chamber measurements; **(c)** Air temperature (°C) (red circles) and radiation (W m^{-2}) (black line).

6.3.2 Photo- and thermal degradation

Photodegradation was studied by comparing opaque and transparent chamber measurements of 3 days (5–8 August) and by analysis of transparent FC data of a period in August (period with fixed location, stable weather conditions and no precipitation). Analysis of different periods (different locations with similar conditions) showed similar patterns.

Possible photo- and/or thermal degradation-induced CH_4 fluxes are not shown or evaluated here: FG CH_4 fluxes were too small for dependency analysis and CH_4 chamber fluxes mostly showed uptake, indicating a different process than photo- or thermal degradation.

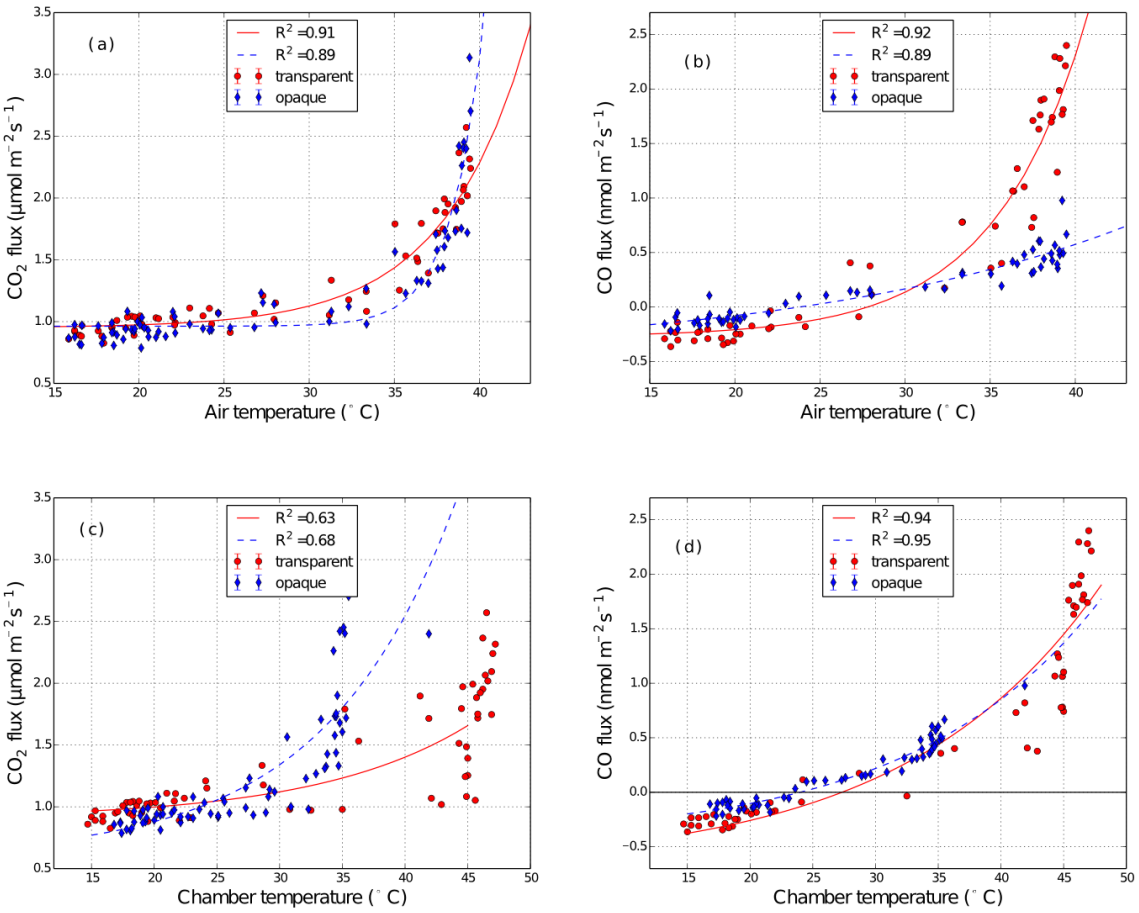

Figure 6.4: Transparent and opaque flux chamber CO_2 fluxes (left) and CO fluxes (right) vs. air temperature **(a, b)** and chamber temperature after 6 min flux chamber closure **(c, d)**. Regression coefficients of polynomial fits are given in the legends.

CO_2 fluxes

Figure 6.4 shows the CO_2 fluxes (of transparent and opaque chamber) vs. air temperatures (Figure 6.4a) and chamber temperatures (after 6 minutes flux chamber closure), Figure 6.4c). FC measurements showed very weak dependency on soil temperatures at 10 cm (data not shown). Blocking radiation showed no distinguished impact on measured CO_2 fluxes. Chamber CO_2 fluxes correlate well with air temperatures and less with chamber temperatures (Figure 6.4a & c). Chamber coverage had an effect on chamber temperatures; during daytime hours, the

opaque chamber temperature differed up to 10 °C from the transparent chamber temperature.

CO fluxes
A clear effect of chamber coverage on CO fluxes was visible; transparent chamber fluxes were higher during the day. FC CO fluxes correlate better with chamber temperatures than with air temperatures (Figure 6.4b & d). Figure 6.5 shows CO fluxes in the transparent chamber vs. air temperatures (Figure 6.5a), chamber temperatures (after 6 min flux chamber closure, Figure 6.5b) and amount of solar radiation (Figure 6.5c) for a period in August. Again, CO fluxes relate best to chamber temperatures, and less to air temperatures and amount of incoming radiation (Figure 6.5).

A temperature dependent biological CO uptake curve was fitted over chamber temperature data from (cold) night conditions (when abiotic fluxes are assumed to be minimal) and extrapolated to warmer temperatures. For biological CO uptake, a Q_{10} value from literature of 1.8 was chosen [192]. An abiotic thermal degradation Q_{10}-curve was fitted, also based on chamber temperature data, with a fitted Q_{10} value of 2.1. The sum of both processes agrees well the observed field CO fluxes ($R^2 = 0.85$, Figure 6.6).

6.3.3 Laboratory experiment

In the laboratory, exposure of senescent plant material from the fieldsite to high intensity UV-radiation did not result in increased CO_2 or CO fluxes in comparison to measurements performed in dark conditions (Figure 6.7). Grass and soil material samples exposed to different temperatures, under dark conditions, showed significant CO_2 production during lower temperatures (<40 °C) and displayed small CO_2 emissions at higher temperatures (> 55 °C) (Figure 6.8a). For CO, clear thermal production was found, exponentially increasing with higher temperatures (Figure 6.8b). A Q_{10} value of 2.14 for senescent grass material and 2.00 for soil material was found to fit best to the observed laboratory thermal degradation CO fluxes (Figure 6.8b).

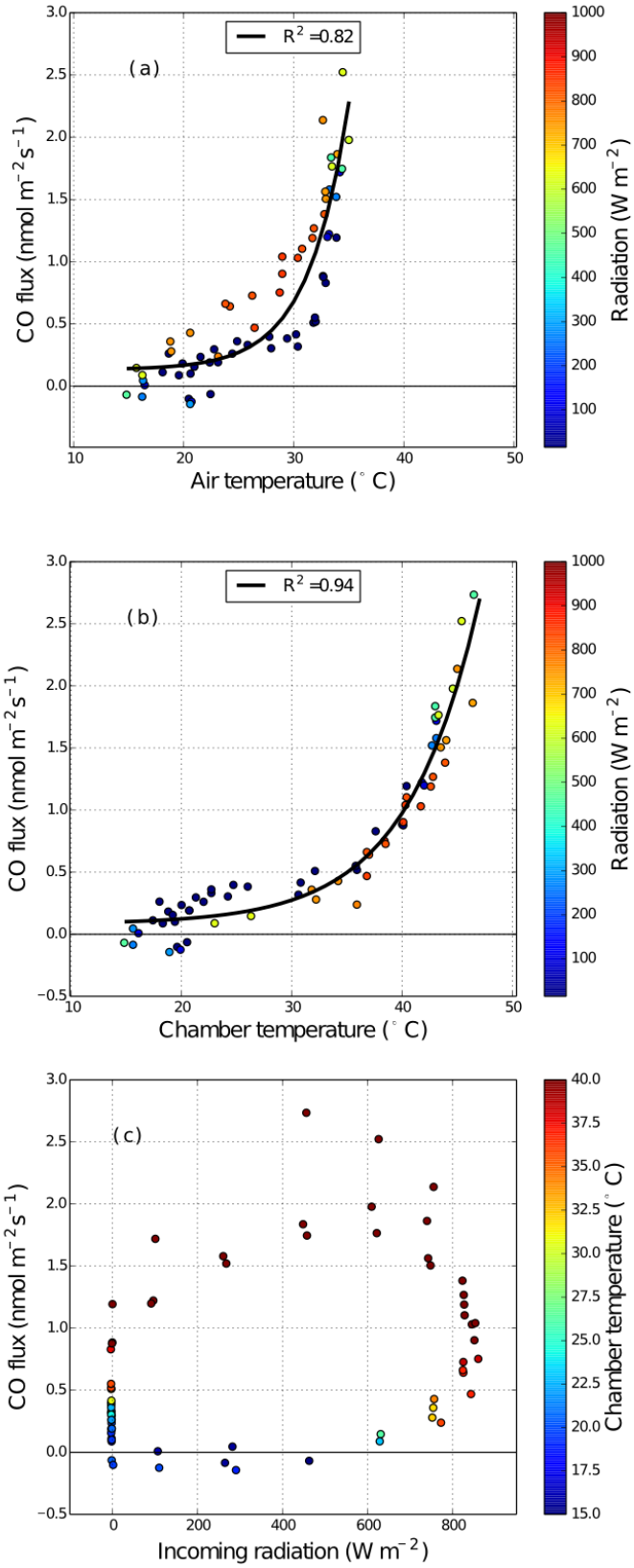

Figure 6.5: Transparent flux chamber CO fluxes for 15–19 August vs. air temperature **(a)**, chamber temperature after 6 min closure **(b)**, and solar radiation **(c)**. Regression coefficients of polynomial fits are given in the legends.

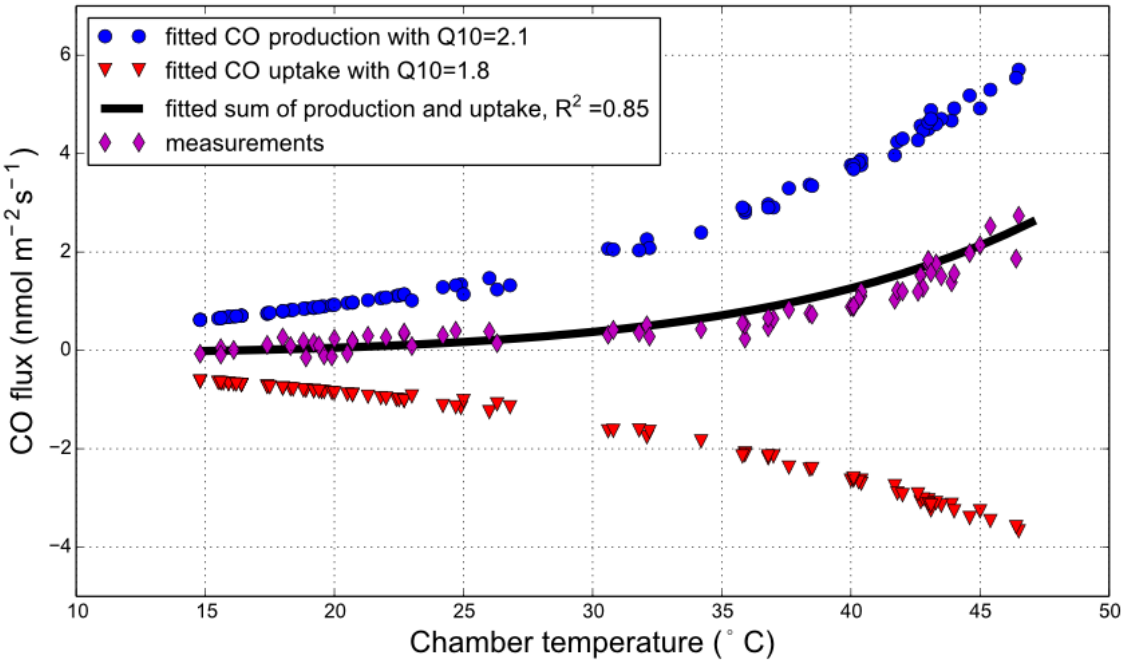

Figure 6.6: Fitted CO fluxes for 15–19 August (the black line) for the measured field CO fluxes (purple diamonds)($R^2 = 0.85$). The cumulative fitted CO flux is a sum of the fitted CO uptake (with $Q_{10} = 1.8$, based on literature [192]) and the fitted CO production (with $Q_{10} = 2.1$) based on chamber temperature (after 6 min flux chamber closure).

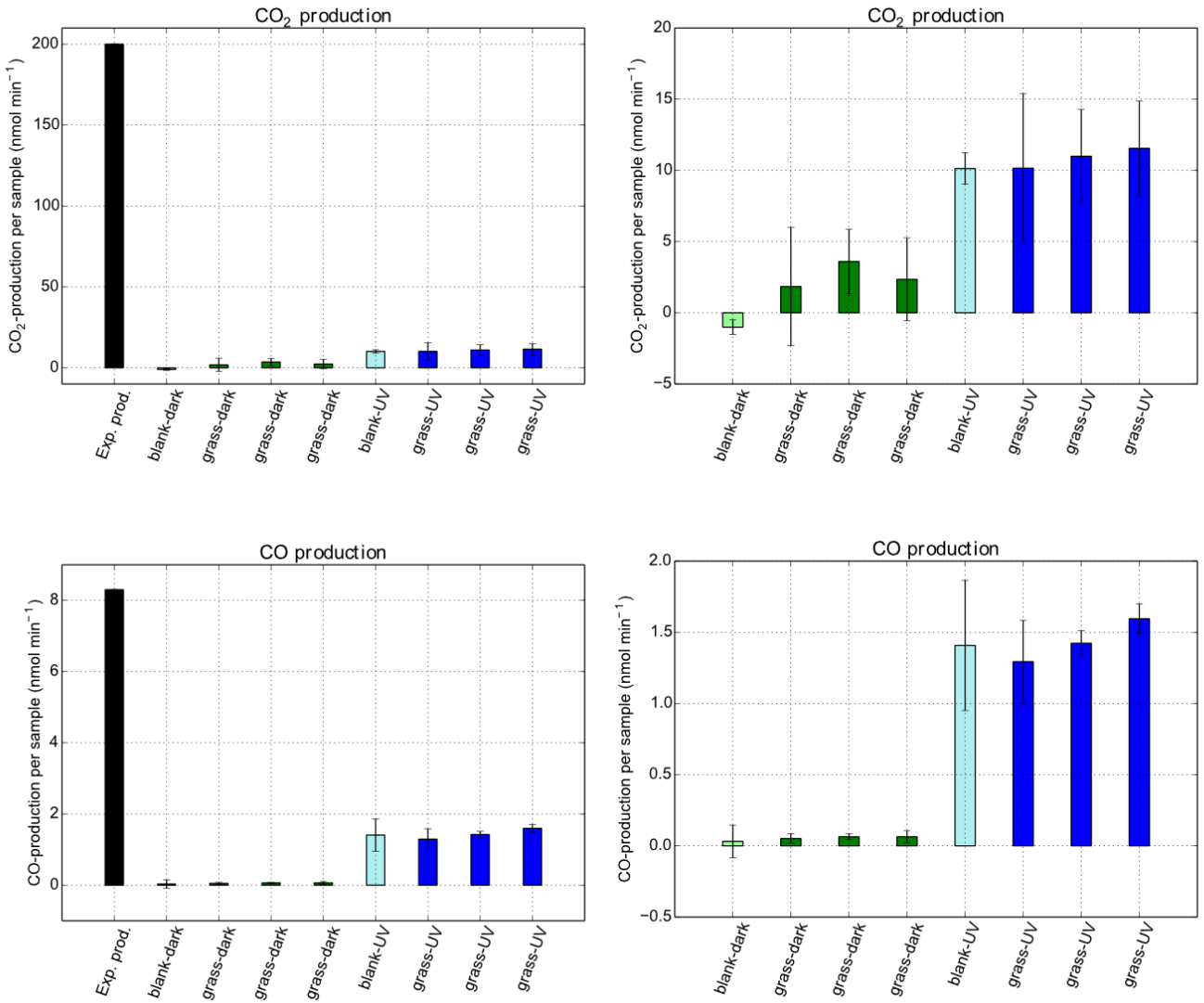

Figure 6.7: Results of the photodegradation laboratory experiment. The measurements are for 2-gram samples, placed in a 33 cm^2 cylinder. Upper figures: CO_2 production under different treatments. Exp. prod. stands for expected production based on comparison to Rutledge (2010). Right figure is zoom-in of the left figure. Lower figures: CO production under different treatments. Exp. prod. stands for expected production based on comparison to Schade (1999). Right figure is zoom-in of the left figure.

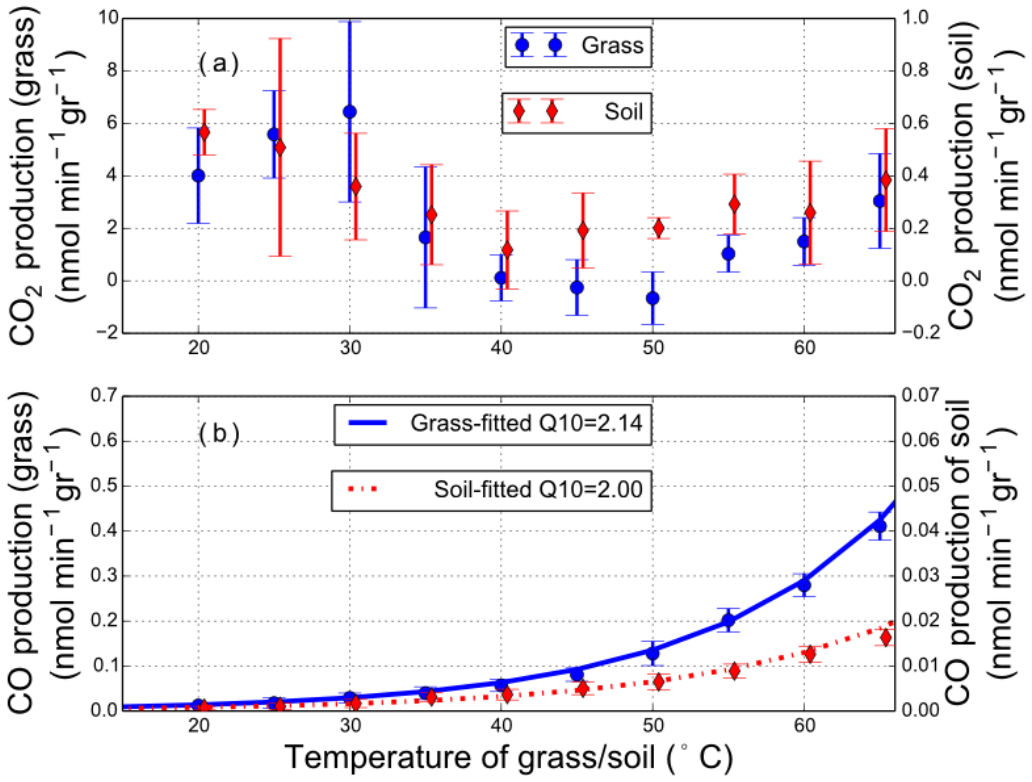

Figure 6.8: Results of the laboratory thermal degradation experiment. **(a)** Average CO_2 production of grass and soil material (nmol min^{-1} gr^{-1}) over different temperatures in the laboratory experiment. **(b)** Average CO production of grass and soil material (nmol min^{-1} gr^{-1}) over different temperatures in the laboratory experiment, with fitted Q_{10} value.

6.4 Discussion

6.4.1 CO_2 fluxes

EC and FG measurements showed that the arid grassland was not yet in a dormant state; significant CO_2 uptake was observed during the day (Figure 6.1). FC CO_2 measurements, performed on locations without photosynthetic active vegetation, solely showed positive CO_2 fluxes, with peak emissions during the day up to 8 μmol m^{-2} s^{-1}. Figure 6.4a shows that CO_2 fluxes mostly relate to air temperatures, and poorly relate to soil temperatures (not shown). Expected is that most CO_2 production takes place close to the surface where the temperature follows air temperatures closer than it follows soil temperatures at 10 cm depth. In the ecosystem, the rain events resulted in an increase in CO_2 production for several days, showing the typical water-dependent response of arid ecosystem respiration (Figures 6.1 and 6.3).

Photo- and thermal degradation
In the thermal degradation laboratory experiment, CO_2 production from senescent plant and soil material was observed during lower temperatures (20–40 °C), indicating remaining biological activity, even after drying. Above 50 °C, an increasing CO_2 production was observed with increasing temperatures, therefore expected to be (partly) of non-biological origin. Possible abiotic CO_2 production of approximately 3 nmol min^{-1} gr^{-1} for senescent grass material was observed. Extrapolating the thermal production rates of the senescent grass material to field conditions (assuming 200 gr of senescent plant material per m^2 at 55 °C), would result in a minor flux of 0.01 μmol m^{-2} s^{-1}, in comparison to observed field fluxes of > 1 μmol m^{-2} s^{-1}. Based on the observations in the laboratory, it is expected that the soil material also produces thermal degradation-induced CO_2 fluxes. However, considering the relative cold and wet conditions of the subsurface soil material in the field, compared to laboratory conditions and to surface temperatures, it is expected that soil thermal degradation fluxes are minor in comparison to soil biological fluxes.

Other studies have observed thermal degradation-induced CO_2 fluxes with higher rates (approximately 125 nmol CO_2 gr^{-1} min^{-1} for C3 grass at 55 °C), but also at lower temperatures [109]. We can not verify this observation for our field material. Based on our observations, we propose that under natural conditions, when soil surface temperatures and especially soil subsurface temperatures rarely exceed 55 °C, thermal degradation-induced CO_2 fluxes do not play an important role in comparison to biological production, even in arid regions such as our study area. We observed that chamber design can strongly influence chamber temperatures: during midday, the opaque and transparent chamber temperatures could differ up to 10 °C. As observed in the laboratory experiment, unnaturally high temperatures might lead to abiotic thermal CO_2 production. A research methodology aimed at measuring photodegradation can unintentionally result in high surface temperature levels, which could lead to unrepresentative high abiotic CO_2 production estimates.

The simultaneous use of opaque and transparent chambers was employed to study the effect of radiation on carbon fluxes in the field. Blocking radiation had no visible effect on field chamber CO_2 fluxes (Figure 6.4a and c). CO_2 flux measurements performed on bare soil locations (soils without organic surface material) seemed lower than other locations; senescent surface material seemed to contribute to total CO_2 fluxes (Figure 6.3a). However, only 3 days of bare soil measurements are available and no opaque chamber measurements on bare soil are present, therefore comparison is restricted.

The flux chambers, which were used to assess photodegradation, had a transparency of 90% or higher in the UV-B, UV-A and visible wavelength band. For our field experiment, we can therefore conclude that no large direct photodegradation fluxes (as suggested by Rutledge (2010) of 1 μmol m^{-2} s^{-1}) have been induced by natural sunlight intensities. In the laboratory experiment, fieldsite grass samples received above natural-intensity UV-radiation. In this experiment, no direct photodegradation fluxes were observed from fieldsite grass material. While the laboratory experiment presented here does not prove that there are no photodegradation fluxes at all, the results from the laboratory experiment support the conclusion from the field experiment that direct photodegradation fluxes in arid ecosystems are not as important as suggested by a previous study [159].

The experiment was conducted on a fieldsite situated in a Mediterranean climate. Based on annual precipitation and on measured respiration values, the ecosystem might seem too wet to be suitable to measure arid ecosystem processes. However, the climate is known for the precipitation free summers with high irradiation, causing the soil surface and surface materials to be fully dried out in summer. Since photodegradation is taking place at the soil surface, the ecosystem can be considered suitable for the assessment of this arid ecosystem process. The absolute amounts of possible photodegradation fluxes are not influenced by the respiration fluxes. The expected rates of photodegradation fluxes (of 1μmol m^{-2} s^{-1}, [159]) should have been detectable, even when mixed with respiratory fluxes.

Similar to what has been found by Kirschbaum et al. [95], Lambie et al. [106], Uselman et al. [182], we did not observe the effects of photodegradation in the field nor in the laboratory: no direct photodegradation-induced CO_2 fluxes have been observed. This is in contrast to other photodegradation studies, which have reported photodegradation fluxes in the field [159] or in the laboratory [109]. Potential explanations for this difference are: (a) the used field methodology in the previous study was not suitable for measuring direct abiotic degradation fluxes; (b) the role and significance of photodegradation differs per material and per fieldsite; (c) studies might (partly) have misinterpreted thermal degradation fluxes as photodegradation fluxes or (d) photodegradation fluxes were too small to be observed by the presented method. We therefore do not question the existence of the photodegradation process, but doubt its suggested large role in arid ecosystems. However, as shown, the magnitude and the potential importance of thermal degradation-induced CO_2 fluxes in arid ecosystems are still unknown.

6.4.2 CO fluxes

During the measurement period, both CO uptake and emission have been observed by the FG method (patches of green active vegetation inside the footprint) as well as by the FC method (no photosynthetic active vegetation contributing to the fluxes) (Figures 6.1, 6.2 and 6.3). CO exchange measurements from FG and FC differed largely, most likely caused by the difference in footprint. During the night, uptake of up to 1 nmol m^{-2} s^{-1} of CO was observed, which is most likely caused by microbial oxidation to CO_2 or CH_4 [9, 21, 36, 85, 168, 192, 198]. The CO uptake was decreasing over time but a rain event caused an enhanced uptake for some days (Figures 6.2 and 6.3). Soil biota being responsible for the CO uptake seems plausible since the effect of drought (decreasing uptake over time) and the effect of the rain (enhanced uptake) indicate a biological process. Nevertheless, with solely biological CO uptake taking place, one would expect higher uptake during warmer temperatures and no CO emission. It is expected that an abiotic process occurs simultaneously with the biotic uptake of CO, leading to a buffering effect on CO uptake. For this reason, CO deposition velocities could not be calculated.

Photo- and thermal degradation

We propose that the observed CO emissions in the flux chambers are caused by thermal degradation. FG measurements showed CO emissions during the day as well as during the night, indicating that CO is not (solely) produced by photodegradation (Figure 6.2). By means of opaque chamber measurements, lower CO fluxes, in comparison to transparent chamber measurements, were detected. However, as described before, FC temperatures were strongly affected by the blocking of solar radiation. Analysis of flux chamber CO fluxes showed a strong correlation with FC temperatures, and no relationship with radiation input, indicating that it was not the absence of radiation, but the indirect effect on chamber temperature that caused the lower CO emissions (Figures 6.4 and 6.5).

FC CO fluxes were ranging between -1 and 2.5 nmol m^{-2} s^{-1} and only originated from soil or surface litter, since photosynthetic active vegetation was absent. Measured CO emissions are higher than reported for CO emissions from living plants and similar to values found for senescent plant material [21, 44, 109, 161, 201]. However, the measurements are a cumulative signal of uptake and emission and can therefore not be compared directly to other studies. In the laboratory experiment, where grass from the fieldsite was exposed to above natural intensity UV-radiation, no photodegradation-induced CO fluxes were observed. However, significant thermal degradation-induced fluxes from the senescent grass and soil material were measured, even measurable at low temperatures (20 °C). At 50 °C, a thermal CO production rate of senescent grass material of 0.13 nmol min^{-1} gr^{-1} was found. Extrapolating this observation to field conditions (assuming 200 grams of senescent plant material per m^2 at 50 °C), would result in a flux of approximately 0.4 nmol m^{-2} s^{-1}, which is approximately 5 times lower than the net measured field CO fluxes. Extrapolating the thermally-induced CO production rate of the soil material to field conditions would result in an estimated production of approximately 1 nmol m^{-2} s^{-1} from the upper 3 cm of the soil during a summer day. However, while this estimate indicates that abiotic thermal soil CO production indeed might play a major role, for accurate estimates for net soil CO uptake or emission, more information about biological CO uptake and about the soil profile is needed.

The observed field chamber CO fluxes are suggested to be a cumulative signal of biological uptake and abiotic thermal degradation. Both processes were fitted over chamber temperatures. For the fitting of biological CO uptake, a Q_{10} value of 1.8 was chosen [192]. To match the cumulative measured CO fluxes (purple diamonds in Figure 6.6), a higher Q_{10} value of 2.1 for the abiotic thermal soil CO production was fitted ($R^2 = 0.85$).

The laboratory measurements were used to experimentally determine the Q_{10} value of thermal degradation-induced CO fluxes. Q_{10} values of 2.14 for senescent grass and 2.00 for soil material were measured. These values are similar to the Q_{10} value which was fitted for the thermal degradation process to match the cumulative field measurements, as described in the previous paragraph (Figure 6.6).

The soil CO uptake process, taking place below the surface, is subject to buffered chamber temperatures, and therefore the chosen Q_{10} value might be an underestimation. Also, the biological soil uptake is not expected to follow the Q_{10}-temperature response at higher temperatures (>35 °C). Nevertheless, the difference in temperature response (as a consequence of different Q_{10} values or as a consequence of buffered temperatures) causes biological CO uptake to be dominant during colder (chamber) temperatures, and thermal degradation to be dominant during warmer (chamber) temperatures. During our field experiment, thermal degradation started to be domi-

nant from approximately 25 °C (chamber temperature) and followed an exponential curve with higher temperatures (Figure 6.6).

The temperatures inside the chamber were higher than the temperatures outside the chamber. Although this will result in higher fluxes inside the chamber compared to the ecosystem around it, the correlation between temperatures inside the chamber and the CO flux should be representative for the ecosystem. The laboratory study shows a similar relationship between temperature and CO flux. According to our results, the temperatures outside the chamber are high enough to induce significant thermal degradation fluxes. This is supported by the measured CO fluxes by the FG technique. FG CO emissions were higher, likely due to its footprint which contained relatively more dead vegetation (thermal degradation material) since, for practical reasons, the chambers were placed over lower dead vegetation. Also, the FG footprint contained active vegetation, which is another possible CO emitting source [21].

Overall, the measurements show that the fieldsite is a net source of CO during the summer months, affecting the atmospheric chemistry, at least at plant level, via OH^- depletion. More field measurements on annual CO exchange are needed to better understand the role of thermal degradation in CO and CO_2 exchange in arid regions.

6.5 Conclusion

In our field and laboratory experiment, direct photodegradation-induced CO_2 and CO fluxes have not been observed. Based on laboratory experiments, the production of thermal degradation-induced CO_2 is expected, but only significant under unnaturally high temperatures. In the laboratory, thermal degradation-induced CO fluxes were clearly observed, also at relatively low temperatures (20 °C). In the field, biological CO uptake as well as abiotic CO production was observed; abiotic CO production is assumed to be mainly a product of thermal degradation. The Q_{10} value of the CO producing thermal degradation process, as determined in the laboratory, agrees well with the fitted Q_{10} value for abiotic CO fluxes measured at the fieldsite.

Not all litter types are reported to be sensitive to photodegradation, which could explain why we did not measure photodegradation-induced fluxes. Also, we realize that in field conditions, partitioning photodegradation from thermal degradation or biological processes is challenging and minor photodegradation fluxes might not be detectable. We therefore do not exclude the existence of photodegradation. However, in our field experiment in an arid ecosystem, we were not able to observe any direct photodegradation-induced carbon fluxes, showing that direct photodegradation does not play a major role in this arid ecosystem. Previous studies suggesting the occurrence of major photodegradation fluxes might possibly have neglected thermal degradation fluxes, which is an indirect effect of radiation. The potential importance of abiotic decomposition in the form of thermal degradation, especially for arid regions, should be considered and be studied in more detail.

7 Diurnal variation in respiratory $\delta^{13}CO_2$ fluxes in an arid ecosystem

Parts of this chapter are modified from the following manuscript:

'Diurnal variation in respiratory $\delta^{13}CO_2$ flux in an arid ecosystem', Hella van Asperen[1], Thorsten Warneke[1], Simone Sabbatini[2], Martin Höpker[3], Giacomo Nicolini[2,4], Tommaso Chiti[2], Dario Papale[2], Michael Böhm[3], Justus Notholt[1], submitted to Agricultural and Forest Meteorology August, 2015.

1) Institute of Environmental Physics, University of Bremen, Otto-Hahn-Allee 1, Bremen, 28359, Germany.
2) Department for innovation in biological agro-food and forest systems, University of Tuscia, via S. Camillo de Lellis s.n.c., 01100 Viterbo, Italy.
3) Center for Industrial Mathematics, University of Bremen, Bibliothekstrasse 1, 28359, Bremen, Germany.
4) EuroMediterranean Center on Climate Changes – Impacts on Agriculture, Forest and Natural Ecosystem Division (IAFENT), 01100 Viterbo, VT, Italy.

My contributions to this publication are the design, the preparation and the set-up of the field experiment concerning the FTIR-analyzer connected to the flux gradient and the flux chamber method, the data processing and analyses of the flux gradient and the flux chamber concentration and flux data, and the writing of the manuscript. The design and the creation of the model, which is described in §7.2.3, was done by the group 'Center for Industrial Mathematics' from the University of Bremen.

7.1 Introduction

Soil respiratory CO_2 fluxes are one of the largest terrestrial carbon fluxes within ecosystems. However, the carbon dynamics in arid ecosystems, such as the Mediterranean, are still poorly understood and soil respiration measurements in these areas are few [34, 162]. Continuous monitoring of CO_2 exchange between soil and ecosystem is valuable for improving our understanding of soil respiration processes. Soil CO_2 fluxes are mostly a product of autotrophic respiration, CO_2 produced during plant metabolism, and heterotrophic respiration, decomposition of soil organic matter (SOM) by microorganisms. Autotrophic and heterotrophic respiration are dependent on different factors and are therefore responding differently to environmental changes [13, 188]. The measurement of the isotopic composition of CO_2 is often used to distinguish autotrophic and heterotrophic respiration fluxes and can serve as a tool to study ecological and biogeochemical processes inside an ecosystem [89].

The isotopic composition of CO_2 is usually defined by its δ value, which is defined as:

$$\delta^{13}CO_2(‰) = (\frac{R_{sample}}{R_{VPDB}} - 1) * 1000, \tag{7.1}$$

wherein $\delta^{13}CO_2$ is the standardized isotopic ratio of the sample (in ‰), R_{sample} is the molar ratio of $^{13}CO_2/^{12}CO_2$ in the sample, and R_{VPDB} is a standard ratio of $^{13}C/^{12}C$ in the Vienna Pee Dee Belemnite laboratory standard (0.0112372).

In terrestrial ecosystems, the atmospheric $\delta^{13}CO_2$ value varies largely due to photosynthetic fractionation: during photosynthesis, plants prefer the uptake of the lighter isotope $^{12}CO_2$, thereby enriching the atmosphere in $^{13}CO_2$ and depleting the ecosystem carbon [55]. Determination of the $\delta^{13}CO_2$ value of respired CO_2 ($\delta^{13}CO_{2resp}$) can be done by use of Keeling plots [15, 90]. The determined $\delta^{13}CO_{2resp}$ value is an integrated signal of different (respiratory) processes; different parts of an ecosystem fractionate and respire CO_2 with a different $\delta^{13}CO_2$ value. By determining the CO_2 fluxes and the $\delta^{13}CO_2$ value of ecosystem respiration in temporal and spatial scale, it is possible to analyze the composition of respiratory sources of an ecosystem. Some studies have observed that CO_2 fluxes originating from non-biological sources, namely the out gassing of CO_2 with a geological origin, can also influence the ecosystem's $\delta^{13}CO_2$ values [52, 152].

In-situ continuous and simultaneous observations of CO_2 concentrations, $\delta^{13}CO_2$ values and $\delta^{13}CO_{2resp}$ values are still sparse and new isotope sampling approaches can be fruitful [15]. In this chapter, I present a system, using the FTIR-analyzer, in which CO_2 concentration, CO_2 flux, and their isotopic components are continuously monitored by use of flux chamber measurements and tower concentration measurements. The aim of this study is to assess the variation in atmospheric and respiratory $\delta^{13}CO_2$ values in an arid ecosystem, and to evaluate and propose hypotheses for the observed diurnal respiratory $\delta^{13}CO_2$ flux variation.

7.2 Materials and methods

A field experiment was performed in the grassland Rocca4 (IT-Ro4, harvested cropland, §4.3). The FTIR-analyzer was set up for tower concentration measurements and for flux chamber measurements. Details about the FTIR-analyzer can be found in §3.3, details about the set-up can be found in §3.5 and §4.3. For the measurement of the isotopic components of CO_2, a calibration routine using two standard gas cylinder was performed weekly (Calibration gas 1 ; CO_2=566.9 ppm ±0.13 ppm, $\delta^{13}CO_2$=-11.49‰ ±0.24‰, Calibration gas 2; CO_2=505.0 ppm ±0.03 ppm, $\delta^{13}CO_2$=-5.83‰ ±0.24‰).

7.2.1 The use of Keeling plots to determine respiratory $\delta^{13}CO_2$ flux values

A Keeling plot functions as a 2-component mixing system and can be used to determine the $\delta^{13}CO_2$ value of added CO_2 in a reservoir, which already contains CO_2. For example, a Keeling plot can be created when CO_2 concentrations and its isotopic components in the atmosphere (the reservoir) are both subject to change due to respiratory fluxes (added CO_2).

A Keeling plot is created by plotting the inverse of the CO_2 concentration against its $\delta^{13}CO_2$ value. The intercept of this plot indicates the $\delta^{13}CO_2$ value of the added CO_2 by respiration: $\delta^{13}CO_{2resp}$ [90]. The use of Keeling plots to determine the respiratory $\delta^{13}CO_2$ value has been studied and evaluated [137]. Pataki (2003) showed the sensitivity of the intercept estimate for the Keeling plot method (Model I regression) to small CO_2 concentration ranges [121, 137] and

estimated a minimum required CO_2 concentration range of 75 ppm. However, when using the chamber technique, larger CO_2 ranges can result in a significant soil CO_2 gradient disturbance [88]. Pataki (2003) showed that the use of geometric mean regression in Keeling plots (Model II regression, [121, 137]), in which the CO_2 concentration and the $\delta^{13}CO_2$ value are both considered as independent variables, can result in up to 3‰ differences in intercept estimates under small CO_2 concentration ranges, in comparison to Model I regression estimates. Keeling plots need a stable background for accurate Keeling plot-intercept estimates. Miller and Tan [121] proposed an alternative to Keeling plots, which does not have this requirement; by plotting the product of the $\delta^{13}CO_2$ value and the CO_2 concentration against the CO_2 concentration, the slope of the regression line serves as a $\delta^{13}CO_{2resp}$ estimate [121].

During data analyses, all three described methods were used to determine the Keeling plot intercept and all methods showed similar $\delta^{13}CO_{2resp}$ values and similar diurnal $\delta^{13}CO_{2resp}$ patterns. Presented data are from Model I regressions [90, 121]. Respiratory values shown in this paper are based on linear regression with a regression coefficient higher than 0.9 and are based on total-night concentrations (20-5 h) measured at the tower at two heights, or increasing chamber concentrations (during chamber closure), measured hourly in the flux chambers.

Keeling plots were also applied on laboratory measurements, which were performed with the FTIR-analyzer, to determine the $\delta^{13}CO_2$ value of organic material. Preliminary results of this experiment are shown in the Appendix (§10.2.4).

7.2.2 Geological emission sampling

The study site is located in a seismic active region with presence of geothermal activity, with multiple extinct volcanoes and thermal wells in the surrounding [6, 147]. To test whether CO_2 fluxes with a geological origin are present at the fieldsite, the isotopic $\delta^{13}CO_2$ value of possible geological fluxes was determined. Air samples from three thermal wells close by the fieldsite were taken by the following method. A large flowerpot ($\pm$ 1 m^3) was placed reversely on top of the bubbling mud and left here for 30 min. Afterwards, 2 separate gas samples (per location) were taken from the flowerpot headspace and stored in gas sampling bags. Gas samples were analyzed by the FTIR-analyzer within 1 week after sampling. Gas samples were introduced into the FTIR-analyzer's measurement cell and stepwise diluted with N_2, to obtain concentration measurements close to the available calibration standards. Location of thermal wells can be found in Table 7.1.

7.2.3 Isotopic diffusion and fractionation model

The production, transport and release into the atmosphere of $^{12}CO_2$ and $^{13}CO_2$ in a soil layer of 0.5 m depth and of a porosity σ of 0.4 was modeled; porosity was measured in the field and layer depth was estimated by average rooting depth (30-50 cm) and the decrease in soil carbon after 50 cm. Soil water content was considered to be constant, based on field observations: volumetric water content measured at 10 cm depth was 18% and decreased less than 1% over the experiment. No precipitation fell 3 weeks prior to the experiment and neither during the first 3 weeks of the experiment. During this time, the diurnal $\delta^{13}CO_{2resp}$ variation as shown in Figure 7.3 was also observed.

For symmetry reasons a 1-dimensional setting is considered, where the units seconds (s) for time and meters (m) for length were chosen. The soil layer under consideration is modeled by the

interval $\Omega{:=}(0;\ 0.5) \subset \mathbb{R}$, where the boundary points z=0 and z=0.5 represent the surface and the bottom, respectively. The main transport in the soil is assumed to be driven by diffusion. No diffusion is assumed to happen across the bottom at z=0.5. At the surface (z=0) an exchange law is assumed, based on the measured external daytime (9-21 h) CO_2 concentration of 786 mg m^{-1} ($\sim$ 400 ppm) with an atmospheric $\delta^{13}CO_2$ value of -9.5‰, and the measured external varying nighttime CO_2 concentration (sinusoidal variation with peak at 3:30 h of 884 mg m^{-1} with an atmospheric $\delta^{13}CO_2$ value of -11‰ ($\sim$ 450 ppm)). The production of CO_2 in the soil (with a $\delta^{13}CO_2$ value of 26‰) is assumed to depend on soil temperature, which is dependent on soil depth.

Temperature
It is assumed that the temperature in the soil is varying in depth z and time t, and is given by the following relation [26, 126]:

$$T(z,t) = T_{ave} + A_0 \exp\left(\frac{-z}{d}\right) \sin\left(w\left(\frac{t}{3600s} - 6\right) - \frac{z}{d}\right).$$

wherein T_{ave} is the average surface temperature, A_o is the half of the peak-to-peak diurnal variability of surface temperature, d is a damping depth and w is p/12 and sets the period to 24 h. The temperature parameters were chosen by fitting the measured soil temperature data at 10, 20 and 30 cm from August 2013. The parameters are T_{ave}=29 °C, A_0=6.2 °C, d=0.14 m, and $\omega = \frac{\pi}{12}$.

Production
We assume the following relation for the temperature dependent production of CO_2 [200]:

$$\mathrm{Prod}(T) = \mathrm{Prod}_0(\mathrm{z}) \cdot Q_{10}^{(\frac{T-T_0}{10°C})}.$$

Here, a Q_{10} based on literature values was chosen [202] and $Prod_0$ was fitted to measured soil temperature values and accompanying field CO_2 fluxes, with T_0=27 °C and Q_{10}=2.5. The unit of both Prod(T) and $Prod_0$(z) is mg m^{-1} s^{-1}.

We considered three different production scenarios, characterized by different distribution of CO_2 production with depth. For simplicity, it is assumed that different production rates occur in different (vertical) layers of the soil profile, and that within each layer the production is constant with depth.

1. Only one layer of soil over the whole considered depth of 0.5 m.
2. Two layers of soil, 80% of CO_2 production in the first 10 cm and 20% of production in the last 40 cm of soil.
3. Two layers of soil, 50% of CO_2 production in the first 10 cm and 50% of production in the last 40 cm of soil.

From the field measurements, an average release of 0.13 mg CO_2 m^{-1} s^{-1} (11232 mg CO_2 m^{-2} per day) of soil surface is known ($\sim$ 3.0 μmol m^{-2} s^{-1}). The function $Prod_0$(z) is chosen accordingly, such that the cumulative (integrated) production over the whole depth of 0.5 m over the cycle of one day is (approximately) equal to the measured fieldsite release at the surface.

This yields the functions

1. $\mathrm{Prod}_0(z) = 0.22$ mg $m^{-1}s^{-1}$

2. $\text{Prod}_0(z) = \begin{cases} 0.846 \text{ mg m}^{-1}\text{s}^{-1} & \text{for 0 m} \leq \text{z} \leq \text{0.1 m} \\ 0.054 \text{ mg m}^{-1}\text{s}^{-1} & \text{for 0.1 m} < \text{z} \leq \text{0.5 m} \end{cases}$

3. $\text{Prod}_0(z) = \begin{cases} 0.528 \text{ mg m}^{-1}\text{s}^{-1} & \text{for 0 m} \leq \text{z} \leq \text{0.1 m} \\ 0.132 \text{ mgm}^{-1}\text{s}^{-1} & \text{for 0.1 m} < z \leq \text{0.5 m} \end{cases}$

The production Prod(T) of CO_2 is split into the respective production terms f_1 (for $^{12}CO_2$) and f_2 (for $^{13}CO_2$) with the unit mg m^{-1} s^{-1}.

System of diffusion equations
D_1 and D_2 denote the effective diffusion coefficients in the soil of $^{12}CO_2$ and $^{13}CO_2$, respectively. Due to ploughing, soil variables such as porosity and bulk density are relatively constant over depth, and diffusion coefficients are assumed to be independent of depth. A diffusion coefficient was calculated by use of available soil data and D_2 was set to $2.5 \cdot 10^{-6}$ m^2 s^{-1} [173]. It is assumed that the ratio $\frac{D_1}{D_2}$ is 1.0044 [27], so that this leads to a D_1 of $2.511 \cdot 10^{-6}$ m^2 s^{-1}. During the modelling process, different diffusivity parameterizations have been tried based on other literature, but this did not result in different outcomes. The diffusion of $^{12}CO_2$ and $^{13}CO_2$ is each modeled by a diffusion equation, where the respective mass concentrations are denoted by c_1 and c_2 (mg m^{-1}).

The complete system of diffusion equations, assuming Fickian diffusion, is given by

$$\begin{aligned} p\frac{\partial c_k}{\partial t} - D_k \Delta c_k &= f_k && \text{in } \Omega, \\ D_k \nabla c_k &= 0 && \text{on } z = 0.5, \\ -D_k \nabla c_k &= \kappa(c_k - c_{ext,k}) && \text{on } z = 0, \\ c_k(0) &= c_{k0} && \text{in } \Omega \end{aligned}$$

for $k \in \{1, 2\}$, where $c_{ext,k}$ is the mass concentration of c_k in the atmosphere above the surface, c_{k0} is the initial value and the coefficient κ determines the magnitude of the CO_2 exchange between soil and air.

The initial conditions c_{k0} of the system can basically be chosen arbitrarily, as a long term simulation is conducted until an equilibrium is reached. The real value of κ is not known. However, the simulation of the $\delta^{13}CO_2$ value of the surface flux proved to be very stable with respect to κ, meaning that the outcome of the simulation is essentially independent of the numerical value of κ. For the simulations, $\kappa = 1$ m s^{-1} is chosen.

7.3 Results

During the field campaign (3 August- 11 September 2013), total precipitation was 15 mm and air temperatures ranged between 13 and 43 °C. Soil water content, measured at 10 cm depth was 18% (VWC) and decreased less than 1% over the experiment.

7.3.1 Atmospheric CO_2 concentrations and $\delta^{13}CO_2$ values

Half hourly-averaged atmospheric CO_2 concentrations, measured at 1.3 m and 4.2 m, varied between 390 and 540 ppm (Figure 7.1). During the day, the lower inlet showed lower CO_2 concentrations than the higher inlet (average difference between inlets: 0.25 ppm), indicating dominating photosynthesis. During the night, respiration dominated and higher CO_2 concentrations were measured at the lower inlet (average maximum difference between inlets: 8 ppm at 4

am). During the night, the formation of a nocturnal boundary layer caused a buildup of CO_2, resulting in an increase of 70 ppm or more in the majority of the nights. The concentrations in the chamber were higher and ranged between 390 and 560 ppm (Figure 7.1).

Half hourly-averaged daytime atmospheric $\delta^{13}CO_2$ values at the tower ranged between -7.7 and -7.0‰; the lower inlet showed more negative atmospheric $\delta^{13}CO_2$ values than the higher inlet (Figure 7.1). Daytime atmospheric $\delta^{13}CO_2$ values in the flux chambers ranged between -10 and -9‰. During the formation of a nocturnal boundary layer, values at the tower dropped to -12‰, and in the flux chambers (before chamber closure) down to -14‰. For the atmospheric concentration measurements at the tower, daily Keeling plots could be created. The average intercept value over the measurement period was -23.35‰ (low inlet) and -23.42‰ (high inlet).

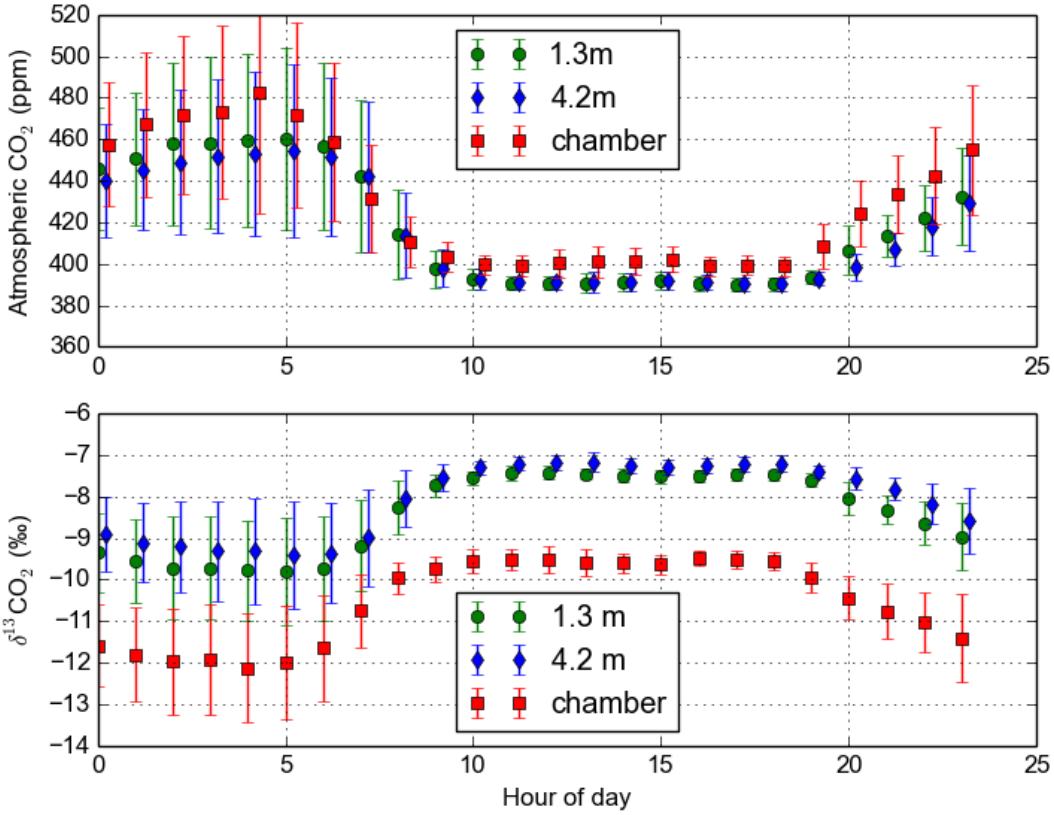

Figure 7.1: Diurnally averaged atmospheric CO_2 concentrations and $\delta^{13}CO_2$ values. Upper figure: the diurnally averaged atmospheric CO_2 concentration as measured at the tower (green circles and blue diamonds) and in the flux chamber (red squares, before flux chamber closure, averaged over different locations). Lower figure: the diurnally averaged atmospheric $\delta^{13}CO_2$ value at the tower (green circles and blue diamonds) and in the flux chamber (red squares before flux chamber closure, averaged over different locations).

7.3.2 CO_2 fluxes and respiratory $\delta^{13}CO_2$ flux values

Chamber CO_2 fluxes from soil and senescent grass material ranged between 0.5 and 10 μmol m^{-2} s^{-1}, with higher flux values during the day (Figure 7.2). CO_2 fluxes, measured by the EC set-up (not shown), showed CO_2 uptake during the day (average maximum of 5 μmol m^{-2} s^{-1}) and emission during the night (average maximum of 4 μmol m^{-2} s^{-1}). During day time, footprint analysis showed that 90% of the source area of the EC signal came from within 150 m, from within the grassland area. Footprint analysis showed that during daytime 90% of flux contributions are within 150 m from the tower while during night-time, flux contributions originate also from outside the grassland boundaries.

For every night, one Keeling plot intercept was calculated per air inlet (1.3 and 4.2 m). For flux chamber measurements, every hour one Keeling plot intercept could be determined. Figure 7.2 shows the Keeling plot intercepts from the tower and the flux chamber for a period in September. The flux chamber measurements showed a diurnal pattern in respiratory $\delta^{13}CO_2$ flux values; daytime values are on average 3.5‰ less depleted than nighttime values. The occurrence and degree of depletion was found to be independent of chamber location. Figure 7.3 shows the average diurnal CO_2 chamber fluxes and the accompanying $\delta^{13}CO_2$ flux values.

7.3.3 Isotopic measurements of geological sources

Gas samples were taken at geothermal-active sites around Viterbo. CO_2 concentrations in sampled air was estimated to be 60%. Analyses of gas samples (2 sample per location, analyzed twice) gave the following results (Table 7.1).

Table 7.1: Isotopic gas measurements of the gas samples taken at the geothermal-active sites around the fieldsite.

Sample	**Number of samples**	**Isotopic signal** (‰)	**Location**
Thermal location 1	2	-1.75 ± 0.02	42 °25.224, E 12 °4.480
Thermal location 2	2	3.87 ± 0.15	42 °25.265, E 12 °3.912
Thermal location 3	2	3.18 ± 0.13	42 °27.555, E 12 °3.949

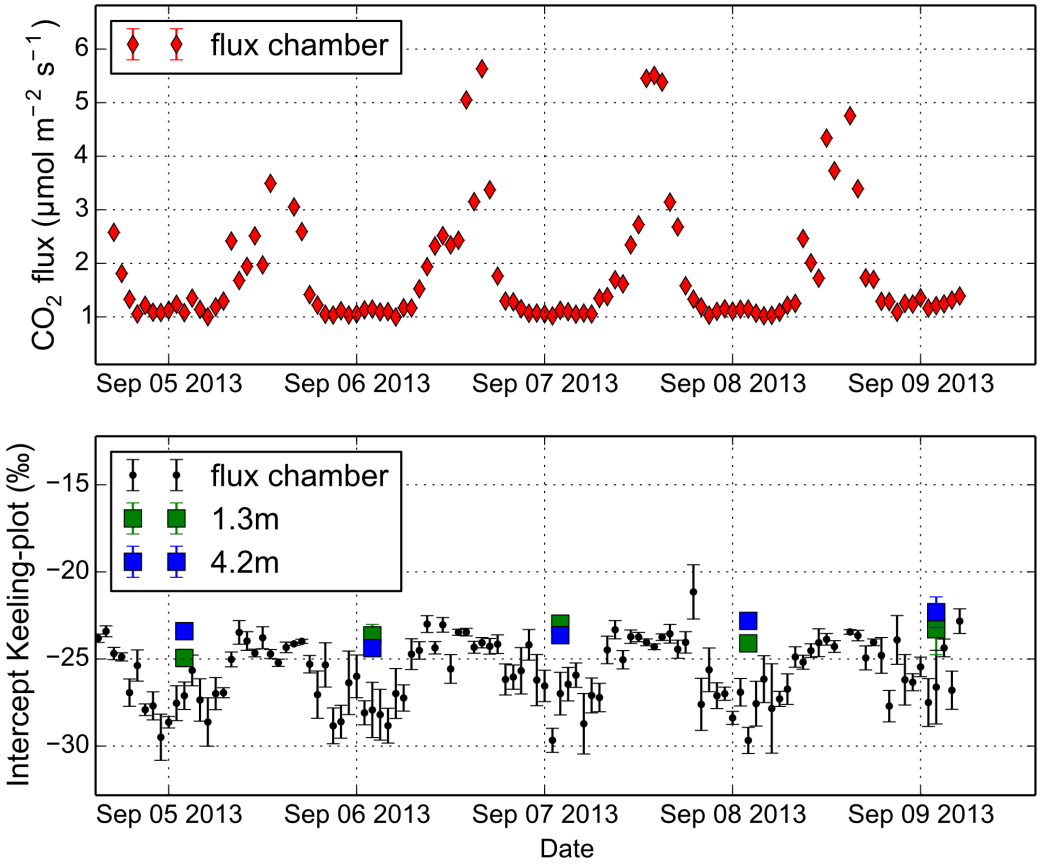

Figure 7.2: Flux chamber CO_2 fluxes and respiratory $\delta^{13}CO_2$ values. Upper figure: CO_2 fluxes as measured by the flux chamber technique, the vertical grid lines are at 24:00. Lower figure: the respiratory $\delta^{13}CO_2$ flux values for the flux chamber measurements and the tower concentration measurements, the vertical grid lines are at 24:00.

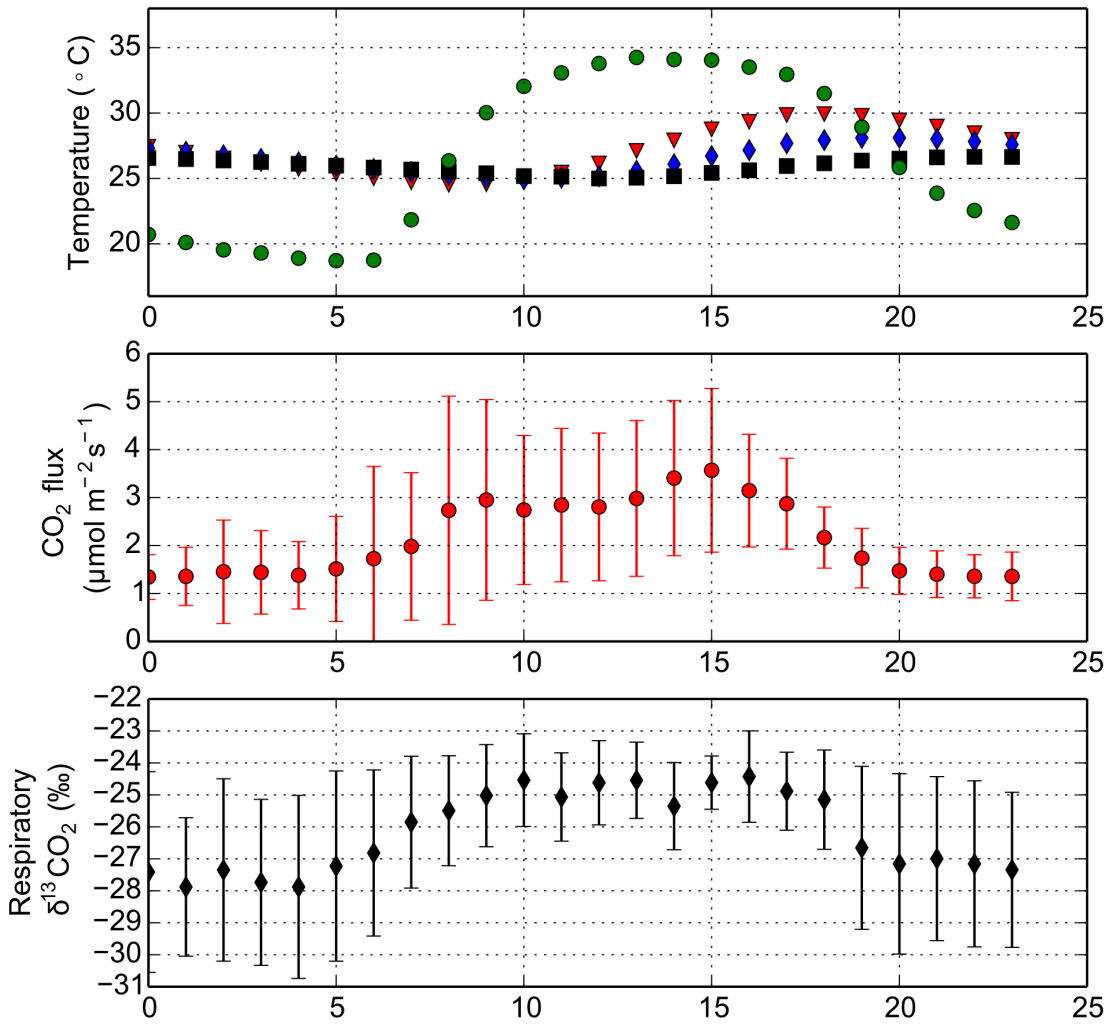

Figure 7.3: Diurnal temperature, CO_2 flux, and respiratory $\delta^{13}CO_2$ flux patterns. Upper figure: average temperature variation during the field experiment: air temperature (green circles) and soil temperature at 10 cm depth (red triangle), 20 cm depth (blue diamonds) and 30 cm depth (black squares); middle figure: diurnal variation of the flux chamber CO_2 fluxes; lower figure: diurnal variation in the flux chamber respiratory $\delta^{13}CO_2$ flux values.

7.4 Discussion

The flux chambers were placed on soil locations without active vegetation (only senescent grass material), wherefore no photosynthetic fluxes and no or minimal soil autotrophic fluxes are expected. Respiration fluxes up to 8 μmol m^{-2} s^{-1} were observed. EC measurements, performed at the tower at 3.5 m height, had a larger footprint and showed ecosystem CO_2 uptake during the day, indicating remaining photosynthetic activity outside the flux chambers.

Large variations in atmospheric and respiratory $\delta^{13}CO_2$ values were observed. Less depleted $\delta^{13}CO_2$ values and lower CO_2 concentrations were measured at the tower in comparison to inside the flux chambers (Figure 7.1). During daytime, the difference between CO_2 concentrations can partly be explained by the absence of photosynthesis in the flux chambers. Also, a not complete mixing of the chamber air with the outside air is expected wherefore respiratory CO_2 is more dominant inside the flux chambers. Keeling plot intercepts determined by the nighttime-tower concentration measurements, in comparison to nighttime chamber measurements, showed less depleted intercept values. Different sources in the ecosystem respire with different $\delta^{13}CO_2$ values and it was found that the tower inlets capture less depleted ecosystem sources than the chamber system. Based on our measurements, soil respiration is more depleted than the total ecosystem respiration.

By chamber measurements, hourly Keeling plots intercept values were obtained and a diurnal variation in $\delta^{13}CO_{2resp}$ values was observed. In the following paragraphs, causes for ecosystem isotopic variation are reviewed and different hypotheses for the observed diurnal respiratory $\delta^{13}CO_2$ flux variation are discussed.

7.4.1 Variation in $\delta^{13}CO_2$ values in ecosystems

Atmosphere has, on average, a $\delta^{13}CO_2$ value of -8.3‰ [1]. Plants fractionate when taking up atmospheric CO_2. C3 plants fractionate stronger to values between -30‰ and -22‰ while C4 plants fractionate to values between -15‰ and -10‰ [55]. Variation in the $\delta^{13}C$ value within carbon pools in terrestrial ecosystems has been observed in different types of ecosystems and over different timescales, and has been studied and described in detail [1, 5, 15, 18, 50, 64, 190].

Different processes within the biosphere have different fractionation mechanisms, causing differences in $\delta^{13}C$ within plant carbon pools. For example, starch, proteins and cellulose are relatively enriched and lignin and lipids are relatively depleted in comparison to leaf tissue [15]. The $\delta^{13}C$ of roots in comparison to plant tissue is varying; some studies indicate an enrichment of $\delta^{13}C$ in roots [15, 191], others observe depletion [65, 126]. The $\delta^{13}C$ of soil organic carbon is mostly determined by the present and past vegetation; soils under C3 plants are more depleted than soils under C4 plants. Differences also occur within soil layers: the litter layer of soils is usually very similar to the $\delta^{13}C$ of leaf tissue. In general, SOM is enriched (less negative) in $\delta^{13}C$, compared to the leaves and (fresh) litter [14, 50]. Also, the $\delta^{13}C$ of SOM is known to increase (become less negative) with soil depth [14, 50, 66, 155, 195]. It is assumed that a fractionation takes place during respiration, which causes the heavier ^{13}C to stay behind. This fractionation is expected to be small but might result in an enrichment with soil depth over longer times [50, 191, 195].

Spatial or temporal differences in $\delta^{13}C$ in carbon pools can often be explained by environmental factors such as precipitation [14], drought and moisture availability [103, 155, 180, 181], freezing [14], temperature changes [15, 55], change in dominating plant type species [50] or human influ-

ence [1]. Bowling [14] showed that a change in environmental conditions can cause a difference in photosynthetic discrimination of up to 5‰.

7.4.2 Hypotheses for observed diurnal respiratory $\delta^{13}CO_2$ flux variation

Diurnal variation in respiratory soil $\delta^{13}CO_2$ values, as observed in our field experiment, has been observed before. An overview of previous studies assessing diurnal variation in soil respiratory $\delta^{13}CO_2$ values, and the given explanation for their observations, is given in Table 7.2. Climate is described by the Köppen-Geiger climate classification [100]. We suggest and discuss seven possible hypotheses for the observed variation in respiratory $\delta^{13}CO_2$ flux values.

A diurnal respiratory $\delta^{13}CO_2$ flux value variation due to varying contributing sources

Hypothesis 1: Influence of geological sources
As observed in previous studies, CO_2 fluxes within the biosphere can originate from biological as well as non-biological sources, namely the out gassing of CO_2 with a geological origin [52, 152]. Rey [152] found that CO_2 fluxes with a geothermal origin can play a major role in ecosystems situated in geological active areas and observed that the out gassing of CO_2 with a geological origin is related to wind speed and turbulence.

Viterbo is located in a seismic active region with presence of geothermal activity, with multiple extinct volcanoes and thermal wells in the surrounding [6, 147]. Thermal well air samples were analyzed and the measured gases deviated far from our lightest calibration gas (-5‰) wherefore accurate estimates are not possible. However, the gases are estimated to be between -2 and 4‰ (Table 7.1), which is more positive than found by other studies: previous studies from this region observed values ranging between -2 and 2‰ [30, 31, 123].

Likeliness of hypothesis
Biological respiratory CO_2 production follows a diurnal pattern, with higher production taking place during the day when higher temperatures are present. Geological fluxes are expected to be related to atmospheric turbulence [152], which is usually also highest during the day. It is difficult to estimate a possible diurnal pattern in relative contribution of both sources. However, geothermal CO_2 fluxes are expected to have a pulse-like character, being sensitive to sudden wind gusts and varying atmospheric turbulence. Therefore, if geothermal fluxes would be the cause of the observed diurnal $\delta^{13}CO_{2resp}$ pattern, a more varying (unstable) respiratory $\delta^{13}CO_2$ flux value of the surface flux during daytime can be expected, instead of the observed fairly constant $\delta^{13}CO_2$ values (Figures 7.2 and 7.3). Therefore, while it does not rule out the existence of geothermal out gassing at the fieldsite, it excludes that geological emissions are the cause for the observed respiratory $\delta^{13}CO_2$ variation in the flux chambers.

Hypothesis 2: Shift in ratio autotrophic and heterotrophic respiration
Diurnal variation in soil respiratory $\delta^{13}CO_2$ flux values has been observed and described by different studies and is often attributed to a variation in the supply of $\delta^{13}C$ of phloem sugars (in ecosystems with active plants), which influences the ratio of autotrophic and heterotrophic respiration [5, 98, 180, 190]. Autotrophic respiration (from root, rhizosphere and algae) and heterotrophic respiration (from microorganisms decomposing SOM) originate from different carbon sources with their own characteristic $\delta^{13}CO_2$ values. Usually, if active vegetation is present,

Table 7.2: Overview of studies assessing diurnal variation in soil respiratory $\delta^{13}CO_2$ values.

Study	**Diurnal variation**	**Peak enrichment**	**CO_2 flux-range (μmol m^{-2} s^{-1})**	**Ecosystem & Climate**	**Explanation**
[12]	no diurnal variation	-	1-6	forest ecosystem-girdled, Sweden), subarctic climate (Dfc), summer	-
[98]	diurnal variation of 4%	midday	1-6	pine plantation (Germany), Temperate climate (Cfb), summer	combination of environmental factors and shift in proportional contribution of autotrophic and heterotrophic components
[117]	diurnal variation of 2 %	afternoon/evening	4-6	Forest-site (Germany), Temperate climate (Cfb), summer	shift in proportional contribution of autotrophic and heterotrophic components
[5]	diurnal variation of 1 %	midday	12-14	mountain grass land (Austria), continental climate (Dwb), summer, active plants, not shaded	several theories, but most likely shift in proportional contribution of autotrophic and heterotrophic components
[5]	diurnal variation of 0.7 %	midday	12-16	mountain grass land (Austria), continental climate (Dwb), summer, active plants, shaded	several theories, but most likely shift in proportional contribution of autotrophic and heterotrophic components
[180]	diurnal variation of 3%	afternoon	1.5-2.5	woodland with grazed pasture under story, Mediterranean climate (Csb), spring	shift in proportional contribution of autotrophic and heterotrophic components
[180]	diurnal variation of 5%	night	1.5-2	woodland with grazed pasture under story, Mediterranean climate (Csb), spring-drought	shift in proportional contribution of autotrophic and heterotrophic components
[126]	diurnal variation of $>$ 5 %	afternoon	0-20	experimental garden, (Utah, USA) steppe climate (BS), untrenched soils, summer	diffusive fractionation
[126]	diurnal variation of $>$ 5 %	afternoon	0-20	experimental garden, (Utah, USA) steppe climate (BS), trenched soils, summer	diffusive fractionation
[16]	no diurnal variation	-	2-5	forest ecosystem (Colorado, USA), subarctic climate (Dfc), summer	-

autotrophic soil respiration represents the major flux with the largest diurnal variation while heterotrophic respiration is expected to be more stable [102, 138, 155]. Most studies find that the $\delta^{13}CO_2$ value of autotrophic (root) respiration is more enriched in comparison to heterotrophic respiration [15, 102, 180] but also reversed patterns are reported [50, 126].

Likeliness of hypothesis
In our ecosystem, it is unexpected that a shift in the ratio autotrophic-heterotrophic respiration is the cause for the observed diurnal respiratory $\delta^{13}CO_2$ flux variation for the following reasons. First of all, the ecosystem studied in this research is in dormant state; no green vegetation was observed (in the flux chambers), wherefore a contribution of autotrophic respiration is expected to be absent. Also, the possible remaining autotrophic respiration (respiring/decaying roots) is not expected to have a diurnal pattern since the supply of photosynthetic assimilates during daytime is absent. Furthermore, temperature variation influences CO_2 production. It has been observed that autotrophic respiration has a higher temperature response ($Q_{10} = 4.6$) than heterotrophic respiration ($Q_{10} = 2.5$-3.5) [13, 51], causing autotrophic respiration to be (relatively) more dominant during warmer temperatures (daytime). Most studies indicate that autotrophic respiration is in general more depleted than heterotrophic respiration. Therefore, a higher Q_{10} for autotrophic respiration would result in more $^{13}CO_2$ depleted respiratory fluxes during the day, which is opposite of what is observed. Therefore, it is unexpected that the observed diurnal respiratory $\delta^{13}CO_2$ flux variation is caused by a diurnal shift in autotrophic and heterotrophic respiration. However, detailed soil analyses would help to exclude this hypothesis with certainty.

Hypothesis 3: Shift in proportional contribution of vertical soil layers
Temperatures in the soil are buffered and phase shifted in comparison to air temperature fluctuations. Since soil respiration is dependent on temperature, this buffering and phase shifting can have an effect on the ratio of contribution between vertical soil layers; during daytime, upper soil layers are expected to contribute (relatively) more than during nighttime. Since soil layers might differ in $\delta^{13}C$, this shift in contribution might result in a different $\delta^{13}CO_2$ value of the net surface flux. Most studies show an increase (less negative) in $\delta^{13}C$ values in SOM with depth, which is expected to cause a more isotopic enriched (less negative) respiratory CO_2 surface flux during the night.

Likeliness of hypothesis
The fieldsite is ploughed every year to a depth of 20 or 50 cm, wherefore upper soil layers are expected to be homogeneous and an increase in $\delta^{13}C$ in SOM with depth is not expected. If such a pattern is still present, it would cause enriched fluxes during the day, which is opposite of what is observed. Also, it is expected that deeper layers (> 10 cm) do not contribute much and most CO_2 production takes place close to the surface since CO_2 surface fluxes relate better to air temperature than to soil temperature at 10 cm (see Chapter 6). However, as mentioned before, recent studies have suggested that 'fresh' organic material (litter layers) might contribute significantly to total CO_2 flux. The studied fieldsite does not have a large litter layer, but the presence of few 'fresh' organic SOM with possible deviating $\delta^{13}CO_2$ is possible [15, 66], wherefore this hypothesis cannot fully be excluded.

A diurnal respiratory $\delta^{13}CO_2$ flux value variation due to physical processes

The physical controls over the $\delta^{13}CO_2$ value of soil CO_2 fluxes have been discussed and evaluated by different studies [2, 16, 89, 126, 129–131, 156]. Physical controls become important when a system is not in steady-state. As pointed out by Nickerson [131], fluxes in field conditions

are rarely in steady-state but mostly moving to an equilibrium. The most important physical process when considering the $\delta^{13}CO_2$ value of CO_2 fluxes, is kinetic fractionation, which is a fractionation caused by the difference in mass between the molecules: $^{12}CO_2$ molecules diffuse faster than $^{13}CO_2$ molecules which, in non-steady-state conditions, causes diffusive fractionation. Diffusive fractionation has been described in detail by Admunson (1998) and Kayler (2010). Both studies point out that, when CO_2 transport is solely diffusion driven, diffusive fractionation can play a major role.

The following hypotheses are based on the assumption that soil respiration is produced with a constant $\delta^{13}CO_2$ value, and variation is caused by a physical process only.

Hypothesis 4: Diffusive fractionation during changing CO_2 production
$^{12}CO_2$ molecules diffuse faster than $^{13}CO_2$ molecules which, in steady-state conditions, does not influence the $\delta^{13}CO_2$ value of the surface flux. However, during non-steady-state conditions, such as during increasing CO_2 production, newly produced $^{12}CO_2$ particles diffuse faster and reach the surface earlier, wherefore the surface CO_2 flux shows more depleted $\delta^{13}CO_2$ values than during steady-state conditions. Moyes (2010) observed diurnal variation in the $\delta^{13}CO_2$ value of respiration (up to 5‰) in trenched (removal of roots) soil profiles, so in absence of autotrophic respiration and suggested that the diurnal respiratory $\delta^{13}CO_2$ flux value variation can also solely be caused by the physical process of diffusive fractionation. Moyes (2010) modeled and explained the observed variation by diffusive fractionation during changing production and concluded that diffusive fractionation especially can play a role in low flux ecosystems with high diurnal flux variation. The significance of this process in soil diffusion processes has been considered plausible by several other studies [5, 126, 131, 190] but also has been questioned [155].

Likeliness of hypothesis
A model study, as described in §7.2.3, was performed, in which 3 different production profiles were tested: one profile with a constant-with-depth (temperature-dependent) production over the total soil profile (50 cm), one profile where 80% of the production originates from the upper 10 cm, and 20% of the production originates from the 10-50 cm soil layer, and one profile where 50% of the production originates from the upper 10 cm, and 50% originates from the 10-50 cm soil layer. All scenarios had the same cumulative daily production of 11232 mg m^{-2} day^{-1}, which is based on measured CO_2 fluxes at the fieldsite. Figure 7.4 shows the model outcomes: the different scenarios show a diurnal pattern in respiratory $\delta^{13}CO_2$ flux values, which is reversed and smaller than field observations. Different values for D_2 did not change this general pattern. Similar model results were found by Nickerson (2009) who found, with similar flux magnitudes, also only small isotopic flux variations. Nickerson (2009) also observed that the depletion peak (the moment that the most isotopic-depleted CO_2 flux occurs during a 24 h cycle) takes place just after the CO_2 flux peak (the moment that the highest CO_2 flux occurs during a 24 h cycle). The differences between the three scenarios show that a relative deeper production (such as the one layer scenario) causes a later depletion peak in the surface flux (in comparison to production peak), in comparison to scenarios with shallower production. Based on a better correlation between air temperature and CO_2 flux, in comparison to soil temperature and CO_2 flux (see Figures 6.4 and 6.5), it is expected that production takes place close to the surface, and therefore the '20%-80% scenario' is considered as the most representative for our field conditions.

The largest variation in the $\delta^{13}CO_2$ value of the surface flux in the field was observed when CO_2 fluxes were the most stable (nighttime). This indicates a different (not flux related) driver for the observed variation. The results of the model confirm the idea that diffusive fractionation during changing production is most likely not the cause for the observed variation in the respi-

ratory $\delta^{13}CO_2$ flux values.

Hypothesis 5: Diffusive fractionation due to flux chamber artifacts
Flux chambers are known to alter the steady-state diffusion profile, which can have different consequences. The application of the Keeling plot method on flux chamber data to determine the respiratory $\delta^{13}CO_2$ flux value has been modeled and evaluated [129–131, 156].

For long chamber deployment times (>1 hr), when chamber headspace air equilibrates with soil air, it has been modeled that a Keeling plot method can overestimate the Keeling plot intercept: under long deployment times, lateral diffusion starts to play a role, which decreases the chamber headspace CO_2 concentration and increases the final $\delta^{13}CO_2$ intercept value. This effect gets stronger with shorter soil collars and larger diffusivities (high porosities, [130]). For these situations, a 3D model is advised.

Also, the concentration buildup of CO_2 in the flux chamber headspace after chamber closure alters the soil-chamber gradient. A headspace concentration buildup will decrease the soil-air gradient, which will (temporary) reduce the absolute flux. To which extent the $\delta^{13}CO_2$ value of the surface flux is influenced by this process is under discussion [130, 156].

Likeliness of hypothesis
In the field experiment, soil collars were deep (10 cm) and chamber deployment times were short, wherefore it is not expected that lateral diffusion plays a role. The second chamber artifact, the effect of chamber headspace concentration buildup, was assessed. Non-linear behavior in the CO_2 concentration increase curve was not observed: Keeling plots created by using different parts of the concentration increase curve did not result in different intercept estimates. Therefore, it is expected that the flux chambers are large enough, and that the flux chamber closure times are too short to cause a change in soil-atmosphere gradient during flux chamber closure. However, more importantly, even if a small effect is present and Keeling plot intercepts are affected by the non-linear behavior, then this effect is expected to be stable during constant fluxes, and is expected to be of a varying magnitude during changing CO_2 production. At the fieldsite, the largest variation in the respiratory $\delta^{13}CO_2$ value was observed during nighttime when CO_2 fluxes were stable. Therefore, even if a possible chamber artifact cannot be excluded, it is not expected that this is the cause for the observed diurnal respiratory $\delta^{13}CO_2$ flux variation.

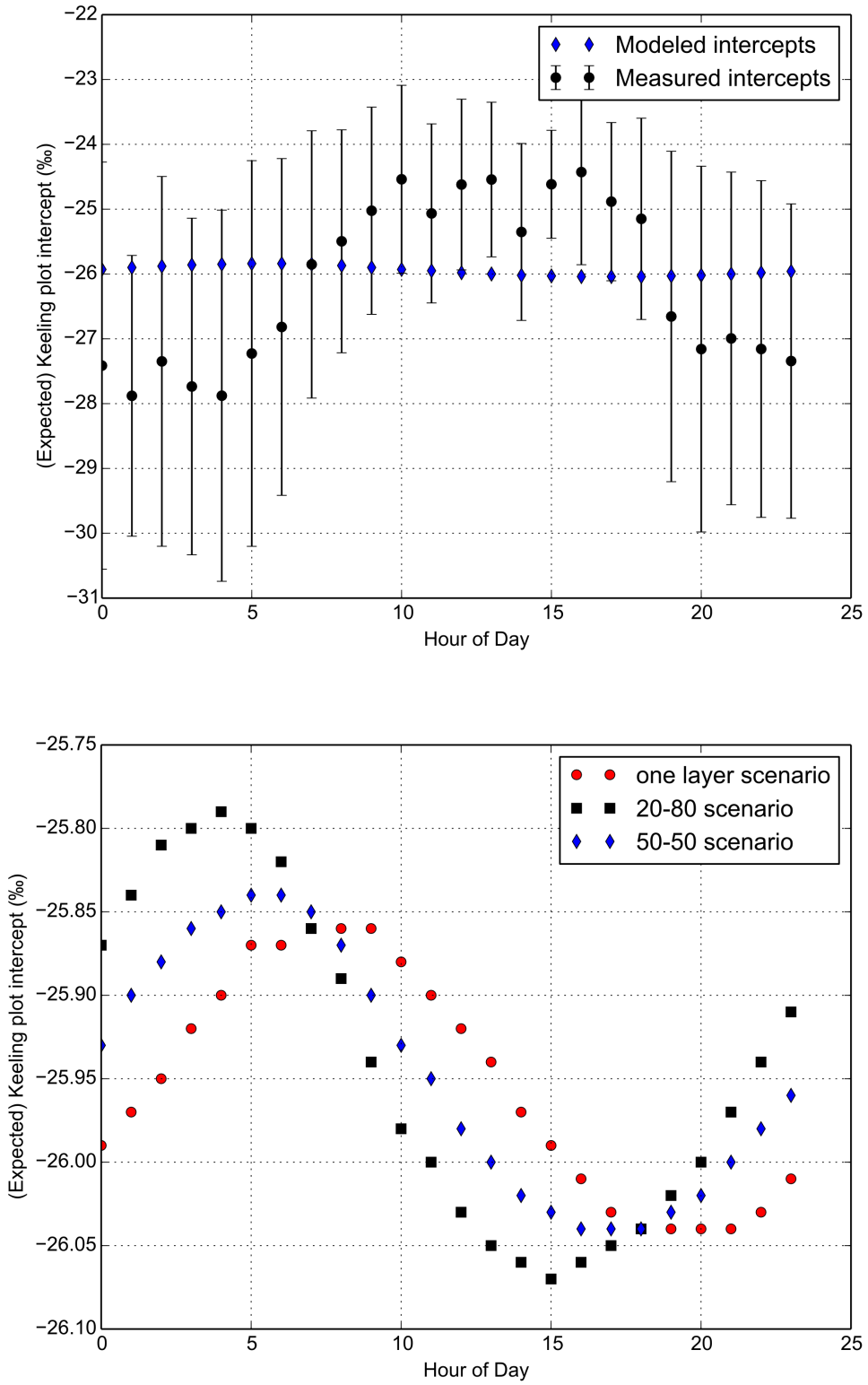

Figure 7.4: Upper figure: modeled Keeling plot intercepts versus the measured Keeling plot intercepts. Lower figure: zoom in of the upper figure, the modeled Keeling plot intercepts are from the different scenarios, which were described in §7.2.3.

Hypothesis 6: Diffusive fractionation during nocturnal boundary layer buildup
During stable night conditions, a boundary layer builds up, causing the atmospheric CO_2 concentrations to increase. This gradually reduces the soil-atmosphere CO_2 gradient which, in response, will lead to an increase in soil subsurface CO_2 concentrations. Faster $^{12}CO_2$ molecules will lead to a quicker re-steepening of the soil-air $^{12}CO_2$ gradient, which will lead to a temporary higher $^{12}CO_2$ flux, in comparison to the $^{13}CO_2$ flux. When atmospheric CO_2 concentrations are decreasing again, $^{12}CO_2$ molecules are quicker settled to the steeper gradient, causing the surface flux to be more $^{13}CO_2$ enriched. This effect was also described by Nickerson (2009), but considered to be dampened by the simultaneous decrease in the atmospheric $\delta^{13}CO_2$ concentration value.

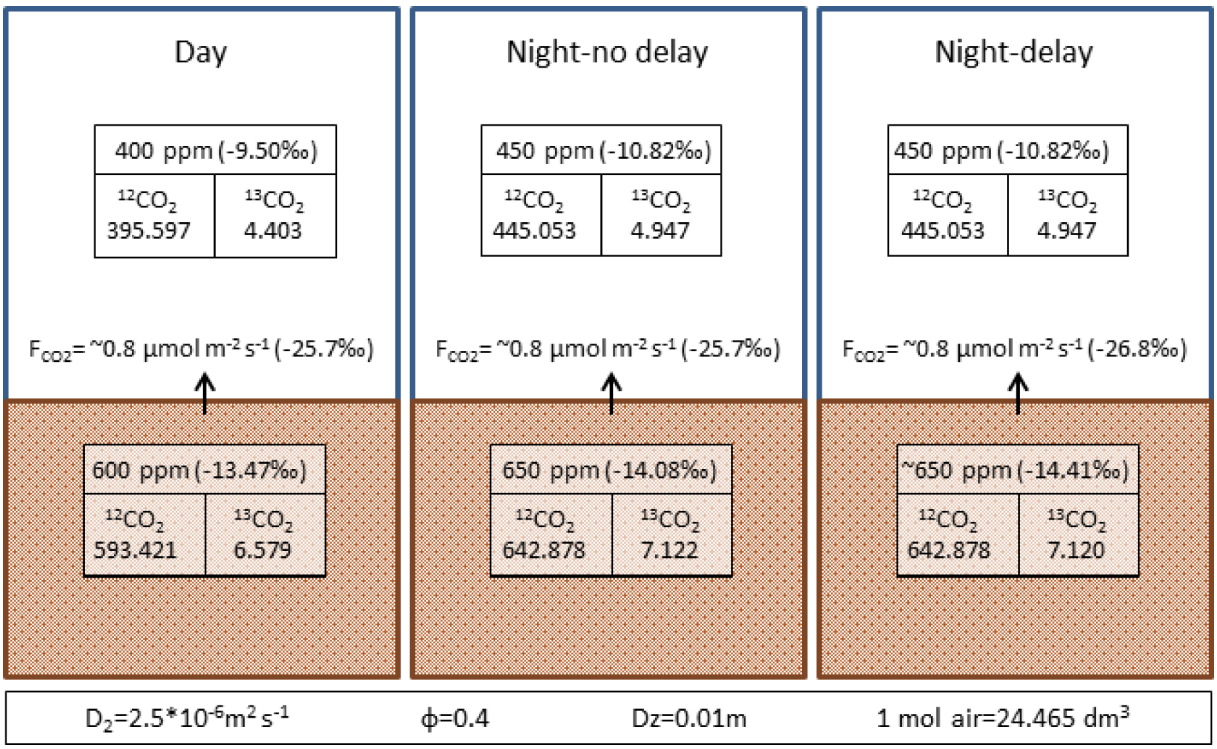

Figure 7.5: Schematic of isotopic CO_2 concentrations in the soil profile. The following assumptions are made: the shown soil concentrations are at 1 cm, the diffusivity for $^{13}CO_2$ is $2.5*10^{-6}$ m^2 s^{-1}, and the diffusivity for $^{12}CO_2$ is $1.0044 \cdot 2.5*10^{-6}$ m^2 s^{-1}, the porosity σ is 0.4, and the air density is 24.465 dm^3 mol^{-1}.

Quantification of the delayed re-steepening effect
To quantify the delay effect during the re-steepening of the soil-atmosphere gradient, a soil profile as shown in Figure 7.5 is considered. CO_2 concentrations and their accompanying $\delta^{13}CO_2$ values in the soil are derived from a fixed mixing profile, which is based on measured chamber concentrations (-9.5‰ at 400 ppm) and expected $\delta^{13}CO_2$ values at depth (-21.415‰). This mixing profile is visualized by the black solid line in Figure 7.6 and is derived as follows: in steady-state conditions, the surface $\delta^{13}CO_2$ flux value is equal to the $\delta^{13}CO_2$ value of CO_2 production at depth. However, soil CO_2 concentrations are enriched by a maximum of 4.4‰ in comparison to the CO_2 production due to the slower diffusion rate of the heavier isotope $^{13}CO_2$ [27]. Therefore, the soil CO_2 concentrations and $\delta^{13}CO_2$ values in the soil are assumed to follow a mixing profile with an enriched intercept, which is shown in Figure 7.6, and can be described by:

$$\delta^{13}CO_2(‰) = 4766 * \frac{1}{CO_2} - 21.415. \tag{7.2}$$

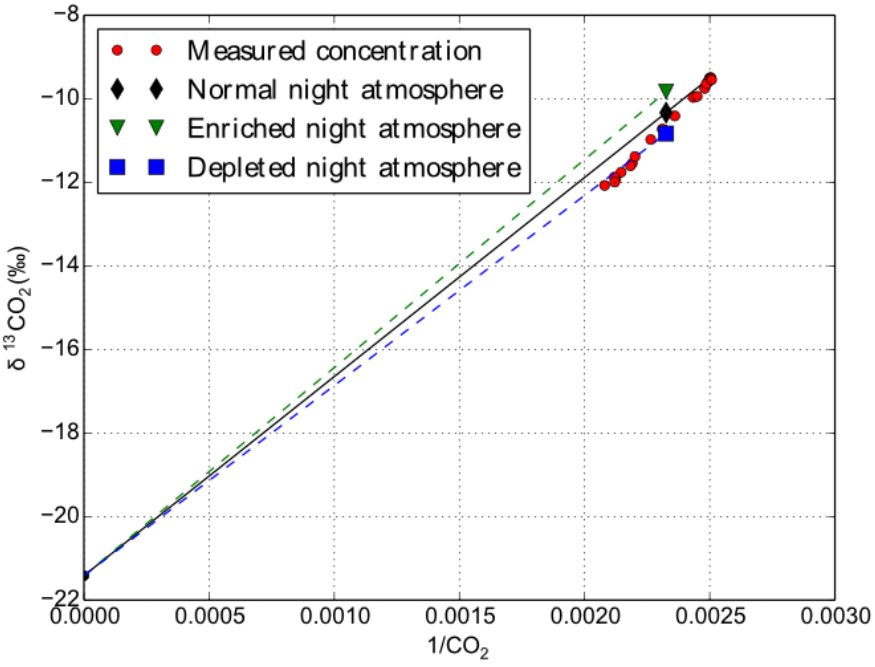

Figure 7.6: Isotopic mixing profiles for different atmospheres.
For hypothesis 6: black line indicates expected mixing profile of CO_2 vs $\delta^{13}CO_2$, with an intercept of -21.4‰, and a value of -9.5‰ at 400 ppm. In steady-state conditions, the surface flux is equal to the $\delta^{13}CO_2$ of the production at depth. However, soil CO_2 concentrations are enriched by a maximum of 4.4‰, in comparison to the production and the flux due to the slower diffusion rate of the heavier isotope $\delta^{13}CO_2$. Therefore, the intercept of the soil concentration CO_2-$\delta^{13}CO_2$ mixing profile is enriched compared to the flux Keeling plot intercept. Figure 7.5 shows that, under steady-state conditions, this concentration profile results in a surface CO_2 flux with a $\delta^{13}CO_2$-signature of -25.7‰.
For hypothesis 7: Measured CO_2 and $\delta^{13}CO_2$ in the chamber headspace of open chamber (red circles). Keeling plot intercepts for open chamber headspace is -25.5‰ (not shown). The lines show mixing plots under a normal (solid black line and diamond), an enriched (dashed green line and triangle), and depleted (dashed blue line and square) atmosphere.

As shown in Figure 7.5 (left profile), this mixing profile results in a CO_2 surface flux with a $\delta^{13}CO_2$ value of -25.7‰, which is similar to the measured $\delta^{13}CO_2$ value of the cumulative surface flux (Figure 7.3).

Soil CO_2 fluxes can be described by Fick's law:

$$F_{CO_2} = D * \frac{\Delta CO_2}{\Delta z}, \tag{7.3}$$

wherein F_{CO_2} is the resulting flux (μmol m^{-2} s^{-1}), ΔCO_2 is the concentration difference (μmol

m^{-3}), Δz the difference in depth (m), and D the diffusivity (m^2 s^{-1}). The ratio between the individual fluxes $F^{12}CO_2$ and $F^{13}CO_2$ can be used to calculate the respiratory $\delta^{13}CO_2$ flux value. The isotopic ratio of the respiratory flux (R_{sample} in Eq. 7.1) can therefore be calculated by:

$$R_{sample} = \frac{F^{13}CO_2}{F^{12}CO_2} = \frac{D^{13}CO_2 * \frac{\Delta^{13}CO_2}{\Delta z}}{D^{12}CO_2 * \frac{\Delta^{12}CO_2}{\Delta z}}, \tag{7.4}$$

wherein $D^{12}CO_2$ and $D^{13}CO_2$ are the independent diffusivity values (as D1 and D2 in §7.2.3).

The soil diffusivity is dependent on the soil type, the porosity, the tortuosity, and the soil moisture content, and many different parameterizations exist [56, 173]. However, due to the mass difference, the diffusivity of $D^{12}CO_2$ is always 4.4‰ faster than the diffusivity of $D^{13}CO_2$ [27]. Therefore, R_{sample} (Eq. 7.1 and Eq. 7.4) can be simplified to:

$$R_{sample} = \frac{\Delta^{13}CO_2}{\Delta^{12}CO_2 * 1.0044} \tag{7.5}$$

Soil CO_2 fluxes were relatively constant (approximately 0.8 μmol m^{-2} s^{-1}) during the night. Considering Equation 7.3 and assuming a relatively constant soil diffusivity value, it is expected that the absolute $\frac{\Delta CO_2}{\Delta z}$ value also remains constant. Therefore, during the nocturnal boundary layer buildup, a concentration increase in the atmosphere will be accompanied by the same concentration increase in the soil.

In Figure 7.5, the left profile shows daytime concentrations in the soil, and the resulting $\delta^{13}CO_2$ value of the surface flux (-25.7‰). During the night, the atmospheric CO_2 concentrations gradually increase, and the soil concentrations will follow, both following the mixing profile as described by Equation 7.2 (Figure 7.6). The middle profile shows that an equal increase in soil and atmospheric concentrations result in the same absolute surface flux (0.8 μmol m^{-2} s^{-1}) and the same $\delta^{13}CO_2$ value of the surface flux (-25.7‰). However, as shown in the right profile, if the re-steepening of the $^{13}CO_2$ concentration gradient is 4.4‰ slower than the re-steepening of the $^{12}CO_2$ concentration gradient, a small shift occurs in the $\delta^{13}CO_2$ value of the CO_2 concentrations at depth and in the resulting $\delta^{13}CO_2$ value of the surface flux.

Likeliness of hypothesis
The pattern of diurnal variation (stable values during the day, variation at night) compares well to the atmospheric CO_2 concentration changes (Figure 7.1). Also, the delay of 4.4‰ in the re-steepening of the $^{13}CO_2$ of concentration profile is proportional to the concentration gradient, wherefore the absolute amount of depletion is independent of the flux rates, the chosen depth or the chosen time lag: as long as the change is continuous and linear, the re-steepening of the soil $^{13}CO_2$ concentrations cannot catch up and will increasingly fall behind on soil $^{12}CO_2$ concentrations.

Exchange parameters of the soil and the soil surface, such as the soil diffusivity, are expected to be relatively stable over the night due to the stable night conditions. However, even if not, the absolute depletion is independent of correct parameterization of the exchange parameters since the ratio $D^{12}CO_2$:$D^{13}CO_2$ will remain the same. The absolute maximum CO_2 concentration increase per night was plotted against the maximum depleted respiratory $\delta^{13}CO_2$ flux value per night: less depletion was observed during nights with weaker or no boundary layer buildup (Figure 7.7). Based on the assumptions shown in Figure 7.5, theoretical depletions were calculated

for different scenarios.

Steady-state conditions during daytime were assumed at 400 ppm. The absolute isotopic depletion of the nighttime CO_2 surface flux is dependent on the daytime $\delta^{13}CO_2$ surface flux value in steady-state conditions, which can be considered as the starting point of the depletion process. Figure 7.7 shows different scenarios with different daytime (steady-state, starting point) respiratory $\delta^{13}CO_2$ flux values. Scenario 1 (daytime respiratory flux with $\delta^{13}CO_2$ value of -25.7 ‰, as in Figure 7.5) is shown as the blue dotted line, scenario 2 (daytime respiratory flux with $\delta^{13}CO_2$ value of -28.2 ‰) is shown as the black dotted line, and scenario 3 (daytime respiratory flux with $\delta^{13}CO_2$ value of -32.7‰) is shown as the red dotted line in Figure 7.7. The magnitude of depletion is dependent on the 'starting point' of the depletion process, but is independent of the chosen mixing profile or intercept value (Eq. 7.2), and is always approximately 1.2‰ depletion per 50 ppm atmospheric CO_2 increase.

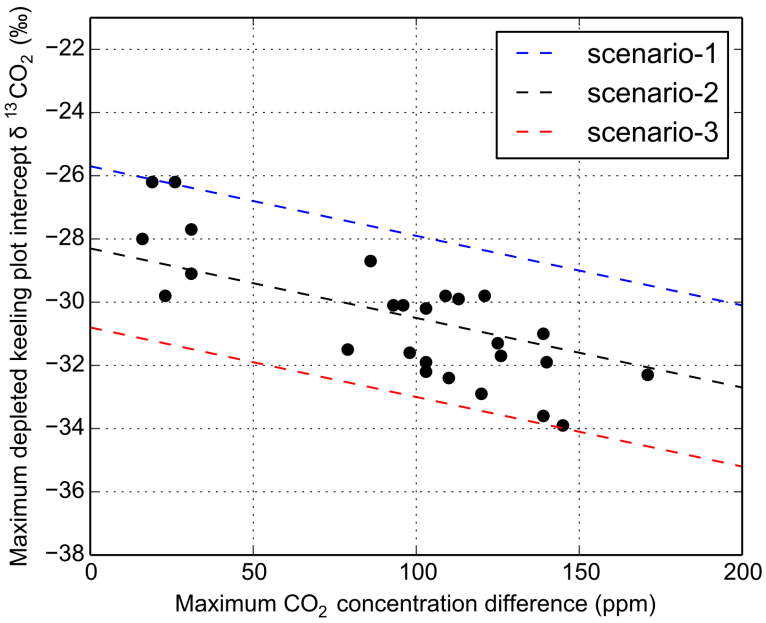

Figure 7.7: Maximum nighttime CO_2 concentration differences (in comparison to daytime values) versus maximum nighttime depletion in measured respiratory Keeling plot intercepts per night (black circles). The dotted lines indicate the theoretical calculated depletion based on scenario 1 (daytime steady-state respiratory CO_2 flux with $\delta^{13}CO_2$ value=-25.7‰, as in Figure 7.5), scenario 2 (daytime steady-state respiratory CO_2 flux with $\delta^{13}CO_2$ value=-28.2‰), and scenario 3 (daytime steady-state respiratory CO_2 flux with $\delta^{13}CO_2$ value=-30.7‰). The slope of the relationship is independent of the chosen mixing profile.

Based on these observations, the theory that an atmospheric CO_2 concentration increase during nocturnal boundary layer buildup can cause temporary isotopic depleted CO_2 fluxes, is considered as a likely explanation for the observed diurnal variation.

Hypothesis 7: Sensitivity of soil $^{12}CO_2$ and $^{13}CO_2$ concentration gradient to heterogeneous ecosystem respiration

For the use of a Keeling plot, it is assumed that the measured air is a mix of one constant source, with a stable CO_2 concentration and a stable $\delta^{13}CO_2$ value, and one increasing/decreasing source (the CO_2 flux). With this assumption, all changes in the atmospheric $\delta^{13}CO_2$ value can be attributed to the incoming CO_2 flux. The intercept of the Keeling plot indicates the $\delta^{13}CO_2$ value of the incoming CO_2 flux. In a homogeneous ecosystem, in which all sources respire with the same $\delta^{13}CO_2$ value, and with stable background concentrations, every measured concentration in the atmosphere will fall into the same mixing plot: e.g. by knowing the CO_2 concentration, the accompanying $\delta^{13}CO_2$ value can be predicted (Figure 7.6).

During the night, due to the buildup of a nocturnal boundary layer, the CO_2 concentration in the ecosystem rises and, with that, the $\delta^{13}CO_2$ value decreases. This will affect the independent soil gradients of $^{12}CO_2$ and $^{13}CO_2$ in a different manner ($\frac{\delta^{12}CO_2}{\Delta z}$ decreases relatively more than $\frac{\delta^{13}CO_2}{\Delta z}$). However, because all concentrations are a product of two fixed mixing sources (black line in Figure 7.6), the resulting ratio between the $^{13}CO_2$ flux and the $^{12}CO_2$ flux will remain constant, and the respiratory $\delta^{13}CO_2$ flux value is not affected.

Less depleted Keeling plot intercepts were observed at the tower (overlooking the whole ecosystem, approximately -23.4‰, Figure 7.2), in comparison to the Keeling plot intercepts from the open-chamber-headspace-air (overlooking the soil area, approximately -25.4‰, red circles in Figure 7.6). Based on this observation, it is expected that the total ecosystem respiration (including soil respiration) is less depleted than the soil respiration alone, which is taking place beneath the chamber. Therefore, the ecosystem is not considered homogeneous.

Since the open-chamber-headspace-air Keeling plot is not equal to the tower-air Keeling plot (at the same CO_2 concentration, they show different $\delta^{13}CO_2$ values), it can be concluded that the chamber headspace air is not fully mixed with its surrounding air during the flux chamber opening times. This means that the headspace chamber air is not a mixing product of one constant reservoir with one changing reservoir, but rather a *varying* mixing product of three different reservoirs, as visualized in Figure 7.8.

The content of the chamber headspace influences the soil air and therefore the individual soil isotopic gradients. In a homogeneous ecosystem, soil respiration respires with a constant $\delta^{13}CO_2$ value and the chamber headspace air is a fixed line in a mixing plot (mix between soil and atmospheric air, black solid line in Figure 7.6), so that all concentrations in the soil will lay on the same mixing line, and every increase in headspace air will follow the same line in the mixing plot. Therefore, these changes will not influence the $\delta^{13}CO_2$ value of the surface CO_2 flux.

In a heterogeneous ecosystem, the chamber headspace $\delta^{13}CO_2$ value might deviate from the fixed mixing plot. To analyze the consequences of such a situation for the surface flux, the following is assumed: atmospheric air of 400 ppm has a $\delta^{13}CO_2$ value of -9.5‰, and soil CO_2 is produced with a $\delta^{13}CO_2$ value of -25.7‰. Other concentrations are derived from a mixing profile of these two sources, which is shown as the black line in Figure 7.6. The assumed soil diffusivity value for $^{13}CO_2$ is $2.5*10^{-6}$ m^2 s^{-1}, and the assumed soil diffusivity value for $^{12}CO_2$ is $1.0044 \cdot 2.5*10^{-6}$ m^2 s^{-1}, the porosity σ is 0.4, and the air density is 24.465 dm^3 mol^{-1}. Table 7.3 shows the effect of a decreasing flux and an increasing atmospheric concentration in a homogeneous ecosystem (upper table, visualized as black diamond in Figure 7.6) and in a

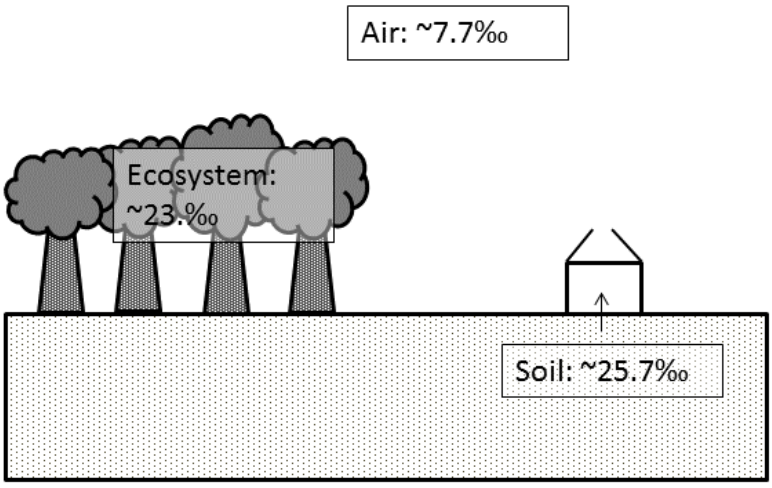

Figure 7.8: Schematic of the ecosystem CO_2 sources with the different isotopic signatures. The numbers in the boxes represent the reservoirs with its isotopic $\delta^{13}CO_2$ value.

heterogeneous ecosystem (lower tables, visualized as green triangle and blue square in Figure 7.6).

Likeliness of hypothesis
Expected is that the daytime soil profile is well in equilibrium with the chamber and ecosystem air. If different ecosystem air is mixing into the chamber headspace during the day, sufficient mixing is expected to take place to keep the effects small. However, during a nocturnal boundary layer buildup, concentrations change fast and possible deviating headspace chamber air will influence the individual isotopic soil CO_2 gradients differently as long as non-steady-state conditions remain.

The cumulative chamber $\delta^{13}CO_2$ flux value is -25.7‰ (Figure 7.2) and the daytime chamber headspace CO_2 concentration is 400 ppm with -9.5‰. When plotting the nighttime open-chamber-headspace-air concentrations on this line, it seems that the nighttime CO_2 concentrations (Figure 7.6, red circles) are more depleted than expected based on the daytime mixing profile. This would mean that, during the night, less ecosystem air mixes in the chamber headspace and the soil mixing profile will slowly move to a more depleted profile with the same intercept, but a less steep slope (Figure 7.6). As can be seen in Table 7.3, during this transition period, the $\delta^{13}CO_2$ value of the CO_2 flux is expected to be more enriched.

Hypothesis 7 is hard to verify since a determination of the exact daytime mixing profile, as visualized as the black line in Figure 7.6, is difficult. Therefore, the determination of the possible deviation from this line can be wrong or misleading. However, based on our measurements, the nighttime open-chamber-headspace-air values show a depleted character in comparison to daytime values, which would cause a temporary enriched $\delta^{13}CO_2$ surface flux during the night, which is opposite of what has been observed. Therefore, it is not expected that this mechanism is the cause for the observed diurnal respiratory $\delta^{13}CO_2$ flux variation.

Table 7.3: Calculated change in the surface $\delta^{13}CO_2$ flux under different atmospheric nighttime scenarios. The left site of the table shows the daytime values with soil and air concentrations both following the mixing concentration plot as indicated with the black line in Figure 7.6. At night, the production goes down (soil concentrations go down (from 600 to 550 ppm), and the atmospheric concentrations go up (from 400 to 430 ppm). The upper table shows the individual soil gradient changes and the corresponding $\delta^{13}CO_2$ value of the flux in a homogeneous ecosystem. The second table shows the individual soil gradient changes and the corresponding $\delta^{13}CO_2$ value of the flux when the nighttime chamber headspace is more enriched than expected, due to influence of the ecosystem (green triangle in Figure 7.6). The lowest table shows the individual soil gradient changes and the corresponding $\delta^{13}CO_2$ value of the flux when the nighttime chamber headspace is more depleted than expected, due to influence of the ecosystem (blue squares in Figure 7.6)

Homogeneous ecosystem

	Day				**Night**			
Depth (cm)	ppm	$^{12}CO_2$ concentration (μmol mol^{-1})	$^{13}CO_2$ concentration (μmol mol^{-1})	$\delta^{13}CO_2$	ppm	$^{12}CO_2$ concentration (μmol mol^{-1})	$^{13}CO_2$ concentration (μmol mol^{-1})	$\delta^{13}CO_2$
0	400	395.597	4.403	-9.500	430	425.271	4.729	-10.331
1	600	593.421	6.579	-13.472	550	543.965	6.035	-12.750
$^{12}CO_2$ & $^{13}CO_2$ flux (μmol m^{-2} s^{-1})		2.431	0.0266	**-25.701**		1.458	0.0160	**-25.701**

Heterogeneous ecosystem- night more enriched

	Day				**Night**			
Depth (cm)	ppm	$^{12}CO_2$ concentration (μmol mol^{-1})	$^{13}CO_2$ concentration (μmol mol^{-1})	$\delta^{13}CO_2$	ppm	$^{12}CO_2$ concentration (μmol mol^{-1})	$^{13}CO_2$ concentration (μmol mol^{-1})	$\delta^{13}CO_2$
0	400	395.597	4.403	-9.500	430	425.268	4.732	-9.831
1	600	593.421	6.579	-13.472	550	543.965	6.035	-12.750
$^{12}CO_2$ & $^{13}CO_2$ flux (μmol m^{-2} s^{-1})		2.431	0.027	**-25.701**		1.458	0.016	**-27.484**

Heterogeneous ecosystem- night more depleted

	Day				**Night**			
Depth (cm)	ppm	$^{12}CO_2$ concentration (μmol/mol)	$^{13}CO_2$ concentration (μmol mol^{-1})	$\delta^{13}CO_2$	ppm	$^{12}CO_2$ concentration (μmol mol^{-1})	$^{12}CO_2$ concentration (μmol mol^{-1})	$\delta^{13}CO_2$
0	400	395.597	4.403	-9.500	430	425.273	4.727	-10.831
1	600	593.421	6.579	-13.472	550	543.965	6.035	-12.750
$^{12}CO_2$ & $^{13}CO_2$ flux (μmol m^{-2} s^{-1})		2.431	0.027	**-25.701**		1.458	0.016	**-23.917**

7.4.3 Proposed explanation for observed diurnal respiratory $\delta^{13}CO_2$ flux variation

Different theories for the observed diurnal variation in respiratory $\delta^{13}CO_2$ flux values have been discussed. While no detailed soil profile information was available, it was possible to evaluate theories and exclude some hypotheses. The following can be concluded.

It is unexpected that a shift in individual carbon sources is the cause for the observed diurnal variation. The diurnal variation was measured on a soil which is yearly ploughed wherefore vertical soil layering should be minimal. Measurements were performed on soil plots where mainly heterotrophic respiration is expected. The existence of geological CO_2 fluxes is not excluded but it being responsible for the observed variation is unlikely. Therefore, it is expected that a physical control is the cause of the observed diurnal variation in the respiratory $\delta^{13}CO_2$ flux value.

Different physical controls on the respiratory $\delta^{13}CO_2$ flux value were evaluated. The influence of chamber design and sampling time on Keeling plot intercept values could not be fully excluded, but it was shown that this is unlikely the reason for the observed variation. The rate of diffusive fractionation during production was modeled and its effects were shown to be small and reverse to the observed variation. The effects of a heterogeneously respiring ecosystem were discussed. The applicability of this theory remains unclear, but it being responsible for the observed diurnal respiratory $\delta^{13}CO_2$ flux pattern is unlikely.

The pattern of the diurnal variation (stable values during the day, variation at night) showed no similarity to the diurnal CO_2 flux pattern but compared well to atmospheric CO_2 concentration changes. Also, less depletion was observed during nights with weak or no boundary layer buildup. These observations point at hypothesis 6, which is considered as the most likely explanation for the observed diurnal variation in respiratory $\delta^{13}CO_2$ flux values.

Not all observed variation can be explained by hypothesis 6. As shown in Figure 7.7 and when studying individual nights (not shown), some observed variation was not resolved. Therefore, it is not excluded that other processes also influence the respiratory $\delta^{13}CO_2$ flux values. However, it is shown that non-steady-state conditions are indeed important in field conditions [131] and that an external factor such as the nocturnal boundary layer buildup can have a major impact on the Keeling plot intercept determination.

These mechanisms are important to consider when using Keeling plots for biosphere studies: if the measured respiration is dominated by soil respiration and active vegetation is absent (such as in the flux chambers in this experiment), soil diffusion processes become an important driver and respiratory $\delta^{13}CO_2$ flux value determination can become biased by a strong nocturnal boundary layer buildup, resulting in an underestimation of the respiratory $\delta^{13}CO_2$ flux value.

7.5 Conclusion

FTIR-spectrometry has successfully been applied to continuously monitor ecosystem CO_2 concentrations, CO_2 fluxes, and their isotopic components by use of the tower concentration method and the flux chamber method simultaneously. Tower concentration and flux chamber measurements were used to quantify daily and hourly respiratory $\delta^{13}CO_2$ flux values. More enriched respiratory $\delta^{13}CO_2$ flux values were determined by tower concentration measurements, overlooking the whole ecosystem, in comparison to flux chamber measurements, overlooking senescent

grass and soil. By means of flux chamber measurements, an average diurnal variation in respiratory $\delta^{13}CO_2$ flux values of 3.5‰ was found. Variation of such magnitudes are usually only found in active ecosystems and are then attributed to a shift in (plant-related) sources [98, 180].

It is proposed that the observed variation is not driven by a shift in carbon sources but is caused by non-steady-state conditions in the soil profile: the change in atmospheric CO_2 concentrations, induced by a nocturnal boundary layer buildup, is proposed to be the cause for the observed diurnal variation in respiratory $\delta^{13}CO_2$ flux values. The influence of an atmospheric boundary layer buildup on respiratory $\delta^{13}CO_2$ flux values should be considered in future isotopic studies performed in soil respiration dominated ecosystems.

8 Conclusion

Concentrations of CO_2, CH_4, N_2O and CO in the atmosphere are increasing as a result of anthropogenic emissions. However, its remains unknown how these changes will feedback into the biosphere-atmosphere exchange rates and mechanisms. Field measurements of current biosphere-atmosphere gas exchange are of great importance because they provide the possibility to study greenhouse gas dynamics and its feedback mechanisms in detail. Continuous in-situ exchange measurements are still sparse, especially for remote areas.

In this thesis, the use of the FTIR-analyzer for biosphere-atmosphere exchange flux measurements was assessed. The FTIR-analyzer is capable of measuring CO_2, CH_4, N_2O, CO and $\delta^{13}CO_2$ continuously, simultaneously, and with high precision. Measurements of the FTIR-analyzer were automated and combined with different flux measurement techniques, such as with the flux gradient technique, the ratio-boundary layer technique, the relaxed eddy accumulation technique, and the flux chamber technique, thereby providing a tool to continuously monitor ecosystem fluxes. A description and evaluation of the measurement set-up was published in van Asperen et al. (2015a). Different variations of the set-up were tested in four different field campaigns and several laboratory studies. This data was used to study different ecosystem processes. This thesis focussed on the use of the set-up to a) apply and assess different (new) flux measurement techniques, and b) to study different flux and ecosystem processes.

A new ratio-boundary layer method (R-NBL) was tested, in which flux estimates can be made without knowledge of the boundary layer height. To estimate the flux of the gas of interest (N_2O), only atmospheric concentration measurements of CO_2 and N_2O, and (eddy covariance) flux measurements of CO_2 were required. The R-NBL N_2O fluxes agreed well with the EC N_2O fluxes, and the R-NBL method performed best when the source area did not include cities, villages or roads. A detection limit of 0.004 nmol m^{-2} s^{-1} for the fieldsite was determined. Such a limit is not reached by most other flux measurement techniques. The R-NBL method is suggested to be suitable for measuring trace gas fluxes in homogeneous ecosystems such as large agricultural fields, wetlands and tundra ecosystems.

The performance of the flux gradient technique was assessed by comparison to eddy covariance measurements. The flux gradient technique requires a parameterization of the diffusion coefficient. In our fieldsite, parameterizations from literature underestimated CO_2 fluxes in comparison to eddy covariance fluxes. A new type of parameterization is suggested, wherein eddy covariance CO_2 measurements are used to derive a field specific empirical parameterization of the diffusion coefficient. The new method ensures correct diffusion coefficient values, thereby guaranteeing reliable flux gradient fluxes for the other gases measured by the FTIR-analyzer.

The eddy covariance storage component in a forest ecosystem was investigated by canopy concentration measurements. Daytime horizontal and vertical gas concentrations were well mixed throughout the canopy. Nighttime vertical concentration profiles showed very distinct patterns. CO_2 showed a strong vertical logarithmic profile with highest concentrations at the lowest inlet, indicating soil respiratory CO_2 emissions, while CO concentrations were lowest at the lowest inlet, indicating soil CO uptake. Other gases showed no clear vertical pattern. Nighttime hori-

zontal concentration measurements showed differences up to 70 ppm for CO_2, 700 ppb for CH_4, 4 ppb for N_2O, and 20 ppb for CO within 10 meters, thereby exceeding the vertical concentration variation. For correct determination of the storage component, it is advised to measure multiple vertical profiles within the canopy.

A ^{15}N-labeling experiment was performed with the aim to study N_2O production pathways after application of different types of agricultural fertilizers. ^{15}N-labeled nitrate- and ammonium-based fertilizer was applied to the soil in flux chambers. Individual concentrations and fluxes of N_2O isotopologues and isotopomers were measured every hour. The results showed that the FTIR-analyzer is capable of measuring different isotopologues and isotopomers of N_2O at low concentrations (1 ppb). The fertilization experiment revealed the fast and large loss of nitrogen by N_2O emission to the atmosphere after application of the nitrate-based fertilizer, in comparison to the ammonium-based fertilizer.

The role of photo and thermal degradation in arid ecosystems was assessed in the field and laboratory. No photodegradation-induced CO_2 and CO fluxes of in literature suggested magnitudes were found in the field nor in the laboratory study. In the laboratory, CO_2 and CO fluxes that were derived from thermal degradation were observed. In the field experiment, CO uptake and emission were measured and are proposed to be a result of biological uptake and abiotic thermal degradation-production. It is suggested that previous studies, addressing direct photodegradation, have overestimated the role of photodegradation and observed fluxes might be due to thermal degradation. The results of this study have been published in van Asperen et al. (2015b). The potential importance of abiotic decomposition in the form of thermal degradation, especially for arid regions, should be considered in future studies.

CO_2 concentrations and its isotopic components were studied by tower concentration and flux chamber measurements. Keeling plots were used to derive the $\delta^{13}CO_2$ flux value of soil and ecosystem respiration. Keeling plot intercepts from the tower, overlooking the arid grassland, showed more enriched $\delta^{13}CO_2$ values than Keeling plot intercepts derived from flux chamber measurements, indicating different dominating respiratory sources in their footprint. Flux chamber respiratory $\delta^{13}CO_2$ values showed a diurnal pattern with on average more depleted $\delta^{13}CO_2$ values during the night. Different (new) theories concerning the biological and physical controls on respiratory $\delta^{13}CO_2$ flux values were discussed and evaluated. It is suggested that the diurnal variation is induced by diffusive fractionation caused by non-steady-state conditions of the soil profile during nocturnal boundary layer buildup. Results of this study have been submitted to the journal of Agricultural and Forest Meteorology.

9 Outlook

During the PhD, different (new) flux measurement techniques have been assessed and multiple ecosystem processes have been studied. For some of the presented topics, several follow up research topics can be relevant. In this chapter, I describe the research topics which can be of interest for follow up research.

Laboratory based thermal degradation studies
The laboratory study focusing on thermal degradation showed very interesting results, which became part of a larger publication concerning the role of abiotic degradation in arid ecosystems (see Chapter 6). However, concerning the thermal degradation of organic material, some research questions are still open. In our laboratory study, only one type of organic material was used. Also, the organic material which was used, was only exposed to heating once, and it is unclear how emission patterns are when organic material is exposed to higher temperatures for longer times. A long term experiment with different type of organic materials is suggested.

Improvement of flux chamber set-up
In sunny conditions, the used flux chambers showed a high temperature increase during chamber closure (see Chapter 6). As shown in this thesis, high temperatures can cause thermal degradation fluxes. This can be avoided by the covering of the glass walls by aluminum foil. However, for photodegradation studies, it is essential that solar radiation can enter the flux chamber, and that temperature differences between transparent and opaque chambers are not too large. The design and testing of a flux chamber, in which solar radiation can enter but flux chamber temperatures are not/less influenced, can be a next possible study item. Possible solutions could include the use of radiation filters, with which only part of the solar radiation can enter, or the use of a small air conditioning to keep flux chamber temperatures representative for the surrounding ecosystem.

Study of complete isotopic ^{13}C budget
Different theories concerning the possible mechanisms behind the observed diurnal respiratory $\delta^{13}CO_2$ flux pattern have been proposed in Chapter 7. Additional soil and field analyses would help to further investigate the isotopic composition of the different soil layers, thereby creating more certainty for the evaluation of the different hypotheses. The method, which is described in §10.2.4, wherein the FTIR-analyzer was used to study the δ^{13}C of organic material, can be developed further and can be used for (part of the) additional isotopic soil and field analyses.

Study of non-steady-state effects on respiratory $\delta^{13}CO_2$ flux values in other ecosystems
The nocturnal boundary layer buildup causing non-steady-state conditions in the soil profile was proposed to be the most likely explanation for the observed diurnal respiratory $\delta^{13}CO_2$ flux pattern (see Chapter 7). Additional field experiments performed in similar conditions (arid ecosystem, minor autotrophic respiration and strong NBL buildup) would help to investigate how strong the non-steady-state effects are in other ecosystems.

^{15}N-labeling experiments
The ^{15}N-labeling experiment, which was described in §5.4, showed the suitability of the FTIR-analyzer for agricultural nitrogen studies. Additional research topics could include the effect of different soil types or different temperatures on the different N_2O production pathways. Future studies should increase the amount of added fertilizer and the length of the measurement campaign to be able to study the long term effects of different type of fertilizer.

R-NBL method in homogeneous ecosystems
The ratio-nocturnal boundary layer method, which was presented in §5.1, showed promising results concerning the measurement of low N_2O fluxes, and was tested at the fieldsite RISØ as part of the InGOS N_2O flux chamber intercomparison campaign. This fieldsite had the disadvantage of being relatively small and being situated in a non-homogeneous environment. A long term field experiment in a large homogeneous ecosystem could be used to further test the applicability of the method.

Different flux measurement techniques
One of the aims of this PhD was to assess different (new) flux measurement techniques. In this thesis, results of the FTIR-analyzer connected to different flux measurement techniques, such as the flux gradient method, the relaxed eddy accumulation method, the flux chamber method, and the ratio-boundary layer method, were shown. Possible future studies could focus on the applicability and the suitability of the FTIR-analyzer for other type of methods, such as the disjunct eddy correlation or the nocturnal boundary layer technique.

10 Appendix

10.1 Collaborative projects

During the PhD, the FTIR-analyzer has been set up in different (collaborative) field experiments. Studies, in which the main part of the research was conducted by me, are shown in the Chapters 5, 6 and 7. In §10.1.1 and §10.1.2, research is shown from collaborative campaigns wherein I have performed part of the field experiment or research. For each project, my contributions are described. In §10.1.3, an overview of different commercially available analyzers is given, which are used in the collaborative studies.

10.1.1 The InGOS N_2O flux chamber measurement campaign

The following paragraph contains data which has been collected by different institutes and authors. My contributions to the collaborative field experiment are the design and set-up of the FTIR experiment, the analyses of the FTIR data, and the writing of this report. The intercomparison campaign has been organized by RISØ, Roskilde. The data collection and the comparison between the different chamber systems were performed by Per Ambus and Mette S. Carter from RISØ. The manuscript which is being written about this project is led by Per Ambus, now at the University of Copenhagen, and has the preliminary title: ***Comparison of six chamber systems for N_2O flux measurement based on a field campaign.***

Introduction

Flux chamber measurements can be associated with different type of uncertainties. One source of uncertainty is related to the inability of flux chambers to capture spatial variation in its source area, due to its small footprint. Also, different type of chambers can induce different type of systematic errors. Studies to systematic errors of different flux chambers are multiple (§3.4.2, [33, 84, 148]).

Current developments in spectroscopic methods may provide faster and more precise N_2O concentration measurements, in comparison to GC methods, and are suitable for either flux chamber methods as for micrometeorological methods. The combination of flux chambers with these new type of analyzers enable detection of N_2O fluxes during relatively short chamber enclosure periods (few minutes). This reduces the risk of potential biased fluxes, which may be imposed by longer chamber enclosure periods ($>$ 1 hr) typical for GC-based measurements. However, to secure the continuity of historical N_2O flux time-series, it is important to test the accuracy of these new chamber systems by comparing them with the current measurement techniques, and among each other.

A field campaign was set up, as part of the InGOS project work package task 13.2, and was directed to compare different N_2O measurement systems from different institutes. Every institute brought their own flux chambers and analyzer. The type of flux chambers which were compared were fast automated flux chamber systems as well as slower semi-automated/manual GC based systems. A general description of the fieldsite and the FTIR experimental set-up can be found in §4.2.

Participating groups, flux chambers and instruments

Table 10.1 shows an overview of the institutes and their analyzers, which participated in the intercomparison campaign. The upper left picture in Figure 10.1 shows the KIT flux chambers (transparent chambers), which were connected to an automated GC-ECD (Gas Chromatography-Electron Capture Detector). The same picture shows the manual chambers from RISØ (opaque chambers), which were manually sampled 3 times during the experiment and also measured by a GC-ECD. The upper right picture in Figure 10.1 shows the flux chamber measurement set-up from the University of Bremen, which has been described in different parts of this thesis (§3.3). The lower left picture in Figure 10.1 shows the flux chambers from the Thünen Institute, which were designed in a way that minimizes the environmental disturbance during chamber opening periods. These flux chambers were connected to a QCL (Quantum Cascade Laser, §10.1.3). The lower right picture in Figure 10.1 shows an automated flux chamber from RISØ. These chambers had an inner transparent wall, which raised up to approximately 0.8 meter and was closed by a lid which moved on top. After several minutes, an outer non-transparent wall raised as well, turning the transparent flux chamber into an opaque flux chamber. With this set-up, fluxes including and excluding solar radiation-related processes (photosynthesis, photodegradation) could be studied with the same chamber and within the same measurement. The semi-automated chambers from Thünen Institute and from RISØ are not shown in Figure 10.1.

Figure 10.2 shows an overview of the fieldsite and the location of the different flux chambers. Some institutes also added micrometeorological methods to the field experiment (flux gradient method by University of Bremen and EC measurements by TI, ECN and RISØ). These results will not be discussed in this paragraph but some results are shown in §5.1.

For the comparison of the flux chambers, information such as chamber dimensions, chamber details (presence of vent and/or fans), type of used regression method and absence or presence of pressure and temperature measurements, were collected. Minimum detectable fluxes were estimated based on flux chamber enclosure time, measurement time interval, chamber dimensions and propagated flux error.

Table 10.1: Participating groups, instruments and flux chambers in the N_2O flux chamber intercomparison campaign. GC = Gas chromatography, ECD = Electron Capture Detector, QCL = Quantum Cascade Laser, FTIR = Fourier Transform Infrared Spectroscopy.

Institute	**Detector**	**Application**
Karlsruhe Institute of Technology, DE (KIT)	Real time GC-ECD	8 auto chambers
Thünen Institute, DE (TI)	Real time QCL	3 auto chambers
	Vials, GC-ECD	3 semi-auto chambers
University of Bremen, DE (UB)	Real time FTIR	2 auto chambers
DTU-RISØ, DK (DTU)	Vials, GC-ECD	36 manual chambers
	Vials, GC-ECD	1 semi-auto chamber

Figure 10.1: Pictures of the N_2O flux chamber intercomparison campaign at fieldsite RISØ. Upper left: automated KIT flux chambers (transparent chamber) and manual RISØ chambers (opaque chambers); upper right: automated flux chambers from the University of Bremen; in background the EC tower; lower left: automated flux chambers from Thünen Institute; lower right: automated photosynthesis-flux chambers from RISØ.

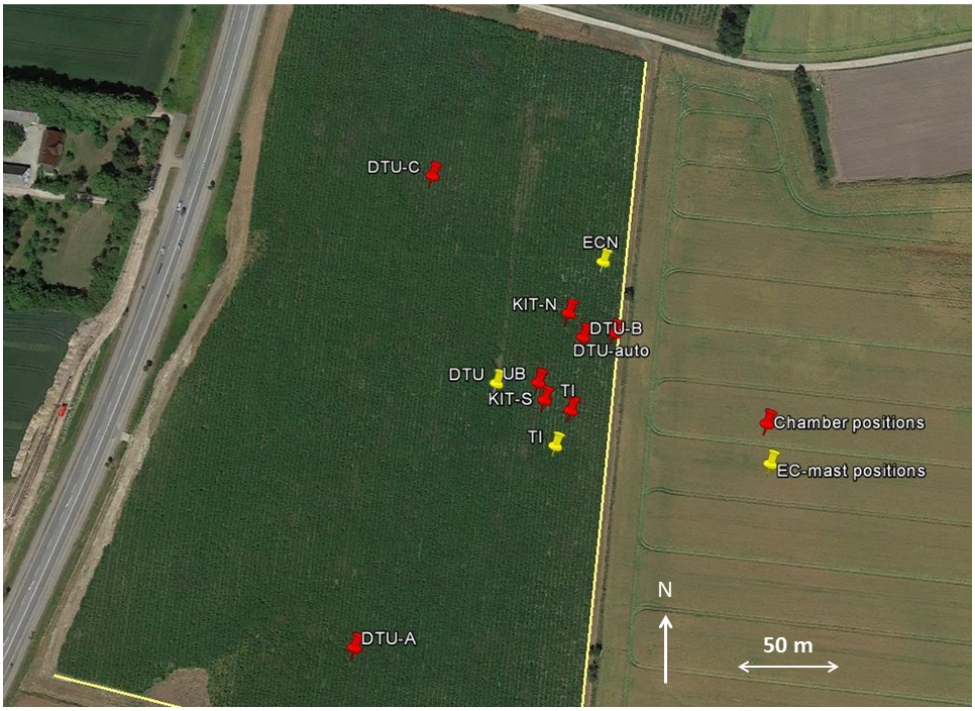

Figure 10.2: Aerial photograph of the fieldsite RISØ and the locations of different flux chambers. The aerial photograph is from Google (2015).

Preliminary results and discussion

Table 10.2 shows the minimal detectable fluxes per flux chamber system, based on instrument's precision, chamber dimension and sampling set-up. The mean N_2O fluxes, with their propagated random error deviation, are shown in Figure 10.3. Individual N_2O fluxes, as measured by the different flux chamber systems, are shown in Figure 10.4. N_2O emissions peaked between 15 and 20 April, with peak emissions ranging between 81 to 526 µg N_2O-N m^{-2} h^{-1} (0.8-5.2 nmol N_2O m^{-2} s^{-1}). The peak emission varied in intensity and time of occurrence between the different chamber systems (Figure 10.4). The temporal differences in peak emission might be caused by a variation in occurrence of optimal nitrification or denitrification conditions throughout the field (change in microbial activity, temperature or moisture availability). The absence of a clear simultaneous peak might be caused by the lack of precipitation during the field campaign; a large precipitation event would probably have triggered N_2O emissions over the field at the same time, reducing the temporal variability. Unclear is why no emission peak was observed in the RISØ-semi-automatic chamber system (Figure 10.4, lower figure, blue triangles).

The spatial variability was assessed by studying the variation in fluxes within the same chamber-type. The automated KIT chambers showed a CV (coefficient of variation) of 63% (n=8), and RISØ-manual chamber types showed a CV of 149% (n=16).

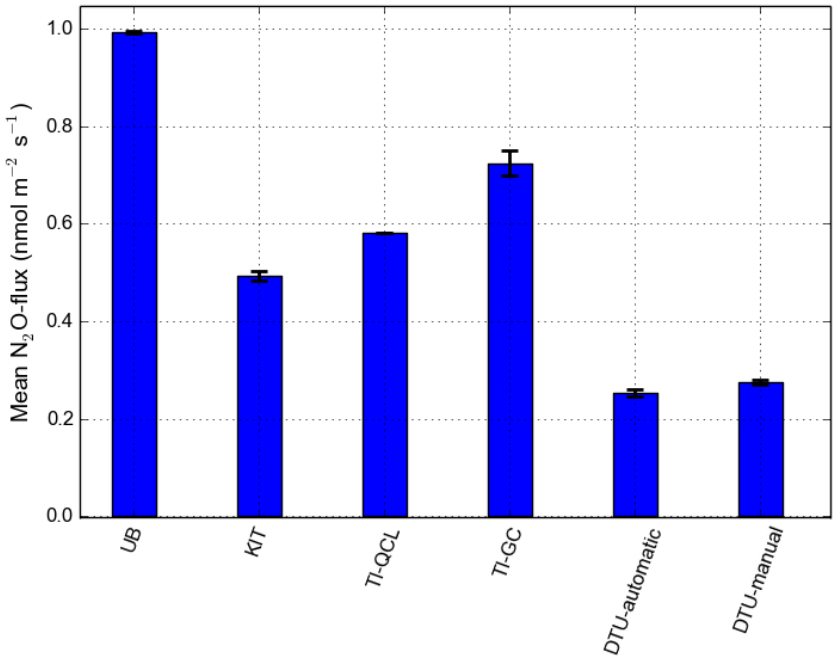

Figure 10.3: Mean N_2O fluxes measured by the different chamber systems; error bars are propagated error estimates.

Table 10.2: Minimum detectable fluxes of the different chamber systems in the intercomparison campaign at fieldsite RISØ.

	UB	KIT	TI-QCL	TI-GC	DTU-auto	DTU-man
Headspace volume: area ratio (L m^{-2})	520	150	591	591	182	193
Enclosure period (hr)	0.20	1.00	0.05	1.00	1.33	1.50
Minimum detectable flux (µg N_2O-N m^{-2} hr^{-1})	3.4	3.2	10.9	9.1	7.2	8.7

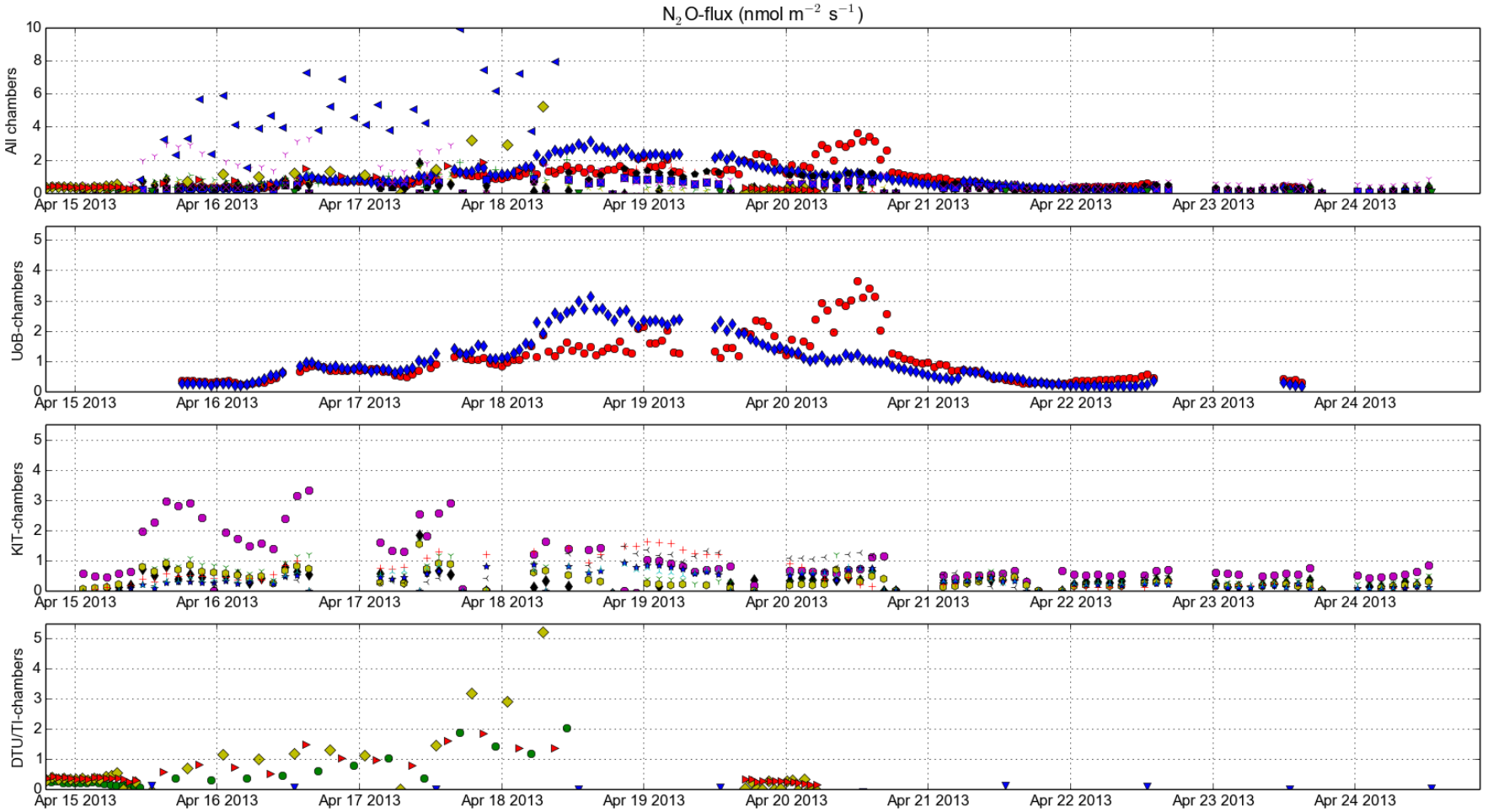

Figure 10.4: Fluxes measured by the different FC systems during the campaign at fieldsite RISØ. 1^{st} picture: N_2O fluxes of all chamber systems together, TI-GC chamber fluxes (blue triangles) went up to 20 nmol m^{-2} s^{-1}. The y-axis scale is different than in the following figures; 2^{nd} figure: N_2O fluxes measured by the 2 University of Bremen flux chambers; 3^{rd} figure: N_2O fluxes measured by the 8 automatic KIT flux chambers; 4^{th} figure: N_2O fluxes measured by semi-automated RISØ flux chamber (blue triangles) and automated Thünen Institute flux chambers. The manual RISØ flux chamber measurements are not shown.

Conclusion and outlook

The N_2O emissions during this field campaign, measured by the different flux chamber systems, revealed high spatial variability of N_2O production, even in this relatively uniform and equally fertilized fieldsite. Also, large temporal variation was observed: the measured areas showed doubling of their N_2O production within several hours without a clear environmental driver. Spatial and temporal variability makes quantitative comparison of different flux chamber systems difficult. These results indicate that the use of one or few flux chambers to estimate N_2O fluxes can result in biased flux estimates.

Nevertheless, 13 automatic chambers, 4 semi-automatic chambers and 36 manual chambers were continuously employed alongside each other for 2 weeks after a fertilization event and showed, before peak emissions started, similar N_2O flux magnitudes between 0.2 and 0.4 nmol m^{-2} s^{-1}. Also, the different flux chamber designs and set-ups were assessed on possible systematic and random errors and minimum detectable fluxes per flux chamber were determined. The flux chamber set-up from University of Bremen showed a very low detection limit in comparison to other deployed chamber systems, due to the measurement precision of the FTIR-analyzer. A manuscript about the results of this N_2O flux chamber intercomparison campaign is in preparation.

10.1.2 The InGOS N_2O micrometeorological measurement campaign: the FTIR-REA set-up

The following paragraph concerns the set-up and the results of the InGOS micrometeorological N_2O flux intercomparison campaign, which took place close to Edinburgh, June 2013. My contributions to this field experiment are the programming of the FTIR-analyzer for the REA-measurement set-up, the coupling of the sampling manifold to the FTIR-analyzer at ECN in Petten (Netherlands), and the on line maintenance and problem solving during the field campaign. The running of the FTIR-field experiment has been done by Marie Laborde (Ecotech) and Pim van den Bulk (ECN). Data analyses of different instruments has been done by the individual groups. The FTIR data analyses are being performed by Alex Vermeulen, Arjan Hensen and Pim van den Bulk (ECN).

The results and field campaign details which are not related to the REA-FTIR set-up are from the InGOS-talk 'Nitrous oxide fluxes from a Scottish grassland measured by eddy covariance: a comparison between different system', which was given by Daniela Famulari at the annual InGOS project meeting 2014 [54].

Introduction

Since several years, fast N_2O analyzers, which are suitable for EC measurements, are commercially available: companies which are producing these analyzers are for example Campbell Scientific Inc., Aerodyne Research Inc., and Los Gatos Research Inc. First evaluation and comparison of the performance of these new fast instruments show that the instrumental noise of these instruments is still a problem, but also show a promising outlook for future EC measurements of new generation instruments that are expected to be able to measure N_2O exchange with high precision [151].

It is important to test the qualitative performance and the accuracy of these new systems in more detail and under different conditions. Also, to secure the continuity of historical slower micrometeorological N_2O flux time-series, the new measurement techniques need to be compared to the current measurement techniques. In this field experiment, several fast and slow N_2O flux measurement methods were set up in parallel in a fertilized agricultural fieldsite to be able to assess the comparability of the different systems and to explore methods to improve future N_2O eddy covariance measurements. The University of Bremen participated in this experiment by providing experimental material, technical support and practical advice during the set-up of the FTIR-analyzer connected to a relaxed eddy accumulation (REA) technique. The FTIR-analyzer used in this study belongs to ECN.

FTIR-REA set-up

For the relaxed eddy accumulation technique, fast vertical wind velocity measurements are required to determine whether the wind direction (the eddy) is upward or downward. Dependent on the air movement being upward or downward, the air, which is continuously being sampled, is led to an upward-eddy or downward-eddy reservoir. Besides fast wind direction measurements, this technique also requires a fast air sampling device which, proportionally to the vertical velocity of the air, divides the air sample in two streams (Figure 10.5).

To be able to connect the FTIR-analyzer to the REA-set-up by use of the sampling manifold which was presented in §3.3, the manifold had to be adjusted. The manifold was designed for

flux gradient-passive air flows (air flows initiated by pumps at the sampling manifold), while the REA method depends on pumps at the sampling inlet. Figure 10.6 shows the sampling box set-up: the sampling bags are now connected to where usually the filling and evacuation pumps are connected. For this set-up, only one evacuation pump is required. The REA air streams are continuously flowing, directed either to bag 1 and bag 3 or, the next half hour, to bag 2 and bag 4. The measurement cycle was set up so that sample measurement preparation took 7.5 minutes: 2 min cell evacuation, 1 min flushing of cell with measurement air, 2 min cell evacuation, filling cell for 100 sec and stabilizing cell for 1 min. Afterwards, seven 1-min spectra were taken. After this 15 minute cycle, the other bags were analyzed. Also, in the measurement cycle, an automatic calibration cycle was implemented wherefore daily calibration measurements could be performed.

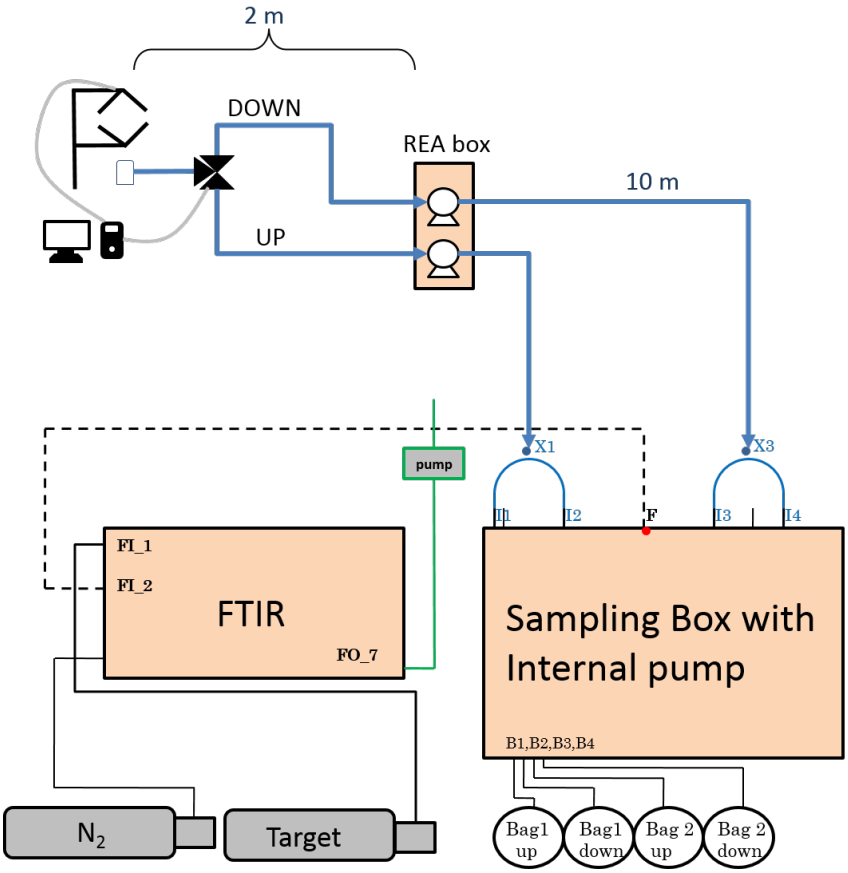

Figure 10.5: Schematic of FTIR-REA measurement set-up. Sampling and separation of air streams is done at the tower, air is led to sampling manifold and stored in sampling bags (BagUp or BagDown), and led to the FTIR-analyzer via FTIR-inlet 2. FTIR-inlet 1 was used for daily calibration measurements.

Field experiment in Easter Bush

The Easter Bush measurement site is located in a rural area 10 km south of Edinburgh, Scotland UK (3 12'W, 55 52'N, 190 m a.s.l.). The site is situated on the border between two intensively-managed grassland fields of approximately 5 ha each. A full meteorological station is installed at the fieldsite providing data for wind speed and direction, air humidity, solar radiation, soil temperature and moisture, atmospheric pressure, PAR, and rainfall.

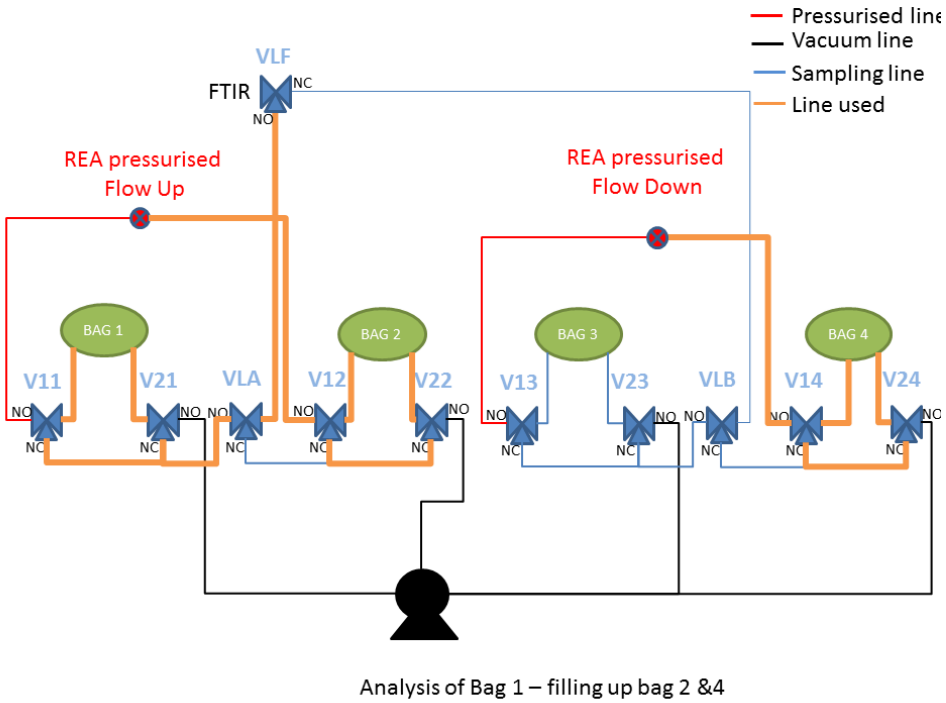

Figure 10.6: Sampling box set-up for the FTIR-REA measurements in Easter Bush. At the valves, the non-labeled outlet is 'always open', the outlet NO is 'normally open', the outlet NC is 'normally closed'. The black shape represents the evacuation pump. This figure indicates the air flow (orange lines) when bag 1 is being analyzed, while bag 2 and bag 4 are being filled by the REA-air streams.

In this field campaign, different EC systems connected to fast N_2O analyzers were set up in parallel to different slower systems. An overview of the accompanying institutes, instruments and systems is given in Table 10.3. The measurements started on 3^{rd} June 2013 and finished on 30^{th} June 2013: the first week of measurements were used for background measurements before fertilization. The fields were fertilized on 11^{th} June, with NH_4NO_3 (34.5% N) at a rate of 150 kg ha^{-1}. Subsequent N_2O emissions were measured for the following 3 weeks.

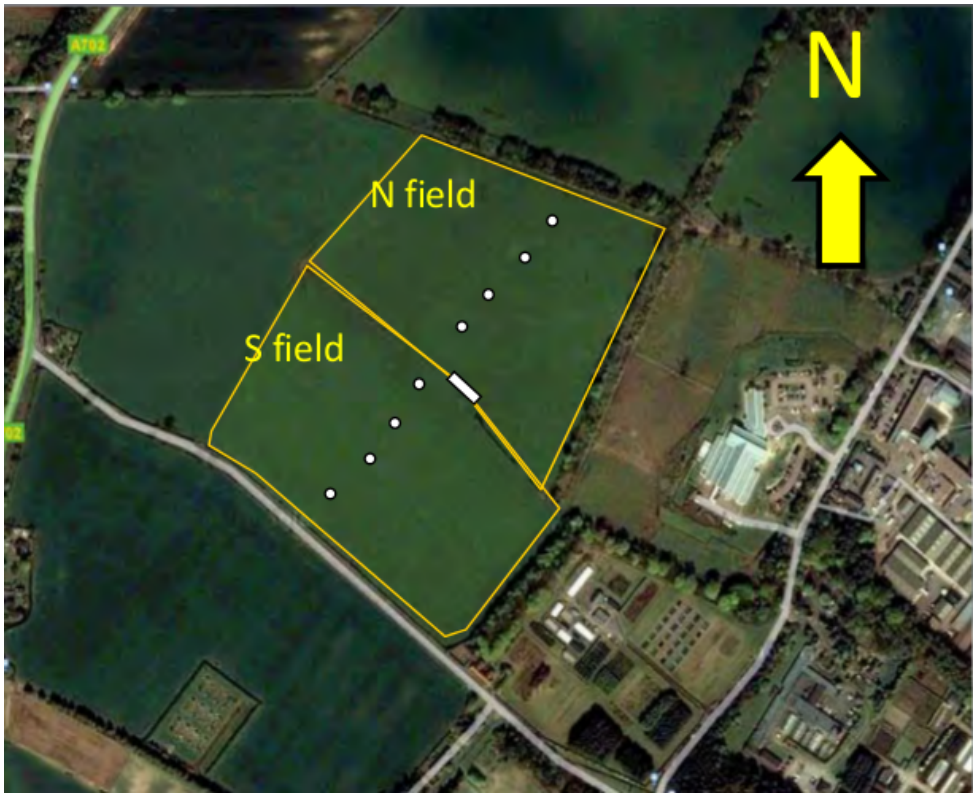

Figure 10.7: Aerial photograph of the fieldsite Easter Bush, the aerial photograph is from Google (2015). White square indicates measurement position. The figure is from Famulari (2014).

Table 10.3: The different institutes who participated in the EC N_2O intercomparison campaign, their instruments and instrument specifications, and the used flux measurement method.

Country	**Institute**	**Instrument**	**Species measured**	**Method**
Switzerland, The Netherlands, Germany, Australia	Ecotech, ECN, Bremen University	Spectronus-FTIR-analyzer	N_2O, CO_2, CH_4, CO, $\delta^{13}CO_2$	relaxed eddy accumulation
France	INRA Orleans	Lab built CW-QCL spectrometer (SPIRIT)	N_2O, CO_2, H_2O	aerodynamic gradient
Italy	West Systems SrL	Transportable accumulation chamber based flux meter	N_2O, CO_2, H_2O	dynamic enclosure
Finland	FMI	CRD Los Gatos Research+dryer	N_2O, CO, H_2O	eddy covariance
Finland	University of Helsinki	CRD Los Gatos Research	N_2O, CO_2, H_2O	eddy covariance
Denmark	Technical University of Denmark	CRD Los Gatos Research	N_2O, CO_2, H_2O	eddy covariance
The Netherlands	ECN	Aerodyne Pulsed QCL	N_2O, CH_4, H_2O	eddy covariance
France	INRA Grignon	Aerodyne CW-QCL	N_2O, CH_4, H_2O	eddy covariance
United Kingdom	NERC-CEH	Aerodyne CW-QCL	N_2O, CO_2, H_2O	eddy covariance

Preliminary results of the FTIR-REA set-up and intercomparison campaign

The FTIR-REA system performed well during the first part of the field campaign, but showed some not understood errors on a later stage. The FTIR-REA flux processing is still ongoing and therefore fluxes can not be shown. Figure 10.8 shows the concentration differences between the upward and the downward bag during one night of the experiment. The values are calculated as *-Concentration BagUp - Concentration BagDown*, wherefore a negative value indicate an upward flow. Figure 10.8 shows continuous clear CO_2, N_2O, and CO fluxes during the night, and clear CH_4 fluxes during some moments. The positive $\delta^{13}CO_2$ difference means that the upward flow was more negative than the downward flow, indicating depleted upward respiratory CO_2 fluxes. Figure 10.9 shows the results of the different EC N_2O flux measurement systems. Data processing of the EC comparison campaign including the different set-ups and analyzers is still ongoing. Expected is a publication of the results of this field campaign in a peer-reviewed journal.

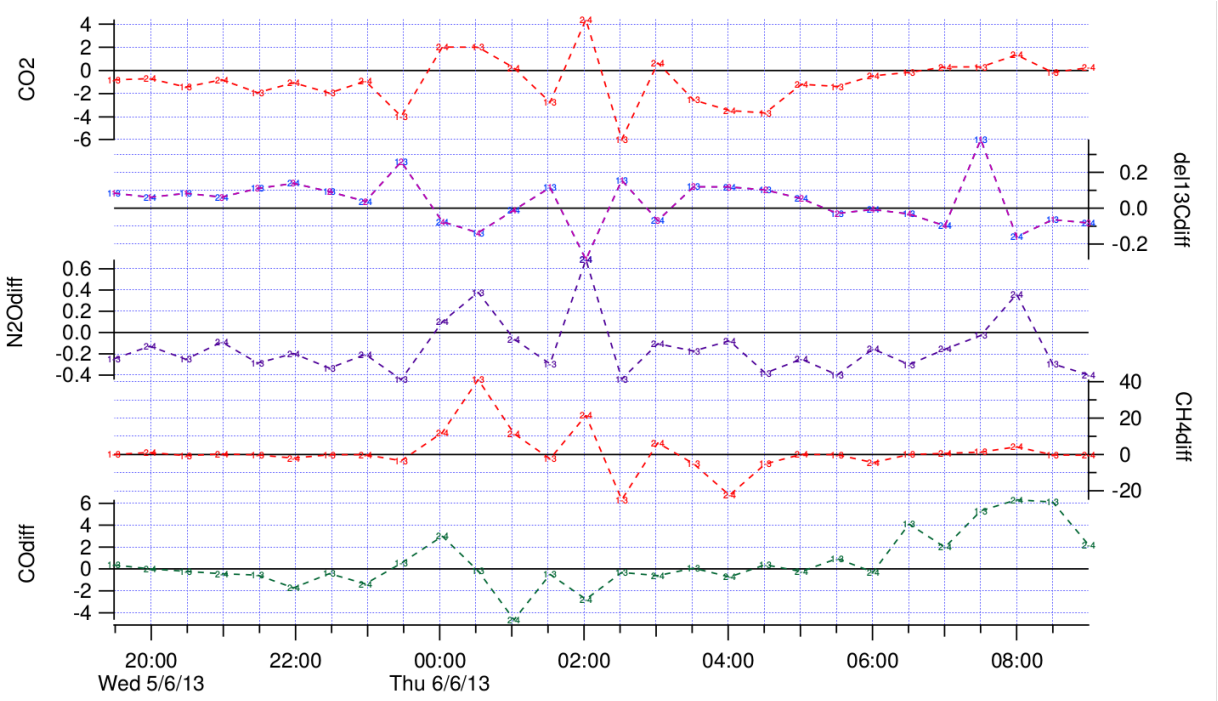

Figure 10.8: Preliminary results of FTIR-REA set-up. Shown are the concentration differences between the upward bag and the downward bag; negative numbers indicate an upward flux.

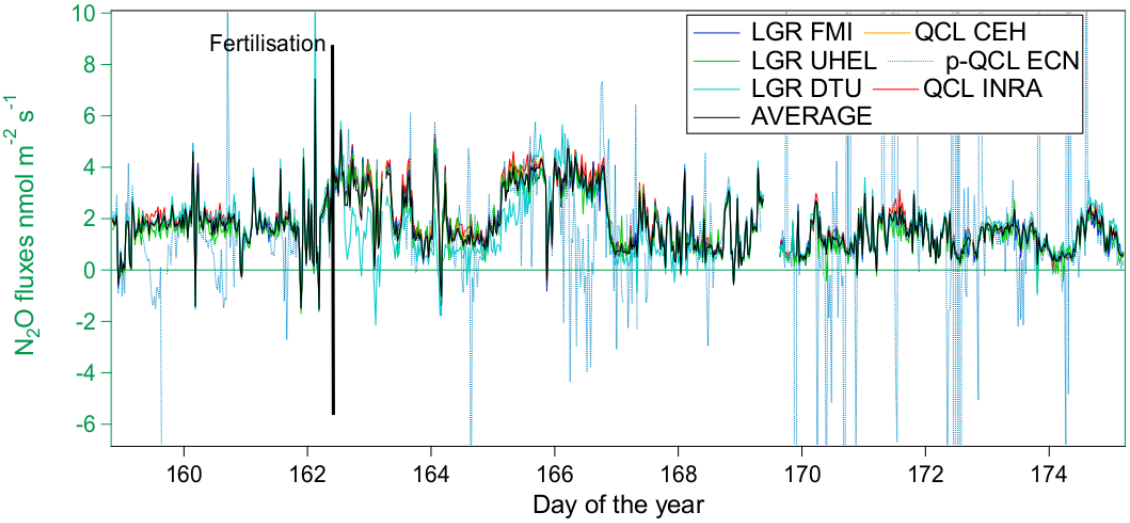

Figure 10.9: Preliminary general results of the N_2O flux intercomparison campaign in Easter Bush. The figure is from Famulari [54].

10.1.3 The FTIR-analyzer in comparison to other instruments used in ecosystem exchange studies

The use of the FTIR-analyzer for flux measurements is a new addition to the commonly employed instruments which are used to measure in-situ on site ecosystem fluxes. In this thesis, the advantages of using an FTIR-analyzer to measure ecosystem fluxes by means of different flux measurement techniques, have been discussed. In this paragraph, an overview of other instruments which can be combined with micrometeorological, chamber or other flux methods to measure ecosystem exchange, will be given. In here, on site laboratory instruments, which are for example suitable for static-non-flow through chamber measurements, will not be discussed.

In general, most studies performing high frequency in-situ ecosystem gas concentration and exchange measurements, use absorption spectroscopy: instruments contain a light source, which is directed to the sample being measured, which can be either in a sample cell or 'outside', in case of open path analyzers. After crossing the sample air, the light source is directed on a detector. Some instruments make use of a reference cell wherein a second light beam is directed for a reference spectra. Concentrations are derived from the absorption features.

The main challenge for the different analyzers is the maximization of the path length: longer path lengths result in stronger absorption features, which makes detection of smaller concentrations possible. However, it also requires stable internal optical alignment of mirrors, which can be hard to maintain in field experiment conditions.

Different analyzers

Tunable Diode Laser Absorption Spectroscopy (TDLAS)
Tunable diode laser absorption spectroscopy (TDLAS) does not use an extended light pathway, wherefore this method is sensitive to errors: under low concentrations, differences between the absorption features are weak. A way to improve the TDLAS method is by reducing the noise in the signal. A light source signal usually contains low frequency noise, which originates from the laser, mechanical instabilities, or possible external fluctuations. Noise decreases with increasing frequency. In Wavelength Modulation Spectroscopy (WMS), the frequency of the laser light is modulated to a higher frequency, wherefore the absorption and the absorption line shape can be measured more accurately. So, in comparison to other methods, the path length used in WMS is relatively short, but still high measurement accuracies can be obtained [112, 142].

Examples of a companies using WMS spectroscopy, are LI-COR and Campbell Scientific who both produce several (open and closed path) instruments, which are suitable for EC measurements (faster than $10 > Hz$), such as individual sensors for CH_4, CO_2 and H_2O. The advantage of the relatively short required path length, is that it reduces the need for very precise and, more importantly, clean mirrors, which can be a challenging requirement in field studies. Studies using TDLAS-instruments for ecosystem flux measurements are multiple, such as Detto (2011), Runkle (2012), Baldocchi (2003) and Peltola (2014). LI-COR-instruments were used in the field experiments Himmelmoor, RISØ and Rocca4 (§4.1, §4.2 and §4.3).

Quantum cascade lasers (QCL)
A quantum cascade laser (QCL) is a semiconductor laser that can emit in middle and longer infrared bands, in contrast to diode lasers which can only emit in near-infrared and visible bands. In a QC laser, the transition between states happens in a fixed quantum well. The advantage of a QCL is that one electron, which is responsible for the emission of a photon, can also initiate

a transition in the next quantum well, which makes the QCL system extremely efficient. This tunneling effect is where the name quantum cascade comes from. QCL instruments are mainly used for single gas determination but recent development and precise determination of cross sensitivities has caused QCL instruments to be able to measure groups of gas species, which have absorption features in similar wavelength bands.

Some QCL lasers do not need cooling and can be run at room temperature, which is an advantage for field experiments. For example, Aerodyne Research (www.aerodyne.com) offers QCL analyzers which measure N_2O concentrations, and which simultaneously measure either CO, CO_2 or CH_4 concentrations. Different types of QCL analyzers are being developed and used for ecosystem flux chamber studies [101] or for EC measurements [74, 128]. A QCL laser was used in the field experiment RISØ (§4.2) and in the field experiment in Easter Bush (§10.1.2), both as part of an intercomparison campaign

Cavity ring-down spectroscopy (CRDS)
Cavity ring-down spectroscopy (CRDS) increases the path length of the light beam by directing the laser signal into a cavity filled with the sampling gas. Due to two opposing mirrors, a path length up to several kilometers can be reached, which is one of the strong points of this method. The method does not focus on the direct absorption of light, but determines the rate of decrease of the laser signal intensity after the switch off of the laser and compares this to an empty (no sample gas) cavity via a so-called ring-down constant [145, 149]. The technique needs very precise alignment of internal optics and can therefore be expensive and of high maintenance.

Companies using this technique are for example Picarro (www.picarro.com) and Tiger Optics (www.tigeroptics.com). For example, Picarro produces an instrument which can simultaneously measure CO_2, CH_4 and H_2O at 10 Hz, thereby being suitable for EC measurements [145]. Ecosystem flux studies using and evaluating these instruments are for example Peltola [141] or Dengel (2011) for eddy covariance studies, or Baird (2010), Nickerson (2013) or Yu (2013) for flux chamber studies.

Off-Axis Integrated Cavity Output Spectroscopy (OA-ICOS)
Off-Axis Integrated Cavity Output Spectroscopy (OA-ICOS) is based on the same principle as cavity ring-down spectroscopy. The OA-ICOS uses a similar arrangement as a Herriott Cell: the laser beam is forced to follow an elliptical path on each mirror before continuing to the next mirror. This prevents the need of a very precise alignment of the internal optics, which makes it a cheaper and easier alternative to CRDS.

Los Gatos (www.logrinc.com) produces the only commercially available instrument which uses this method and delivers different type of instruments. For EC measurements, they offer the 10 Hz CH_4, CO_2 and H_2O analyzers, but also slower analyzers for different type of slower flux measurement techniques are available [114, 136]. Ecosystem flux studies using and evaluating the OA-ICOS technique are for example Tuzson (2010), Peltola (2014) or Wang (2013) in eddy covariance studies, or Baird (2010), Christiansen (2011) or Mastepanov (2008) in flux chamber studies. A Los Gatos instrument was placed in parallel to the FTIR-analyzer in Rocca4.

Methods not suitable for EC measurements

Photo Acoustic Spectroscopy (PAS) is based on the principle of infrared light energy being absorbed by gas molecules, however, in PAS the light energy is converted into pressure variations i.e. sound energy. The sound energy in the gas sample cell is then converted into electric signal

using a microphone. By use of an optical filter, different gases can be measured simultaneously, however not with eddy covariance required frequency of 10 Hz [115]. Ecosystem flux studies using and evaluating the PAS technique are for example Yamulki (1999), Iqbal (2013), Berhe (2009), Tirol (2014) and Christiansen (2011).

Non-Dispersive Infrared techniques are also based on infrared light absorption but the technique is only possible for single gases and with slower speed, thereby being suitable for flux chamber measurements. Many different companies produce this type of sensor. For ecosystem studies, the most commonly used are from LI-COR, Vaisala or Lumasense.

FTIR-analyzer in comparison to other instruments

In current day ecosystem exchange studies, different type of instruments are being used. For continuous flux measurements, mostly instruments using absorption spectroscopy are being operated. A clear difference can be made between fast instruments, which can measure with a speed of 10 Hz, and can be connected to eddy covariance measurements, and slower instruments, suitable for other flux methods. Nowadays, most ecosystem flux sites make use of eddy covariance systems, which are considered an efficient and qualitative method, which data can easily be compared between ecosystem flux sites. As shown above, suitable commercially available instruments are multiple, and their capabilities are increasing, especially now different greenhouse gases (CO_2, CH_4, N_2O, H_2O) can be measured simultaneously. For many years, the FTIR-analyzer had the advantage over other instruments of being able to measure different gases simultaneously and with high precision. However, as described, in recent years this advantage is devaluating now new developments cause other instruments to be also capable of measuring gases simultaneously and with high precision. Furthermore, other instruments are suitable for EC measurements, while the FTIR-analyzer is not. Also, the FTIR-analyzer is less mobile and relatively heavy in comparison to other instruments and has a high power demand [49].

When considering the FTIR-analyzer for ecosystem flux measurements, the previous concerns should be considered. However, more important is to realize the unique properties of the FTIR-analyzer, which still has many advantages over other instruments. The FTIR-analyzer still has the widest range of simultaneously measured gases, and obtains concentrations measurements with high precision, especially for 'difficult' gases such as N_2O. The concentrations measurements have shown to be stable over time and linear over a wide concentration range, which is unique [76]. Furthermore, the instrument and the software are flexible to connect to different flux methodologies simultaneously. But, most important, the FTIR-analyzer saves the spectra of the gases measured, giving the opportunity to re-analyze gases at a later stage or for different gases when new retrieval information is available. Also, multiple slower micrometeorological methods have proven to capture the main flux patterns and correlate well with eddy covariance methods. For these reasons, we consider the FTIR-analyzer a valuable addition to ecosystem flux sites, which can attribute to ecosystem flux studies in many different ways. However, as will also be shown in §5.2, an FTIR-analyzer to measure greenhouse gas fluxes is even a stronger tool when supported by on site EC measurements.

10.2 Additional laboratory and field measurements

10.2.1 Cross sensitivities and calibration data for the FITR-analyzer

Pressure, water content and CO_2 cross sensitivities
Measurements performed by the FTIR-analyzer need correction for (deviations in) pressure, water content and CO_2 concentration. Correction is done by the following equation:

$$gas\_X_{corrected} = gas\_X_{reading} - ((P - P_0) * P_X) - ((Q - Q_0) * Q_X) - ((C - C_0) * C_X) \quad (10.1)$$

wherein gas$_X_{corrected}$ is the corrected concentration reading of gas X (ppm or ppb), gas$_X_{reading}$ is the uncorrected raw concentration reading of gas X (ppm or ppb), P is the cell pressure (mb), P_0 is the standard cell pressure (mb), P_X is the correction factor for gas X, Q is the water content (ppm), Q_0 is the standard water content (ppm), Q_x is the correction factor for gas X, C is the CO_2 concentration (ppm), C_0 is the standard CO_2 concentration (ppm), and C_x is the correction factor for gas X.

The standard values are:

C_0=380 ppm
Q_0= 0 ppm
P_0=1013 mb

The available pressure, water and CO_2 cross sensitivities are shown in Tables 10.4, 10.5 and 10.6.

For most data processing performed during the PhD, the values published by Hammer (2013) were used. For the measurements made at the fieldsite Poplar (§4.4), in which cell pressure sometimes dropped to 750 mb, the pressure corrections from §10.2.2 were used.

Table 10.4: Pressure, water and CO_2 cross sensitivity correction factors from Ecotech, delivered with the instrument.

	CO_2	**$\delta^{13}CO_2$**	**CH_4**	**N_2O**	**CO**
P_X	0.00788263	-0.00138193	0.0177577	0.011854	0.014999
Q_X	0.00340349	-0.00215766	0.00522149	0.0038086	-0.00253255
C_X	-	-2921.7	-0.00195939	-0.00274095	0.00251016

Table 10.5: Pressure, water and CO_2 cross sensitivity correction factors from Hammer 2013.

	CO_2	**$\delta^{13}CO_2$**	**CH_4**	**N_2O**	**CO**
P_X	0.0085	0.005	0.031	0.007	0.006
Q_X	0.04	-	< 0.2	-	< 0.2
C_X	-	0.006	-		< 0.015

Table 10.6: Measured pressure cross sensitivity correction factors as measured at ambient concentrations. More elaborated pressure sensitivities are shown in §10.2.2.

	CO_2	**$\delta^{13}CO_2$**	**CH_4**	**N_2O**	**CO**
P_X	0.018	0.006	0.035	0.0083	-0.005

Calibration procedure

For the calibration procedure, two calibration gases were used, which were produced by Deuste Steiniger GmbH and gravimetrically analyzed. After purchasing of the calibration gases, calibration gases were send to the Max Planck Institute for Biogeochemistry in Jena for further analyses. The concentrations as given by Deuste Steiniger GmbH and as measured by the Max Planck Institute for Biogeochemistry in Jena are given in Table 10.7. Calibration gas concentration readings were first corrected with the cross sensitivity parameters which are displayed above (Tables 10.4 -10.6). For the correct determination of $\delta^{13}CO_2$, the uncorrected values for CO_{2_2} and CO_{2_1} were taken to calculate $\delta^{13}CO_2$, and then the correction factors for $\delta^{13}CO_2$ were used. As an example, Figure 10.11 shows the calibration gas measurements performed during the field campaign Rocca4. The values on the x-axis show the measured calibration gas concentration readings, and the values on the y-axis show the calibration gas concentration values, as measured by the Max Planck Institute for Biogeochemistry in Jena. Table 10.7 shows the values of the calibration gases, as measured by Max Planck Institute in Jena. The last row shows the determined gas concentrations of the so called 'green tank', which was used as a drift gas during several experiments.

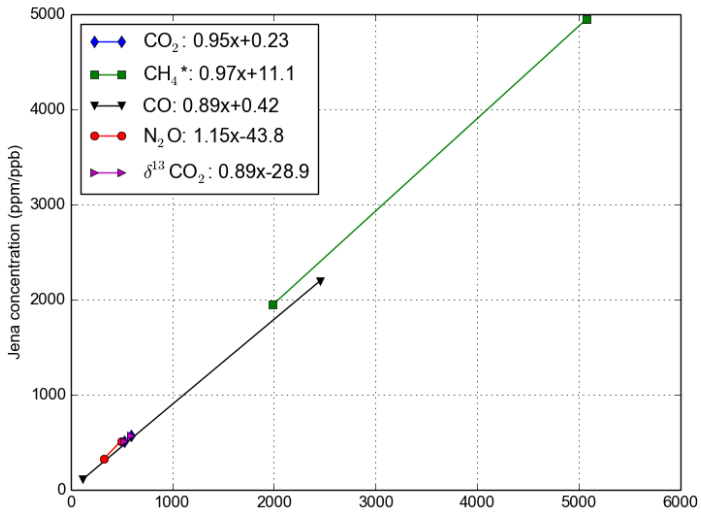

Figure 10.10: Example of calibration curve determination measurements. Shown measurements are performed at fieldsite Rocca4 and are derived from gas tank M153815 and M153778.

Table 10.7: Overview of the used calibration gases and drift gas concentration values. Numbers between brackets indicate standard deviation. The calibration gas concentrations were determined by Max Planck Institute in Jena, the 'green tank' concentrations were determined by use of the determined calibration curves.

	CO_2 (ppm)	$\delta^{13}CO_2$ (‰)	CH_4 (ppb)	N_2O (ppb)	CO (ppb)
	Jena value	**Jena value**	**Jena value**	**Jena value**	**Jena value**
M153815	566.9 (0.13)	-11.5	1944.9 (2.21)	323.7 (0.10)	2189.2 (5.89)
M153778	505.0 (0.03)	-5.8	4948.9 (2.51)	510.0 (0.25)	105.9 (0.33)
Green Tank	379.7	-7.9	1796.8	328.79638	285.5

10.2.2 Measurement of pressure cross sensitivities

Introduction

During the field campaign Poplar (Methodology in §4.4, Results in §5.3), problems with the chemical dryer material caused a varying resistance in the sampling lines, which resulted in a varying final pressure in the cell during the measurements. Cell pressure during the field campaign varied between 700-970 mb. To correct the measurements for this pressure variation, a pressure sensitivity experiment was performed.

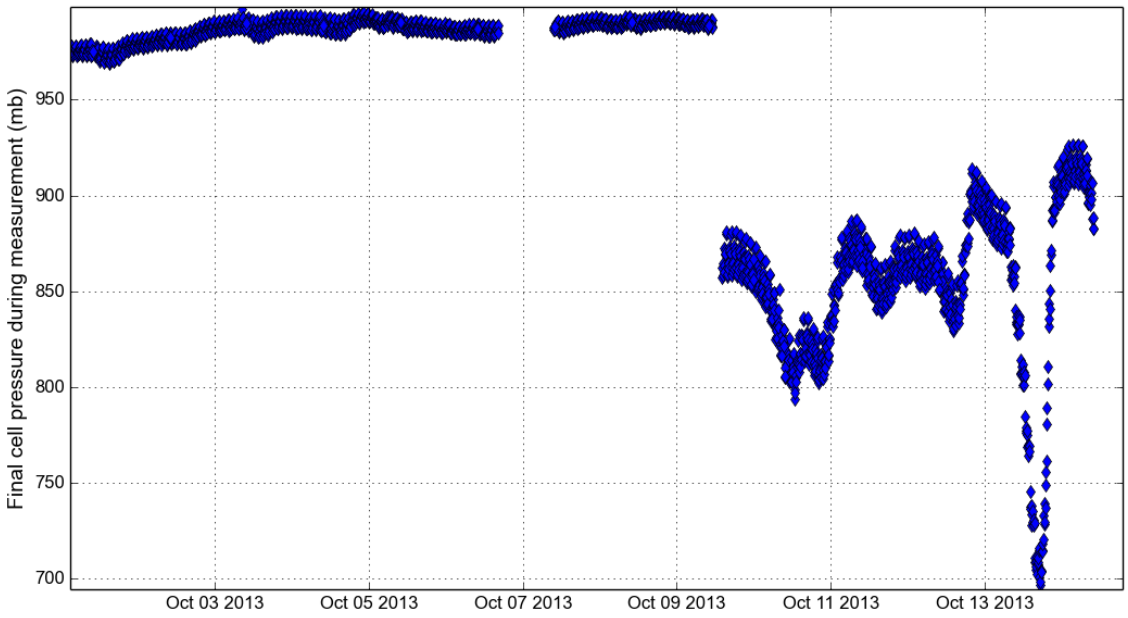

Figure 10.11: Varying cell pressure during the campaign at fieldsite Poplar. The cell pressure was varying due to problems with the chemical dryer material.

The calibration gases M153778 and M153815, and the drift gas the 'green tank' were used to assess the pressure sensitivity of the FTIR-analyzer over a large pressure range. Information about these calibration gases can be found in Table 10.7. The calibration gases M153778 and M153815 were measured twice over different pressures, and the 'green tank' was measured three times over different pressures. Between 900 and 1000 mb, three pressures steps were aimed to be made. Between 600-900 mb, pressure steps of approximately 50 mb were made.

Results and conclusion

The results of the pressure sensitivity experiments are shown in the Figures 10.12 to 10.15. Every figure is divided into three sub figures, each representing a different calibration gas with its own specific concentrations. The upper figure shows measurements from the 'green tank', the middle figure shows measurements from the calibration gas M153778, and the lower figure shows measurements from the calibration gas M153815. Measurements shown in the same color indicate measurements performed during the same experiment. At every pressure step, two measurements were made.

The different experiments were performed on different days and were processed with different background spectra, which explains the difference in observed absolute concentrations. In the

legend, the calculated slope per experiment is shown. The first value is the slope calculated over the entire experiment, the second value represents the slope over 850-1000 mb. Pressures are expressed as a reference to the standard pressure of 1013 mb. In the following text, the observed pressure values are compared to the values from Ecotech (2011), and Hammer (2013).

For $\mathbf{CO_2}$, a stronger pressure dependency was found between 850-1000 mb, in comparison to values found for the whole pressure range (600-1000 mb). The pressure dependency between 850 and 1000 mb for ambient concentrations (380-600 ppm) can be considered linear and was between 0.011 and 0.018, which is much larger than found by Ecotech (0.0078) and Hammer (0.0085). A stronger non-linear behavior was found for higher CO_2 concentrations.

For **CO**, a weak negative pressure dependency was found for ambient concentrations (100-400 pbb) of approximately -0.004 to -0.006, which is different from the positive pressure sensitivities found by Ecotech and Hammer (0.001499 and 0.006 respectively). However, either positive or negative, the correction is very small and will only be important under strong pressure fluctuations. A stronger positive pressure sensitivity of 0.025-0.027 was found for higher CO concentrations.

For $\mathbf{CH_4}$, a stronger pressure dependency was found between 850-1000 mb, in comparison to values found for the whole pressure range (600-1000 mb). The pressure dependency between 850 and 1000 mb for ambient concentrations (1800-2200 ppb) can be considered linear and was between 0.032 and 0.034, which is close to the value found by Hammer of 0.031. For the higher concentration range, stronger pressure sensitivities of 0.0675 and higher were found.

For $\mathbf{N_2O}$ a stronger pressure dependency was found between 850-1000 mb, in comparison to values found for the whole pressure range (600-1000 mb), and a quadratic equation fitted the pressure sensitivity measurements best. A linear fit over the 850-1000 mb range would result in a value of approximately 0.010-0.011 (not shown), which is similar to the values reported by Hammer (0.011).

Also for $\delta^{13}\mathbf{CO_2}$ a stronger pressure dependency was found between 850-1000 mb, in comparison to values found for the whole pressure range (600-1000 mb), and a quadratic equation fitted the pressure sensitivity measurements best. A linear fit over the 850-1000 mb range would result in a value of approximately 0.005-0.0069 (not shown), which is similar to the values reported by Hammer (0.006).

As an example, Figure 10.16 shows measured $\delta^{13}CO_2$ values (in a Keeling plot) in the field experiment Poplar with and without the new pressure correction: as can be seen, quite some noise can be explained by the sensitivity of the analyses to pressure fluctuations. Therefore, for future experiments, it is important to keep the cell pressure as stable as possible.

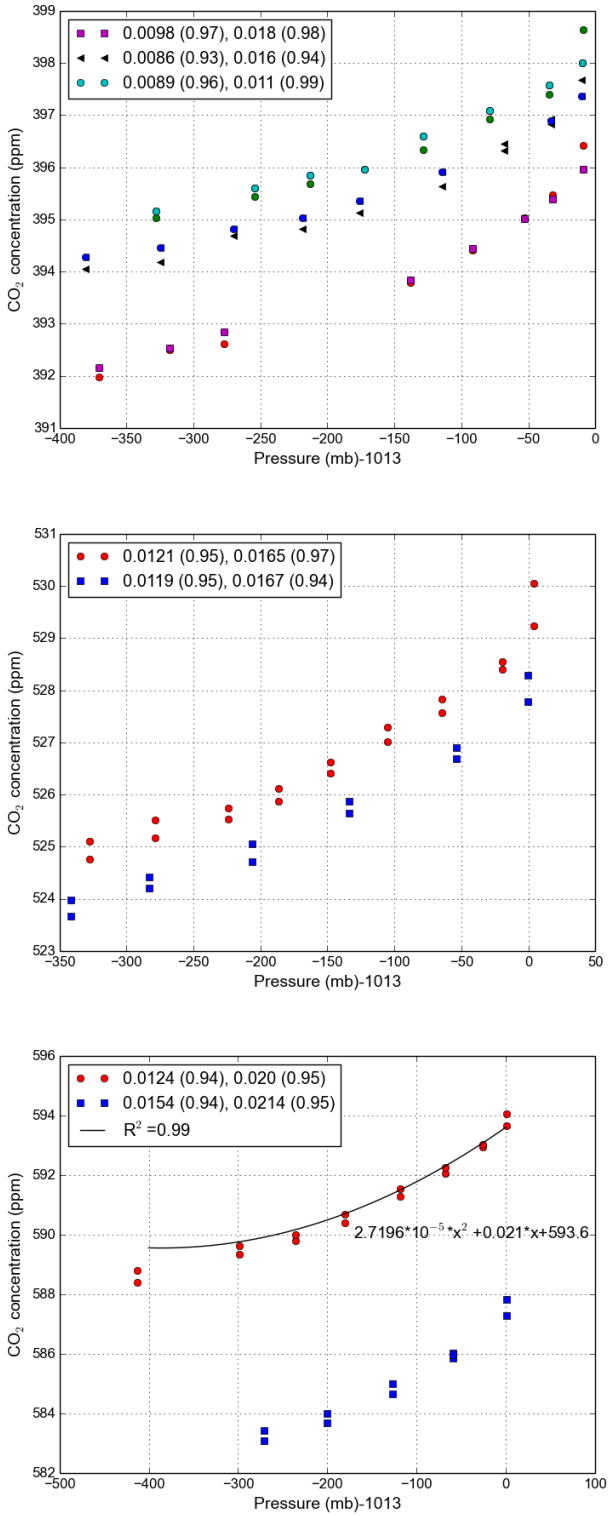

Figure 10.12: CO_2 concentrations measured at different cell pressures. Measurements shown in the same color indicate measurements performed during the same experiment. At every pressure step, two measurements were made. The first value presented in the legend is the slope calculated over the entire experiment, the second value represents the slope over 850-1000 mb. The upper figure shows concentrations measured from the 'green tank' gas, the middle figure shows concentrations measured from the calibration gas M153778, the lower figure shows concentrations measured from the calibration gas M153815.

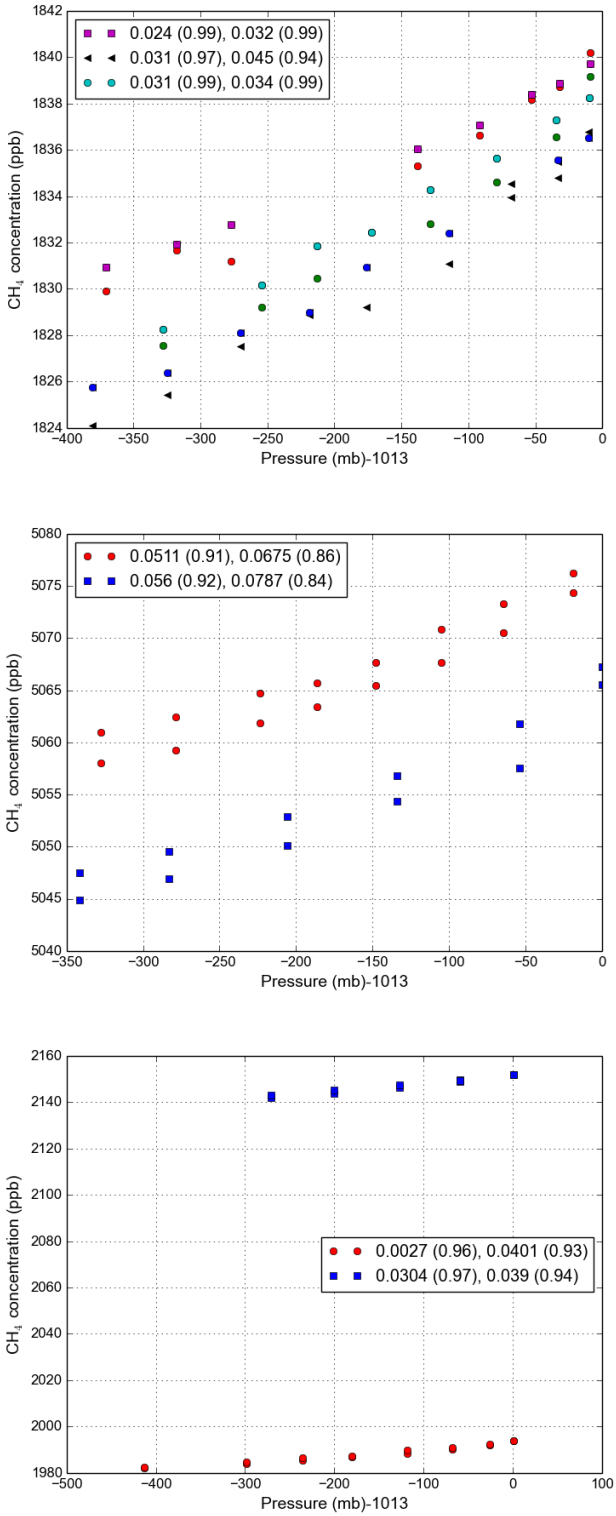

Figure 10.13: CH_4 concentrations measured at different cell pressures. Measurements shown in the same color indicate measurements performed during the same experiment. At every pressure step, two measurements were made. The first value presented in the legend is the slope calculated over the entire experiment, the second value represents the slope over 850-1000 mb. The upper figure shows concentrations measured from the 'green tank' gas, the middle figure shows concentrations measured from the calibration gas M153778, the lower figure shows concentrations measured from the calibration gas M153815.

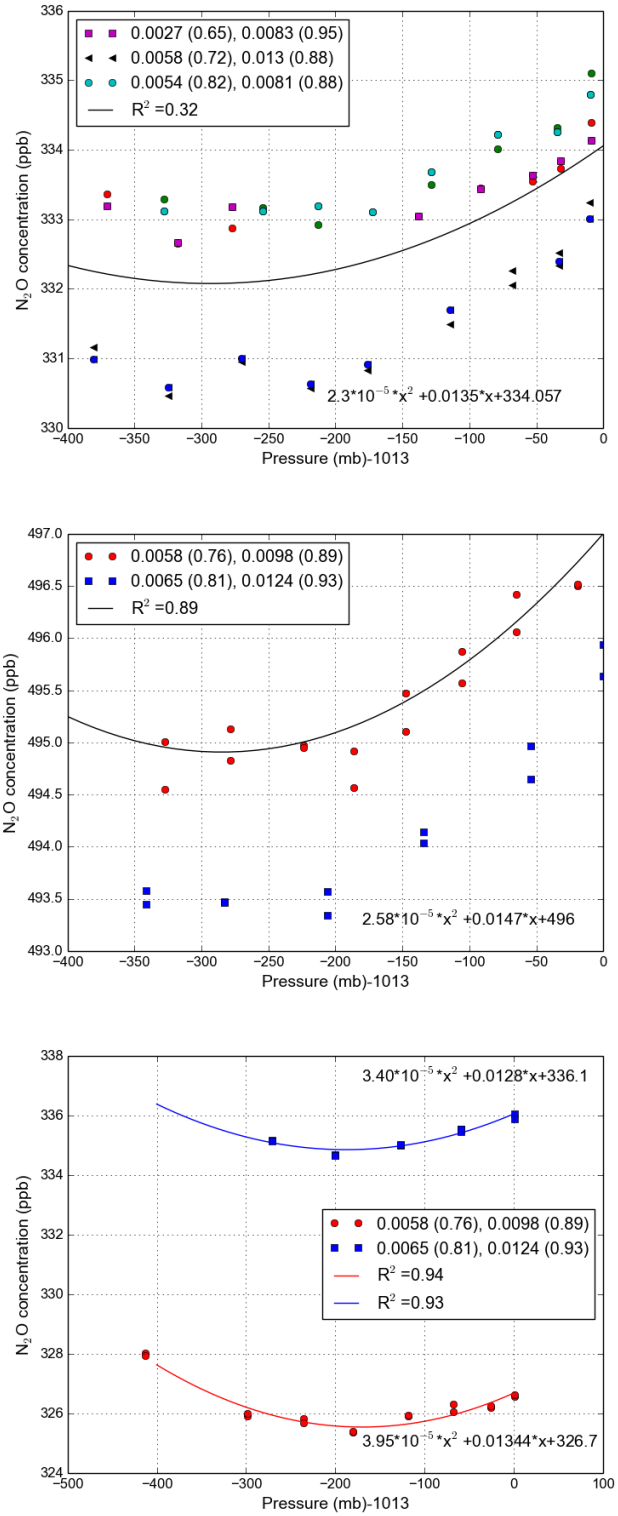

Figure 10.14: N_2O concentrations measured at different cell pressures. Measurements shown in the same color indicate measurements performed during the same experiment. At every pressure step, two measurements were made. The first value presented in the legend is the slope calculated over the entire experiment, the second value represents the slope over 850-1000 mb. The upper figure shows concentrations measured from the 'green tank' gas, the middle figure shows concentrations measured from the calibration gas M153778, the lower figure shows concentrations measured from the calibration gas M153815.

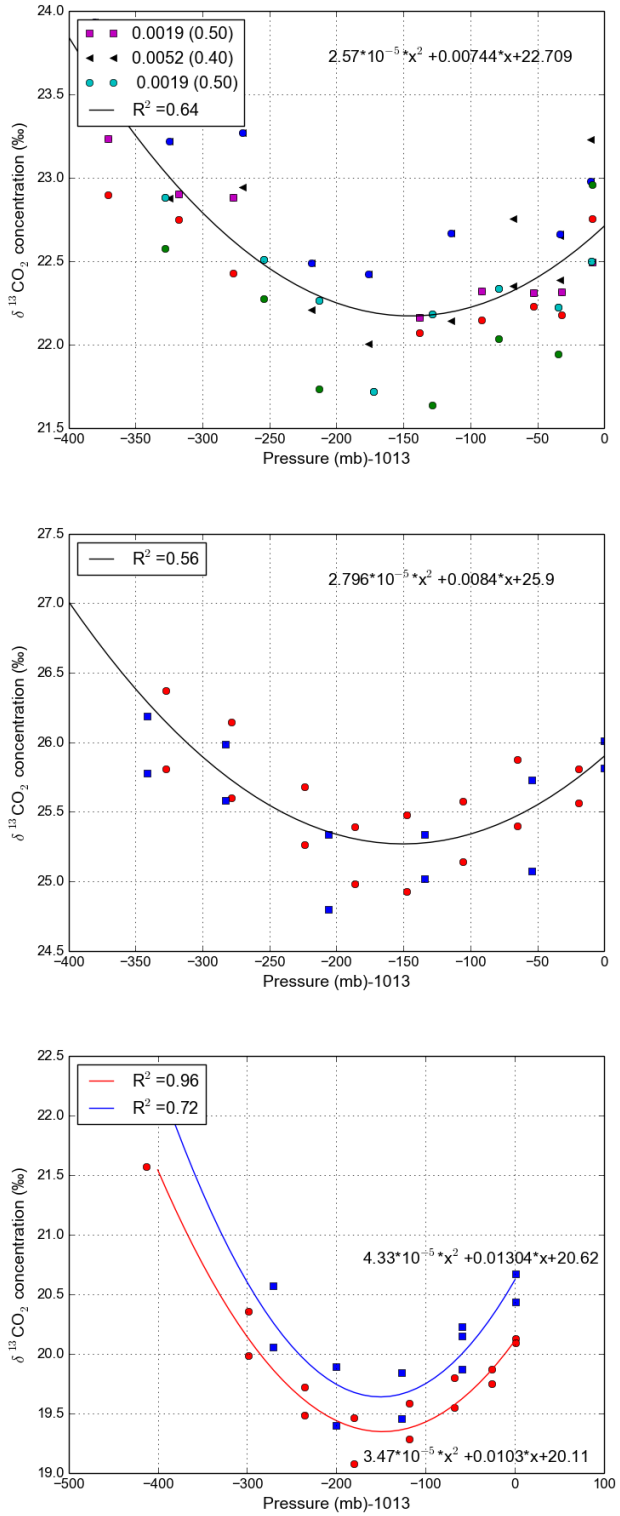

Figure 10.15: $\delta^{13}CO_2$ concentrations measured at different cell pressures. Measurements shown in the same color indicate measurements performed during the same experiment. At every pressure step, two measurements were made. The first value presented in the legend is the slope calculated over the entire experiment, the second value represents the slope over 850-1000 mb. The upper figure shows concentrations measured from the 'green tank' gas, the middle figure shows concentrations measured from the calibration gas M153778, the lower figure shows concentrations measured from the calibration gas M153815.

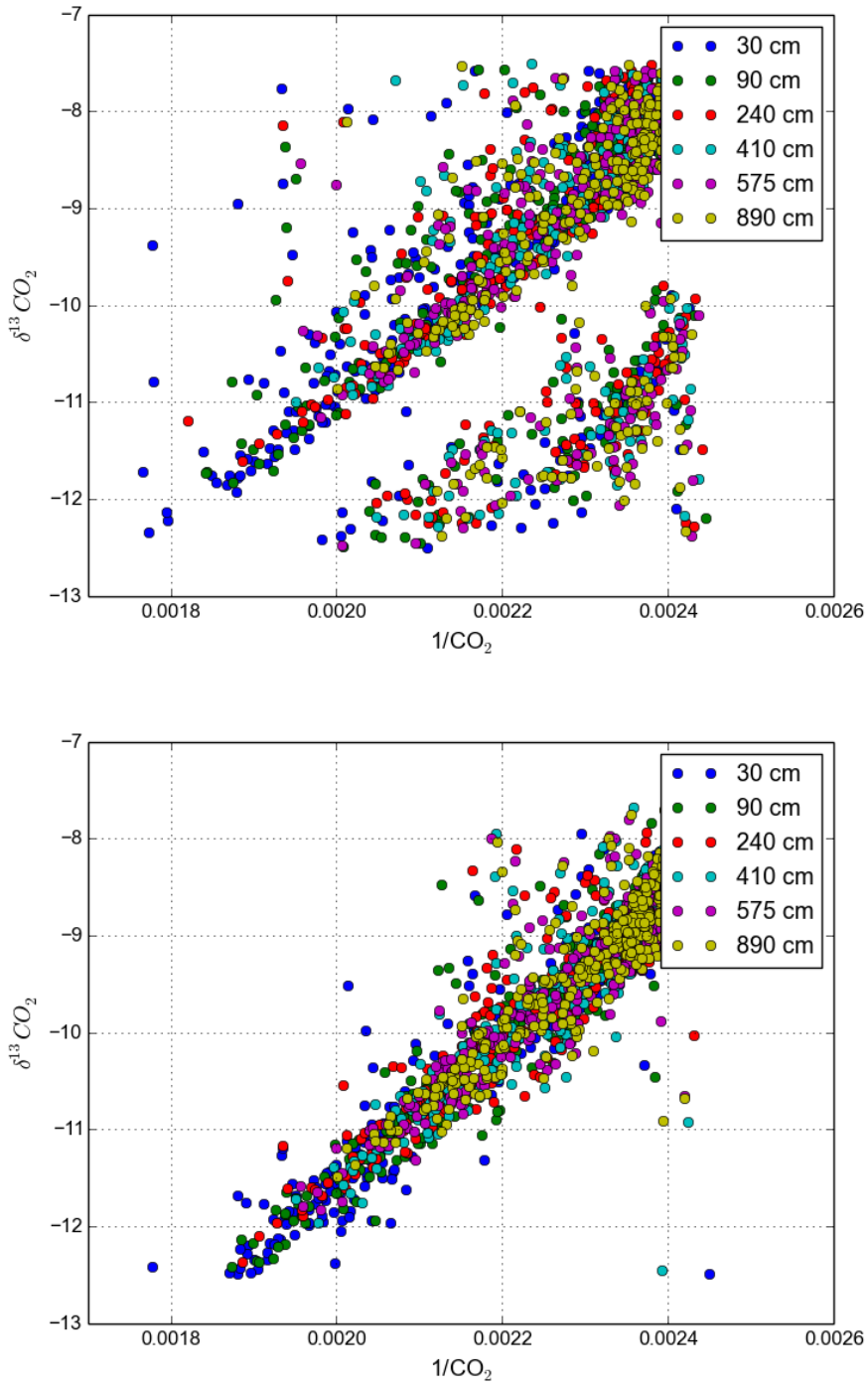

Figure 10.16: $\delta^{13}CO_2$ values for the campaign at the fieldsite Poplar with regular pressure corrections (upper figure) and with the new pressure correction (lower figure).

10.2.3 Blank test for internal CO production

During the different field experiments, it was observed that CO sometimes is produced/formed inside the PTFE lines. The production of CO was tested in the field campaign RISØ. One FG line was placed in the sun for 3 hours without being flushed. The FTIR-analyzer was constantly measuring another line in flow mode but was, after 3 hours, suddenly switched to the sun exposed FG line: this moment is indicated with a black vertical line in Figure 10.17. In Figure 10.17, a sudden CO concentration jump from 150 to 450 ppb is visible, which is expected to be caused by the accumulated CO inside the sampling line.

As a very rough estimate, the following is calculated: 300 ppb difference in a 3.5 L cell is caused by an addition of 40 nmol. This is produced in 3 hours over 20 meters, which results in a production of 0.67 nmol CO per meter PTFE sampling line per hour. For the measured FG line, it remains unclear if the CO is produced internally by the PTFE material, or produced by internal air chemistry, or that the FG line has become polluted by previous experiments. However, it remains clear that CO production can occur and that it should be checked for in field experiments.

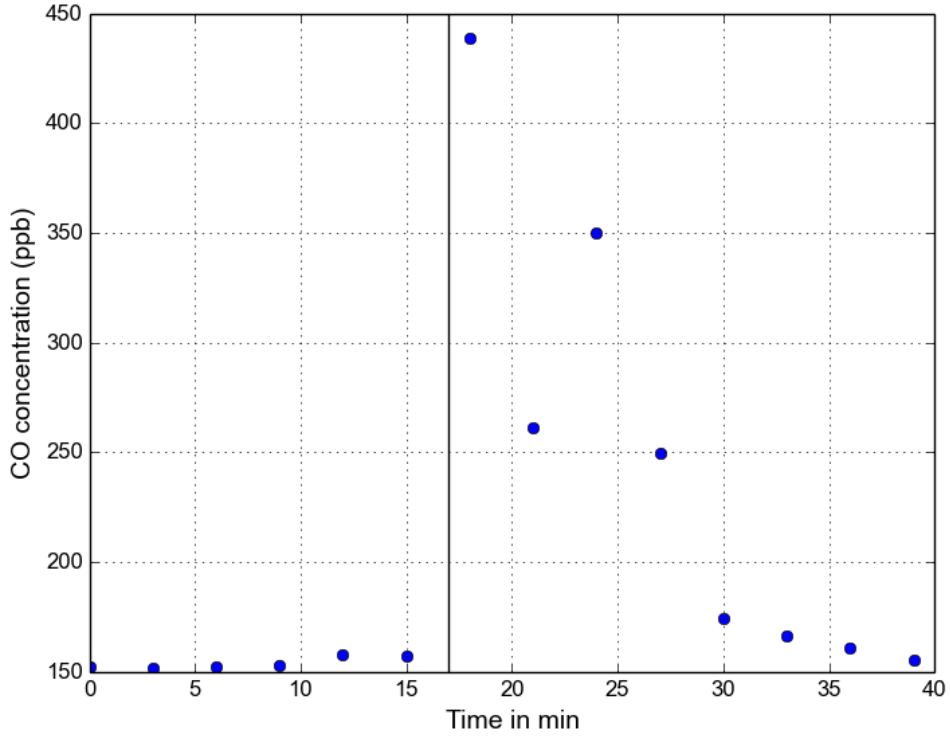

Figure 10.17: Internal CO production by PTFE sampling lines. CO production was observed in one of the FG sampling lines during the campaign at fieldsite RISØ. A sampling line of approximately 20 meters was laying in the sun for 3 hours and was not flushed. After the 3 hours, (this moment is indicated with the black vertical line), the FG inlet was sampled and measured by the FTIR-analyzer in flow mode by 3-min spectra.

For flux gradient measurements in Rocca4, the possible interference with internal CO production was avoided by replacing the PTFE lines with stainless steel lines. The pieces of PTFE

tubing which were still used, were covered with aluminum foil. Also, for the FG experiment, it was made sure that sampling lines were continuously flushed. For the chamber system, the use of stainless steel tubing was not possible: 1/4 inch stainless steel tubing is not practical for field experiments (not bendable), and 1/8 inch tubing is too small for the required sampling speed over such long distances. Therefore, to quantify possible CO production taking place in the flux chamber measurement set-up, twice an experiment was performed.

Figure 10.19 shows the results from the 'sealing' experiment performed in Himmelmoor. The left figure shows the usual CO concentration increase during chamber closure, the right figure shows the CO concentration increase during chamber closure when the bottom of the soil collar was 'sealed' (see Figure 10.18). Figure 10.19 shows the results from the 'sealing' experiment performed in Rocca4. The left figure shows the usual CO concentration increase during chamber closure, the right figure shows the CO concentration increase during chamber closure when the bottom of the soil collar was 'sealed' (see Figure 10.18).

Small CO concentration changes are visible during soil collar sealing, in comparison to usual CO concentration changes. For example, a 10 ppm increase was observed in the sealed chamber, in comparison to the 'usual' 50 ppm increase. This could be caused by internal production of the set-up. However, it cannot be excluded that the CO produced by the soil by thermal degradation, does not still enter the flux chamber. Therefore, it is hypothesized that the remaining CO increase observed in the chamber during the sealing experiment is a cumulative effect of both, and that the internal chamber CO production is at the most responsible for 20% of the observed CO chamber fluxes.

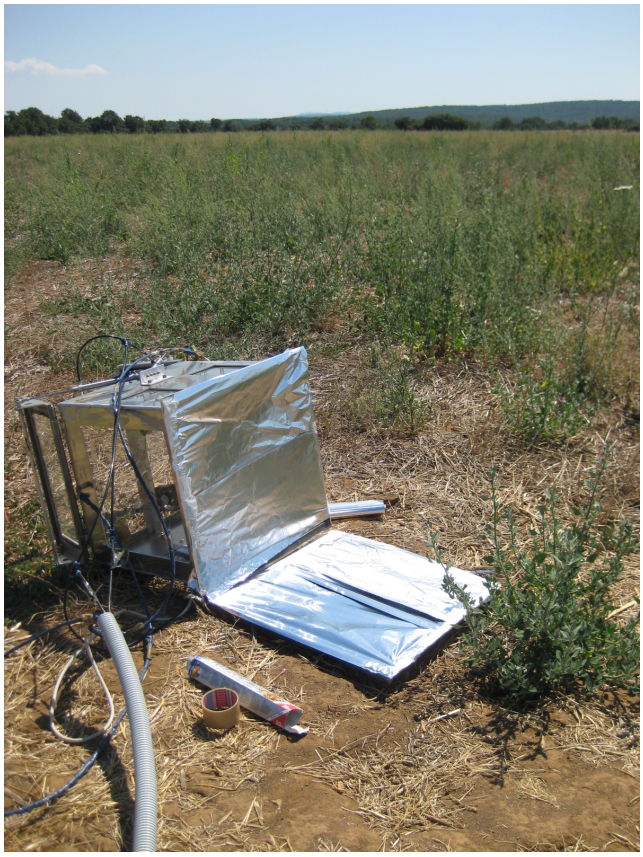

Figure 10.18: Picture of the 'sealing' experiment in Rocca4. The experiment in Himmelmoor was done in the same way.

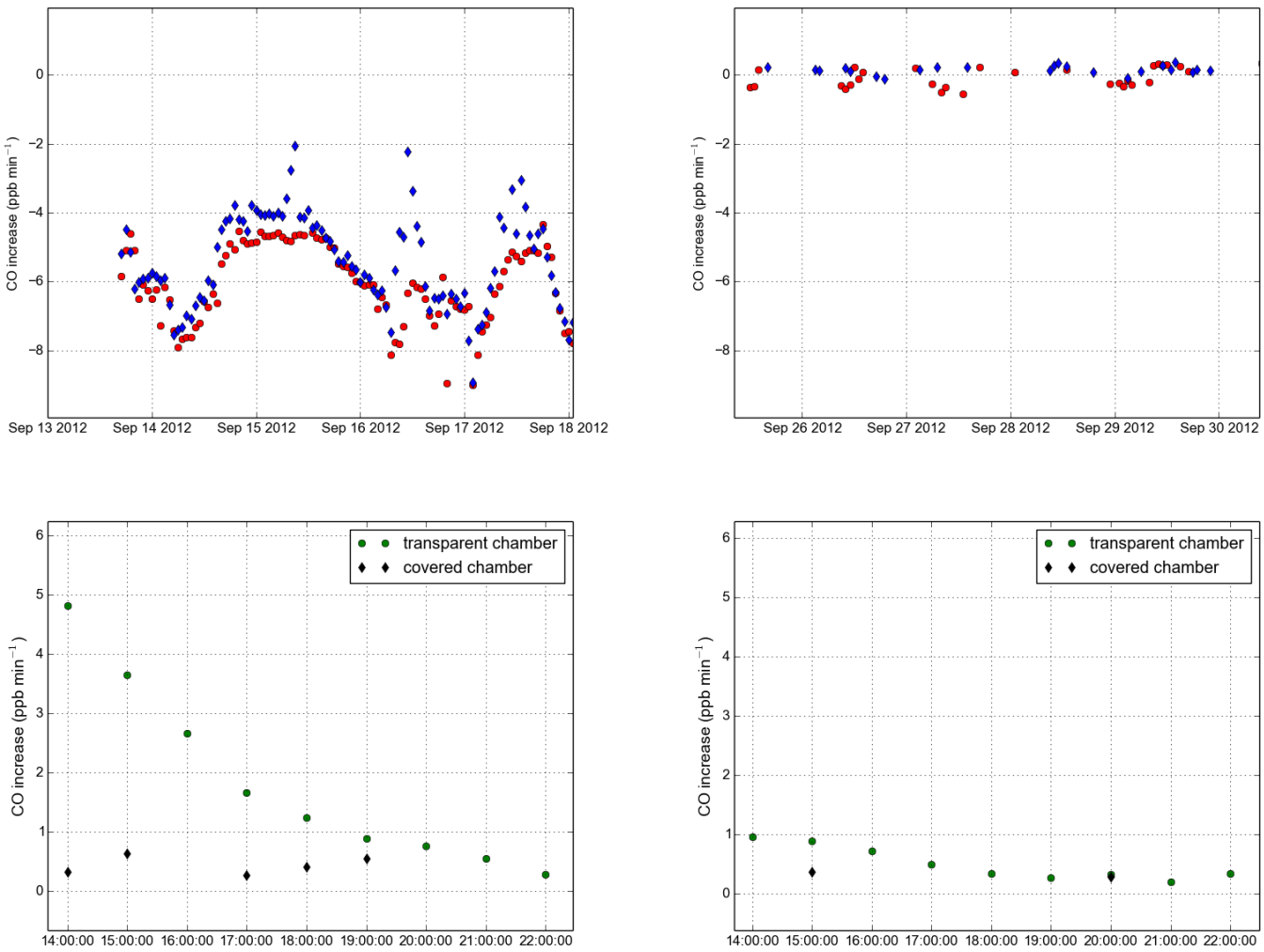

Figure 10.19: Results of the test for internal CO production measurement set-up. Upper figures: results from the covering experiment at the fieldsite Himmelmoor. The left figure shows the CO concentration increase (ppb per min) during chamber closure without soil collar coverage, the right figure shows the CO concentration increase (ppb per min) during chamber closure with soil collar coverage. Both chambers were transparent. The shown values are derived from a linear regression with $R^2 > 0.90$. Lower figures: results from the covering experiment at the fieldsite Rocca4. The left figure shows the CO concentration increase (ppb per min) during chamber closure without soil collar coverage, the right figure shows the CO concentration increase (ppb per min) during chamber closure with soil collar coverage. Chamber A (green circles) was transparent, and chamber B (black diamonds) was opaque. The shown values are derived from a linear regression with $R^2 > 0.90$.

10.2.4 Determination of δ^{13}C of organic material by use of the FTIR-analyzer

Introduction

As part of the photo and thermal degradation laboratory experiment, described in Chapter 6, soil and grass samples were obtained from the fieldsite Rocca4 (§4.3) and sent to Bremen in November 2014 (grass samples) and January 2015 (soil samples). As described in §6.2.2, the samples were dried for over 72 h to reduce the biological respiration as much as possible, which is necessary for studying abiotic carbon fluxes. Every experiment consisted of the placement of organic material in a metal tube (photodegradation experiment) or glass flask (thermal degradation experiment), and samples were in a closed loop connected to the FTIR-analyzer, resulting in increasing gas concentrations (if production was present). The fact that data was sampled in a closed loop, and over a range of CO_2 concentrations, makes the dataset also suitable for the creation of Keeling plots, to be able to determine the δ^{13}C of the added CO_2.

As can be read in Chapter 6, CO_2 fluxes from dried grass and soil were very minor, wherefore most CO_2 concentration ranges were less than 20 ppm. Therefore, in most cases, accurate Keeling plot intercept estimates were not possible. The few data sets which were suitable for Keeling plots are shown below.

Results

In the photodegradation experiment (6 November 2014), grass samples were dried wherefore CO_2 production was very minor (§6.3.3). However, one sample was rewetted to test whether respiration fluxes were easily triggered by moisture. This sample was measured twice. Large decomposition fluxes were observed, in light and dark conditions. The CO_2 concentration range was 800 ppm (450-1250 ppm). This data was not used for the photo and thermal degradation experiment. Figure 10.20 shows the Keeling plot created from this sub-experiment, both experiments showed a Keeling plot intercept of -33.05‰.

For the grass thermal degradation experiment (20-26 November 2014), grass samples were also dried wherefore CO_2 production was very minor (§6.3.3). No rewetting experiment was performed during this experiment. Figure 10.21 shows data with long incubation time (CO_2 concentration range: 40 ppm) and data with a relative good fit ($R^2 > 0.50$) even within a small CO_2 concentration range (20 ppm).

During the soil thermal degradation experiment (8-9 January 2015), a small rewetting experiment was performed. The data from the rewetting experiment (red circles in Figure 10.22) and data from experiments with extended incubation times (Figure 10.22, other data), could be used for Keeling plot intercept determination.

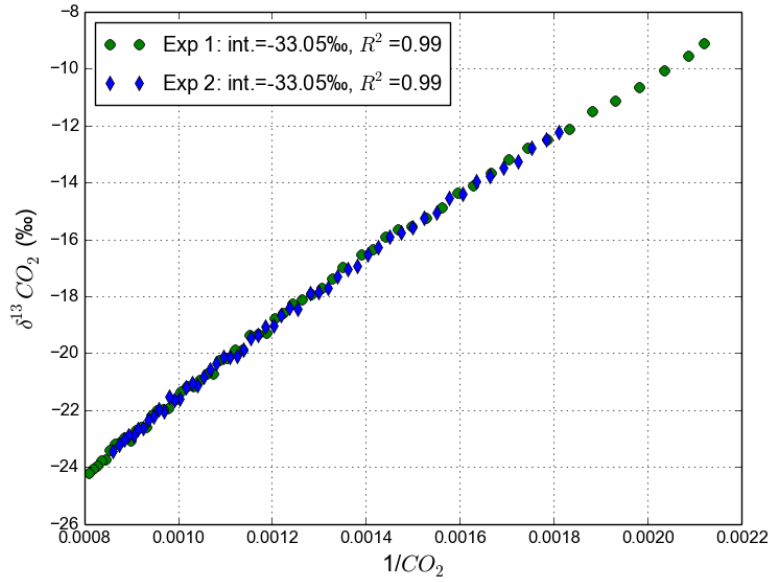

Figure 10.20: Laboratory Keeling plots for the data from the photodegradation experiment. The shown **grass** sample was rewetted and measured twice.

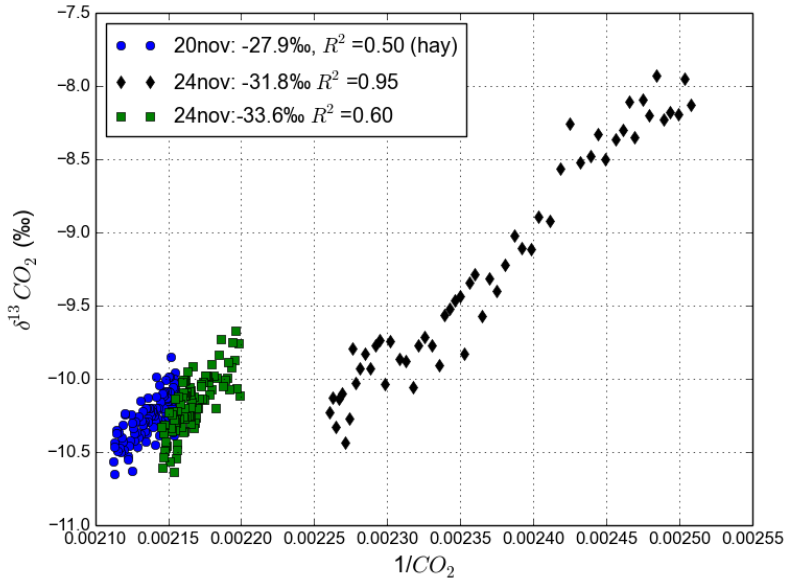

Figure 10.21: Laboratory Keeling plots for the data from the thermal degradation experiment for different **grass** samples. The shown data sets are from long incubation times (CO_2 concentration range: 40 ppm), or have a relative good fit ($R^2 > 0.50$) even within a small CO_2 concentration range (20 ppm).

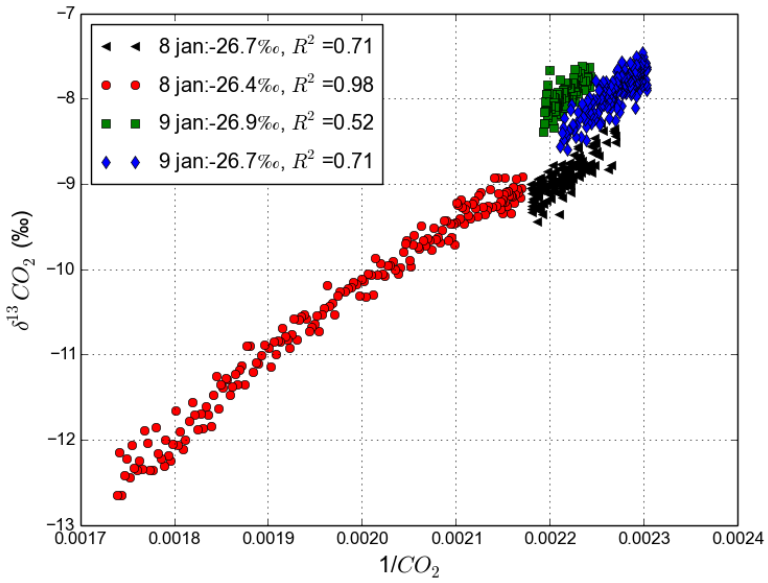

Figure 10.22: Laboratory Keeling plot of data from thermal degradation experiment for **soil** samples. Shown are data sets with long incubation time (CO_2 concentration range: 40 ppm) and data from a rewetting experiment (red circles).

Conclusion

The laboratory experiment was not aimed at isotopic analyses wherefore the preparation of the samples (drying) and the amount of samples was not optimal. Also, no isotopic calibrations have been performed, wherefore absolute values might be off. However, a quick rewetting experiment for grass samples (during the photodegradation experiment) and for soil samples (during the thermal degradation experiment), showed that the samples were not biologically dead, but rather in a dormant state: the addition of just a few drops of water resulted in major biological production in both sample types. These data sets could be used to determine the δ^{13}C of incubated organic material.

Based on the experimental data with the highest R^2, a δ^{13}C of approximately -33‰ is expected for the grass material (Figure 10.20). Based on the experimental data, shown in Figure 10.22, a δ^{13}C of approximately -26‰ is expected for the soil material. For soil material, the intercept value fits in the range of expected values, based on Keeling plots performed during the field experiment (Chapter 7).

The grass material showed the unlikely largely depleted value of -33‰, which is not fitting to regular C3 plants. Also, it is not expected that soil and grass values differ so much, since most soil carbon originates from grass material and only soil ^{13}C enrichment, in comparison to fresh grass material, is expected [50, 195]. For further investigation, more samples would need to be analyzed and the determined δ^{13}C value for soil and grass sample should originate from a fixed methodology with larger CO_2 concentration ranges and isotopic calibrations. However, even when considering the limitations of this experiment, this experiment shows that it is possible to determine (the range of) δ^{13}C of organic material by use of the FTIR-analyzer.

10.3 General concentration and flux measurements at the different field experiments

Concentration and flux measurements have been performed during four different field campaigns. In the thesis, only part of the data was shown. In this appendix paragraph, all concentration measurements and fluxes are shown so that this paragraph provides an overview of fluxes measured in the different ecosystems. A general comparison between the different flux rates observed in the different ecosystems is shown in Figure 10.8. The flux chamber fluxes, the flux gradient fluxes and the concentration data from the campaign at fieldsite Himmelmoor will shortly be discussed (§10.3.1), the data from the other field campaigns have been discussed elsewhere in the thesis.

Table 10.8: Overview of measured fluxes during the different campaigns. The fluxes from Himmelmoor and RISØ are based on flux chamber (FC) measurements. For the fieldsite Rocca4, also flux gradient (FG) measurements are available.

	FC Himmelmoor: dry position	FC Himmelmoor: wet position	FC RISØ	FC Rocca4	FG Rocca4
CO_2 fluxes	0 to 20	0 to 2	0 to 8	0 to 10	0 to 10
CH_4 flux	-4 to 2	-2 to 1	-1 to 1	-2 to 2	0 to 20
CO fluxes	-2 to 8	-1 to 3	-0.5 to 0	-1 to 3	0 to 15
N_2O fluxes	0-60	0-12	0 to 3.5	0 to 0.2	-1 to 1

10.3.1 Himmelmoor

During the field experiment 'Himmelmoor', some of the pumps which were used to lead air from the FG tower to the sampling bags, were leaking (for more information, see §4.5). The leaking of the pump connected to bag 2 was so severe that data could not be used for flux gradient measurements. Therefore, fluxes derived from the bag-pair '2 and 4' are not shown. The start and degree of the leaking of the other pumps could not be determined, therefore the FG concentration data but especially the calculated FG fluxes should be interpreted with caution.

Flux gradient measurements
Figure 10.23 shows the concentrations of the gases CO_2, CH_4, CO, and N_2O during the field campaign. The missing concentration data is caused by the filtering for high water levels or leaking sampling bags. Figure 10.23 shows several concentrations peaks for the different gases, for example in the end of August (zoom in in Figure 10.24) and in November (zoom in in Figure 10.25). The large CO_2 concentration changes in August are accompanied by a similar concentration change pattern for CH_4 and N_2O (Figure 10.24), but not for CO. A similar pattern was observed end of November. The beginning of November however showed an increase of all gases at the same time, including the CO concentrations (Figure 10.25). Studying the ratios between the different gases can give an indication of the source of the concentration change. A rise in CO_2 and CH_4 accompanied by a rise in CO can indicate industrial sources, while the absence of a CO concentration peak can indicate fluxes from inside the ecosystem.

The fluxes shown in Figure 10.26 show decreasing emissions for all gases during the field campaign. CO_2 and N_2O fluxes even seem to indicate uptake processes during the second part of the field campaign. However, as mentioned before, the flux data should be interpreted with caution

since the FG data are highly sensitive to the possible leaking pumps.

Flux chamber measurements on dry location
Flux chamber measurements performed at the dry wall (Figure 4.1) are shown in Figure 10.27: only measurements derived from linear regression fits with $R^2 > 0.90$, are shown. Chamber A (red circles and blue diamonds) and chamber B (green squares) were not moved during this time. Chamber A was covered at 16 August as part of the photodegradation experiment. Large CO_2 emissions were observed of up to 20 μmol m^{-2} s^{-1}, which did not seem to be influenced by the covering of the chamber. As well CO uptake as emission was observed, most likely as a result of biological soil CO uptake and abiotic thermal degradation [183]. The CO emissions were influenced by the chamber coverage and showed lower CO emission/more CO uptake after the covering, possibly indicating a reduced thermal degradation flux [183]. CH_4 emissions were high but very irregular. N_2O emissions were very high and fluxes up to 60 nmol m^{-2} s^{-1} were measured.

Flux chamber measurements on wet location
Flux chamber measurements performed at the wet location (for map, see Figure 4.1) are shown in Figure 10.28: only measurements derived from linear regression fits with $R^2 > 0.90$, are shown. During the shown period, chamber A (red circles) and chamber B (blue diamonds) were not moved and both chambers were transparent. Emissions were very small in comparison to the dry wall location. CO_2 emissions of maximum to 1.6 μmol m^{-2} s^{-1} were observed. CH_4 fluxes were usually below 1 nmol m^{-2} s^{-1}, but peak fluxes of 5 nmol m^{-2} s^{-1} were observed (not shown in Figure 10.28). Clear CO uptake fluxes were observed which were largest during daytime. This may point at biological soil uptake, which is usually larger during warmer temperatures. No CO emission was observed, so it is unclear whether thermal degradation fluxes occurred. Also here, clear N_2O fluxes were observed, but much smaller than measured at the dry location. Most days, fluxes of 1 nmol m^{-2} s^{-1} were observed, but peak emissions of 10 nmol m^{-2} s^{-1} were also measured. Differences between chamber positions in the wet region were large: chamber B consistently showed lower N_2O and CO_2 emissions and lower CO uptake, pointing at lower biological activity on this location.

Comparison of flux chamber and flux gradient measurements
The flux chambers have measured a dry wall position, which can be considered representative for the active excavation areas, and have measured a wet (not flooded) location (for map, see 4.1). Wind direction often originated from the rewetted areas wherefore the flux gradient method measured mostly wet and flooded areas. Table 10.9 shows an overview of the range of the measured fluxes measured by the different systems. The fluxes are hard to compare for multiple reasons: first of all, the chamber measurements at the two different locations have not been performed at the same time. The dry location was measured in August and September, while the wet location was measured in October and November. Furthermore, the flux gradient method overlooked a flooded area, but flux chamber measurements for these regions were not performed. However, if the FG measurements are correct, than larger CO and CH_4 fluxes were observed by the FG method than observed on any of the chamber locations. This could indicate that these gas fluxes derive from the flooded areas, which were not monitored by the flux chambers.

Water measurements
Water emissions in the peatland Himmelmoor were tried to be measured by use of a floating chamber (large flowerpot in Figure 4.2). The chamber was first placed in the rewetted area (Figure 4.1, close to 2^{nd} chamber location) for half an hour. Concentration changes were too small and inconsistent for flux estimations. Secondly, the chamber was placed in the partly

Table 10.9: Measured flux ranges from the different flux measurement methods at fieldsite Himmelmoor. As mentioned in the text, flux gradient fluxes should be interpreted with caution.

Gas	**Chamber-dry**	**Chamber-wet**	**Flux gradient**
CO_2 flux (μmol m^{-2} s^{-1})	0 to 20	0 to 1	0 to 8
CH_4 flux (nmol m^{-2} s^{-1})	0 to 15	0 to 1	0 to 40
CO (nmol m^{-2} s^{-1})	-3 to 2	-.8 to -0.2	-5 to 10
N_2O (nmol m^{-2} s^{-1})	0 to 60	0 to 5	0 to 15

vegetated drainage ditch for half an hour. Small concentration changes for all gases were visible (Figure 10.29). The third time, the chamber was placed in the drainage ditch again and left here for 3 days. As can be seen in Figure 10.30, all concentrations went up during the first few hours. For CO_2, a concentration increase of 20 ppm during the first 4 hours was observed, from which a rough flux estimate of 0.05 μmol m^{-2} s^{-1} can be derived (area=$\pm$1.75 m^2, volume=$\pm$1.5 m^3). For CH_4 a flux of 7.5 nmol m^{-2} s^{-1} was estimated. However, CO_2 and CH_4 concentrations in the flowerpot headspace went down at the same time a few hours later (4 am) and showed an unclear pattern afterwards. Analysis of these results are preliminary.

Outlook

The data shown here is to provide an overview of the fluxes observed in Himmelmoor during the field campaign and can be considered as preliminary results. Flux measurement data are so far not linked to environmental factors such as temperature, wind speed direction and precipitation. Also, correlation between different gas concentration and fluxes should be studied to obtain possible gas source information. The data will be provided to the University of Hamburg for the further scientific interpretation.

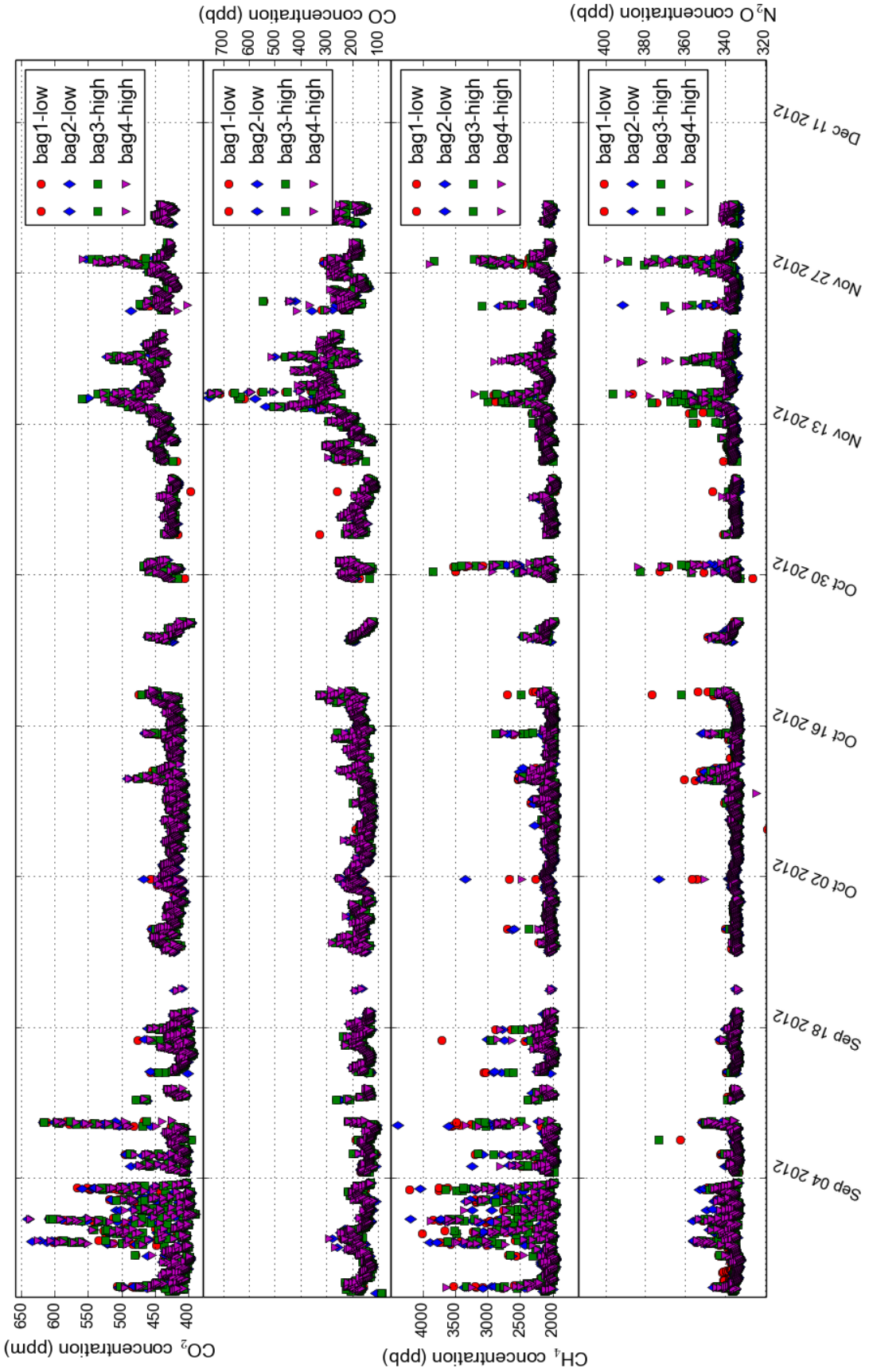

Figure 10.23: Atmospheric concentrations measured at the FG tower at 0.55 and 1.95 m during the campaign at the fieldsite Himmelmoor. The location of the tower is shown in Figure 4.1. The months August and November showed concentration peaks for different gases, a zoom in of these periods is shown in Figure 10.24 and Figure 10.25.

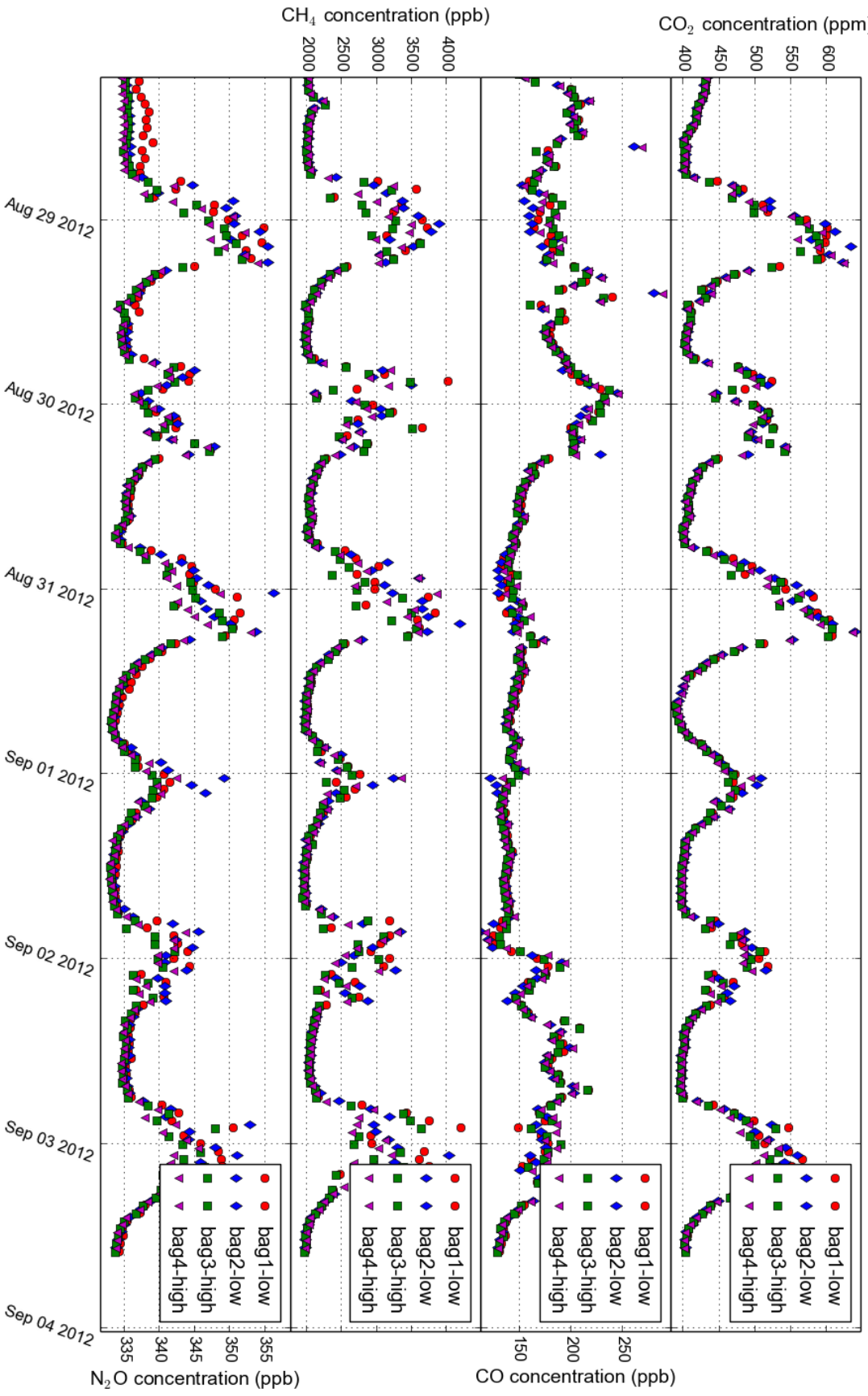

Figure 10.24: Atmospheric concentrations measured at the FG tower at 0.55 and 1.95 m at the fieldsite Himmelmoor in the end of August.

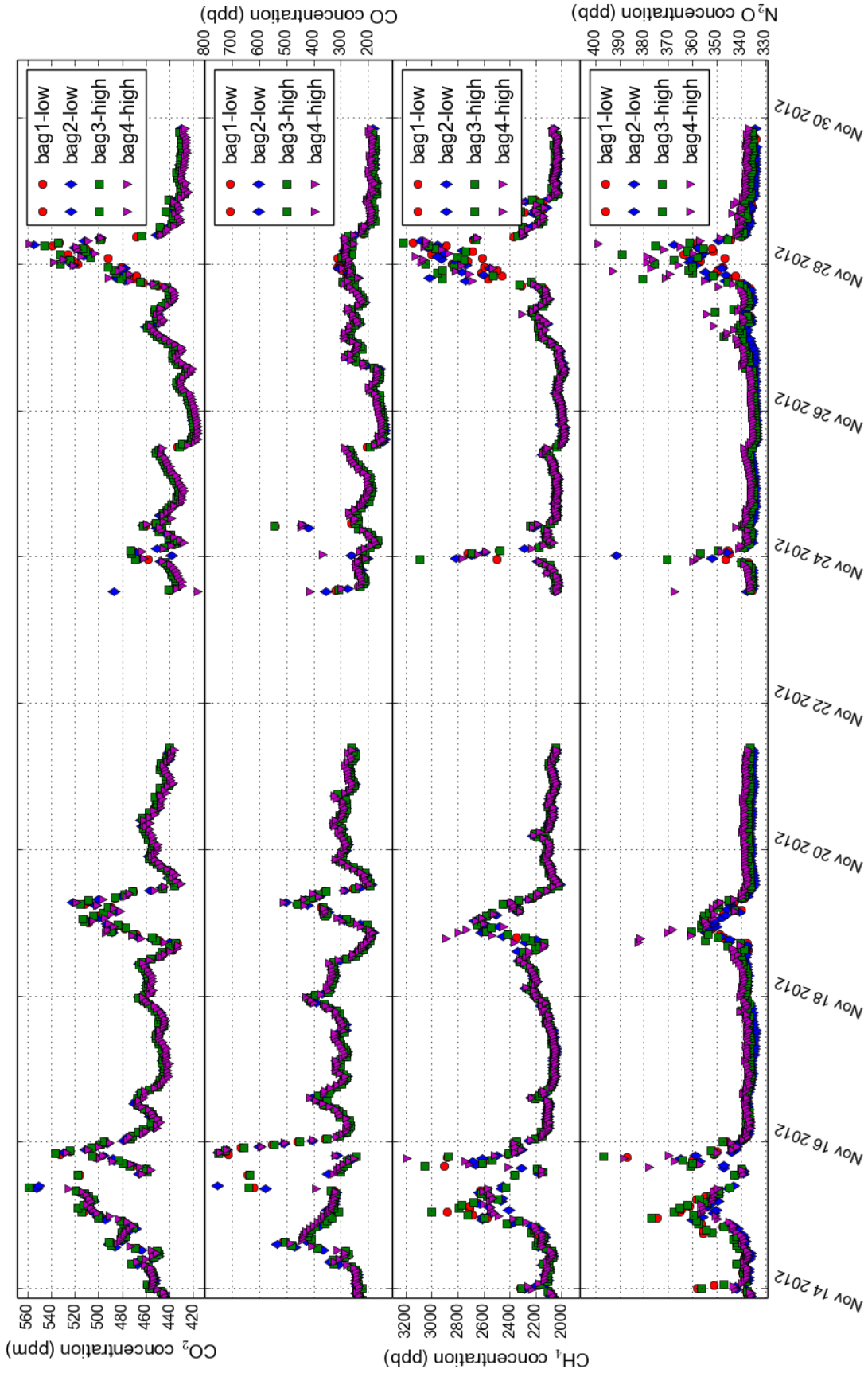

Figure 10.25: Atmospheric concentrations measured at the FG tower at 0.55 and 1.95 m at the fieldsite Himmelmoor in November.

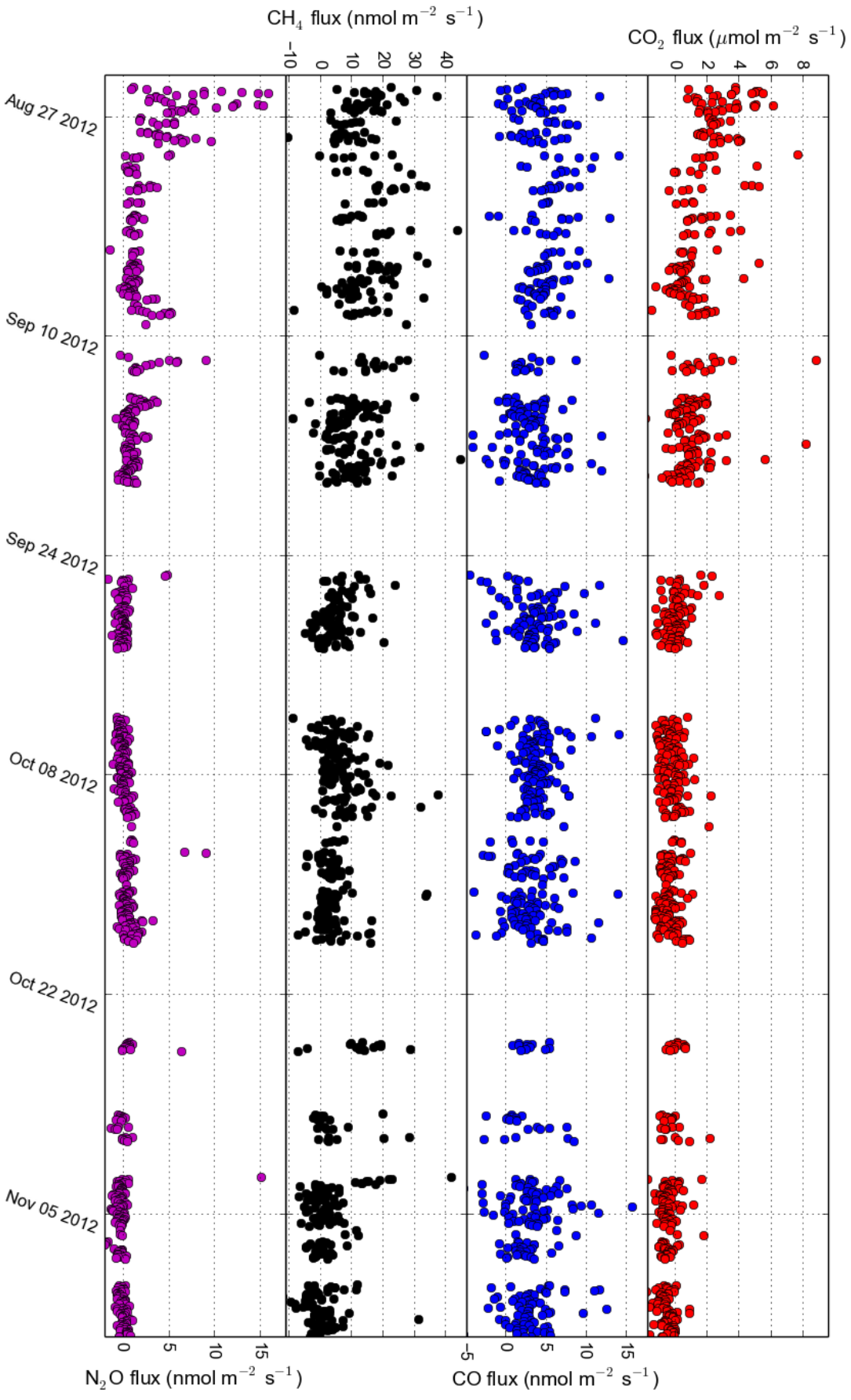

Figure 10.26: Calculated FG fluxes for the campaign at the fieldsite Himmelmoor, based on bag-pair 1 and 3. As mentioned in the text, it is unclear to which extent the sampling pumps have been leaking, wherefore the presented fluxes should be interpreted with caution.

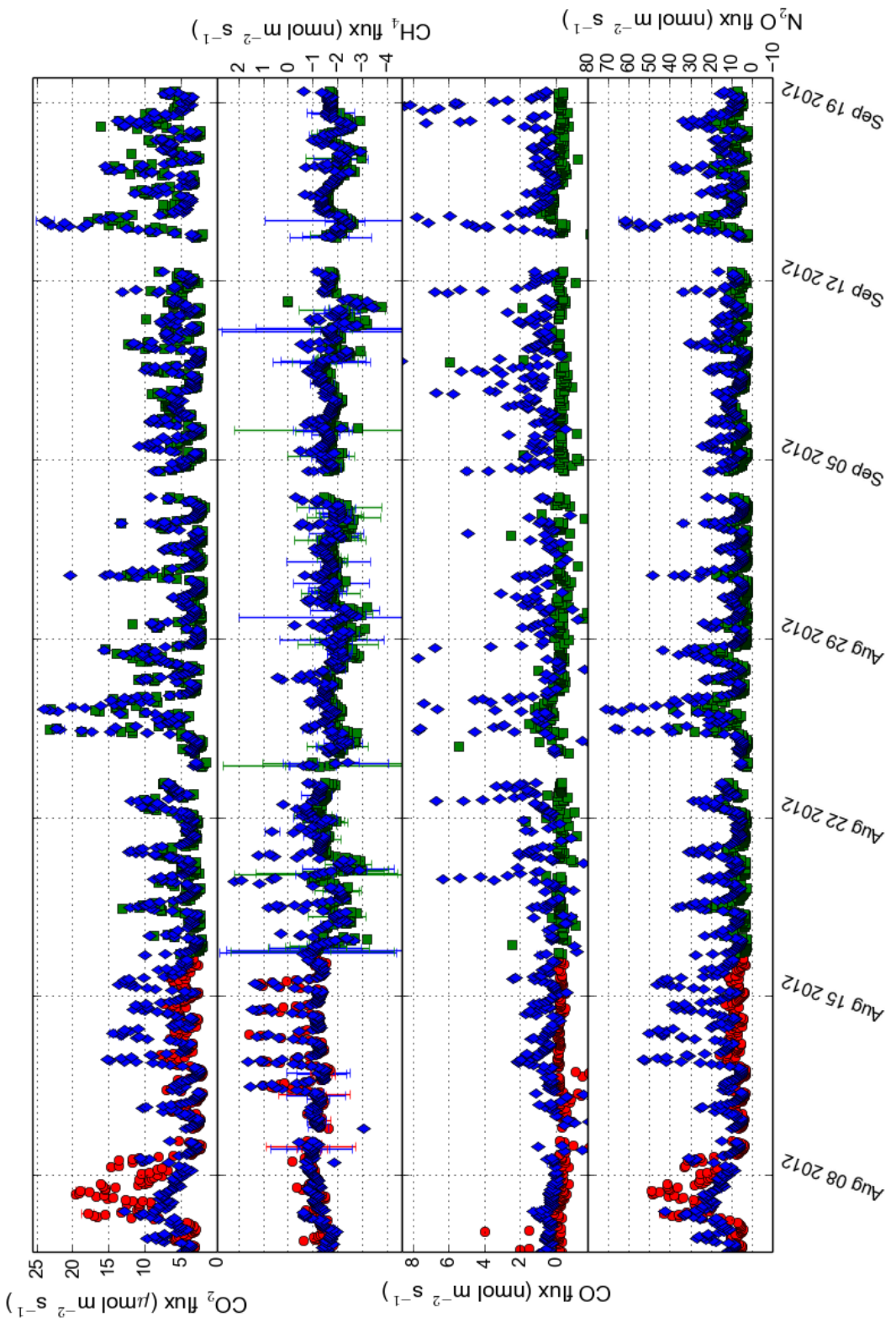

Figure 10.27: Flux chamber fluxes at the dry wall during the campaign at the fieldsite Himmelmoor. Blue diamonds are measurements from chamber B, which was transparent over the entire experiment. Red circles indicate measurements of chamber A when transparent, green squares indicate measurements of chamber A when opaque. Only chamber fluxes derived from linear regression fits with $R^2 > 0.90$ are shown.

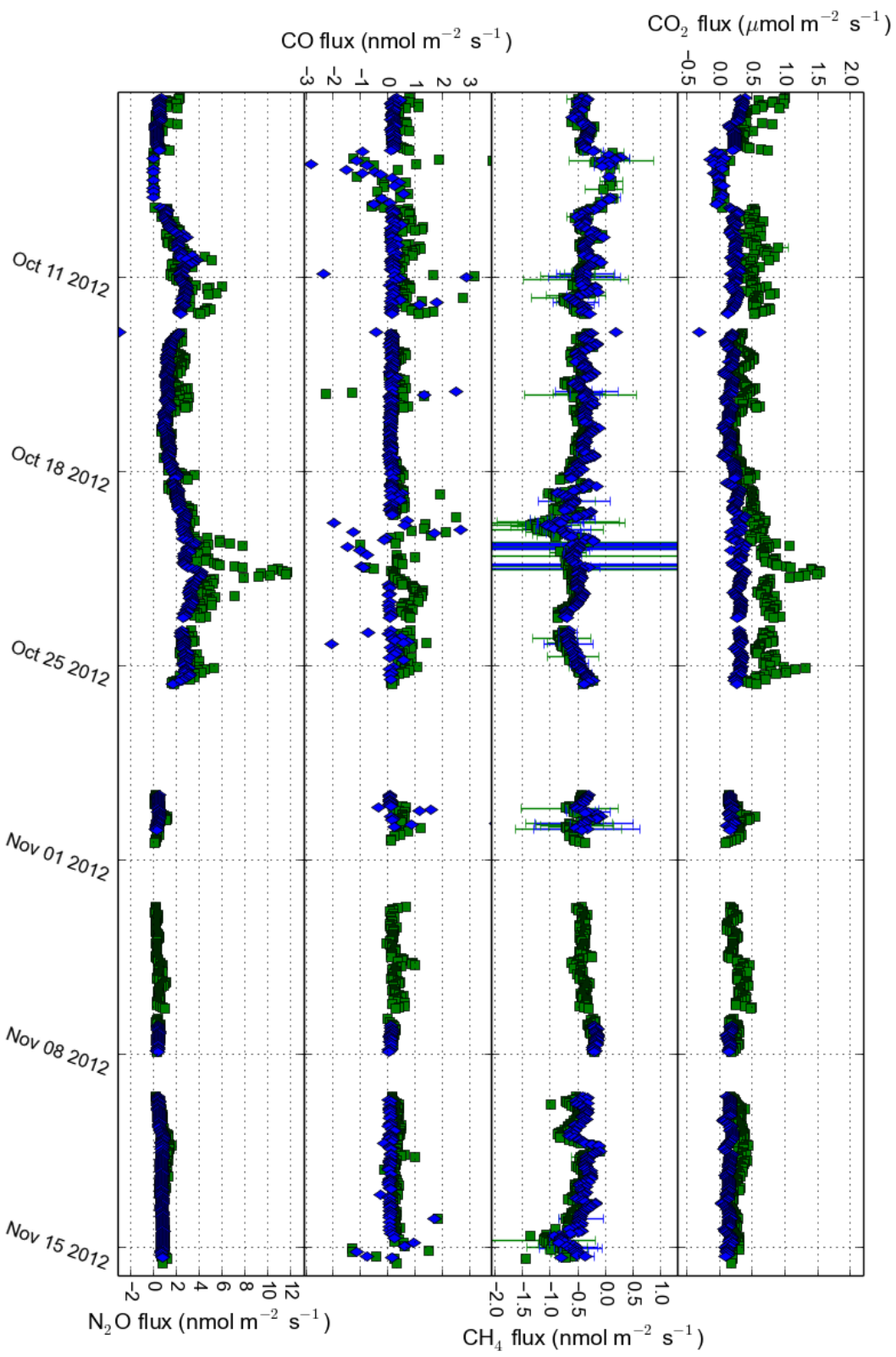

Figure 10.28: Flux chamber fluxes at a wet position during the campaign at the fieldsite Himmelmoor. Both chambers were transparent. Green squares indicate measurements from chamber A and blue diamonds indicate measurements from chamber B. Only chamber fluxes derived from linear regression fits with an $R^2 > 0.90$ are shown.

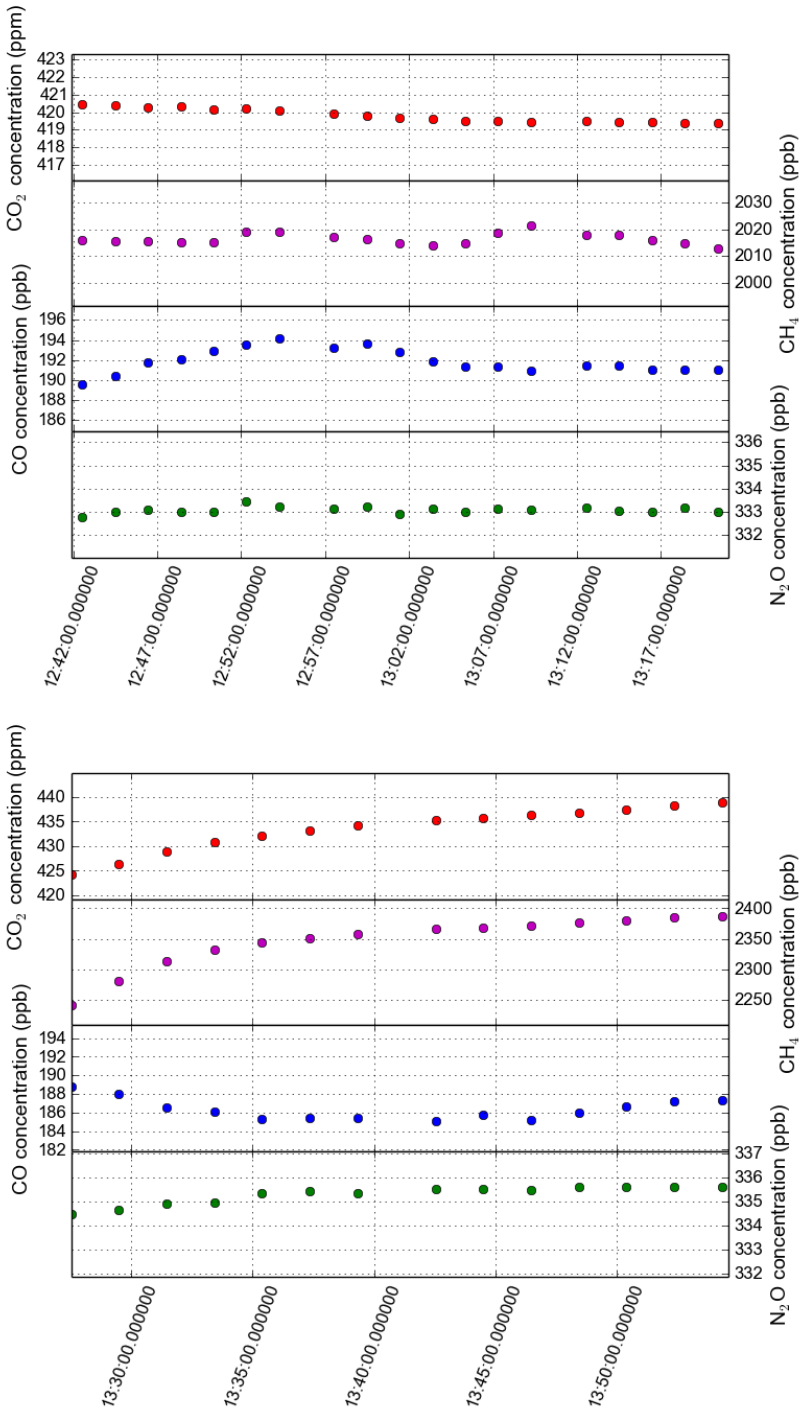

Figure 10.29: Concentrations in the flower pot headspace. Left figure: the gas concentration increases when the flower pot was placed on the water surface in the rewetted area (for map, see Figure 4.1, close to the 2^{nd} chamber location). Right figure: the gas concentration increases when the flower pot was placed northwest of the 1^{st} chamber location, in the partly vegetated drainage ditch.

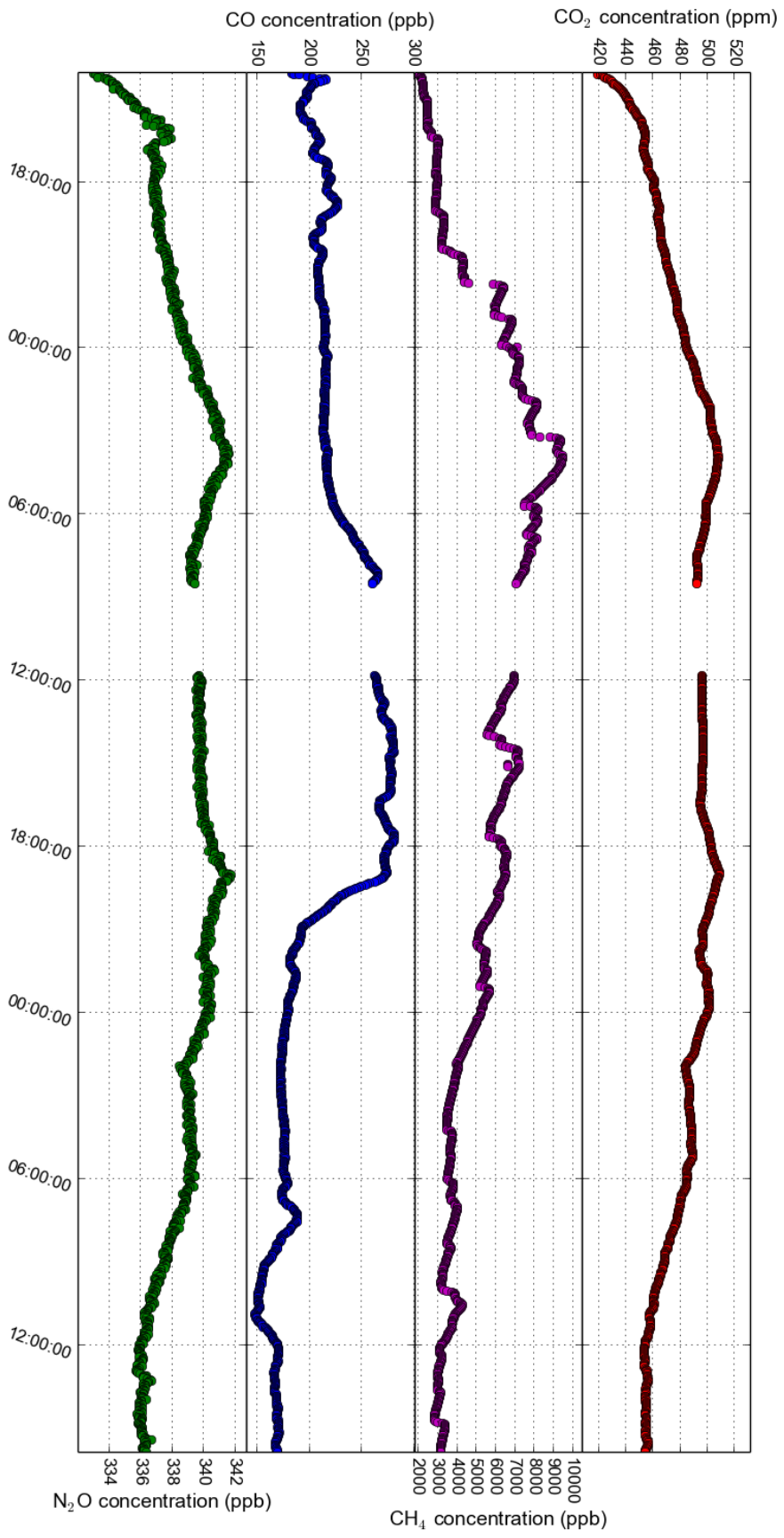

Figure 10.30: Concentrations in the flower pot headspace when placed in the partly vegetated drainage ditch for 3 days. The flower pot has not been moved during these 3 days. The gap in the data is caused by a remotely performed background measurement.

10.3.2 RISØ

During the field experiment 'RISØ', the pumps which were used to lead air from the FG tower to the sampling bags were leaking (for more information, see §4.5). Therefore, the flux gradient fluxes were not calculated. Figure 10.31 shows the concentration values, measured at the two inlets. Figure 10.32 shows the flux chamber fluxes of chamber A and B. Both chambers were alternating between 'normal positions' and '^{15}N-labeled positions' (§5.4). The times that the chambers were measuring the ^{15}N-labeled soils, are indicated with the colors green and magenta (only shown for N_2O fluxes, but applicable for all gases).

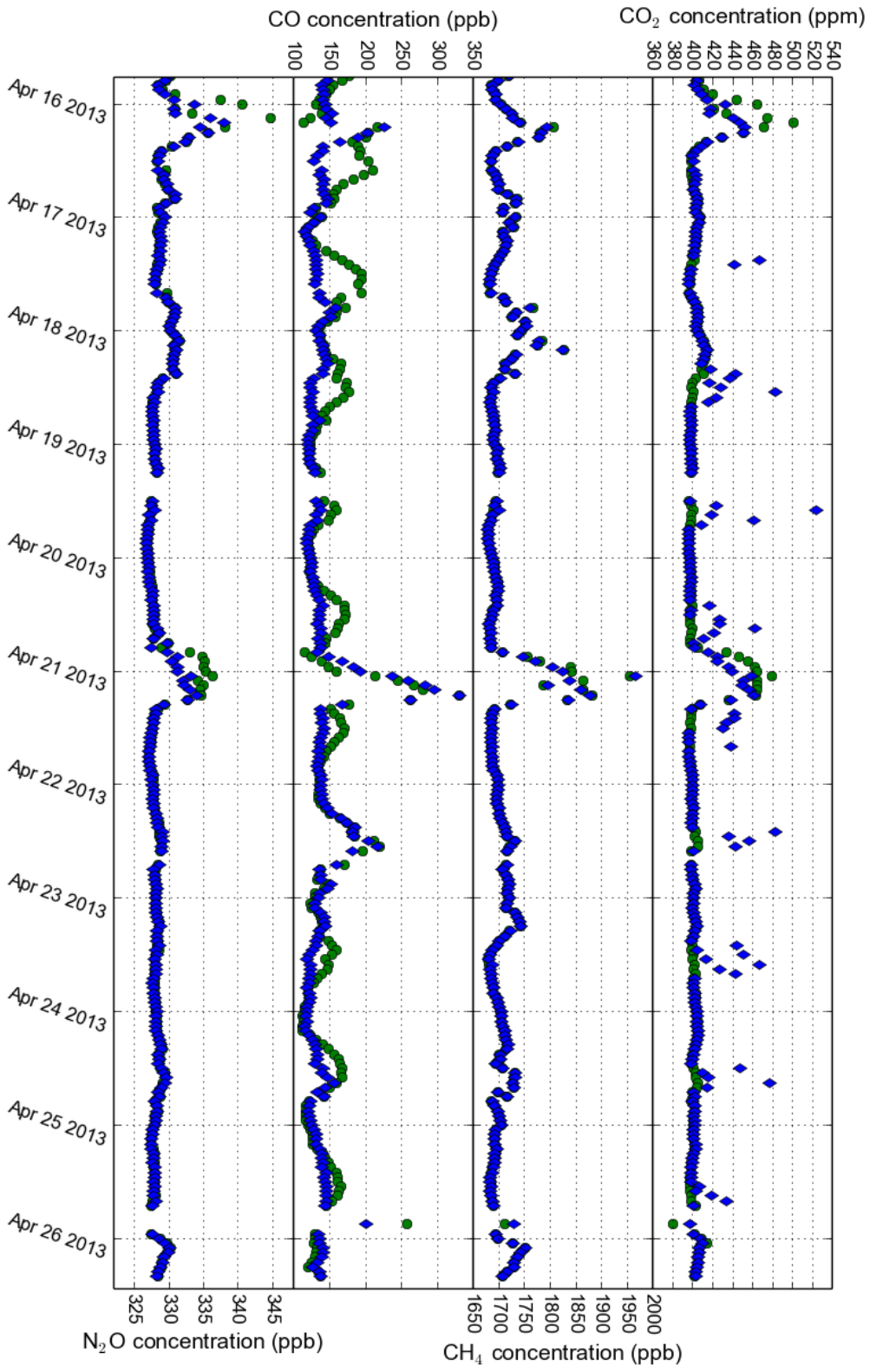

Figure 10.31: Atmospheric concentrations at the FG tower measured at 0.42 (green circle) and 2.42 m (blue diamonds) m height, during the campaign at the fieldsite RISØ.

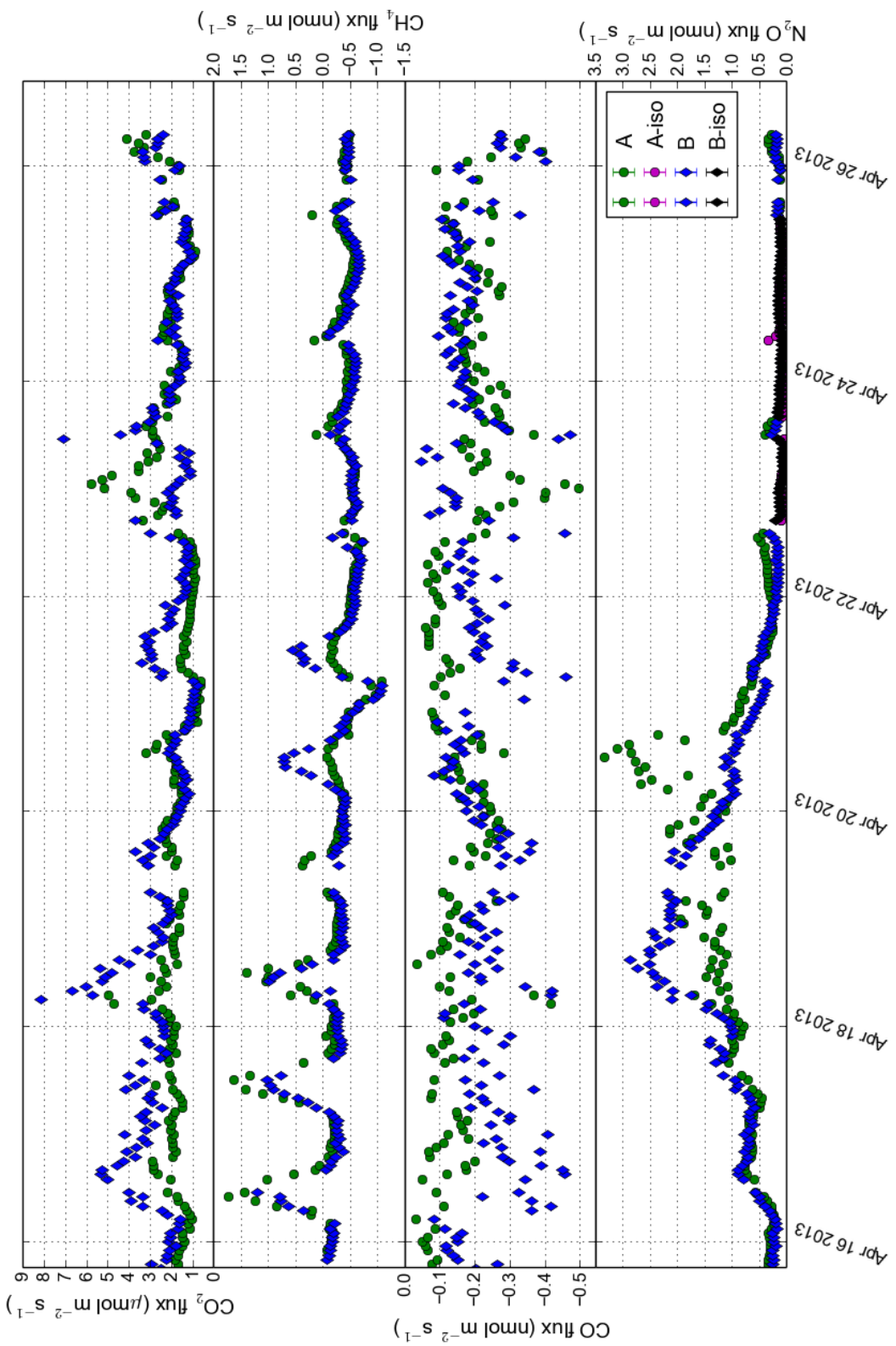

Figure 10.32: Flux chamber measurements during the campaign at the fieldsite RISØ. Flux chamber A fluxes are shown in green cirles, flux chamber B fluxes are shown in blue circles. The black and magenta colors (only shown for N_2O fluxes, but applicable for all gases) indicate the use of the different chamber locations, which were used for ^{15}N-labeling experiment (§5.4).

10.3.3 Rocca4

Information about the fieldsite Rocca4 can be found in §4.3. Figure 10.33 shows the concentration measurements for all gases at 4.1 m height at the EC tower. Figure 10.34 shows all FG gradient fluxes measured during the field campaign, fluxes are calculated with the new parameterization, explained in §5.2. Figure 10.35 shows the flux chamber fluxes of chamber A and Figure 10.35 shows the flux chamber fluxes of chamber B in Rocca4. Chamber A has been constantly transparent, while chamber B was made opaque on 5 August. It is expected that on 8 August, a leak has formed in chamber B.

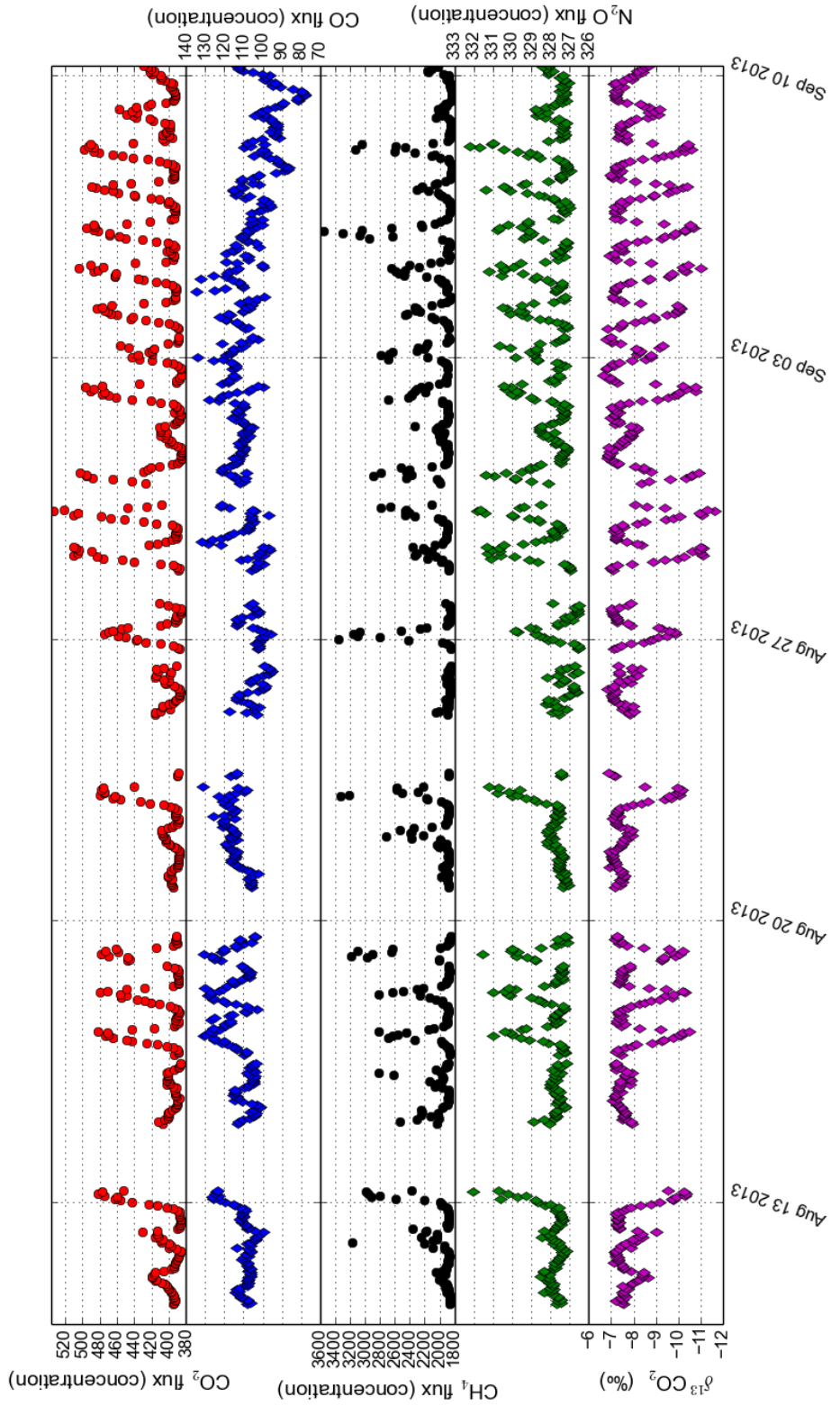

Figure 10.33: Atmospheric concentration measurements for all gases during the campaign at the fieldsite Rocca4, measured at the high inlet of the FG tower (4.1 m).

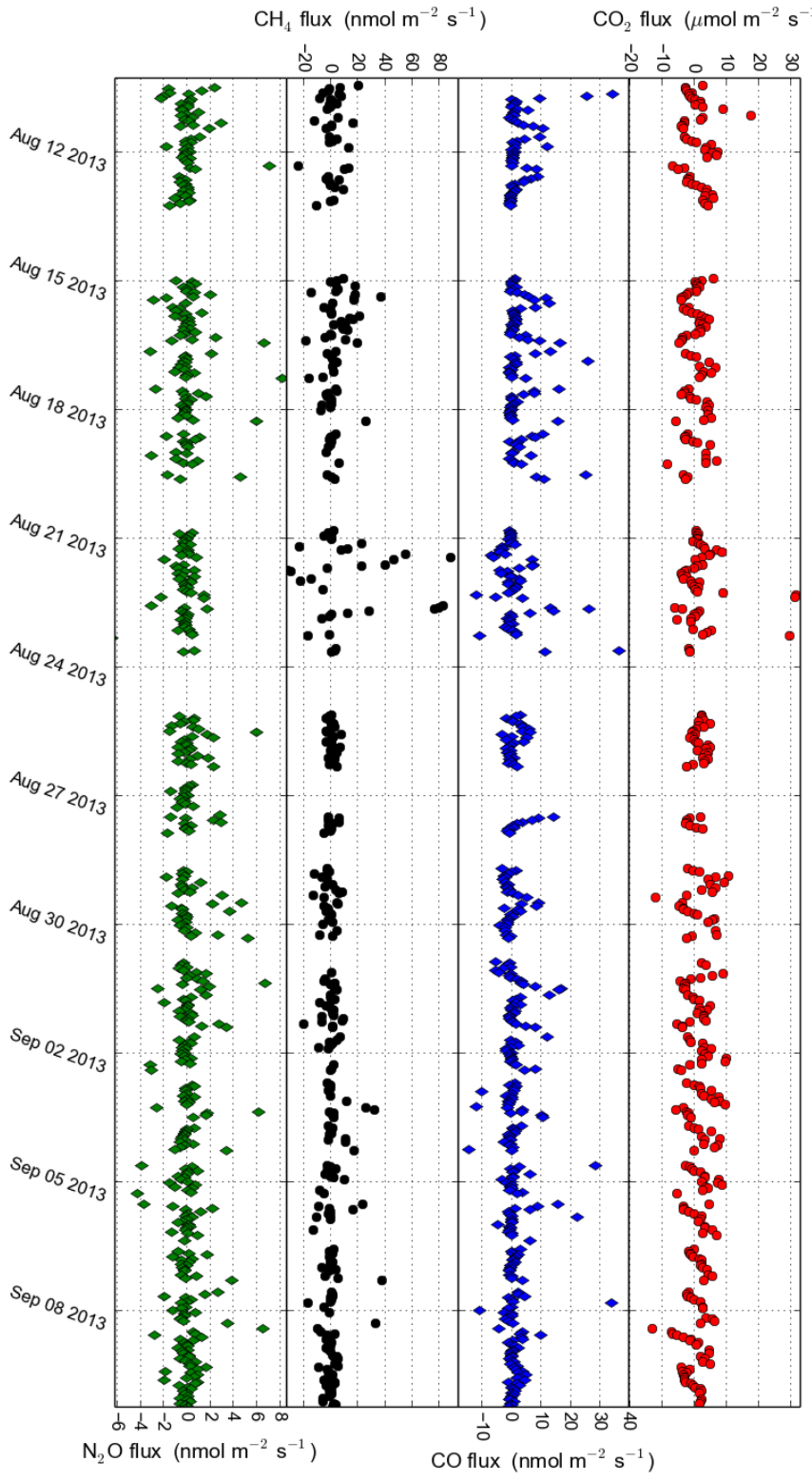

Figure 10.34: Flux gradient fluxes for all gases during the campaign at the fieldsite Rocca4. A comparison to eddy covariance fluxes can be found in §5.2 and §6.3.

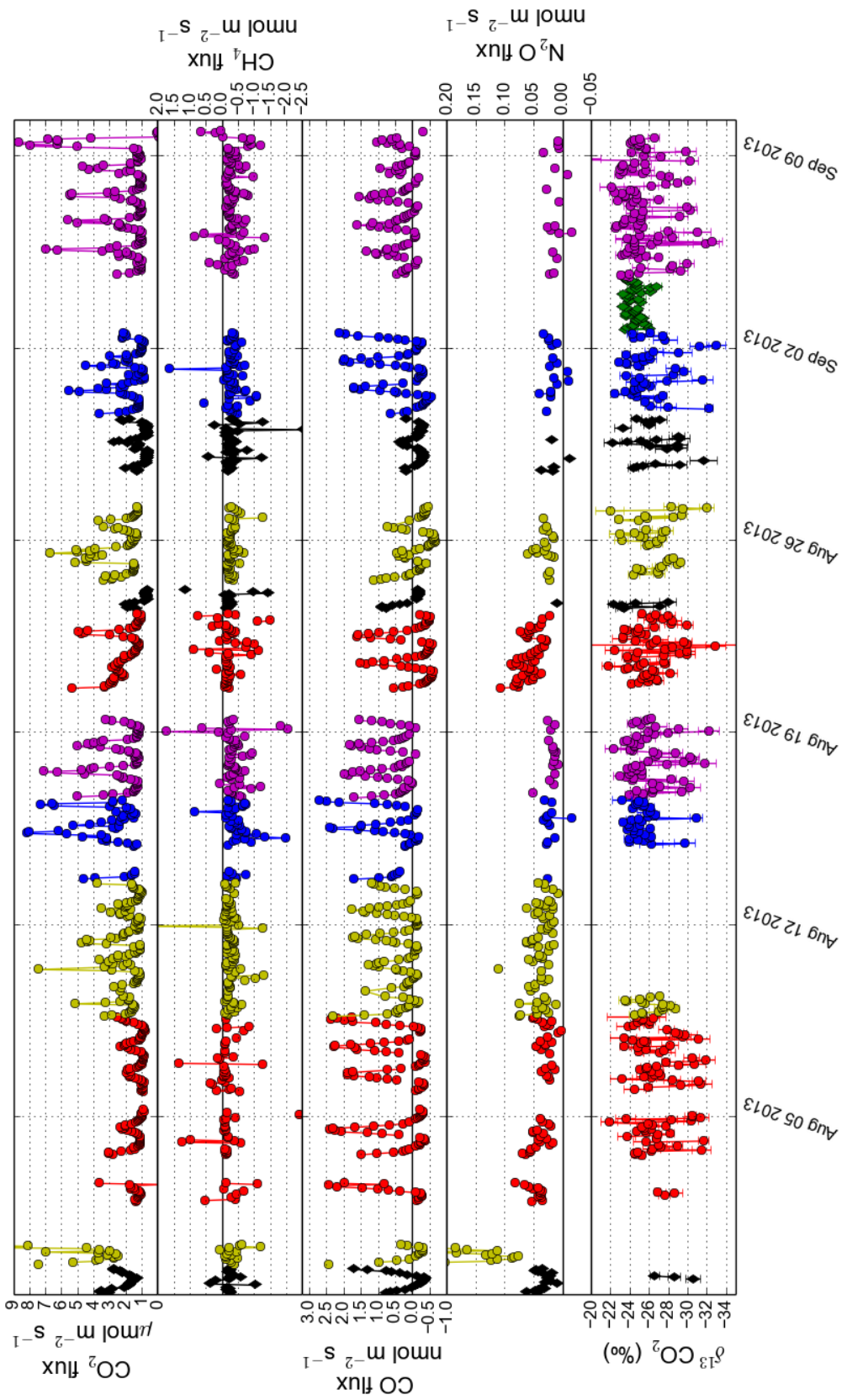

Figure 10.35: Flux chamber measurements during the campaign at the fieldsite Rocca4 from chamber A (transparent); pos. 1 = green circles, pos. 2 = magenta circles, pos. 3 = blue circles, pos. 4 = black circles, pos. 5 red circles, pos. 6 = yellow circles. Position 1 and 4 were bare locations (see Figure 4.4).

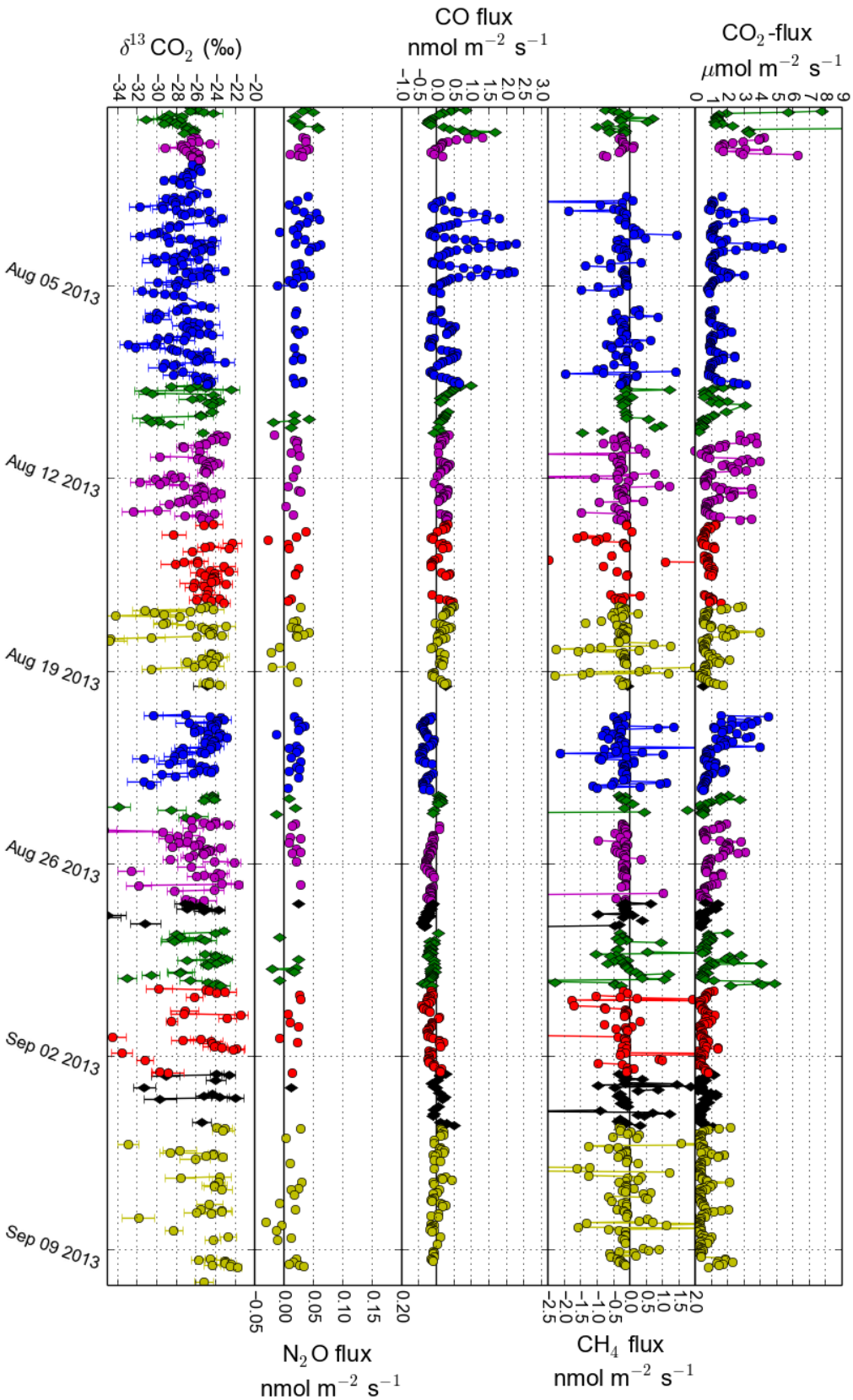

Figure 10.36: Flux chamber measurements during the campaign at the fieldsite Rocca4, from chamber B (opaque); pos. 1 = green circles, pos. 2 = magenta circles, pos. 3 = blue circles, pos. 4 = black circles, pos. 5 red circles, pos. 6 = yellow circles. Position 1 and 4 were bare locations (see Figure 4.4). On 8 August, possibly a leak has formed in chamber B wherefore data from this chamber was not used for further analyses.

10.3.4 Poplar

Information about the fieldsite Poplar can be found in §4.4. Figures 10.37 and 10.38 show the concentrations measured at the different heights at fieldsite Poplar. Figure 10.39 shows the concentrations measured at the horizontal inlets.

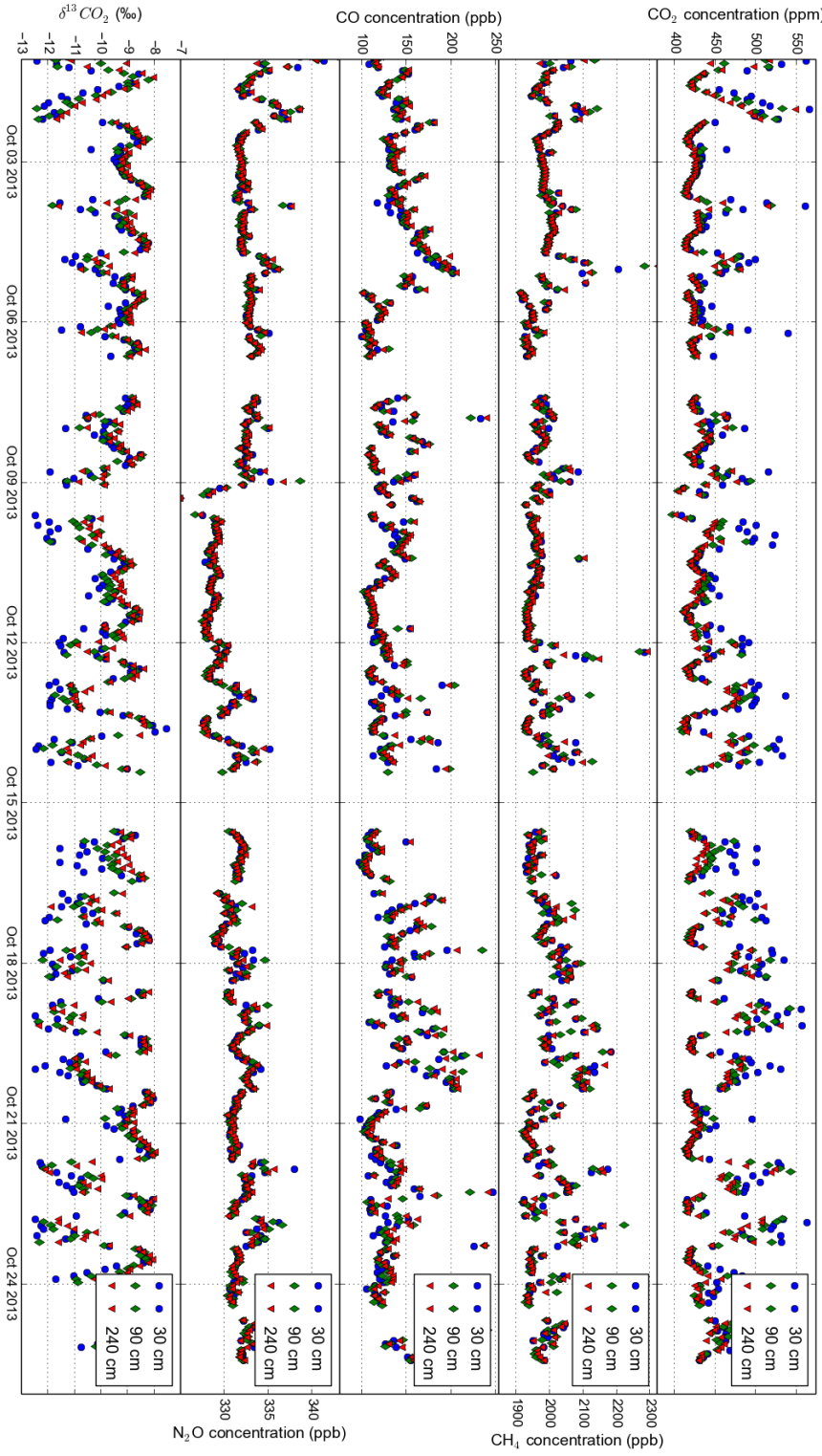

Figure 10.37: Forest canopy concentration data measured in the vertical plane at 30, 90 and 240 cm during the campaign at the fieldsite Poplar.

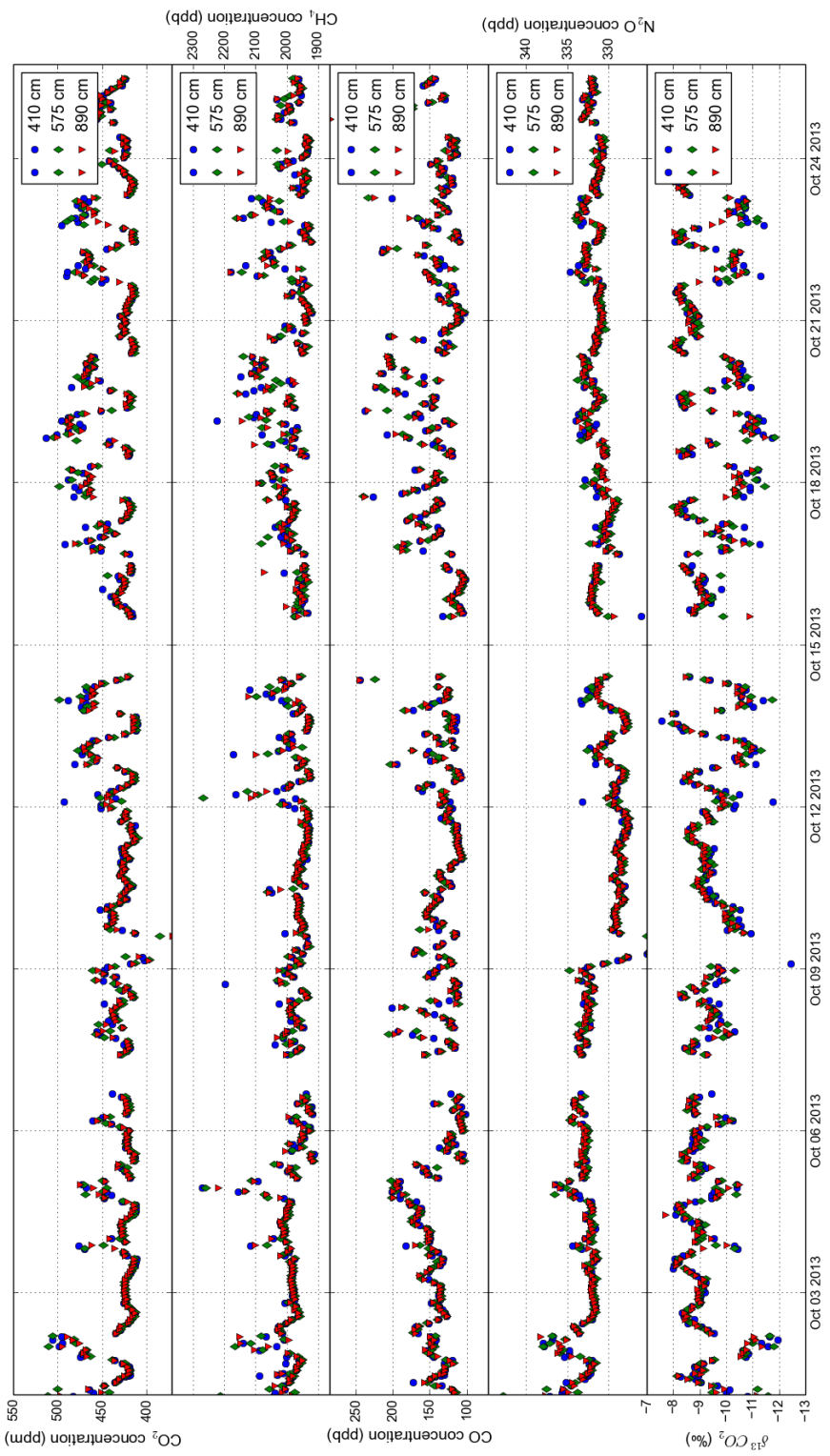

Figure 10.38: Forest canopy concentration data measured in the vertical plane at 410, 575 and 890 cm during the campaign at the fieldsite Poplar.

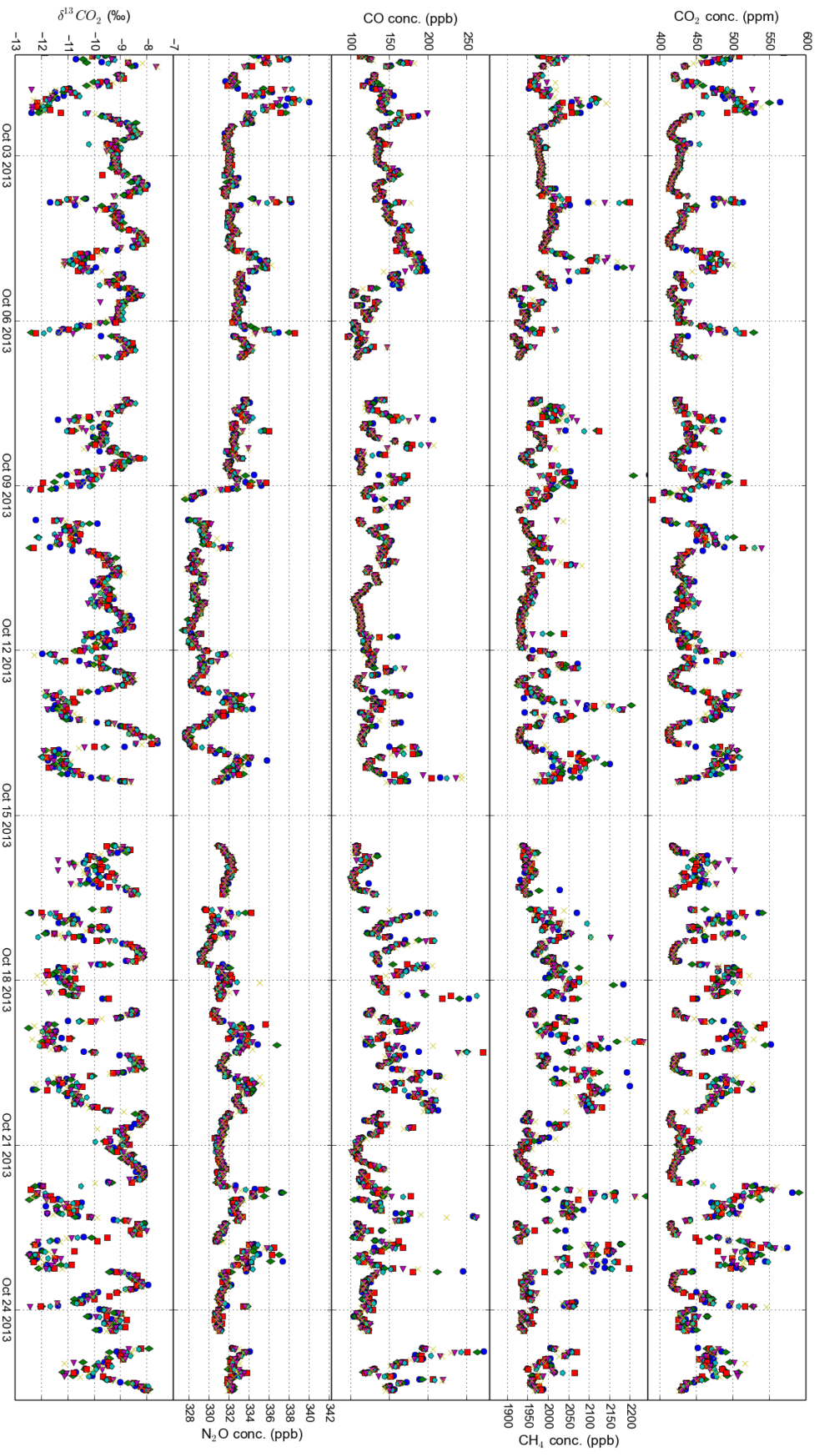

Figure 10.39: Forest canopy concentration data measured in the horizontal plane at 90 cm during the field campaign at the fieldsite Poplar; Blue circles = inlet A, green diamonds = inlet B, red squares = inlet C, light blue pentagons = inlet D, purple right triangle = inlet E, yellow cross = inlet F (for map, see Figure 4.7).

Glossary

$\delta^{13}CO_2$	Standardized isotopic signature §7.1
CRDS	Cavity Ring-Down Spectroscopy, §10.1.3
DEA	Disjunct Eddy Accumulation, §3.4.1
DEC	Disjunct Eddy Correlation, §3.4.1
DTU	Technical University Denmark, §10.1.1
EC	Eddy Covariance method, §3.4.1
ECN	Energy Centrum Nederland, Chapter 5
FACE	Free-Air Concentration Enrichment: experiments with increased atmospheric CO_2 investigate ecosystem's reponse, §2.2.1
FC	Flux Chamber, §3.4.2
FG	Flux Gradient, §3.4.1
FTIR	Fourier Transform InfraRed, §3.2
GC-ECD	Gas Chromatography-Electron Capture Detector,§10.1.1
GWP	Global Warming Potential, a relative measure of how much heat a greenhouse gas traps in the atmosphere, §2.1
InGOS	Integrated non-CO_2 Greenhouse gas Observing System, Chapter 5
IPCC	Intergovernmental Panel on Climate Change, Chapter 1
NBL	Nocturnal Boundary Layer, §5.1
OA-ICOS	Off-Axis Integrated Cavity Output Spectroscopy
PAS	Photo Acoustic Spectroscopy, §10.1.3
PTFE	PolyTetraFluoroEthylen, a chemical resistant material used in many laboratory applications, Chapter 4
REA	Relaxed Eddy Accumulation, §3.4.1
RF	Radiative Forcing, measurement gas' capacity to affect earth's energy balance, §2.1
R-NBL	Ratio-Nocturnal Boundary Layer, §5.1
TDLAS	Tunable Diode Laser Absorption Spectroscopy, §10.1.3
TI	Thünen Institute, §10.1.1
Q10	Temperature coefficient, the factor by which the reaction rate increases for a 10 °C rise in the temperature, Chapter 6
QCL	Quantum Cascade Laser, increasingly for instruments used for ecosystem flux measurements, §10.1.3
UNITUS	University of Tuscia, Chapter 6
UV-A	UltraViolet-A, light in wavelength band 320-400 nm, which is only partly absorbed by the earth's atmosphere, and is required for plant growth, Chapter 6
UV-B	UltraViolet-B, light in wavelength band 280-320 nm, which is almost completely absorbed by the earth's atmosphere, and can inhibit microbial growth and damage vegetation structure, Chapter 6
VPDB	Vienna Pee Dee Belemnite standard, §7.1
WMS	Wavelength Modulation Spectroscopy, §10.1.3

Bibliography

[1] HP Affek and D Yakir. 5.7 the stable isotopic composition of atmospheric co2. 2014.

[2] Ronald Amundson, Libby Stern, Troy Baisden, and Yang Wang. The isotopic composition of soil and soil-respired co 2. *Geoderma*, 82(1):83–114, 1998.

[3] Amy T Austin and Carlos L Ballaré. Dual role of lignin in plant litter decomposition in terrestrial ecosystems. *Proceedings of the National Academy of Sciences*, 107(10):4618–4622, 2010.

[4] Amy T Austin and Lucía Vivanco. Plant litter decomposition in a semi-arid ecosystem controlled by photodegradation. *Nature*, 442(7102):555–558, 2006.

[5] Michael Bahn, Michael Schmitt, Rolf Siegwolf, Andreas Richter, and Nicolas Brüggemann. Does photosynthesis affect grassland soil-respired co2 and its carbon isotope composition on a diurnal timescale? *New Phytologist*, 182(2):451–460, 2009.

[6] Antonella Baiocchi, Francesca Lotti, and Vincenzo Piscopo. Influence of hydrogeological setting on the arsenic occurrence in groundwater of the volcanic areas of central and southern italy. *AQUA mundi*, pages 131–142, 2011.

[7] Andrew J Baird, Imelda Stamp, Catherine M Heppell, and Sophie M Green. Ch4 flux from peatlands: a new measurement method. *Ecohydrology*, 3(3):360–367, 2010.

[8] Dennis D Baldocchi. Assessing the eddy covariance technique for evaluating carbon dioxide exchange rates of ecosystems: past, present and future. *Global Change Biology*, 9(4):479–492, 2003.

[9] GW Bartholomew and M Alexander. Microbial metabolism of carbon monoxide in culture and in soil. *Applied and environmental microbiology*, 37(5):932–937, 1979.

[10] Jake J Beaulieu, Jennifer L Tank, Stephen K Hamilton, Wilfred M Wollheim, Robert O Hall, Patrick J Mulholland, Bruce J Peterson, Linda R Ashkenas, Lee W Cooper, Clifford N Dahm, et al. Nitrous oxide emission from denitrification in stream and river networks. *Proceedings of the National Academy of Sciences*, 108(1):214–219, 2011.

[11] AA Berhe, CM Khoi, HV Asperen, J Gillabel, and JW Six. Effect of wetting and drying on deep soil co2 production and fluxes. In *AGU Fall Meeting Abstracts*, volume 1, page 0369, 2009.

[12] Nicholas R Betson, Sabine G Göttlicher, Marianne Hall, Göran Wallin, Andreas Richter, and Peter Högberg. No diurnal variation in rate or carbon isotope composition of soil respiration in a boreal forest. *Tree Physiology*, 27(5):749–756, 2007.

[13] Richard D Boone, Knute J Nadelhoffer, Jana D Canary, and Jason P Kaye. Roots exert a strong influence on the temperature sensitivityof soil respiration. *Nature*, 396(6711): 570–572, 1998.

[14] David R Bowling, Nate G McDowell, Barbara J Bond, Beverly E Law, and James R Ehleringer. 13c content of ecosystem respiration is linked to precipitation and vapor pressure deficit. *Oecologia*, 131(1):113–124, 2002.

[15] David R Bowling, Diane E Pataki, and James T Randerson. Carbon isotopes in terrestrial ecosystem pools and co2 fluxes. *New Phytologist*, 178(1):24–40, 2008.

[16] DR Bowling, JE Egan, SJ Hall, and DA Risk. Environmental forcing does not induce diel or synoptic variation in carbon isotope content of forest soil respiration. *Biogeosciences Discussions*, 12(8), 2015.

[17] LA Brandt, JY King, SE Hobbie, DG Milchunas, and RL Sinsabaugh. The role of photodegradation in surface litter decomposition across a grassland ecosystem precipitation gradient. *Ecosystems*, 13(5):765–781, 2010.

[18] N Brüggemann, A Gessler, Z Kayler, SG Keel, F Badeck, M Barthel, Pascal Boeckx, N Buchmann, E Brugnoli, J Esperschütz, et al. Carbon allocation and carbon isotope fluxes in the plant-soil-atmosphere continuum: a review. 2011.

[19] Dan Bruhn, Teis Nørgaard Mikkelsen, Jens Øbro, William George Tycho Willats, and Per Ambus. Effects of temperature, ultraviolet radiation and pectin methyl esterase on aerobic methane release from plant material. *Plant Biology*, 11(s1):43–48, 2009.

[20] Dan Bruhn, Ian M Møller, Teis N Mikkelsen, and Per Ambus. Terrestrial plant methane production and emission. *Physiologia plantarum*, 144(3):201–209, 2012.

[21] Dan Bruhn, Kristian Rost Albert, Teis Nørgaard Mikkelsen, and Per Ambus. Uv-induced carbon monoxide emission from living vegetation. *Biogeosciences Discussions*, 10(6), 2013.

[22] Dan Bruhn, Kristian R Albert, Teis N Mikkelsen, and Per Ambus. Uv-induced n 2 o emission from plants. *Atmospheric Environment*, 99:206–214, 2014.

[23] G Burba and D Anderson. Introduction to the eddy covariance method: General guidelines and conventional workflow, licor, 2005.

[24] George Burba. *Eddy covariance method for scientific, industrial, agricultural and regulatory applications: A field book on measuring ecosystem gas exchange and areal emission rates*. Li-Cor Biosciences, 2013.

[25] Joost A Businger, John C Wyngaard, Y Izumi, and Edward F Bradley. Flux-profile relationships in the atmospheric surface layer. *Journal of the atmospheric Sciences*, 28(2): 181–189, 1971.

[26] Gaylon S Campbell and John M Norman. *An introduction to environmental biophysics*. Springer Science & Business Media, 1998.

[27] Thure E Cerling, D Kip Solomon, Jay Quade, and John R Bowman. On the isotopic composition of carbon in soil carbon dioxide. *Geochimica et Cosmochimica Acta*, 55(11): 3403–3405, 1991.

[28] Intergovernmental Panel On Climate Change. 2006 ipcc guidelines for national greenhouse gas inventories, 2006.

[29] Lydie Chapuis-Lardy, Nicole Wrage, Aurelie Metay, Jean-Luc CHOTTE, and Martial Bernoux. Soils, a sink for n2o? a review. *Global Change Biology*, 13(1):1–17, 2007.

[30] G Chiodini, S Caliro, C Cardellini, D Granieri, R Avino, A Baldini, M Donnini, and C Minopoli. Long-term variations of the campi flegrei, italy, volcanic system as revealed by the monitoring of hydrothermal activity. *Journal of Geophysical Research: Solid Earth (1978–2012)*, 115(B3), 2010.

[31] Giovanni Chiodini, Stefano Caliro, Alessandro Aiuppa, Rosario Avino, Domenico Granieri, Roberto Moretti, and Francesco Parello. First 13c/12c isotopic characterisation of volcanic plume co2. *Bulletin of volcanology*, 73(5):531–542, 2011.

[32] TW Choularton, MW Gallagher, KN Bower, D Fowler, M Zahniser, A Kaye, JL Monteith, and RJ Harding. Trace gas flux measurements at the landscape scale using boundary-layer budgets [and discussion]. *Philosophical Transactions of the Royal Society of London A: Mathematical, Physical and Engineering Sciences*, 351(1696):357–369, 1995.

[33] Jesper Riis Christiansen, Janne FJ Korhonen, Radoslaw Juszczak, Michael Giebels, and Mari Pihlatie. Assessing the effects of chamber placement, manual sampling and headspace mixing on ch4 fluxes in a laboratory experiment. *Plant and soil*, 343(1-2):171–185, 2011.

[34] Philippe Ciais, Christopher Sabine, Govindasamy Bala, Laurent Bopp, Victor Brovkin, Josep Canadell, Abha Chhabra, Ruth DeFries, James Galloway, Martin Heimann, et al. Carbon and other biogeochemical cycles. In *Climate change 2013: the physical science basis. Contribution of Working Group I to the Fifth Assessment Report of the Intergovernmental Panel on Climate Change*, pages 465–570. Cambridge University Press, 2014.

[35] F Conen and KA Smith. A re-examination of closed flux chamber methods for the measurement of trace gas emissions from soils to the atmosphere. *European Journal of Soil Science*, 49(4):701–707, 1998.

[36] Ralf Conrad. Soil microorganisms as controllers of atmospheric trace gases (h2, co, ch4, ocs, n2o, and no). *Microbiological reviews*, 60(4):609–640, 1996.

[37] Ralf Conrad and Wolfgang Seiler. Role of microorganisms in the consumption and production of atmospheric carbon monoxide by soil. *Applied and environmental microbiology*, 40(3):437–445, 1980.

[38] Ralf Conrad and Wolfgang Seiler. Arid soils as a source of atmospheric carbon monoxide. *Geophysical Research Letters*, 9(12):1353–1356, 1982.

[39] Harmon Craig. Isotopic standards for carbon and oxygen and correction factors for mass-spectrometric analysis of carbon dioxide. *Geochimica et cosmochimica acta*, 12(1):133–149, 1957.

[40] B Crawford and A Christen. Quantifying the co 2 storage flux term in urban eddy-covariance observations. In *8th international conference on urban climates. Dublin*, 2012.

[41] Sigrid Dengel, Peter E Levy, John Grace, Stephanie K Jones, and Ute M Skiba. Methane emissions from sheep pasture, measured with an open-path eddy covariance system. *Global Change Biology*, 17(12):3524–3533, 2011.

[42] OT Denmead. Approaches to measuring fluxes of methane and nitrous oxide between landscapes and the atmosphere. *Plant and Soil*, 309(1-2):5–24, 2008.

[43] OT Denmead, MR Raupach, FX Dunin, HA Cleugh, and R Leuning. Boundary layer budgets for regional estimates of scalar fluxes. *Global Change Biology*, 2(3):255–264, 1996.

[44] L Derendorp, JB Quist, R Holzinger, and T Röckmann. Emissions of h2o and co from leaf litter of sequoiadendron giganteum and their dependence on uv radiation and temperature. *Atmospheric Environment*, 45(39):7520–7524, 2011.

[45] Raymond Louis Desjardins. study of carbon dioxide and sensible heat fluxes using the eddy correlation technique. 1973.

[46] Matteo Detto, Joseph Verfaillie, Frank Anderson, Liukang Xu, and Dennis Baldocchi. Comparing laser-based open-and closed-path gas analyzers to measure methane fluxes using the eddy covariance method. *Agricultural and forest meteorology*, 151(10):1312–1324, 2011.

[47] Nicholas M Deutscher. *Investigating greenhouse gases in Australia using atmospheric measurements with fourier transform spectrometry and atmospheric modeling*. PhD thesis, School of Chemistry, Faculty of Science, University of Wollongong, 2009.

[48] Tom A Dueck, Ries De Visser, Hendrik Poorter, Stefan Persijn, Antonie Gorissen, Willem De Visser, Ad Schapendonk, Jan Verhagen, Jan Snel, Frans JM Harren, et al. No evidence for substantial aerobic methane emission by terrestrial plants: a 13c-labelling approach. *New Phytologist*, 175(1):29–35, 2007.

[49] Ecotech. *Spectronus Trace & Isotopes Analyser*. Ecotech, Australia-Head office, 1492 Fentree Gully rd Knoxfield Victoria, 3180, Australia, 3 edition, 11 2011.

[50] James R Ehleringer, Nina Buchmann, and Lawrence B Flanagan. Carbon isotope ratios in belowground carbon cycle processes. *Ecological Applications*, 10(2):412–422, 2000.

[51] Daniel Epron, Valerie Le Dantec, Eric Dufrene, and Andre Granier. Seasonal dynamics of soil carbon dioxide efflux and simulated rhizosphere respiration in a beech forest. *Tree Physiology*, 21(2-3):145–152, 2001.

[52] Giuseppe Etiope. Subsoil co2 and ch4 and their advective transfer from faulted grassland to the atmosphere. *Journal of Geophysical Research: Atmospheres (1984–2012)*, 104(D14): 16889–16894, 1999.

[53] Werner Eugster and Franziska Siegrist. The influence of nocturnal co 2 advection on co 2 flux measurements. *Basic and Applied Ecology*, 1(2):177–188, 2000.

[54] Daniela Famulari. Nitrous oxide fluxes from a scottish grassland measured by eddy covariance: a comparison between different systems. In *InGOS annual conference 2014*, 2014.

[55] Graham D Farquhar, James R Ehleringer, and Kerry T Hubick. Carbon isotope discrimination and photosynthesis. *Annual review of plant biology*, 40(1):503–537, 1989.

[56] Noah Fierer, Oliver A Chadwick, and Susan E Trumbore. Production of co2 in soil profiles of a california annual grassland. *Ecosystems*, 8(4):412–429, 2005.

[57] Thomas Foken and Carmen J Nappo. *Micrometeorology*. Springer, 2008.

[58] Pavel Formánek, Klement Rejšek, and Valerie Vranová. Effect of elevated co 2, o 3, and uv radiation on soils. *The Scientific World Journal*, 2014, 2014.

[59] Piers Forster, Venkatachalam Ramaswamy, Paulo Artaxo, Terje Berntsen, Richard Betts, David W Fahey, James Haywood, Judith Lean, David C Lowe, Gunnar Myhre, et al. Changes in atmospheric constituents and in radiative forcing. chapter 2. In *Climate Change 2007. The Physical Science Basis*. 2007.

[60] HD Freyer. Atmospheric cycles of trace gases containing carbon. *The global carbon cycle*, pages 101–28, 1979.

[61] Pierre Friedlingstein, Peter Cox, R Betts, Laurent Bopp, W Von Bloh, Victor Brovkin, P Cadule, S Doney, Michael Eby, I Fung, et al. Climate-carbon cycle feedback analysis: Results from the c4mip model intercomparison. *Journal of Climate*, 19(14):3337–3353, 2006.

[62] Dale W Funk, Erik R Pullman, Kim M Peterson, Patrick M Crill, and WD Billings. Influence of water table on carbon dioxide, carbon monoxide, and methane fluxes from taiga bog microcosms. *Global Biogeochemical Cycles*, 8(3):271–278, 1994.

[63] J.N. Galloway. *The global Nitrogen Cycle*, volume 8. Gulf Professional Publishing, 2005.

[64] Arthur Gessler, Claudia Keitel, Naomi Kodama, Christopher Weston, Anthony J Winters, Heather Keith, Kliti Grice, Ray Leuning, and Graham D Farquhar. δ13c of organic matter transported from the leaves to the roots in eucalyptus delegatensis: short-term variations and relation to respired co2. *Functional Plant Biology*, 34(8):692–706, 2007.

[65] Jaleh Ghashghaie and Franz W Badeck. Opposite carbon isotope discrimination during dark respiration in leaves versus roots–a review. *New Phytologist*, 201(3):751–769, 2014.

[66] Stéphanie Goffin, Marc Aubinet, Martin Maier, Caroline Plain, Helmer Schack-Kirchner, and Bernard Longdoz. Characterization of the soil co 2 production and its carbon isotope composition in forest soil layers using the flux-gradient approach. *Agricultural and Forest Meteorology*, 188:45–57, 2014.

[67] Google. Google maps 2015, 2015. URL `www.google.de`.

[68] David Griffith. private communication, 2014.

[69] David Griffith, Nicholas Deutscher, Paul Krummel, Paul Fraser, Mvd Schoot, and Colin Allison. The uow ftir trace gas analyser: Comparison with loflo, agage and tank measurements at cape grim and gaslab. *Baseline atmospheric program (Australia)*, 2008:7–22, 2007.

[70] David WT Griffith. Synthetic calibration and quantitative analysis of gas-phase ft-ir spectra. *Applied spectroscopy*, 50(1):59–70, 1996.

[71] David WT Griffith and Bo Galle. Flux measurements of nh3, n2o and co2 using dual beam ftir spectroscopy and the flux-gradient technique. *Atmospheric environment*, 34(7): 1087–1098, 2000.

[72] DWT Griffith, R Leuning, OT Denmead, and IM Jamie. Air–land exchanges of co 2, ch 4 and n 2 o measured by ftir spectrometry and micrometeorological techniques. *Atmospheric Environment*, 36(11):1833–1842, 2002.

[73] PR Griffiths and JA De Haseth. Fourier transform infrared spectroscopy, vol 83 in, 1986.

[74] A Grossel, V Zeninari, B Parvitte, L Joly, and D Courtois. Optimization of a compact photoacoustic quantum cascade laser spectrometer for atmospheric flux measurements: Application to the detection of methane and nitrous oxide. *Applied Physics B*, 88(3): 483–492, 2007.

[75] S. Hammer, D. W. T. Griffith, G. Konrad, S. Vardag, C. Caldow, and I. Levin. Assessment of a multi-species in situ ftir for precise atmospheric greenhouse gas observations. *Atmospheric Measurement Techniques*, 6(5):1153–1170, 2013. doi: 10.5194/amt-6-1153-2013. URL `http://www.atmos-meas-tech.net/6/1153/2013/`.

[76] S Hammer, D WT Griffith, G Konrad, S Vardag, C Caldow, and I Levin. Assessment of a multi-species in situ ftir for precise atmospheric greenhouse gas observations. 2013.

[77] Daniel C Harris. Charles david keeling and the story of atmospheric co2 measurements†. *Analytical chemistry*, 82(19):7865–7870, 2010.

[78] DL Hartmann, AMG Klein Tank, M Rusicucci, LV Alexander, B Broenniman, Y Charabi, FJ Dentener, EJ Dlugokencky, DR Easterling, Alexey Kaplan, et al. Observations: atmosphere and surface. 2013.

[79] SE Hobbs. Climate change, the ipcc scientific assessment: Houghton jt, jenkins gj and ephraums jj (eds), 1990, 364 pp., cambridge university press, cambridge,£ 44.50 (hb),£ 17.95 (pb), 1992.

[80] Ulf Högström, Hans Bergström, Ann-Sofi Smedman, Sven Halldin, and Anders Lindroth. Turbulent exchange above a pine forest, i: Fluxes and gradients. *Boundary-Layer Meteorology*, 49(1-2):197–217, 1989.

[81] Richard A Houghton. *The contemporary carbon cycle*, volume 8. Gulf Professional Publishing, 2005.

[82] Cheng-I Hsieh, Gabriel Katul, and Tze-wen Chi. An approximate analytical model for footprint estimation of scalar fluxes in thermally stratified atmospheric flows. *Advances in Water Resources*, 23(7):765–772, 2000.

[83] H Huang, J Wang, D Hui, DR Miller, S Bhattarai, S Dennis, D Smart, T Sammis, and KC Reddy. Nitrous oxide emissions from a commercial cornfield (zea mays) measured using the eddy covariance technique. *Atmospheric Chemistry and Physics*, 14(23):12839–12854, 2014.

[84] GL Hutchinson and GP Livingston. Vents and seals in non-steady-state chambers used for measuring gas exchange between soil and the atmosphere. *European Journal of Soil Science*, 52(4):675–682, 2001.

[85] RB Ingersoll, RE Inman, and WR Fisher. Soil's potential as a sink for atmospheric carbon monoxide. *Tellus*, 26(1-2):151–159, 1974.

[86] Javed Iqbal, Michael J Castellano, and Timothy B Parkin. Evaluation of photoacoustic infrared spectroscopy for simultaneous measurement of n2o and co2 gas concentrations and fluxes at the soil surface. *Global change biology*, 19(1):327–336, 2013.

[87] WG IUSS. World reference base for soil resources 2014. international soil classification system for naming soils and creating legends for soil maps. *World Soil Resources Reports*, (106), 2014.

[88] Adrian Kammer, Béla Tuzson, Lukas Emmenegger, Alexander Knohl, Joachim Mohn, and Frank Hagedorn. Application of a quantum cascade laser-based spectrometer in a closed chamber system for real-time δ 13 c and δ 18 o measurements of soil-respired co 2. *Agricultural and Forest Meteorology*, 151(1):39–48, 2011.

[89] Zachary E Kayler, Elizabeth W Sulzman, William D Rugh, Alan C Mix, and Barbara J Bond. Characterizing the impact of diffusive and advective soil gas transport on the measurement and interpretation of the isotopic signal of soil respiration. *Soil Biology and Biochemistry*, 42(3):435–444, 2010.

[90] Charles D Keeling. The concentration and isotopic abundances of carbon dioxide in the atmosphere. *Tellus*, 12(2):200–203, 1960.

[91] Charles D Keeling. The concentration and isotopic abundances of carbon dioxide in rural and marine air. *Geochimica et Cosmochimica Acta*, 24(3):277–298, 1961.

[92] Frank Keppler, John TG Hamilton, Marc Braß, and Thomas Röckmann. Methane emissions from terrestrial plants under aerobic conditions. *Nature*, 439(7073):187–191, 2006.

[93] Jennifer Y King, Leslie A Brandt, and E Carol Adair. Shedding light on plant litter decomposition: advances, implications and new directions in understanding the role of photodegradation. *Biogeochemistry*, 111(1-3):57–81, 2012.

[94] Volker WJH Kirchhoff, IMO Da Silva, and Edward V Browell. Ozone measurements in amazonia: Dry season versus wet season. *Journal of Geophysical Research: Atmospheres (1984–2012)*, 95(D10):16913–16926, 1990.

[95] Miko UF Kirschbaum, Suzanne M Lambie, and Hui Zhou. No uv enhancement of litter decomposition observed on dry samples under controlled laboratory conditions. *Soil Biology and Biochemistry*, 43(6):1300–1307, 2011.

[96] Keith W Kisselle, Richard G Zepp, Roger A Burke, Alexandre de Siqueira Pinto, Mercedes Bustamante, Stephen Opsahl, Renato F Varella, and Laura T Viana. Seasonal soil fluxes of carbon monoxide in burned and unburned brazilian savannas. *Journal of Geophysical Research: Atmospheres (1984–2012)*, 107(D20):LBA–18, 2002.

[97] Natascha Kljun, P Calanca, MW Rotach, and HP Schmid. A simple parameterisation for flux footprint predictions. *Boundary-Layer Meteorology*, 112(3):503–523, 2004.

[98] Naomi Kodama, Romain L Barnard, Yann Salmon, Christopher Weston, Juan Pedro Ferrio, Jutta Holst, Roland A Werner, Matthias Saurer, Heinz Rennenberg, Nina Buchmann, et al. Temporal dynamics of the carbon isotope composition in a pinus sylvestris stand: from newly assimilated organic carbon to respired carbon dioxide. *Oecologia*, 156(4):737–750, 2008.

[99] Robert Kormann and Franz X Meixner. An analytical footprint model for non-neutral stratification. *Boundary-Layer Meteorology*, 99(2):207–224, 2001.

[100] Markus Kottek, Jürgen Grieser, Christoph Beck, Bruno Rudolf, and Franz Rubel. World map of the köppen-geiger climate classification updated. *Meteorologische Zeitschrift*, 15 (3):259–263, 2006.

[101] PS Kroon, A Hensen, WCM Van den Bulk, PAC Jongejan, and AT Vermeulen. The importance of reducing the systematic error due to non-linearity in n2o flux measurements by static chambers. *Nutrient cycling in Agroecosystems*, 82(2):175–186, 2008.

[102] Y Kuzyakov. Sources of co 2 efflux from soil and review of partitioning methods. *Soil Biology and Biochemistry*, 38(3):425–448, 2006.

[103] C-T Lai, JR Ehleringer, AJ Schauer, PP Tans, DY Hollinger, U Paw, JW Munger, SC Wofsy, et al. Canopy-scale δ13c of photosynthetic and respiratory co2 fluxes: observations in forest biomes across the united states. *Global Change Biology*, 11(4):633–643, 2005.

[104] Jukka Laine, Jouko Silvola, Kimmo Tolonen, Jukka Alm, Hannu Nykänen, Harri Vasander, Tapani Sallantaus, Ilkka Savolainen, Jukka Sinisalo, and Pertti J Martikainen. Effect of water-level drawdown on global climatic warming: Northern peatlands. *Ambio*, pages 179–184, 1996.

[105] Rattan Lal. Carbon sequestration in dryland ecosystems. *Environmental management*, 33 (4):528–544, 2004.

[106] SM Lambie, MUF Kirschbaum, and J Dando. No photodegradation of litter and humus exposed to uv-b radiation under laboratory conditions: No effect of leaf senescence or drying temperature. *Soil Biology and Biochemistry*, 69:46–53, 2014.

[107] J. Laubach, M. Barthel, A. Fraser, J. E. Hunt, and D. W. T. Griffith. Combining two complementary micrometeorological methods to measure ch_4 and n_2o fluxes over pasture. *Biogeosciences Discussions*, 12(18):15245–15299, 2015. doi: 10.5194/bgd-12-15245-2015. URL `http://www.biogeosciences-discuss.net/12/15245/2015/`.

[108] Andrew DB Leakey, Elizabeth A Ainsworth, Carl J Bernacchi, Alistair Rogers, Stephen P Long, and Donald R Ort. Elevated co2 effects on plant carbon, nitrogen, and water relations: six important lessons from face. *Journal of experimental botany*, 60(10):2859–2876, 2009.

[109] Hanna Lee, Thom Rahn, and Heather Throop. An accounting of c-based trace gas release during abiotic plant litter degradation. *Global Change Biology*, 18(3):1185–1195, 2012.

[110] K Lenhart, F Althoff, M Greule, and F Keppler. Technical note: Methionine, a precursor of methane in living plants. *Biogeosciences*, 12(6):1907–1914, 2015.

[111] Jan Peter Lesschen, Gerard L Velthof, Wim de Vries, and Johannes Kros. Differentiation of nitrous oxide emission factors for agricultural soils. *Environmental Pollution*, 159(11): 3215–3222, 2011.

[112] Li-cor. Wavelength modulation spectroscopy, 2015. URL `http://www.licor.com/env/products/gas_analysis/LI-7700/wms.html`.

[113] Yang Lin and Jennifer Y King. Effects of uv exposure and litter position on decomposition in a california grassland. *Ecosystems*, 17(1):158–168, 2014.

[114] Losgatos. Trace gas analyzers, 2015. URL `http://www.lgrinc.com/analyzers/trace-gas/`.

[115] lumasenseinc. Lumasense gas monitoring instruments, 2015. URL `www.lumasenseinc.com/EN/products/gas-monitoring-instruments/`.

[116] Marja Maljanen, Pertti J Martikainen, Heikki Aaltonen, and Jouko Silvola. Short-term variation in fluxes of carbon dioxide, nitrous oxide and methane in cultivated and forested organic boreal soils. *Soil Biology and Biochemistry*, 34(5):577–584, 2002.

[117] Nicolas Marron, Caroline Plain, Bernard Longdoz, and Daniel Epron. Seasonal and daily time course of the 13c composition in soil co2 efflux recorded with a tunable diode laser spectrophotometer (tdls). *Plant and soil*, 318(1-2):137–151, 2009.

[118] Mikhail Mastepanov, Charlotte Sigsgaard, Edward J Dlugokencky, Sander Houweling, Lena Ström, Mikkel P Tamstorf, and Torben R Christensen. Large tundra methane burst during onset of freezing. *Nature*, 456(7222):628–630, 2008.

[119] D McDermitt, G Burba, L Xu, T Anderson, A Komissarov, B Riensche, J Schedlbauer, G Starr, D Zona, W Oechel, et al. A new low-power, open-path instrument for measuring methane flux by eddy covariance. *Applied Physics B*, 102(2):391–405, 2011.

[120] AR McLeod and SP Long. Free-air carbon dioxide enrichment (face) in global change research: a review. *Advances in ecological research*, 28:1–56, 1999.

[121] John B Miller and Pieter P Tans. Calculating isotopic fractionation from atmospheric measurements at various scales. *Tellus B*, 55(2):207–214, 2003.

[122] RJ Millington and JP Quirk. Permeability of porous solids. *Transactions of the Faraday Society*, 57:1200–1207, 1961.

[123] Angelo Minissale, Williams C Evans, Gabriella Magro, and Orlando Vaselli. Multiple source components in gas manifestations from north-central italy. *Chemical Geology*, 142 (3):175–192, 1997.

[124] John Moncrieff, Riccardo Valentini, Susanna Greco, Seufert Guenther, and Paolo Ciccioli. Trace gas exchange over terrestrial ecosystems: methods and perspectives in micrometeorology. *Journal of experimental botany*, 48(5):1133–1142, 1997.

[125] Tim Moore, Nigel Roulet, and Roger Knowles. Spatial and temporal variations of methane flux from subarctic/northern boreal fens. *Global Biogeochemical Cycles*, 4(1):29–46, 1990.

[126] Andrew B Moyes, Sarah J Gaines, Rolf TW Siegwolf, and David R Bowling. Diffusive fractionation complicates isotopic partitioning of autotrophic and heterotrophic sources of soil respiration. *Plant, cell & environment*, 33(11):1804–1819, 2010.

[127] MC Myklebust, LE Hipps, and Ronald J Ryel. Comparison of eddy covariance, chamber, and gradient methods of measuring soil co2 efflux in an annual semi-arid grass, bromus tectorum. *agricultural and forest meteorology*, 148(11):1894–1907, 2008.

[128] Albrecht Neftel, Christof Ammann, Cornelia Fischer, Christoph Spirig, Franz Conen, Lukas Emmenegger, Bela Tuzson, and Susanne Wahlen. N 2 o exchange over managed grassland: Application of a quantum cascade laser spectrometer for micrometeorological flux measurements. *Agricultural and Forest Meteorology*, 150(6):775–785, 2010.

[129] Nick Nickerson and Dave Risk. Keeling plots are non-linear in non-steady state diffusive environments. *Geophysical Research Letters*, 36(8), 2009.

[130] Nick Nickerson and Dave Risk. A numerical evaluation of chamber methodologies used in measuring the δ13c of soil respiration. *Rapid Communications in Mass Spectrometry*, 23 (17):2802–2810, 2009.

[131] Nick Nickerson and Dave Risk. Physical controls on the isotopic composition of soil-respired co2. *Journal of Geophysical Research: Biogeosciences (2005–2012)*, 114(G1), 2009.

[132] Nick Nickerson, Jocelyn Egan, and Dave Risk. Iso-fd: A novel method for measuring the isotopic signature of surface flux. *Soil Biology and Biochemistry*, 62:99–106, 2013.

[133] Elena Norina. Northern wetlands. *Term paper, ETH*, 2007.

[134] Rajendra K Pachauri, MR Allen, VR Barros, J Broome, W Cramer, R Christ, JA Church, L Clarke, Q Dahe, P Dasgupta, et al. Climate change 2014: Synthesis report. contribution of working groups i, ii and iii to the fifth assessment report of the intergovernmental panel on climate change. 2014.

[135] Dario Papale, M Reichstein, Marc Aubinet, E Canfora, C Bernhofer, W Kutsch, B Longdoz, S Rambal, R Valentini, T Vesala, et al. Towards a standardized processing of net ecosystem exchange measured with eddy covariance technique: algorithms and uncertainty estimation. *Biogeosciences*, 3(4):571–583, 2006.

[136] Krishnan R Parameswaran, David I Rosen, Mark G Allen, Alan M Ganz, and Terence H Risby. Off-axis integrated cavity output spectroscopy with a mid-infrared interband cascade laser for real-time breath ethane measurements. *Applied optics*, 48(4):B73–B79, 2009.

[137] DE Pataki, JR Ehleringer, LB Flanagan, D Yakir, DR Bowling, CJ Still, N Buchmann, JO Kaplan, and JA Berry. The application and interpretation of keeling plots in terrestrial carbon cycle research. *Global Biogeochemical Cycles*, 17(1), 2003.

[138] Eric Paterson, Andrew J Midwood, and Peter Millard. Through the eye of the needle: a review of isotope approaches to quantify microbial processes mediating soil carbon balance. *New Phytologist*, 184(1):19–33, 2009.

[139] E Pattey, IB Strachan, RL Desjardins, and J Massheder. Measuring nighttime co 2 flux over terrestrial ecosystems using eddy covariance and nocturnal boundary layer methods. *Agricultural and Forest Meteorology*, 113(1):145–158, 2002.

[140] ERLP Pattey, RL Desjardins, and P Rochette. Accuracy of the relaxed eddy-accumulation technique, evaluated using co2 flux measurements. *Boundary-Layer Meteorology*, 66(4): 341–355, 1993.

[141] O Peltola, A Hensen, C Helfter, L Belelli Marchesini, FC Bosveld, WCM Van Den Bulk, JA Elbers, S Haapanala, Jutta Holst, T Laurila, et al. Evaluating the performance of commonly used gas analysers for methane eddy covariance flux measurements: the ingos inter-comparison field experiment. *Biogeosciences Discussions*, 11(1):797–852, 2014.

[142] Olli Peltola et al. Field intercomparison of four methane gas analysers suitable for eddy covariance flux measurements. 2011.

[143] Anna Katinka Petersen. *Atmospheric Trace Gas Measurements in the Tropics*. Citeseer, 2009.

[144] Rebecca Phillips, David WT Griffith, Feike Dijkstra, Glenys Lugg, Roy Lawrie, and Ben Macdonald. Tracking short-term effects of nitrogen-15 addition on nitrous oxide fluxes using fourier-transform infrared spectroscopy. *Journal of environmental quality*, 42(5): 1327–1340, 2013.

[145] Picarro. Picarro g2301 and g2401 analyzers, 2015. URL `http://www.picarro.com/products_solutions/trace_gas_analyzers/co_co2_ch4_h2o`.

[146] M Pihlatie, J Rinne, P Ambus, K Pilegaard, JR Dorsey, Ü Rannik, T Markkanen, S Launiainen, and T Vesala. Nitrous oxide emissions from a beech forest floor measured by eddy covariance and soil enclosure techniques. *Biogeosciences Discussions*, 2(3):581–607, 2005.

[147] V Piscopo, M Barbieri, V Monetti, G Pagano, S Pistoni, E Ruggi, and D Stanzione. Hydrogeology of thermal waters in viterbo area, central italy. *Hydrogeology Journal*, 14 (8):1508–1521, 2006.

[148] Jukka Pumpanen, Pasi Kolari, Hannu Ilvesniemi, Kari Minkkinen, Timo Vesala, Sini Niinistö, Annalea Lohila, Tuula Larmola, Micaela Morero, Mari Pihlatie, et al. Comparison of different chamber techniques for measuring soil co2 efflux. *Agricultural and Forest Meteorology*, 123(3):159–176, 2004.

[149] Radboud. Trace gas research group, wavelength modulation spectroscopy (wms) and frequency modulation spectroscopy (fms), 2015. URL `http://www.ru.nl/tracegasfacility/trace_gas_research/spectroscopic/wavelength/`.

[150] KIT Ralf Kiese. private communication, 2015.

[151] Ü Rannik, S Haapanala, NJ Shurpali, I Mammarella, S Lind, N Hyvönen, O Peltola, M Zahniser, PJ Martikainen, and T Vesala. Intercomparison of fast response commercial gas analysers for nitrous oxide flux measurements under field conditions. *Biogeosciences*, 12(2):415–432, 2015.

[152] Ana Rey, Luca Belelli-Marchesini, Ana Were, Penelope Serrano-ortiz, Giuseppe Etiope, Dario Papale, Francisco Domingo, and Emiliano Pegoraro. Wind as a main driver of the net ecosystem carbon balance of a semiarid mediterranean steppe in the south east of spain. *Global Change Biology*, 18(2):539–554, 2012.

[153] HJI Rinne, AC Delany, JP Greenberg, and AB Guenther. A true eddy accumulation system for trace gas fluxes using disjunct eddy sampling method. *Journal of Geophysical Research: Atmospheres (1984–2012)*, 105(D20):24791–24798, 2000.

[154] HJI Rinne, AB Guenther, C Warneke, JA De Gouw, and SL Luxembourg. Disjunct eddy covariance technique for trace gas flux measurements. *Geophysical Research Letters*, 28 (16):3139–3142, 2001.

[155] D Risk, N Nickerson, CL Phillips, L Kellman, and M Moroni. Drought alters respired δ 13 co 2 from autotrophic, but not heterotrophic soil respiration. *Soil Biology and Biochemistry*, 50:26–32, 2012.

[156] David Risk and Lisa Kellman. Isotopic fractionation in non-equilibrium diffusive environments. *Geophysical Research Letters*, 35(2), 2008.

[157] W Roedel. Physik unserer umwelt. dynamik der bodennahen luftschichten, diffusion und austausch in bodennähe, 1992.

[158] Benjamin RK Runkle, Christian Wille, Michal Gažovič, and Lars Kutzbach. Attenuation correction procedures for water vapour fluxes from closed-path eddy-covariance systems. *Boundary-layer meteorology*, 142(3):401–423, 2012.

[159] Susanna Rutledge, David I Campbell, Dennis Baldocchi, and Louis A Schipper. Photodegradation leads to increased carbon dioxide losses from terrestrial organic matter. *Global Change Biology*, 16(11):3065–3074, 2010.

[160] Michael G Sanderson. Emission of carbon monoxide by vegetation and soils. *A Literature Review and Recommendations for STOCHEM*, 286, 2002.

[161] Gunnar W Schade, Rolf-M Hofmann, and Paul J Crutzen. Co emissions from degrading plant matter. *Tellus B*, 51(5):889–908, 1999.

[162] David S Schimel. Drylands in the earth system. *Science*, 327(5964):418–419, 2010.

[163] Hans Peter Schmid. Footprint modeling for vegetation atmosphere exchange studies: a review and perspective. *Agricultural and Forest Meteorology*, 113(1):159–183, 2002.

[164] KA Smith, T Ball, F Conen, KE Dobbie, J Massheder, and A Rey. Exchange of greenhouse gases between soil and atmosphere: interactions of soil physical factors and biological processes. *European Journal of Soil Science*, 54(4):779–791, 2003.

[165] LC Smith, GM MacDonald, AA Velichko, DW Beilman, OK Borisova, KE Frey, KV Kremenetski, and Y Sheng. Siberian peatlands a net carbon sink and global methane source since the early holocene. *Science*, 303(5656):353–356, 2004.

[166] W Kolby Smith, Wei Gao, Heidi Steltzer, Matthew D Wallenstein, and Roger Tree. Moisture availability influences the effect of ultraviolet-b radiation on leaf litter decomposition. *Global Change Biology*, 16(1):484–495, 2010.

[167] Susan Solomon. *Climate change 2007-the physical science basis: Working group I contribution to the fourth assessment report of the IPCC*, volume 4. Cambridge University Press, 2007.

[168] Henry G Spratt and Jerry S Hubbard. Carbon monoxide metabolism in roadside soils. *Applied and environmental microbiology*, 41(5):1192–1201, 1981.

[169] Thomas F Stocker, Dahe Qin, Gian-Kasper Plattner, M Tignor, Simon K Allen, Judith Boschung, Alexander Nauels, Yu Xia, Vincent Bex, and Pauline M Midgley. Climate change 2013: The physical science basis. *Intergovernmental Panel on Climate Change, Working Group I Contribution to the IPCC Fifth Assessment Report (AR5)(Cambridge Univ Press, New York)*, 2013.

[170] Roland B Stull. *Meteorology for scientists and engineers: a technical companion book with Ahrens' Meteorology Today*. Brooks/Cole, 2000.

[171] Patrick Sturm, Werner Eugster, and Alexander Knohl. Eddy covariance measurements of co2 isotopologues with a quantum cascade laser absorption spectrometer. *Agricultural and Forest Meteorology*, 152:73–82, 2012.

[172] Alfi Syakila and Carolien Kroeze. The global nitrous oxide budget revisited. *Greenhouse Gas Measurement and Management*, 1(1):17–26, 2011.

[173] Jianwu Tang, Dennis D Baldocchi, Ye Qi, and Liukang Xu. Assessing soil co 2 efflux using continuous measurements of co 2 profiles in soils with small solid-state sensors. *Agricultural and Forest Meteorology*, 118(3):207–220, 2003.

[174] Matthew A Tarr, William L Miller, and Richard G Zepp. Direct carbon monoxide photoproduction from plant matter. *Journal of Geophysical Research: Atmospheres (1984–2012)*, 100(D6):11403–11413, 1995.

[175] Heather L Throop and Steven R Archer. Interrelationships among shrub encroachment, land management, and litter decomposition in a semidesert grassland. *Ecological Applications*, 17(6):1809–1823, 2007.

[176] Heather L Throop and Steven R Archer. Resolving the dryland decomposition conundrum: some new perspectives on potential drivers. In *Progress in botany*, pages 171–194. Springer, 2009.

[177] Agnes Tirol-Padre, Munmun Rai, Mahesh Gathala, Sheetal Sharma, Virender Kumar, Parbodh C Sharma, Dinesh K Sharma, Reiner Wassmann, and Jagdish Ladha. Assessing the performance of the photo-acoustic infrared gas monitor for measuring co2, n2o, and ch4 fluxes in two major cereal rotations. *Global change biology*, 20(1):287–299, 2014.

[178] Susan Trumbore. Age of soil organic matter and soil respiration: radiocarbon constraints on belowground c dynamics. *Ecological Applications*, 10(2):399–411, 2000.

[179] B Tuzson, RV Hiller, K Zeyer, W Eugster, A Neftel, C Ammann, and L Emmenegger. Field intercomparison of two optical analyzers for ch 4 eddy covariance flux measurements. *Atmospheric Measurement Techniques*, 3(6):1519–1531, 2010.

[180] Stephan Unger, Cristina Máguas, João S Pereira, Luis M Aires, Teresa S David, and Christiane Werner. Disentangling drought-induced variation in ecosystem and soil respiration using stable carbon isotopes. *Oecologia*, 163(4):1043–1057, 2010.

[181] Stephan Unger, Cristina Máguas, João S Pereira, Teresa S David, and Christiane Werner. Interpreting post-drought rewetting effects on soil and ecosystem carbon dynamics in a mediterranean oak savannah. *Agricultural and Forest Meteorology*, 154:9–18, 2012.

[182] Shauna M Uselman, Keirith A Snyder, Robert R Blank, and Timothy J Jones. Uvb exposure does not accelerate rates of litter decomposition in a semi-arid riparian ecosystem. *Soil Biology and Biochemistry*, 43(6):1254–1265, 2011.

[183] H. van Asperen, T. Warneke, S. Sabbatini, G. Nicolini, D. Papale, and J. Notholt. The role of photo- and thermal degradation for co_2 and co fluxes in an arid ecosystem. *Biogeosciences*, 12(13):4161–4174, 2015. doi: 10.5194/bg-12-4161-2015. URL `http://www.biogeosciences.net/12/4161/2015/`.

[184] T Vesala, N Kljun, Ü Rannik, J Rinne, Andrey Sogachev, T Markkanen, K Sabelfeld, Th Foken, and MY Leclerc. Flux and concentration footprint modelling: State of the art. *Environmental Pollution*, 152(3):653–666, 2008.

[185] I Vigano, H Van Weelden, R Holzinger, F Keppler, T Röckmann, et al. Effect of uv radiation and temperature on the emission of methane from plant biomass and structural components. *Biogeosciences Discussions*, 5(1):243–270, 2008.

[186] secretariaat van de Commissie Bemesting Akkerbouw/Vollegrondsgroententeelt Wageningen University. Handboek bodem en bemesting, 2015. URL `http://www.handboekbodemenbemesting.nl/nl/handboekbodemenbemesting/Handeling/Bemesting/Type-meststoffen-en-hun-werking-en-efficientie.htm`.

[187] JM Wang, JG Murphy, JA Geddes, CL Winsborough, N Basiliko, and SC Thomas. Methane fluxes measured by eddy covariance and static chamber techniques at a temperate forest in central ontario, canada. *Biogeosciences*, 10(6):4371–4382, 2013.

[188] Xin Wang, Lingli Liu, Shilong Piao, Ivan A Janssens, Jianwu Tang, Weixing Liu, Yonggang Chi, Jing Wang, and Shan Xu. Soil respiration under climate warming: differential response of heterotrophic and autotrophic respiration. *Global change biology*, 20(10):3229–3237, 2014.

[189] Spencer R Weart. *The discovery of global warming: revised and expanded edition*. Harvard University Press, 2008.

[190] Christiane Werner and A Gessler. Diel variations in the carbon isotope composition of respired co (2) and associated carbon sources: a review of dynamics and mechanisms. *Biogeosciences*, 8(9), 2011.

[191] Martin Werth and Yakov Kuzyakov. 13 c fractionation at the root–microorganisms–soil interface: a review and outlook for partitioning studies. *Soil Biology and Biochemistry*, 42 (9):1372–1384, 2010.

[192] SC Whalen and WS Reeburgh. Carbon monoxide consumption in upland boreal forest soils. *Soil Biology and Biochemistry*, 33(10):1329–1338, 2001.

[193] Craig E Williamson, Susanne L Metzgar, Patricia A Lovera, and Robert E Moeller. Solar ultraviolet radiation and the spawning habitat of yellow perch, perca flavescens. *Ecological Applications*, 7(3):1017–1023, 1997.

[194] HM Worden, MN Deeter, Christian Frankenberg, Maya George, Florian Nichitiu, John Worden, Ilse Aben, KW Bowman, Cathy Clerbaux, Pierre-François Coheur, et al. Decadal record of satellite carbon monoxide observations. *Atmospheric Chemistry and Physics*, 13 (2):837–850, 2013.

[195] Jonathan G Wynn, Jennifer W Harden, and Terry L Fries. Stable carbon isotope depth profiles and soil organic carbon dynamics in the lower mississippi basin. *Geoderma*, 131 (1):89–109, 2006.

[196] S Yamulki and SC Jarvis. Automated chamber technique for gaseous flux measurements: Evaluation of a photoacoustic infrared spectrometer-trace gas analyzer. *Journal of Geophysical Research: Atmospheres (1984–2012)*, 104(D5):5463–5469, 1999.

[197] PC Yang, T Andrew Black, Herman H Neumann, MD Novak, and PD Blanken. Spatial and temporal variability of co2 concentration and flux in a boreal aspen forest. 1999.

[198] S Yonemura, S Kawashima, and H Tsuruta. Carbon monoxide, hydrogen, and methane uptake by soils in a temperate arable field and a forest. *Journal of Geophysical Research: Atmospheres (1984–2012)*, 105(D11):14347–14362, 2000.

[199] Lingfei Yu, Hao Wang, Guangshuai Wang, Weimin Song, Yao Huang, Sheng-Gong Li, Naishen Liang, Yanhong Tang, and Jin-Sheng He. A comparison of methane emission measurements using eddy covariance and manual and automated chamber-based techniques in tibetan plateau alpine wetland. *Environmental Pollution*, 181:81–90, 2013.

[200] J Curiel Yuste, IA Janssens, and R Ceulemans. Calibration and validation of an empirical approach to model soil co2 efflux in a deciduous forest. *Biogeochemistry*, 73(1):209–230, 2005.

[201] Richard G Zepp, TV Callaghan, and DJ Erickson. Effects of enhanced solar ultraviolet radiation on biogeochemical cycles. *Journal of Photochemistry and Photobiology B: Biology*, 46(1):69–82, 1998.

[202] Tao Zhou, Peijun Shi, Dafeng Hui, and Yiqi Luo. Global pattern of temperature sensitivity of soil heterotrophic respiration (q10) and its implications for carbon-climate feedback. *Journal of Geophysical Research: Biogeosciences (2005–2012)*, 114(G2), 2009.

[203] Donatella Zona, IA Janssens, Marc Aubinet, B Gioli, Sara Vicca, Regis Fichot, Reinhart Ceulemans, et al. Fluxes of the greenhouse gases (co2, ch4 and n2o) above a short-rotation poplar plantation after conversion from agricultural land. *Agricultural and Forest Meteorology*, 169(Complete):100–110, 2013.